

UC Merced

UC Merced Electronic Theses and Dissertations

Title

Additive Manufacturing of Conjugated Polymers

Permalink

<https://escholarship.org/uc/item/57z9t3n7>

Author

Hill, Ian Michael

Publication Date

2024

Copyright Information

This work is made available under the terms of a Creative Commons Attribution License, available at <https://creativecommons.org/licenses/by/4.0/>

Peer reviewed|Thesis/dissertation

UNIVERSITY OF CALIFORNIA, MERCED

Additive Manufacturing of Conjugated Polymers

A dissertation submitted in partial satisfaction of the requirements for the degree
of
Doctor of Philosophy
in
Materials and Biomaterials Science and Engineering

by
Ian M. Hill

December 2024

Dissertation Committee:

Professor Sarah Kurtz, Chair

Professor Po-Ya Abel Chuang

Professor Andy LiWang

Professor Yue Jessica Wang, Advisor

SIGNATURE PAGE

The Dissertation of Ian M. Hill is approved, and it is acceptable in quality and form for publication on microfilm and electronically:

Professor Sarah Kurtz, Chair and Committee Member

Professor Po-Ya Abel Chuang, Committee Member

Professor Andy LiWang, Committee Member

Professor Yue Jessica Wang, Advisor and Committee Member

TABLE OF CONTENTS

- 1. Overview of the Additive Manufacturing of Conjugated Polymers**
 - 1.1. General Overview
 - 1.2. Factors Influencing Conductivity
 - 1.2.1. Chemical Doping to Increase CP Conductivity
 - 1.2.2. Secondary Doping
 - 1.3. Improving Solution Processability of CPs
 - 1.4. Conventional 2D Processing of CPs and Their Limitations
 - 1.5. Overview of 3D Printing Methods
 - 1.5.1. Inkjet Printing
 - 1.5.2. Vat Polymerization
 - 1.5.3. Extrusion-Based Methods
 - 1.5.3.1. Fused Deposition Modeling
 - 1.5.3.2. Direct Ink Writing
 - 1.6. Summary of AM Techniques Suitable for CPs
 - 1.6.1. Inkjet Printing
 - 1.6.2. Direct Ink Writing
 - 1.6.3. Vat Polymerization
 - 1.7. Chapter Outline
 - 1.8. References
- 2. Imparting High Conductivity to DIW-Printing PEDOT:PSS**
 - 2.1. Abstract
 - 2.2. Introduction
 - 2.3. Printer Modification
 - 2.4. PEDOT:PSS Ink Optimization
 - 2.4.1. Ink Preparation
 - 2.4.2. Ink Rheology Tuning
 - 2.4.3. Rheology Experimental
 - 2.4.3.1. *Rheological characterization for PEDOT:PSS ink*
 - 2.4.3.2. *Time-dependence of the rheological properties for PEDOT:PSS ink*
 - 2.5. Printing Parameter Optimization and 3D Printing
 - 2.5.1. Experimental for 3D Printing Parameter Tuning
 - 2.5.2. 3D Printing Parameter Tuning
 - 2.5.3. Scanning Electron Microscopy
 - 2.5.4. 3D Printing of PEDOT:PSS
 - 2.6. Electrical Conductivity Characterization
 - 2.6.1. Experimental
 - 2.6.2. Comparison Between 2-Point and 4-Point Measurements
 - 2.6.3. Anisotropic Conductivity of Printed Filament
 - 2.7. Mechanistic Investigation

- 2.7.1. Probing Chain Alignment Through Rheology Simulation
 - 2.7.1.1. *Shear rate calculation for rheology simulation*
 - 2.7.1.2. *Rheology simulation*
- 2.7.2. Wide Angle X-Ray Scattering
- 2.7.3. Atomic Force Microscopy
- 2.7.4. Phase Separation
 - 2.7.4.1. *Identity of the transparent film around the prints*
 - 2.7.4.2. *XPS peak fitting*
- 2.7.5. Relationship Between Phase Separation and Conductivity
 - 2.7.5.1. *Electrode configuration*
 - 2.7.5.2. *Effect of phase separation on conductivity*
- 2.8. Post-Printing DMSO Treatment to Improve Conductivity
 - 2.8.1. Additional data on the effect of DMSO treatment on phase separation
 - 2.8.1.1. *XPS spectra and peak fitting*
- 2.9. Demonstration for 3D Applications
 - 2.9.1. 3D Scanning and Printing
 - 2.9.2. The 3D printing, processing, characterization, and applications of PEDOT:PSS springs
 - 2.9.3. 3D printed PEDOT:PSS omnidirectional LED device
- 2.10. Conclusions and Outlook
- 2.11. References
- 3. Pure PEDOT with complex architectures via 3D printing-assisted casting**
 - 3.1 Abstract
 - 3.2 Introduction
 - 3.3 Experimental
 - 3.4 Results
 - 3.4.1 DBEDOT and SSP-PEDOT Characterization
 - 3.4.1.1 NMR Analysis of DBEDOT Polymerization
 - 3.4.1.1.1 DBEDOT
 - 3.4.1.1.2 SSNMR
 - 3.4.1.2 Characterization of Cast Material
 - 3.4.1.2.1 WAXS
 - 3.4.1.2.2 Electrical and Mechanical Characterization
 - 3.4.2 Molten DBEDOT as a Carrier for Highly Conductive Silver Flakes
 - 3.5 Summary and Outlook
 - 3.6 Supplementary Figures
 - 3.7 References
- 4. Oligoaniline-Assisted Self-Assembly of Polyaniline Crystals**
 - 4.1. Abstract
 - 4.2. Introduction
 - 4.3. Experimental

- 4.3.1. Materials
- 4.3.2. Synthesis of phenyl/amine-capped tetraaniline (Ph/NH₂ TANI)
- 4.3.3. Self-assembly
- 4.3.4. Electron microscopy
- 4.3.5. Spectroscopic characterization
- 4.3.6. Single wire measurement
- 4.4. Chemical characterization of phenyl/amine-capped tetraaniline (Ph/NH₂ TANI)
- 4.5. Results and discussion
 - 4.5.1. Conceptual demonstration
 - 4.5.2. Mechanistic understanding
 - 4.5.3. TANI-assisted crystallization of PANI with defined molecular weights
 - 4.5.4. Spectroscopic and electrical characterization
- 4.6. Conclusions and Outlook
- 4.7. Appendix
- 4.8. References
- 5. Synthesis of modified PAMPSA for rate-adaptive polymers**
 - 5.1. Introduction
 - 5.2. MAMPSA Synthesis
 - 5.2.1. Synthesis Procedure
 - 5.2.2. Results and Discussion
 - 5.2.3. Ion Exchange Reaction for MAMPSA
 - 5.2.3.1. Procedure
 - 5.2.3.2. Results and Discussion
 - 5.3. Urea Monomer Synthesis
 - 5.3.1. Synthesis Procedure
 - 5.3.2. Results and Discussion
 - 5.4. AMPSA and AMPSA-Derivatives Polymerization
 - 5.4.1. Free Radical Polymerization
 - 5.4.1.1. PAMPSA Polymerization
 - 5.4.1.1.1. Procedure
 - 5.4.1.1.2. Results and Discussion
 - 5.4.1.2. Squaramide Polymerization
 - 5.4.1.2.1. Protonation with Cation Exchange Resin Procedure
 - 5.4.1.2.1.1. Observations
 - 5.4.1.2.2. Squaramide Polymerization
 - 5.4.1.2.2.1. Procedure
 - 5.4.1.2.2.2. Results and Observations
 - 5.4.2. RAFT Polymerization
 - 5.4.2.1. RAFT Mechanism and Advantages
 - 5.4.2.2. AMSPA RAFT Polymerization Methods and Procedure

- 5.4.2.2.1. Results and Discussion
- 5.4.2.2.2. MAMPSA Polymerization
- 5.5. Synthesis of PANI:PMAMPSA
 - 5.5.1. Procedure
 - 5.5.2. Observation and Discussion
- 5.6. Conclusions and Outlook
- 5.7. References
- 6. Outlook**

ACKNOWLEDGEMENT

My long journey to getting my PhD involved a lot of time and effort, but also with the help and support from others, I could not have done it without you, thank you.

I would first like to thank my family who has been there for everything. My parents have always been there to support me and encourage me to explore my interests in science and how things work. Thank you for letting me take apart your old phones and electronic devices to see what was inside, and helping me make an electromagnet from a paperclip and old phone cables, interesting books about how things work. I also want to thank Grandma and Grandpa for seeing my scientific curiosity and encouraged me to pursue my interests, and all of the conversations about science and what the future may hold. I also would like to thank Uncle Scott, Brent, and all of my other family for your help.

Second, I'd like to thank my academic advisor, Dr. Jessica Wang, for your mentorship, and guidance. As the first graduate student and graduating PhD from her new lab, I feel that I owe you a great debt for your help, time, and taking a chance on me. Your feedback has helped me become a better critical thinker and scientist, has set the bar high, and has changed what I thought I was capable of doing. Additionally, I am grateful to my colleagues throughout the years, lab mates Victor Hernandez Coreno, especially those long tiring nights collecting data at the synchrotron. Bohao for all of the insightful conversations and travel partner. Dr. Di Wu, Dr. Rob Jordan, Hansong Lee, Kiana Shirzad, and many others.

I would also like to thank members of my previous lab, Dr. Jennifer Lu, Dr. Zihan Zhao, Dr. Wenxin Fu, Dr. Tianyi Kou, and Dr. Dennis McKean for all of your helpful feedback and opportunities to explore the chemistry of materials science.

I would also like to thank my committee members, Dr. Sarah Kurtz, Dr. Po-Ya Abel Chuang, and Dr. Andy LiWang for your feedback, support, and help navigating the process of getting a PhD.

I would like to thank Distinguished Toastmaster Karen Mous for her encouragement to go to Toastmasters and improve my confidence and public speaking skills that I will carry with me for the rest of my life.

I'd like to thank all my friends as well, the staff at UC Merced for all of their help and hard work to make the university and program work, and the professors of classes I took that helped me learn about the fields of materials science and see the world from a new perspective.

CURRICULUM VITAE

EDUCATION

Ph.D., Materials and Biomaterials Science and Engineering

December 2024

University of California, Merced

B.S., Biological Sciences, Genetics concentration, Chemistry minor

2014

California State University, Stanislaus

AWARD(S)

UC Merced Graduate Dean's Dissertation Fellowship

2022

PUBLICATIONS

- R. S. Jordan, J. Frye, V. Hernandez, I. Prado, A. Giglio, N. Abbasizadeh, M. Flores-Martinez, K. Shirzad, B. Xu, **I. M. Hill**, Y. Wang. "3D printed architected conducting polymer hydrogels." *J. Mater. Chem. B*, **2021**, 9, 7258.
- V. Hernandez, R. S. Jordan, **I. M. Hill**, B. Xu, C. Zhai, J. Misiaszek, K. Shirzad, M. F. Martinez, A. Kusoglu, J. Yeo, Y. Wang. "Deformation Rate-Adaptive Conducting Polymers and Composites." *Small*, **2023**, 9, 2207100.
- **I. M. Hill**, V. Hernandez, B. Xu, J. A. Piceno, J. Misiaszek, A. Giglio, E. Junez, J. Chen, P. D. Ashby, R. S. Jordan, Y. Wang. "Imparting High Conductivity to 3D Printed PEDOT:PSS." *ACS Appl. Polym. Mater.*, **2023**, 5, 3989.
***ACS Editor's Choice**
- **I. M. Hill**, D. Wu, B. Xu, Y. Wang. "Oligoaniline-Assisted Self-Assembly of Polyaniline Crystals." *Mater. Horiz.*, **2023**, 10, 1282.
* **Highlighted in Chemistry World**
- B. Xu, D. Wu, **I. M. Hill**, M. Halim, Y. Rubin, Y. Wang. "A new and versatile template towards vertically oriented nanopillars and nanotubes." *Nanoscale Adv.*, **2023**, 5, 4489.
- H. Lee[†], **I. M. Hill**[†], B. Xu, D. Wu, Y. Wang. "Complex 3D structures of PEDOT:PSS via freeze-aging and direct ink printing." (**In preparation**)
[†] **Equal contribution**

- **I. M. Hill**, B. Xu, A. Rosenberg, J. Chang, D. Wu, W. Rice, E. Tran, L. Gutierrez, Y. Rubin, M. T. Yeung, Y. Wang. “3D Printing-Assisted Casting of Pure PEDOT with Complex Architectures” **(In preparation)**

MEDIA MENTION(S)

“Pure conjugated polymer nanowires crystallised using oligomers.” *Chemistry World*, 8 March **2023**. [<https://www.chemistryworld.com/news/pure-conjugated-polymer-nanowires-crystallised-using-oligomers/4017093.article>]

RESEARCH EXPERIENCE

Graduate Student Researcher, University of California, Merced May
2018-Present

Advisor: *Prof. Yue Jessica Wang*

- Developed and prepared comprehensive sample lists for Wide- and Small-Angle X-ray Scattering (WAXS and SAXS) analysis at the ALS research facility at Lawrence Berkeley National Laboratory and the Stanford Synchrotron Radiation Lightsource (SSRL) on a semiannual basis. Responsible for sample preparation under tight deadlines and delivering high-quality results.
- Developed a new approach to 3D print highly conductive poly(3,4-ethylenedioxythiophene) polystyrene sulfonate (PEDOT:PSS) polymer inks using the direct ink write (DIW) method.
- Expanded our DIW process to reliably print and pattern other conducting polymers in both 2D and 3D.
- Created and documented standard operating procedures (SOPs) for laboratory-related activities, including the operation of laboratory equipment, appropriate glassware cleaning procedures, and ordering of laboratory supplies.
- Designed and performed experiments for understanding the anisotropic conductivity of PEDOT:PSS that results from phase separation during 3D printing.
- Designed complementary investigation to understand the structure-property relationships of DIW printed PEDOT:PSS.
- Managed the maintenance, troubleshooting activities, usage, and training of multiple 3D printers (BioX, Ultimaker 2+, & homebuilt DIW printers).
- Demonstrated the complete removal of product impurities by modifying the synthetic process of aniline oligomer synthesis.
- Designed and performed synthesis of amphiphilic polymers with various degree of hydrogen-bonding with over 90% yields.
- Performed troubleshooting and solved instability problems that occur in the synthesis of a novel, strong hydrogen-bonding monomer.
- Validated chemicals purchased from suppliers using gel permeation chromatography (GPC), proton nuclear magnetic resonance spectroscopy (¹H NMR), and thin layer chromatography (TLC).

- Delineated the chemical identity of various polymers through complementary characterization.
- Developed synthesis for polyethylene glycol-based crosslinkers for SLA printing.
- Played an instrumental role in developing the project idea of fabricating microscale conductive PEDOT with complex 3D shapes using 3D printed sacrificial molds as a key member of the team.

Graduate Student Researcher, University of California, Merced June 2016-
April 2018

Advisor: *Prof. Jennifer Lu*

- Synthesized dibenzocycloocta-1,5-dienes with arene and hydrogen bonding substituents.
- Synthesized comb-type poly(*N*-isopropylacrylamide) hydrogels containing functionalized graphene oxide.

Undergraduate Research Assistant, California State University, Stanislaus
2014

Advisor: *Prof. Chad Stessman*

- Carried out bromination of 4-methylanisole.

TECHNICAL SKILLS & SOFTWARES

Small-molecule and polymer design and synthesis

- Air-sensitive organic synthesis
- RAFT polymerization, free radical polymerization, Fe-catalyzed polymerization
- Proton nuclear magnetic resonance spectroscopy (¹H NMR)
- Organic extraction
- Short-path distillation
- Silica gel column chromatography, ion exchange chromatography
- Gel permeation chromatography (GPC)

Materials characterization

- Fourier-transform infrared spectroscopy (FTIR)
- Ultraviolet-visible-near-infrared spectroscopy (UV-Vis-NIR)
- Scanning Electron Microscopy (SEM)
- Contact profilometry
- Four-point probe measurements
- Rheometry
- Synchrotron X-ray small-angle and wide-angle scattering (SAXS and WAXS)
- Differential scanning calorimetry (DSC)

3D printing and patterning

- Computer aided design (CAD)
- G-code editing
- Direct ink write (DIW) 3D printing
- Light-based 3D printing: stereolithography (SLA) and digital light projection (DLP)

Software

- AutoCAD, Inventor, Tinkercad
- ChemDraw
- Reaxys
- MestReNova
- Origin
- Microsoft Word, Excel, PowerPoint

SELECTED PRESENTATIONS

I. M. Hill, V. Hernandez, B. Xu, J. A. Piceno, J. Misiaszek, A. Giglio, E. Junez, J. Chen, P. D. Ashby, R. S. Jordan, Y. Wang, Imparting High Conductivity to 3D Printed Conducting Polymers. Oral presentation at the *264th ACS Fall National Meeting*, Chicago, IL, United States, 21-25 August **2022**.

I. M. Hill, V. Hernandez, B. Xu, J. A. Piceno, J. Misiaszek, A. Giglio, E. Junez, J. Chen, P. D. Ashby, R. S. Jordan, Y. Wang, Imparting High Conductivity to 3D Printed Conducting Polymers. Poster presentation at the *Additive Manufacturing of Soft Materials Gordon Research Conference*, Ventura, CA, United States, 7-12 August **2022**.

I. M. Hill, W. Fu, Large Negative Thermal Expansion of a Polymer Driven by a Submolecular Conformational Change. Poster presented at the *255th ACS Spring National Meeting*, New Orleans, LA, United States, 18-22 March **2018**.

I. M. Hill, Near Infrared Responsive Hydrogels with Fast and Spatially Controlled Responses. Poster presented at the *253rd ACS Spring National Meeting*, San Francisco, CA, United States, 2-6 April **2017**.

LEADERSHIP EXPERIENCE

Leadership

- Club President of Toastmasters International, Linguistic Lynx Club, 2019-2021.

- Safety officer of Wang Lab at UC Merced—led annual safety audits, monthly self-inspections, weekly lab cleanups, organization of chemical inventory, and safety training for new lab members, *2019-2022*.

Mentorship

- One postdoctoral researcher on polymer synthesis, *2022*,
- Three junior PhD students on organic synthesis and 3D printing, *2021*,
- Six undergraduate research students on organic synthesis and 3D printing, *2017-2019*.

Outreach

- Co-designer and co-leader of a 3D printing workshop through CalTeach for junior high students in the San Joaquin area, *2021*.
- Lead volunteer for MACES undergraduate outreach program “Crime lab sensors module,” *2017*.

ABSTRACT

Conducting polymers (CPs) are widely used in applications including wearable electronics, on-skin biosensors, and tissue engineering, all of which can benefit from custom 3D topographies via additive manufacturing (AM), also known as 3D printing. However, the environmental and processing sensitivities of CPs render the combination of structural complexity and high electrical conductivity difficult to achieve. In this dissertation, I will discuss the strategies developed through my PhD work that have overcome some of these challenges. First, by taking advantage of the solution processability of CPs, we employed direct ink write (DIW) to print a custom poly(3,4-ethylenedioxythiophene):poly(styrenesulfonate) (PEDOT:PSS) ink. The printed specimens exhibit moderate conductivity and high anisotropy. A variety of complementary characterizations revealed that the anisotropic conductivity is a result of the phase separation between PEDOT and PSS. Removal of the PSS shell has reduced anisotropy and led to a significant increase of conductivity to over 1200 S/cm. However, the structural complexity of the resulting prints is low due to the intrinsic limitations of the DIW technique, prompting us to explore a two-step vat-polymerization method to first 3D print the dopant network followed by infiltrating CPs through interfacial polymerization. Excellent geometric complexity has been achieved; however, the conductivity is unsatisfactory (<0.1 S/cm) due to the high dopant polymer concentration. Finally, we developed a 3D printing-assisted casting method to balance shape complexity and high conductivity. A PEDOT precursor is melt-processed into vat-photopolymerized 3D molds. Upon mold removal, the precursor is polymerized into PEDOT in the solid-state with excellent shape-retention. Complex objects such as octet, truncated octahedron, and trees have been achieved. Their electrical conductivity can be made as high as 7000 S/cm by compositing the molten precursor with silver flakes. Collectively, this body of work has led to an improved understanding of processing-structure-property relationships of 3D printed conducting polymers as well as new methods for additively manufacturing these chemically temperamental electronic materials, opening doors to new applications.

Chapter 1

Overview of the additive manufacturing of conjugated polymers

1.1 General overview

Conjugated polymers (CPs) are organic materials that are conducting or semiconducting (Figure 1.1). Their discovery and development have led to innovations in lightweight, low-cost solar cells, light-emitting diodes, and field-effect transistors.¹ These devices are typically two-dimensional (2D), and hence can be fabricated from spin-coated CP thin films followed by top-down patterning techniques such as lithography. In recent years, CPs have been extensively used in emerging applications such as on-skin, wearable, and implantable electronics and bioelectronics or even tissue engineering due to their tunable mechanical, electronic, and chemical properties.²⁻⁶ These applications require intimate contact between soft electronics and the body or organ, which have three-dimensional (3D) contour that differ from person-to-person. Devising strategies to process CPs into 3D topographies while retaining their electrical properties has emerged as a new challenge and research priority. Therefore, developing additive manufacturing (AM), also known as 3D printing, routes to process this class of materials carries urgency and can provide new opportunities for the field of CPs.

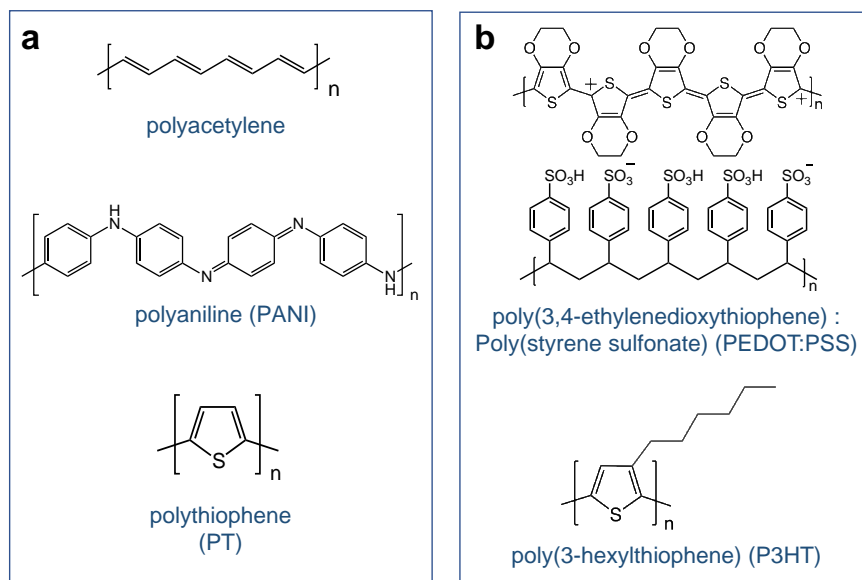


Figure 1.1. Examples of common CPs with properties (a) controlled through chemical structures through synthetic design, (b) examples of synthetic tuning to make CPs solution-processable.

The AM of CPs presents more challenges than most other classes of polymers due to a number of processability restrictions that arise from their chemical structures. Specifically, the mobility of CP chains is strongly restricted by intermolecular π - π interactions, which result in poor solubility and meltability.⁷ At the same time, the delocalization of π electrons along this conjugated backbone is responsible for endowing CPs with electrically conductive properties.⁸

Each of these double bonds, or π bonds, forms from overlapping p-orbitals (Figure 1.2a). Electronic interactions between these π bonds of the conjugated backbone system causes energy level splitting of π orbitals into π (bonding) and π^* (antibonding) orbitals. Every additional monomer unit added to a CP increases the number of π and π^* orbitals to the conjugated system, leading to the formation of a conduction band with a lowest unoccupied molecular orbital (LUMO) and a valence band with a highest occupied molecular orbital (HOMO). These additional energy states increase the energy level of the HOMO and decrease the energy level of the LUMO, which are separated by a band gap (E_g) energy barrier (Figure 1.2b). For charges to conduct, sufficient energy must be introduced to π electrons in the valence band to allow for a transition through the E_g to the conduction band.⁸ Materials with a E_g above 3.0 eV are generally considered insulators, between 0.1 and 3.0 eV are generally considered semiconductors, and below 0.1 eV are generally considered conductors.⁹

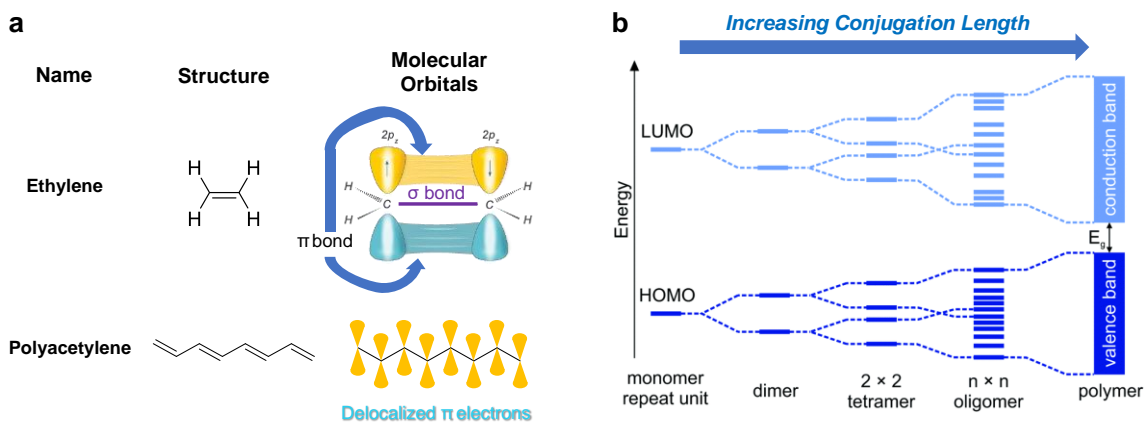


Figure 1.2. (a) Figure showing the overlapping p orbitals (π bonds) in ethylene (top) and polyacetylene (bottom). (b) Diagram showing the emergence of valence and conduction bands from the numerous energy levels that emerge from longer conjugation length of a CP.¹⁰

1.2 Factors Influencing Conductivity

Conductivity can be generally expressed mathematically by eq. 1.1.¹¹

$$\sigma = ne\mu, \quad \text{eq. 1.1}$$

where σ is electrical conductivity of a material, e is the charge of an electron in coulombs, n is the number of charge carriers, which can be holes in p-type or electrons in n-type materials, and μ is the mobility of charge carriers.¹¹ Since most CPs are p-type, including the ones in this dissertation, the primary focus here will be dedicated to main strategies to control the conductivity of p-type CPs.⁸

However, eq. 1.1 mostly describes the charge transport within polymer chains, or intrachain conductivity ($\sigma_{intrachain}$). CPs in film or bulk forms can often have very different crystallinity and microstructures depending on processing conditions. These factors can greatly affect the bulk conductivity (σ_{bulk}) of CPs. The quality of interchain conductivity ($\sigma_{interchain}$) is dictated by the quality of p-orbital overlapping between adjacent chains, which is often related to the degree of crystallinity of CPs. In addition, the degree of overlap or connectivity between adjacent domains, which can be between two crystallites or between a crystallite and the surrounding amorphous regions, within the CP microstructure also dictates the bulk conductivity. This is commonly referred to as interdomain conductivity ($\sigma_{interdomain}$). Collectively, the bulk conductivity of CPs can be expressed by eq. 1.2.¹¹

$$\sigma_{bulk} = F(\sigma_{intrachain}, \sigma_{interchain}, \sigma_{interdomain}) \quad \text{eq. 1.2}$$

1.2.1 Chemical Doping to Increase CP Conductivity

One important factor influencing a CP's conductivity is its number of charge carriers, n (eq. 1.1). For example, the emeraldine base form of polyaniline (PANI) contains the conjugated backbone structure of overlapping π electrons characteristic of CPs, which is necessary for charge transport along the conjugated system.¹² However, it contains very few charge carriers, and thus behaves as an insulator. A common strategy used to improve conductivity is by increasing the number of hole carriers in CPs by the addition of a primary dopant, which can be carried out by protonation or addition of an oxidant to remove π electrons from the

conjugated system. One example of using oxidative dopant strategy to increase conductivity is by introducing oxidizing halogens such as Br₂ or I₂ to trans-polyacetylene.^{13,14} Another approach to creating hole carriers is by using an acid to protonate the CP. For instance, adding an acid dopant to the electrically insulating emeraldine base form of PANI protonates its nitrogen atoms and converts it into the highly conductive emeraldine salt form (Figure 1.3a).

1.2.2 Secondary Doping

The conductivity of CPs relies on the transport of charges along the delocalized π electrons of their conjugated backbone, and is an influential component of a CP's charge mobility (μ). However, when the polymer does not adopt a linear conformation due to kinks, π orbitals do not overlap, which hinders their charge transport ability and decreases the $\sigma_{interchain}$ and $\sigma_{interdomain}$. One method to overcome this is to use a 'secondary dopant' which is an 'inert' additive that can increase a CP's conductivity, often by alternating its chain conformation, and is retained even after the secondary dopant is removed. An example of this phenomena is when the conductive emeraldine salt form of polyaniline is cast from chloroform. This solvent has little interaction with the charged groups on polyaniline, leading the polymer to adopt a compact coil conformation with many kinked chains due to twist defects between aromatic rings. The localization of charges between two kinks decreases the charge mobility along the polymer chain, resulting in poor conductivity. In a better solvent, the polymer has an extended coil structure with fewer kinks and straighter segments. The fewer twist defects between aromatic rings allow for polarons to be delocalized along the chain, resulting in higher conductivity from greater intrachain μ .

The electronic transitions from different states absorb a characteristic wavelength of light based on the amount of energy required to excite electrons to a new state. These electronic transitions typically occur with light ranging from the ultraviolet to the near infrared region, which makes ultraviolet-visible-near-infrared spectroscopy (UV-Vis-NIR) a valuable tool for probing these electronic transitions.

Using polyaniline (PANI) as a representative CP, it typically has an absorption peak at around 360 nm from the excitement of π band electrons to the π^* band, 440 nm from the excitement of the polaron band electrons to the π^* band, and 780 nm from the excitement of localized π band electrons to the polaron band. However, PANI with delocalized electrons from an extended backbone conformation have a free carrier tail that begins around 1000 nm, and extends into the IR region, rather than the 780 nm peak of the localized electrons.

When the emeraldine salt form of polyaniline has a compact coil conformation, it absorbs at the three characteristic regions of CPs, with absorption

at 360, 440, and 780 nm (Figure 1.3b). The presence of a peak at 360 nm and 780 nm indicates that the coil structure causes twist defects between aromatic rings that prevent delocalization of the polarons, causing them to be localized. This localization remains in films cast from these solutions, and results in low conductivity of ~ 0.1 S/cm.

However, when cast from a more polar solvent like *m*-cresol, the polymer adopts an expanded coil conformation, where the peak at 780 nm disappears and a prominent free-carrier tail appears from around 1000 nm and extending into the IR region. This indicates that a more linear backbone conformation and twist defects between aromatic rings have subsided, allowing for enhanced delocalization of polarons. The polaron band- π^* peak remains at 440 nm, but the π - π^* peak at 360 nm disappears due to the elimination of that energy gap from the merging of the polaron band with the π band. Films cast from these solutions result in high conductivity of ~ 150 S/cm, indicating that chains remain extended after casting.^{11,15}

In order to achieve long-range conductivity, CPs must effectively transfer charges between polymer chains, as noted in eq. 1.2, which is efficiently done in tightly packed crystalline regions, as well as through tie chains which bridge the distances between crystalline regions.¹⁶ Introducing a secondary dopant can improve the ability of CPs to adopt a more linear conformation that allows for more efficient π - π stacking between adjacent polymer chains and improve interchain stacking of highly crystalline regions, leading to higher conductivity. Additionally, some CPs contain insulating components to promote solubility, such as the poly(styrene sulfonate) in poly(3,4-ethylenedioxythiophene):poly(styrene sulfonate) (PEDOT:PSS), which hinders charge transfer between the conductive PEDOT chains. Secondary dopants can be used to improve phase separation between PEDOT and PSS, selectively removing the insulating PSS component, and increase the PEDOT crystallinity. These collective effects can result in conductivity increases of over three orders of magnitude.¹⁷

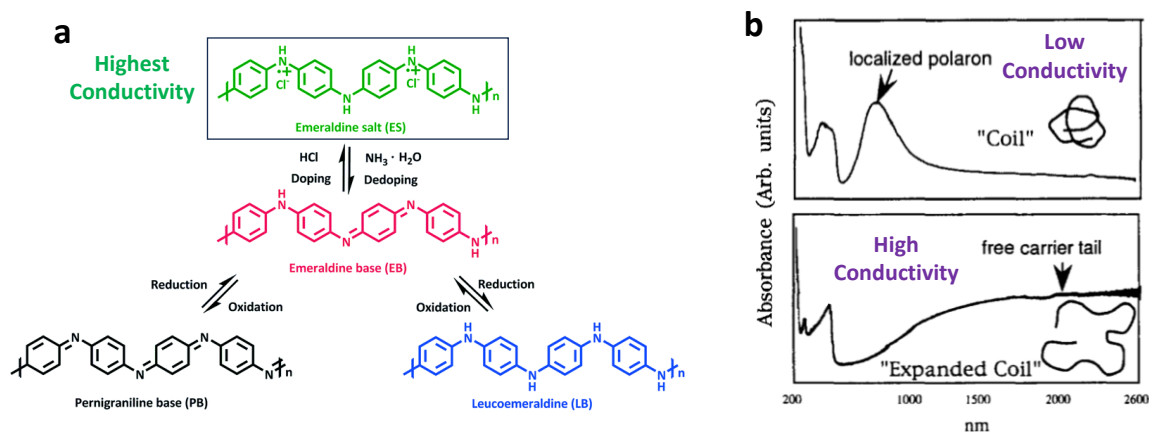


Figure 1.3. (a) Example of doping with acid and oxidant to dope/dedope polyaniline,¹⁸ (b) example of the influence of ‘secondary doping’ effect, where polyaniline has a coil-like shape in a poor solvent (top) and expanded coil in a good solvent with high conductivity in the UV-Vis spectrometry.¹⁵

1.3 Improving Solution Processability of CPs

Processability from melt or solution are standard properties of most polymers, but not for CPs. CPs have a rigid backbone, which makes them exceedingly difficult to dissolve or melt, limiting their widespread use upon their initial discovery and development.¹ Over time, strategies have been developed to make CPs more solution processable, which has become an essential part of their growing appeal. One general strategy to realize solution processability is to attach a solubilizing side chain to the repeating units of CPs, which can increase the resulting polymer’s interactions with a solvent and make it solution processable. Common examples of this approach include the long hydrocarbon chains of poly(3-hexylthiophene) P3HT (Figure 1.1b), or the sulfonic acid sidechain of self-doped PEDOT.^{19,20} Another approach to improving a CP’s solution processability is to use a soluble anionic polymer as the dopant for the insoluble, cationic CP. The most widespread example is PEDOT:PSS (Figure 1.1b). In this example, PEDOT is polymerized via oxidative polymerization in the presence of excess water-soluble PSS. PEDOT becomes positively charged during the oxidative polymerization process, and electrostatically attracts to the negatively charged sulfonate groups of PSS, which keeps the hydrophobic PEDOT in suspension. To minimize the exposure of the hydrophobic PEDOT to the surrounding aqueous solution, the excess PSS forms a hydrophilic shell which encapsulates a PEDOT-rich core.²¹

1.4 Conventional 2D Processing of CPs and Their Limitations

Solution processable CPs are widely used in applications that require thin, lightweight, conductive films, and are typically processed using 2D fabrication methods, such as spin coating or solution casting. However, these fabrication approaches limit the use of these materials to having a flat 2D geometry, and limits what electronics could be made. For instance, wearable electronic devices depend on conformal contact with the uneven surface of an organ, such as the skin, in order to have accurate sensing. Electronics that are designed to fit the uneven 3D surfaces would have more accurate sensing of the desired physiological signals. Additionally, in contrast to 2D fabricated electronics, 3D electronics can have a wide range of geometries to fit into unused spaces.

1.5 Overview of 3D Printing Methods

Before I delve into the details of the 3D printing of CPs, the most commonly used 3D printing methods will be reviewed in this section. They are inkjet printing, vat polymerization (VP), and extrusion-based 3D printing, which contains fused deposition modeling (FDM) and direct ink writing (DIW). Each of these methods follows a distinctive operational mechanism that associates with certain advantages and limitations, including ease of implementation, resolution, scalability, material versatility, and printing speed. An overview of these methods, along with their mechanisms, advantages, and limitations is provided in Figure 1.4.

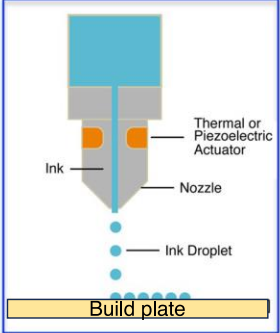
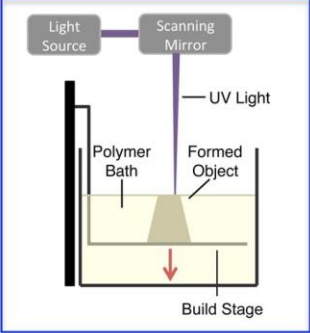
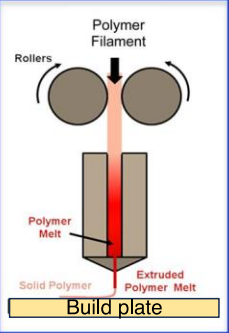
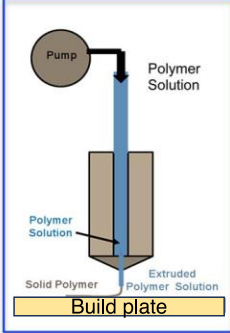
	Inkjet Printing	Vat Polymerization (VP)	Fused Deposition Modeling (FDM)	Direct Ink Writing (DIW)
				
Mechanism	Solution/dispersion jetting	Photopolymerization (curing) of precursors (resin)	Melting or softening (by heating)	Shear thinning (by pressure or displacement)
Advantages	High throughput patterning	<ul style="list-style-type: none"> – High resolution – Excellent shape retention 	<ul style="list-style-type: none"> – Low cost – Applicable to most thermoplastics 	Diverse materials
Limitations	<ul style="list-style-type: none"> – More suitable for 2D structures – Requires low viscosity materials 	<ul style="list-style-type: none"> – Strict resin requirements 	<ul style="list-style-type: none"> – Slow – Limited resolution – Meltable materials only 	<ul style="list-style-type: none"> – Limited resolution – Limited z-dimension – Requires flowability

Figure 1.4. Illustrations of different AM methods.²²

1.5.1 Inkjet Printing

Inkjet printing is a widely used AM technique due to its ability to rapidly produce customized 2D patterns with a range of desirable materials (Figure 1.4). This process is similar to the one used in commercial desktop inkjet printing, but the material can be deposited repeatedly to create 3D objects. In this method, a cartridge containing a low viscosity liquid ink material is positioned above the substrate at the desired locations along an x-y axis, and sprays small ink droplets onto the substrate.²³ The solvent in the ink can then evaporate leading to a solid, or it can be chemically cured into a solid by exposure to light or heat. Once the deposited layer has solidified, the build plate moves along the z-axis, and the deposition and solidification process is repeated to form a 3D printed object. One advantage of using this method is its ability to produce patterned, customizable thin films with high resolution on the order of tens of microns and high print speed, making it valuable for commercially producing thin films of patterned materials.

However, this method requires complex ink formulations to have specific surface tension and low viscosity to control the drop formation process and control the printing resolution, which can greatly limit the loading of a desired solid material in the ink. Additionally, this method of depositing thin layers of material for the purpose of creating 3D objects can take an impractical amount of time for objects beyond millimeter sizes. Because of these limitations, inkjet printing is mostly used for producing patterned flat 2D objects or tall 2D objects (sometimes referred to as “2.5D objects”).

1.5.2 Vat Photopolymerization

Light-based, vat photopolymerization (VP) AM methods, such as stereolithography (SLA) or digital light processing (DLP) are proficient at producing complex 3D objects (Figure 1.4). VP consists of a vat of UV-curable resin with a transparent window on its bottom side. This resin typically consists of a radical polymerizable monomer and crosslinker to produce a solid polymer, a UV-activated polymerization initiator to start the polymerization reaction, a radical inhibitor to control the polymerization process, light-absorbing dye to increase resolution. A reactive diluent is often added to reduce the resin viscosity to promote flow of resin. If species in a resin are solids, a solvent is added for dissolution. A build plate is lowered into the resin to form a thin layer of resin between the build plate and the window. Then, a 2D pattern of ultraviolet (UV) light is projected to the thin layer of resin to cure it in the pattern of the light. Then, the build plate moves up along the z-axis to allow for more resin to flow into the thin space between the window and the previously printed layer, and the curing process repeats until the pre-programmed 3D object is produced. The ability to rapidly produce complex, 3D objects with high resolution makes this a widely used AM method, but its resin chemistry requirements limit what materials can be incorporated without interfering with the polymerization process. The light-based mechanism also largely prohibits sizable quantities of light-scattering particles or opaque materials from being incorporated, limiting the diversity of printable materials.

1.5.3 Extrusion-Based Methods

Extrusion-based AM methods are widely used, due to their generality with materials. To pattern using these methods, a material is extruded from a nozzle onto a build plate along a pre-programmed x-y axis to produce a 2D layer of material. The build plate then moves along the z-axis to allow for another layer to be deposited, and the process is repeated to produce a 3D object. The following two methods are the most commonly explored within this general category.

1.5.3.1 Fused Deposition Modeling

Fused deposition modeling (FDM) is a commonly used extrusion-based AM method that can produce 3D objects from fusible polymers (Figure 1.4). The

polymer filament to be patterned is first fed into a heated nozzle that melts and extrudes it as a narrow filament of molten polymer onto a build plate, and is moved along the x-y axis to produce a 2D pattern. The extruded polymer rapidly cools and solidifies after deposition, which allows the next layer to be deposited on top of it, and the process is repeated to produce a 3D object. The ability to produce 3D objects from a wide range of thermoplastics, the low amount of waste produced, and the lack of solvents are attractive features that makes this a widely used AM method. However, it can only be used for processing materials that flow when heated and remain stable without degradation, restricting the material diversity.

1.5.3.2 Direct Ink Writing

Another commonly used extrusion-based AM method is direct ink writing (DIW), where a flowable ink is extruded through a nozzle by displacement, either by a piston, air pressure, or a screw driver (Figure 1.4). DIW can deposit inks that can shear-thin (i.e., decreasing viscosity with increasing shear stress) when pressure is applied, allowing a thick paste to flow through the nozzle, but returns to the initial high viscosity state upon the release of shear stress to create stackable layers.²⁴ After a layer of ink has been deposited, it must have enough internal cohesive forces to be able to maintain its extruded shape and resist the downward force of gravity, as well as the weight of other layers that will be printed on top of it. Inks with a moderate yield stress are able to meet that requirement. Low viscosity inks with Newtonian flow behavior (i.e., constant viscosity with changing shear stress) can be used, but in order to retain their shape and produce 3D objects, their physical form must be rapidly changed after deposition to increase their cohesive force, either through solidifying through rapid cooling,²⁵ precipitation through solvent loss or exposure to a poor solvent,²⁶ or solidification by a chemical reaction,²⁷ or cured using UV-light.²⁸ This diverse range of possibilities make DIW a versatile method to manufacture 3D objects with the widest range of materials, including materials that are sensitive to high heat that are not suitable for processing with FDM.

1.6 Summary of AM Techniques Suitable for CPs

While the AM techniques reviewed in the previous section have been widely explored in recent year, applying them to CPs poses myriad challenges due to the chemical sensitivity of CPs. Various innovative approaches have been developed to adapt many of these techniques for CPs, with the main approaches being inkjet printing, DIW, and VP methods. While each of the studies brings the field one step forward, the field is nascent, and significant challenges remain.

Within the limited examples of 3DP CPs due to existing challenges to processing this class of material, they often suffer from poor conductivity. For

example, 2D thin films of PEDOT:PSS can achieve conductivity over 1000 S/cm,^{8,17,29} but values have been limited to around 1-155 S/cm for 3D printed versions,³⁰⁻³⁴ indicating that there is a knowledge gap in understanding and manipulating the 3D printing-structure-property relationships of CPs. Moderately high conductivity from 3DP CPs has been achieved, but it comes at the expense of limited 3D printing capabilities. In these studies, complex 2D patterns with height limited to merely a few layers^{30,31,34-39} or very simple 3D shapes without overhanging structures (2.5D structures) have been produced from CPs (Table 1.2).^{33,39-42} A few examples of printing CPs into truly 3D structures have been achieved, but the resulting prints suffer from low conductivity.⁴³⁻⁴⁷ Overall, these examples demonstrate the challenge of harnessing both high conductivity and high 3D shape complexity for CPs.

These limitations are the result of a number of intrinsic properties of CPs that make them difficult to process with available 3D printing mechanisms. First, it is important to consider whether the 3DP method of choice can preserve the chemical structure of the conductive polymer. CPs are electron-rich from the extended backbone π bonds, making many susceptible to permanent oxidation and degradation when exposed to oxygen and heat for extended periods of time or for short periods of time at high temperature.⁴⁸⁻⁵⁰ This sensitivity makes their printing using heat-based 3DP methods like FDM impractical.

Additionally, CPs are dark in color due to the extensive conjugation. Their absorption of visible and UV light makes the UV light used in VP methods difficult to penetrate and cure a CP-containing resin, making resin formulation challenging.^{51,52} The opaque color of CP means that only 2-3 wt.% of CPs can be loaded into the resin, which leads to poor conductivity of printed structures (Table 1.2).^{37,43-45}

These advantages and limitations of processing PEDOT:PSS with each 3DP method are summarized in Table 1.1. Case studies along with more detailed discussions on the advantages and limitations of each approach are delineated in the subsequent sections.

Table 1.1. Table correlating the CP properties and the suitability of each commonly used AM method. CP properties that make a 3D printing technique difficult to be applicable are represented by red crosses, whereas those that promote the applicability of a certain technique is presented by green checks.

		Fused deposition modeling (FDM)	Direct ink write (DIW)	Vat photopolymerization (VP)
	3DP mechanism	Melt	Pressure / displacement	Light
CP properties	Easily oxidized	✗	—	—
	Not meltable	✗	—	—
	Deeply colored	—	—	✗
	Solution processable	—	✓	—

1.6.1 Inkjet Printing for CPs

Inkjet printing is an excellent option for fabricating CPs into thin layers of electronic materials with good resolution.^{30,53} Of the many solution processable CPs, PEDOT:PSS is commonly used in order to achieve high conductivity. However, the low viscosity requirements of inkjet printing requires that solutions have a low amount of loaded solid material, and often requires dilution with solvents.⁵⁴ The resulting printed layers are very thin when dried out, and require the deposition of many layers to make an object that is not limited to a flat geometry, making it difficult to produce 3D CP objects using this technique (Table 1.2).^{30,53} Due to the limit on dimensionality, this technique will not be addressed in this dissertation.

1.6.2 Direct Ink Writing for CPs

In contrast to inkjet printing, DIW is compatible with a wider range of CP formulations, due to its ability to process higher viscosity inks, enabling it to print concentrated solutions that can produce 3D objects with high conductivity formulations. However, despite this formulation advantage, most efforts failed to produce even moderate conductivity in comparison to what could be achieved using 2D fabrication methods. For instance, spin-coating of highly conductive PEDOT:PSS formulations can achieve over 700 S/cm.^{8,17,29} In contrast, PEDOT:PSS that has been formulated using conductive inks to produce 2D electronic arrays or simple 3D shapes using DIW printing only achieves conductivity from 1-155 S/cm (Table 1.2).^{31–36,41} These examples were used for the fabrication of PEDOT:PSS hydrogels for bioelectronic applications, including soft neural probes, which only require conductivity in the range of 0.1-50 S/cm.^{8,17,29} For high conductivity devices with PEDOT:PSS in its dry form, these materials should ideally meet or exceed the benchmark value of 1000 S/cm for PEDOT:PSS²⁹ to reach the full potential of high-performance 3D printed organic electronics.

Additionally, these 3D printing efforts have been limited to printing either complex 2D patterns or simple, multi-layer 3D structures without overhanging structures. For instance, Wei and coworkers demonstrated the patterning of complex 2D patterns with a PEDOT:PSS ink, as well as simple cones and dome shapes.³² Zhang and coworkers demonstrated the fabrication of vertical PEDOT:PSS pillars, demonstrating the limited ability to fabricate complex, vertical structures with this material.³³

1.6.3 Vat Polymerization for CPs

Although DIW printing is capable of processing a wide range of CP materials, it has several limitations. It can achieve limited shape complexity, especially with overhanging structures, because the shear-thinning inks typically lack the strength to hold their own weight without support. It is also limited in throughput due to the line-by-line, layer-by-layer deposition mechanism. One method for overcoming these shortcomings is VP-based methods. However, the difficulty of directly printing CPs from precursors using this light-based AM technique is the UV-light absorption of CPs and their precursors limits the penetration of light needed to initiate the resin polymerization. Efforts to directly incorporate CPs into the resin result in low conductivity of printed objects, due to the limited amount of light-absorbing CP that can be added. For instance, Lopez-Larrea and coworkers added a PEDOT:PSS suspension to a VP resin mixture, and were able to print a variety of arbitrarily complex 3D structures, such as a 3D snail and abstract shapes with overhanging segments.⁴³ However, only 0.65% of PEDOT:PSS suspension could be added to their resin without becoming inhomogeneous and without hindering light penetration that could lead to defects in the printed objects, leading to low conductivity values up to 0.1 S/cm. Others have demonstrated the use of PEDOT:PSS-containing resins to produce conductive, 3D shapes, but the same issue of low PEDOT:PSS content led to low conductivity ranging from 0.0171 S/cm to 0.05 S/cm (Table 1.2).^{37,44,45}

Table 1.2. Comparison of electrical performance, shape complexity, and resolution capabilities of 3D printed PEDOT:PSS using different 3D printing methods. Desirable traits are shown in green, moderate ones in tan, and undesirable traits in red.

Method	Reference	Conductivity or Power Density	Shape Complexity	Resolution
DIW	H. Yuk ³¹	155 S/cm	2D	30 μm
	S. Ghaderi ⁴⁰	967 S/cm	Simple 3D shapes	295.6 μm
	I. Hill ⁵⁵	1200 S/cm	Complex 3D shapes	50 μm
	Y. J. Kim ⁴¹	101.7 $\mu\text{W}/\text{cm}^2$	Simple 3D stacks	270 μm
	Y. Zheng ³⁵	≈ 600 S/cm	Simple 2D woodpile	<10 μm
	X. Wang ³⁶	72 S/cm	2D patterns	479 μm
	H. Wei ³²	0.5 S/cm	Simple cone structure	100 μm
	P. Zhang ³³	50.4 S/cm	Simple vertical columns	50 μm
	S. Kee ³⁴	137 S/cm	2D films	800 μm
VP	N. Lopez-Larrea ⁴³	0.1 S/cm	Simple 3D shapes, overhangs	150 μm
	G. Scordo ⁴⁴	0.05 S/cm	Complex 3D shapes	50 μm hatch spacing
	G. Scordo ⁴⁵	0.055 S/cm	Complex 3D shapes	not reported
	H. Zhu ³⁷	≈ 0.0171 S/cm	Simple 3D shapes	≈ 70 μm
Inkjet	M. Y. Teo ⁵³	900 S/cm	Low	Low
	C. A. Mire ³⁰	0.21 S/cm	Linear tracks	50 μm
2PP	K. Kurselis ⁴⁶	0.04 S/cm	3D Micro-scaffolds	50 μm , 1 μm hatch distance
	Y. Tao ⁴⁷	0.42 S/cm	Complex 3D shapes	≈ 300 nm
	O. Dadras-Toussi ³⁹	281 S/cm	Complex 2D shapes	1 μm

1.7 Chapter outline

My PhD work addresses many of the key challenges in the field of 3DP CPs and bridges many of the knowledge gaps. First, the fundamental printing

processing-structure-property relationship of 3DP CPs is studied to gain an understanding of the origins of low conductivity. These insights were instructive to understanding how to improve the conductive properties of 3DP CPs, leading to significant conductivity enhancement. Additionally, we developed individualized approaches to fabricating highly conductive CPs with the capability of producing highly complex 3D structures with traditionally difficult-to-produce overhanging segments, uniting the currently exclusionary properties of high conductivity and 3D geometric freedom. A chapter outline for this dissertation along with the highlights of findings are overviewed below.

Chapter 2: Imparting High Conductivity to 3D Printed PEDOT:PSS

- Improved the conductivity of DIW-printable ink to have conductivity over 700 S/cm by mimicking the formulation of highly conductive spin-coated PEDOT:PSS.
- Identified anisotropic conductivity arising from the printing process, and carried out a systematic investigation of the printing processing-structure-property relationship.
- Found that the source of anisotropy is due to phase separation, which causes migration, insulating PSS to outer parts of printed filament.
- Discovered that using a simple DMSO solvent wash eliminates anisotropic conductivity by removing insulating PSS and improves conductivity to over 1200 S/cm, well above the 1000 S/cm benchmark for high conductivity, finally making printed PEDOT:PSS performance on-par with highly conductive 2D-processed PEDOT:PSS.
- Fully took advantage of the structural design capabilities of 3D printing by using two-material extrusion to produce elastic PEDOT:PSS free-standing 3D structures, capable of decoupling the mechanical performance from its intrinsically brittle nature.

Chapter 3: Pure PEDOT with complex architectures via 3D printing-assisted casting

- Previous efforts to produce 3D-printed PEDOT:PSS suffer from either low conductivity or poor structural fidelity with respect to intended printed object, limiting its use for electronics where high precision is required.
- Our new approach bridges this gap in fidelity and conductivity by using high-resolution VP-printed casting molds that serve as highly detailed 3D templates for casting a molten PEDOT monomer which produces highly detailed 3D electronically conductive objects.

- A systematic investigation into the incomplete solid-state polymerization of PEDOT led to the discovery of a method to improve the polymerization yield and conductivity of these electronically conductive materials.
- The flowable nature of the molten precursor allows for the incorporation of highly conductive silver flakes, to produce highly conductive 3D materials embedded in insoluble PEDOT for solvent-resistant electronics applications.
- In contrast to other soluble molds that require caustic chemicals to remove, ours are a green alternative that can be easily removed with water.
- This approach is widely applicable for fabricating a wide range of materials, including silicones, into arbitrary 3D shapes, without the need for developing new chemistries to make them processable with other 3D printing methods.

Chapter 4: Oligoaniline-Assisted Self-Assembly of Polyaniline Crystals

- We found that the incorporation of a small amount of tetraaniline oligomer can induce crystallization of the parent polymer, polyaniline, through a single-step self-assembly process, without the introduction of any impurities.
- This approach can be used to control the crystal growth and orientation of polyaniline of desired molecular weights.
- Investigation of the UV-vis-NIR spectra indicates that this crystallization process improves the charge carrier delocalization for producing highly conductive CPs.
- This simple self-assembly process can be used to improve the self-assembly of many other CPs for much greater control of crystal growth in solution, and for enhanced performance of thin film electronics.

Chapter 5: Synthesis of modified PAMPSA for rate-adaptive polymers

- The rate-adaptive behavior of a polymeric material developed and investigated by Hernandez and coworkers⁵⁶ is strongly dependent on the dynamic hydrogen bonding of hydrogen bond-containing polymer poly(2-acrylamido-2-methyl-1-propanesulfonic acid) (PAMPSA).
- A systematic investigation into the mechanism of this interaction can inform us as to how we can potentially tune this property for higher impact-adaptive electronic devices.
- To investigate this effect, PAMPSA derivatives of varying hydrogen-bonding strengths are synthesized, as well as methods to control their polymer length.
- Several issues arose and were solved when perusing these synthetic goals, including the premature polymerization of a modified AMPSA monomer, and

the premature termination of the polymerization of the modified AMPSA monomer.

- This work almost achieved its goal of developing all of the intended hydrogen-bonding rate-adaptive polymers, but provides valuable instructions for future work.

1.8 References

- (1) Namsheer, K.; Rout, C. S. Conducting Polymers: A Comprehensive Review on Recent Advances in Synthesis, Properties and Applications. *RSC Adv.* **2021**, *11* (10), 5659–5697. <https://doi.org/10.1039/d0ra07800j>.
- (2) Zimmermann, J.; Schliske, S.; Held, M.; Tisserant, J.-N.; Porcarelli, L.; Sanchez-Sanchez, A.; Mecerreyes, D.; Hernandez-Sosa, G. Ultrathin Fully Printed Light-Emitting Electrochemical Cells with Arbitrary Designs on Biocompatible Substrates. *Adv. Mater. Technol.* **2019**, *4* (3), 1800641. <https://doi.org/https://doi.org/10.1002/admt.201800641>.
- (3) Chang, J.; He, J.; Lei, Q.; Li, D. Electrohydrodynamic Printing of Microscale PEDOT:PSS-PEO Features with Tunable Conductive/Thermal Properties. *ACS Appl. Mater. Interfaces* **2018**, *10* (22), 19116–19122. <https://doi.org/10.1021/acsami.8b04051>.
- (4) Wu, Q.; Wei, J.; Xu, B.; Liu, X.; Wang, H.; Wang, W.; Wang, Q.; Liu, W. A Robust, Highly Stretchable Supramolecular Polymer Conductive Hydrogel with Self-Healability and Thermo-Processability. *Sci. Rep.* **2017**, *7* (1), 41566. <https://doi.org/10.1038/srep41566>.
- (5) Heo, D. N.; Lee, S. J.; Timsina, R.; Qiu, X.; Castro, N. J.; Zhang, L. G. Development of 3D Printable Conductive Hydrogel with Crystallized PEDOT:PSS for Neural Tissue Engineering. *Mater. Sci. Eng. C* **2019**, *99* (January), 582–590. <https://doi.org/10.1016/j.msec.2019.02.008>.
- (6) Lei, Q.; He, J.; Li, D. Electrohydrodynamic 3D Printing of Layer-Specifically Oriented, Multiscale Conductive Scaffolds for Cardiac Tissue Engineering. *Nanoscale* **2019**, *11* (32), 15195–15205. <https://doi.org/10.1039/C9NR04989D>.
- (7) Arnold, J. C. Environmental Effects on Crack Growth in Polymers; Aliabadi, M. H. F., Soboyejo, W. O. B. T.-C. S. I. (Second E., Eds.; Elsevier: Oxford, 2003; pp 242–276. <https://doi.org/https://doi.org/10.1016/B978-0-12-822944-6.00154-7>.
- (8) Kroon, R.; Mengistie, D. A.; Kiefer, D.; Hynynen, J.; Ryan, J. D.; Yu, L.; Müller, C. Thermoelectric Plastics: From Design to Synthesis, Processing and Structure–Property Relationships. *Chem. Soc. Rev.* **2016**, *45* (22), 6147–6164. <https://doi.org/10.1039/C6CS00149A>.
- (9) Abdelhamid, M. E.; O'Mullane, A. P.; Snook, G. A. Storing Energy in Plastics: A Review on Conducting Polymers & Their Role in Electrochemical Energy Storage. *RSC Adv.* **2015**, *5* (15), 11611–11626. <https://doi.org/10.1039/c4ra15947k>.
- (10) Gutzler, R. Band-Structure Engineering in Conjugated 2D Polymers. *Phys. Chem. Chem. Phys.* **2016**, *18* (42), 29029–29100.

<https://doi.org/10.1039/c6cp06101j>.

- (11) Xia, Y.; Wiesinger, J. M.; MacDiarmid, A. G.; Epstein, A. J. Camphorsulfonic Acid Fully Doped Polyaniline Emeraldine Salt: Conformations in Different Solvents Studied by an Ultraviolet/Visible/Near-Infrared Spectroscopic Method. *Chem. Mater.* **1995**, *7* (3), 443–445. <https://doi.org/10.1021/cm00051a002>.
- (12) J. Heeger, A. Polyaniline with Surfactant Counterions: Conducting Polymer Materials Which Are Processible in the Conducting Form. *Synth. Met.* **1993**, *57* (1), 3471–3482. [https://doi.org/10.1016/0379-6779\(93\)90462-6](https://doi.org/10.1016/0379-6779(93)90462-6).
- (13) Audenaert, M.; Gusman, G.; Deltour, R. Electrical Conductivity of I₂-Doped Polyacetylene. *Phys. Rev. B* **1981**, *24* (12), 7380–7382. <https://doi.org/10.1103/PhysRevB.24.7380>.
- (14) N. Basescu; Z.X. Liu; D. Moses; A.J. Heeger; H. Naarmann; N. Theophilou. High Electrical Conductivity in Doped Polyacetylene. *Nature* **1987**, *327* (4), 403–405.
- (15) MacDiarmid, A. G.; Epstein, A. J. The Concept of Secondary Doping as Applied to Polyaniline. *Synth. Met.* **1994**, *65* (2–3), 103–116. [https://doi.org/10.1016/0379-6779\(94\)90171-6](https://doi.org/10.1016/0379-6779(94)90171-6).
- (16) Noriega, R.; Rivnay, J.; Vandewal, K.; Koch, F. P. V.; Stingelin, N.; Smith, P.; Toney, M. F.; Salleo, A. A General Relationship between Disorder, Aggregation and Charge Transport in Conjugated Polymers. *Nat. Mater.* **2013**, *12* (11), 1038–1044. <https://doi.org/10.1038/nmat3722>.
- (17) Shi, H.; Liu, C.; Jiang, Q.; Xu, J. Effective Approaches to Improve the Electrical Conductivity of PEDOT:PSS: A Review. *Adv. Electron. Mater.* **2015**, *1* (4), 1–16. <https://doi.org/10.1002/aelm.201500017>.
- (18) Stejskal, J. *Interaction of Conducting Polymers, Polyaniline and Polypyrrole, with Organic Dyes: Polymer Morphology Control, Dye Adsorption and Photocatalytic Decomposition*; Springer International Publishing, 2020; Vol. 74. <https://doi.org/10.1007/s11696-019-00982-9>.
- (19) McCullough, R. D. The Chemistry of Conducting Polythiophenes. *Adv. Mater.* **1998**, *10* (2), 93–116. [https://doi.org/10.1002/\(SICI\)1521-4095\(199801\)10:2<93::AID-ADMA93>3.0.CO;2-F](https://doi.org/10.1002/(SICI)1521-4095(199801)10:2<93::AID-ADMA93>3.0.CO;2-F).
- (20) Yano, H.; Kudo, K.; Marumo, K.; Okuzaki, H. Fully Soluble Self-Doped Poly(3,4-Ethylenedioxythiophene) with an Electrical Conductivity Greater than 1000 S Cm⁻¹. *Sci. Adv.* **2019**, *5* (4), 1–10. <https://doi.org/10.1126/sciadv.aav9492>.
- (21) Takano, T.; Masunaga, H.; Fujiwara, A.; Okuzaki, H.; Sasaki, T. PEDOT Nanocrystal in Highly Conductive PEDOT:PSS Polymer Films. *Macromolecules* **2012**, *45* (9), 3859–3865.

<https://doi.org/10.1021/ma300120g>.

- (22) Guvendiren, M.; Molde, J.; M.D. Soares, R.; Kohn, J. Designing Biomaterials for 3D Printing. *ACS Biomater. Sci. & Eng.* **2016**, *2* (10), 1679–1693. <https://doi.org/10.1021/acsbiomaterials.6b00121>.
- (23) Guo, Y.; Patanwala, H. S.; Bognet, B.; Ma, A. W. K. Inkjet and Inkjet-Based 3D Printing: Connecting Fluid Properties and Printing Performance. *Rapid Prototyp. J.* **2017**, *23* (3), 562–576. <https://doi.org/10.1108/RPJ-05-2016-0076>.
- (24) Lewis, J. A. Direct Ink Writing of 3D Functional Materials. *Adv. Funct. Mater.* **2006**, *16* (17), 2193–2204. <https://doi.org/10.1002/adfm.200600434>.
- (25) Garg, A.; Yerneni, S. S.; Campbell, P.; LeDuc, P. R.; Ozdoganlar, O. B. Freeform 3D Ice Printing (3D-ICE) at the Micro Scale. *Adv. Sci.* **2022**, *9* (27), 1–11. <https://doi.org/10.1002/advs.202201566>.
- (26) Gratson, G. M.; Xu, M.; Lewis, J. A. Direct Writing of Three-Dimensional Webs. *Nature* **2004**, *428* (6981), 386–386. <https://doi.org/10.1038/428386a>.
- (27) Robertson, I. D.; Yourdkhani, M.; Centellas, P. J.; Aw, J. E.; Ivanoff, D. G.; Goli, E.; Lloyd, E. M.; Dean, L. M.; Sottos, N. R.; Geubelle, P. H.; Moore, J. S.; White, S. R. Rapid Energy-Efficient Manufacturing of Polymers and Composites via Frontal Polymerization. *Nature* **2018**, *557* (7704), 223–227. <https://doi.org/10.1038/s41586-018-0054-x>.
- (28) Hausladen, M. M.; Gorbea, G. D.; Francis, L. F.; Ellison, C. J. UV-Assisted Direct Ink Writing of Dual-Cure Polyurethanes. *ACS Appl. Polym. Mater.* **2024**, *6* (4), 2253–2265. <https://doi.org/10.1021/acsapm.3c02806>.
- (29) Ouyang, J. “Secondary Doping” Methods to Significantly Enhance the Conductivity of PEDOT:PSS for Its Application as Transparent Electrode of Optoelectronic Devices. *Displays* **2013**, *34* (5), 423–436. <https://doi.org/10.1016/j.displa.2013.08.007>.
- (30) Mire, C. A.; Agrawal, A.; Wallace, G. G.; Calvert, P.; In Het Panhuis, M. Inkjet and Extrusion Printing of Conducting Poly(3,4- Ethylenedioxythiophene) Tracks on and Embedded in Biopolymer Materials. *J. Mater. Chem.* **2011**, *21* (8), 2671–2678. <https://doi.org/10.1039/c0jm03587d>.
- (31) Yuk, H.; Lu, B.; Lin, S.; Qu, K.; Xu, J.; Luo, J.; Zhao, X. 3D Printing of Conducting Polymers. *Nat. Commun.* **2020**, *11* (1), 4–11. <https://doi.org/10.1038/s41467-020-15316-7>.
- (32) Wei, H.; Lei, M.; Zhang, P.; Leng, J.; Zheng, Z.; Yu, Y. Orthogonal Photochemistry-Assisted Printing of 3D Tough and Stretchable Conductive Hydrogels. *Nat. Commun.* **2021**, *12* (1), 2082. <https://doi.org/10.1038/s41467-021-21869-y>.

- (33) Zhang, P.; Aydemir, N.; Alkaisi, M.; E. Williams, D.; Travas-Sejdic, J. Direct Writing and Characterization of Three-Dimensional Conducting Polymer PEDOT Arrays. *ACS Appl. Mater. & Interfaces* **2018**, *10* (14), 11888–11895. <https://doi.org/10.1021/acsami.8b02289>.
- (34) Kee, S.; Haque, M. A.; Corzo, D.; Alshareef, H. N.; Baran, D. Self-Healing and Stretchable 3D-Printed Organic Thermoelectrics. *Adv. Funct. Mater.* **2019**, *29* (51). <https://doi.org/10.1002/adfm.201905426>.
- (35) Zheng, Y.; Wang, Y.; Zhang, F.; Zhang, S.; Piatkevich, K. D.; Zhou, N.; Pokorski, J. K. Coagulation Bath-Assisted 3D Printing of PEDOT:PSS with High Resolution and Strong Substrate Adhesion for Bioelectronic Devices. *Adv. Mater. Technol.* **2022**, *7* (7), 1–11. <https://doi.org/10.1002/admt.202101514>.
- (36) Wang, X.; Plog, J.; Lichade, K. M.; Yarin, A. L.; Pan, Y. Three-Dimensional Printing of Highly Conducting PEDOT: PSS-Based Polymers. *J. Manuf. Sci. Eng.* **2023**, *145* (1), 1–10. <https://doi.org/10.1115/1.4055850>.
- (37) Zhu, H.; Hu, X.; Liu, B.; Chen, Z.; Qu, S. 3D Printing of Conductive Hydrogel–Elastomer Hybrids for Stretchable Electronics. *ACS Appl. Mater. & Interfaces* **2021**, *13* (49), 59243–59251. <https://doi.org/10.1021/acsami.1c17526>.
- (38) Teo, M. Y.; Ravichandran, N.; Kim, N.; Kee, S.; Stuart, L.; Aw, K. C.; Stringer, J. Direct Patterning of Highly Conductive PEDOT:PSS/Ionic Liquid Hydrogel via Microreactive Inkjet Printing. *ACS Appl. Mater. Interfaces* **2019**, *11* (40), 37069–37076. <https://doi.org/10.1021/acsami.9b12069>.
- (39) Dadras-Toussi, O.; Khorrami, M.; Abidian, M. R. Femtosecond Laser 3D-Printing of Conductive Microelectronics for Potential Biomedical Applications. *Proc. Annu. Int. Conf. IEEE Eng. Med. Biol. Soc. EMBS* **2021**, 1197–1200. <https://doi.org/10.1109/EMBC46164.2021.9630885>.
- (40) Ghaderi, S.; Hosseini, H.; Haddadi, S. A.; Kamkar, M.; Arjmand, M. 3D Printing of Solvent-Treated PEDOT:PSS Inks for Electromagnetic Interference Shielding. *J. Mater. Chem. A* **2023**, *11* (30), 16027–16038. <https://doi.org/10.1039/d3ta01021j>.
- (41) Jae Kim, Y.; Il Kim, S.; Kim, J.; Yun, J.; Hong, H.; Kim, J.; Ryu, W. 3D Printing of Thylakoid-PEDOT:PSS Composite Electrode for Bio-Photoelectrochemical Cells. *ACS Appl. Energy Mater.* **2023**, *6* (2), 773–781. <https://doi.org/10.1021/acsaem.2c03033>.
- (42) Zhang, B.; Li, S.; Hingorani, H.; Serjouei, A.; Larush, L.; Pawar, A. A.; Goh, W. H.; Sakhaei, A. H.; Hashimoto, M.; Kowsari, K.; Magdassi, S.; Ge, Q. Highly Stretchable Hydrogels for UV Curing Based High-Resolution Multimaterial 3D Printing. *J. Mater. Chem. B* **2018**, *6* (20), 3246–3253. <https://doi.org/10.1039/c8tb00673c>.

- (43) Lopez-Larrea, N.; Criado-Gonzalez, M.; Dominguez-Alfaro, A.; Alegret, N.; del Agua, I.; Marchiori, B.; Mecerreyes, D. Digital Light 3D Printing of PEDOT-Based Photopolymerizable Inks for Biosensing. *ACS Appl. Polym. Mater.* **2022**, *4* (9), 6749–6759. <https://doi.org/10.1021/acsapm.2c01170>.
- (44) Scordo, G.; Bertana, V.; Scaltrito, L.; Ferrero, S.; Cocuzza, M.; Marasso, S. L.; Romano, S.; Sesana, R.; Catania, F.; Pirri, C. F. A Novel Highly Electrically Conductive Composite Resin for Stereolithography. *Mater. Today Commun.* **2019**, *19* (September 2018), 12–17. <https://doi.org/10.1016/j.mtcomm.2018.12.017>.
- (45) Scordo, G.; Bertana, V.; Ballesio, A.; Carcione, R.; Marasso, S. L.; Cocuzza, M.; Pirri, C. F.; Manachino, M.; Gomez, M. G.; Vitale, A.; Chiodoni, A.; Tamburri, E.; Scaltrito, L. Effect of Volatile Organic Compounds Adsorption on 3D-Printed Pegda:Pedot for Long-Term Monitoring Devices. *Nanomaterials* **2021**, *11* (1), 1–15. <https://doi.org/10.3390/nano11010094>.
- (46) Kurselis, K.; Kiyani, R.; Bagratashvili, V. N.; Popov, V. K.; Chichkov, B. N. 3D Fabrication of All-Polymer Conductive Microstructures by Two Photon Polymerization. *Opt. Express* **2013**, *21* (25), 31029–31035. <https://doi.org/10.1364/OE.21.031029>.
- (47) Tao, Y.; Wei, C.; Liu, J.; Deng, C.; Cai, S.; Xiong, W. Nanostructured Electrically Conductive Hydrogels Obtained: Via Ultrafast Laser Processing and Self-Assembly. *Nanoscale* **2019**, *11* (18), 9176–9184. <https://doi.org/10.1039/c9nr01230c>.
- (48) Edition, S. *Handbook of Thermoplastics*.
- (49) Jørgensen, M.; Norrman, K.; Krebs, F. C. Stability/Degradation of Polymer Solar Cells. *Sol. Energy Mater. Sol. Cells* **2008**, *92* (7), 686–714. <https://doi.org/10.1016/j.solmat.2008.01.005>.
- (50) Louis, B.; Caubergh, S.; Larsson, P. O.; Tian, Y.; Scheblykin, I. G. Light and Oxygen Induce Chain Scission of Conjugated Polymers in Solution. *Phys. Chem. Chem. Phys.* **2018**, *20* (3), 1829–1837. <https://doi.org/10.1039/c7cp07347j>.
- (51) Xia, Y.; M. Wiesinger, J.; G. MacDiarmid, A.; J. Epstein, A. Camphorsulfonic Acid Fully Doped Polyaniline Emeraldine Salt: Conformations in Different Solvents Studied by an Ultraviolet/Visible/Near-Infrared Spectroscopic Method. *Chem. Mater.* **2002**, *7* (3), 443–445. <https://doi.org/10.1021/cm00051a002>.
- (52) Zhang, W. J.; Feng, J.; MacDiarmid, A. G.; Epstein, A. J. Synthesis of Oligomeric Anilines. *Synth. Met.* **1997**, *84* (1), 119–120. [https://doi.org/https://doi.org/10.1016/S0379-6779\(97\)80674-1](https://doi.org/https://doi.org/10.1016/S0379-6779(97)80674-1).
- (53) Ying Teo, M.; RaviChandran, N.; Kim, N.; Kee, S.; Stuart, L.; C. Aw, K.;

Stringer, J. Direct Patterning of Highly Conductive PEDOT:PSS/Ionic Liquid Hydrogel via Microreactive Inkjet Printing. *ACS Appl. Mater. & Interfaces* **2019**, *11* (40), 37069–37076. <https://doi.org/10.1021/acsami.9b12069>.

- (54) Lo, L. W.; Zhao, J.; Wan, H.; Wang, Y.; Chakrabarty, S.; Wang, C. An Inkjet-Printed PEDOT:PSS-Based Stretchable Conductor for Wearable Health Monitoring Device Applications. *ACS Appl. Mater. Interfaces* **2021**, *13* (18), 21693–21702. <https://doi.org/10.1021/acsami.1c00537>.
- (55) M. Hill, I.; Hernandez, V.; Xu, B.; A. Piceno, J.; Misiaszek, J.; Giglio, A.; Junez, E.; Chen, J.; D. Ashby, P.; S. Jordan, R.; Wang, Y. Imparting High Conductivity to 3D Printed PEDOT:PSS. *ACS Appl. Polym. Mater.* **2023**, *5* (6), 3989–3998. <https://doi.org/10.1021/acsapm.3c00232>.
- (56) Hernandez, V.; Jordan, R. S.; Hill, I. M.; Xu, B.; Zhai, C.; Wu, D.; Lee, H.; Misiaszek, J.; Shirzad, K.; Martinez, M. F.; Kusoglu, A.; Yeo, J.; Wang, Y. Deformation Rate-Adaptive Conducting Polymers and Composites. *Small* **2023**, *19* (35), 1–12. <https://doi.org/10.1002/sml.202207100>.

Chapter 2

Imparting High Conductivity to 3D Printed PEDOT:PSS

2.1 Abstract

Complex 3D geometry and high conductivity have generally been mutually exclusive characteristics for conducting polymers. For instance, poly(3,4-ethylenedioxythiophene):poly(styrenesulfonate) (PEDOT:PSS), a benchmark conducting polymer, typically exhibits conductivity 1 to 2 orders of magnitude lower in 3D-printed forms compared to 2D-processed thin films, due to its sensitivity to processing conditions. Here, we investigate the main causes of this reduced conductivity, which are found to be (1) the ink formulation strategy and (2) the strong lateral phase separation of the printed filaments. Processing approaches that overcome these factors have produced significant conductivity enhancement to 1200 S/cm, higher than the typical 2D-processed PEDOT:PSS. Our study also unveils a set of guiding principles for optimizing the conductivity of direct ink writing (DIW)-printed PEDOT:PSS, including printing orientation, print bed temperature, and nozzle diameter. With the combination of high conductivity and 3D geometric freedom, potential applications such as omnidirectionally deformable LED devices with strain-independent electrical behavior and bespoke electronics that replicate the shape of human body parts have been demonstrated.

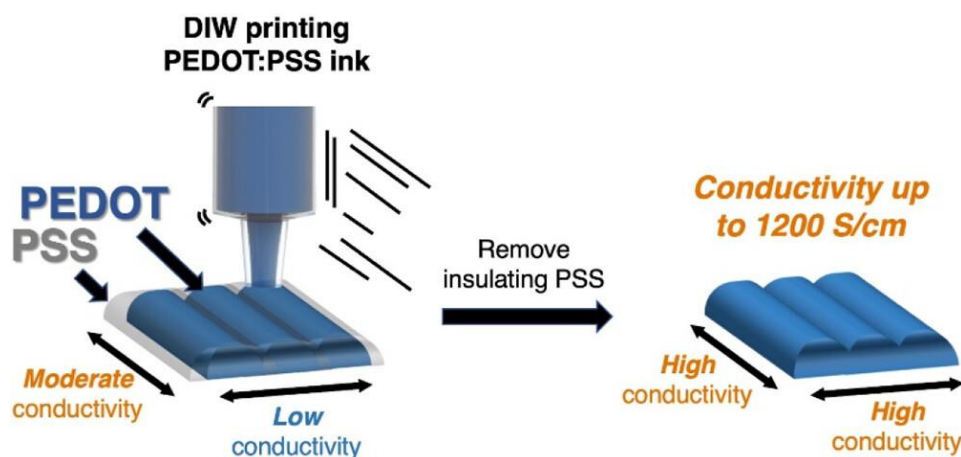


Figure 2.1. Summary figure for Imparting High Conductivity to 3D Printed PEDOT:PSS.

2.2 Introduction

Three-dimensional (3D) printing offers a range of benefits, such as geometric freedom, rapid prototyping, and additive patterning capabilities, across fields including automotive, aerospace, robotics, biomedicine, and electronics.¹⁻³ While the use of 3D printing technology has become widespread, the challenges of printing organic electronic materials like conjugated, conducting polymers (CPs) persist. This is mainly due to the delicate nature of CPs, which are sensitive to chemical, thermal, and processing conditions.⁴ The electron-rich nature of CPs makes them prone to irreversible oxidation or decomposition at elevated temperatures, rendering them incompatible with 3D printing mechanisms such as fused deposition modeling (FDM) or selective laser sintering (SLS), which rely on elevated temperature to produce parts from molten or semimolten polymers.⁵⁻⁷ Furthermore, even at short chain length, CPs absorb strongly in the ultraviolet and visible wavelength range,^{8,9} hindering photoinitiation in light-based 3D printing methods such as stereolithography (SLA) and digital light processing (DLP).¹⁰

A number of methods, primarily utilizing composite materials or secondary networks, have been used to generate 3D structures with CPs.¹¹⁻¹⁶ However, the electrical properties of the resulting materials are generally poor due to the insulating additives or chemical modification that improve printability but reduce conductivity. Several recent reports have shown that, among the major 3D printing technologies, direct ink writing (DIW) yields the best electrical performance retention for CPs.¹⁷⁻¹⁹ CPs' solution processability and shear-thinning behavior make them suitable for a shear-based extrusion mechanism of DIW. In particular, poly(3,4-ethylenedioxythiophene):poly(styrenesulfonate) (PEDOT:PSS) (**Error! Reference source not found..2**) is the most heavily investigated CP due to its high conductivity and its wide applications in organic electronics, optoelectronics, and bioelectronics.²⁰⁻²²

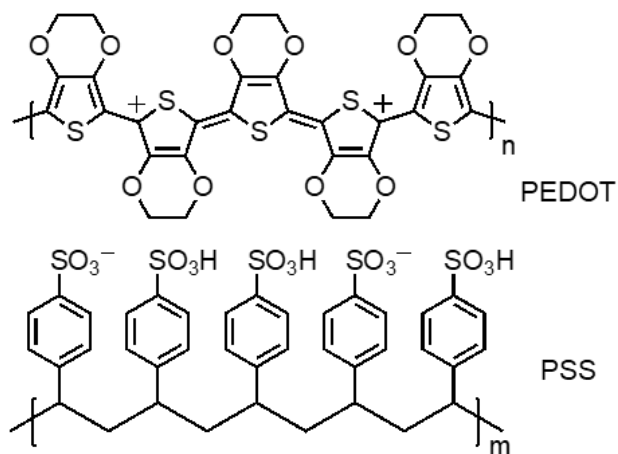


Figure 2.2. Chemical structure of PEDOT:PSS.

However, CPs' sensitivity to processing conditions is clearly reflected in their significantly lower conductivity when 3D printed compared to conventional 2D methods. For example, spin-coated PEDOT:PSS has a conductivity of nearly 1000 S/cm, making it the benchmark material in organic electronic devices.^{20–22} However, its DIW-printed counterparts typically have conductivity values ranging between 1 and 155 S/cm in the solid state.^{16–19,23,24} Most of these reports retain the printed PEDOT:PSS in the as-processed hydrogel form for bioelectronics applications, such as pressure sensors or soft neural probes, for which moderate conductivity in the range of 0.1–50 S/cm is satisfactory.^{12,17–19} However, high conductivity, ideally equal to or exceeding the benchmark value of 1000 S/cm for PEDOT:PSS,²⁰ is necessary to reach the full potential of 3D printing in high performance, solid-state organic electronics, such as organic photovoltaics or field effect transistors. Reaching this milestone is crucial for advancing the field of 3D organic electronics.

We aim to address the challenge of inferior conductivity in DIW printed PEDOT:PSS by first gaining a fundamental understanding of the factors causing it. We then use this knowledge to improve the conductivity of 3D PEDOT:PSS to surpass that of its 2D thin film counterparts. The combination of intricate geometry and high conductivity in the resulting PEDOT:PSS has the potential to enable new applications, such as organic electronics with geometries that can fill unused spaces, electronics that merge with art, and personalized biomedical devices through integration of 3D scanning and printing.

2.3 Printer Modification

Aside from the objects shown in Figures 2.30-35, all remaining samples in this work were printed using a Discov3ry Complete Paste Extruder (Structur3D) coupled to an Ultimaker 2+ to enable piston-based DIW printing. A number of machine modifications were carried out to optimize the printer setup for our ink.

A Discov3ry Complete Paste Extruder coupled to an Ultimaker 2+ was used for the majority of this work (Figures 2.1-29). The original design included a standalone syringe pump connected to the extrusion nozzle via approximately 60 cm of Tygon tubing (inner diameter: 3.175 mm). The syringe pump operated via a single-start, 8 mm OD, 2 mm pitch stainless steel lead screw attached to an approximate 200:1 gear reduction (50:1 from gearbox and 4:1 from differing size of gears), powered by a Nema 17 stepper motor.



Figure 2.3. Original Discov3ry Complete Paste Extruder. The enclosure to the right of the Ultimaker 2+ houses the syringe pump. [Adapted in part with permission from Discov3ry Complete. Structur3D Printing Home Page. <https://www.structur3d.io/> (accessed 2018-01-01) Copyright 2016, Structur3d Printing.]

Unfortunately, this as-purchased design became problematic with the use of high viscosity extrudates, such as the PEDOT:PSS ink in this work. High head loss caused by the long tubing resulted in low pressure generation at the nozzle. Simply increasing the power input of the printer was undesirable, as the plastic syringe and housing components would experience significant deflection under the applied loads.

To reduce the head loss, a fixture comprised of two angle-bracket supports with adjustable slots was mounted to one side of the Ultimaker 2+ (Figure 2.4a). Atop of this support structure is the syringe pump device. Using this modified apparatus, the length of the tubing has been reduced to 20-23 cm, which is around a third of the tube length in the as-purchased setup. This machine modification significantly reduced head loss whilst offering a more compact extrusion apparatus.

A 500-watt, 8 inch by 8 inch square silicone heating plate (Keenovo 110V) was added underneath the stock build plate to provide extended heating temperature range for the printing surface (Figure 2.4a).

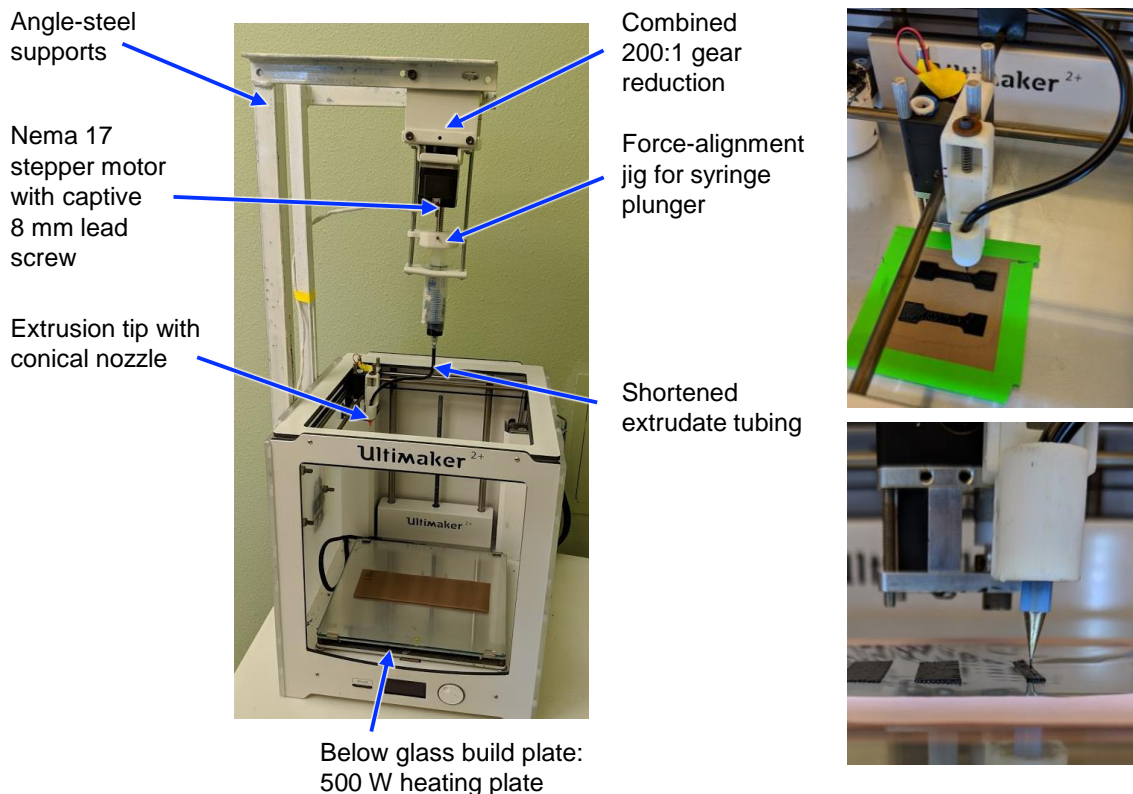


Figure 2.4. (a) Modified Discov3ry Paste Extruder mounted on a support structure above the Ultimaker 2+ with the key components labeled. (b) and (c) angled and side views, respectively, of the extrusion assembly area.

2.4 PEDOT:PSS Ink Optimization

In order to optimize the rheological behavior of the PEDOT:PSS ink for DIW printing, we carried out ink rheological modification via drying, then used rheological tests to determine which ink was most suitable for DIW printing.

2.4.1 Ink Preparation

For a typical ink, 100 mL of aqueous PEDOT:PSS dispersion (Clevios PH 1000, 1–1.3 wt % solid content) was added to a 600 mL beaker containing a magnetic stir bar. 5.3 mL (5 vol %) of DMSO (Fisher Scientific) was added to the solution while stirring. The mixture was stirred and heated at 70 °C until it reached a concentration of 3 wt %, at which point it became a viscous paste. It was left to cool at room temperature for 20 min prior to being pressed through a filtration membrane composed of 16 layers of overlapping cheesecloth followed by a polyester filter with a 500 μm wide mesh opening (Elko Filtering Co.) to remove aggregates. The ink is then homogenized in a planetary centrifugal mixer (Thinky

AR-100) for 4 min, followed by a 30 s defoaming cycle. The ink is left undisturbed for approximately 10 min to cool to room temperature before syringe loading.

2.4.2 Ink Rheology Tuning

Rheology characterizations were performed on an Anton Paar MCR 102 rheometer at room temperature. Testing parameters were detailed in subsequent sections.

DIW printing requires the ink to be shear-thinning so that it can flow out of the nozzle under shear force, and to have moderate yield stress so that the extruded filaments can maintain shape and stack vertically upon extrusion.¹ These are rheological properties typically associated with viscous polymer solutions or dispersions. The as-purchased PEDOT:PSS aqueous colloidal dispersion has a solid content of 1-1.3 wt % and low viscosity, making it unsuitable for DIW printing (Figures 2.6 and 7). To circumvent this issue, previous reports reformulated the PEDOT:PSS dispersion through lyophilization followed by redistribution, used a gelation agent, or carried out *in situ* polymerization in the presence of another polymer network.^{12,17,19} Given the well-known effects that processing solvents, additives, and other conditions often have on factors that control the electrical properties of CPs, including chain conformation, packing arrangement, crystallinity, and phase separation, we hypothesize that these formulation strategies may have led to the significantly lower conductivity of PEDOT:PSS compared to the counterparts processed via conventional 2D methods. Therefore, we prepared a DIW-printable ink simply by mixing in 5 vol % of dimethyl sulfoxide (DMSO), the most commonly used “secondary dopant” for PEDOT:PSS,²⁰ into the as-purchased aqueous dispersion, followed by slowly evaporating the solvent under gentle heating. This procedure mimics the natural solvent evaporation process in the drop casted or spin coated films where high conductivity is readily obtained.

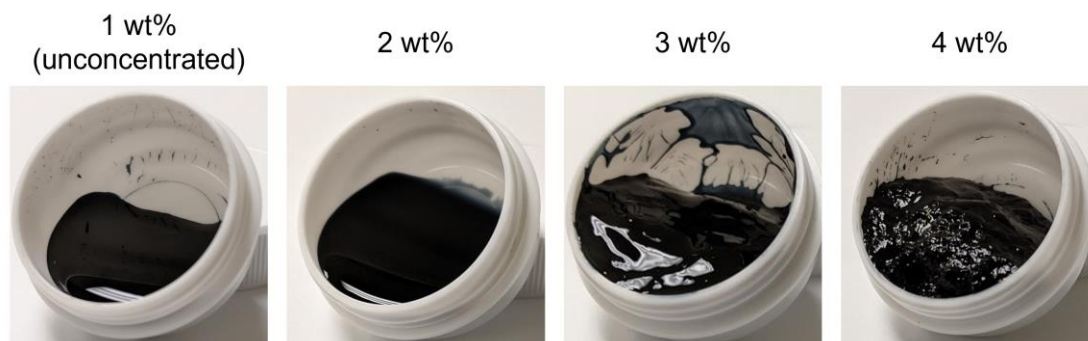


Figure 2.5. Images of PEDOT:PSS ink at different concentrations after mixing and defoaming.

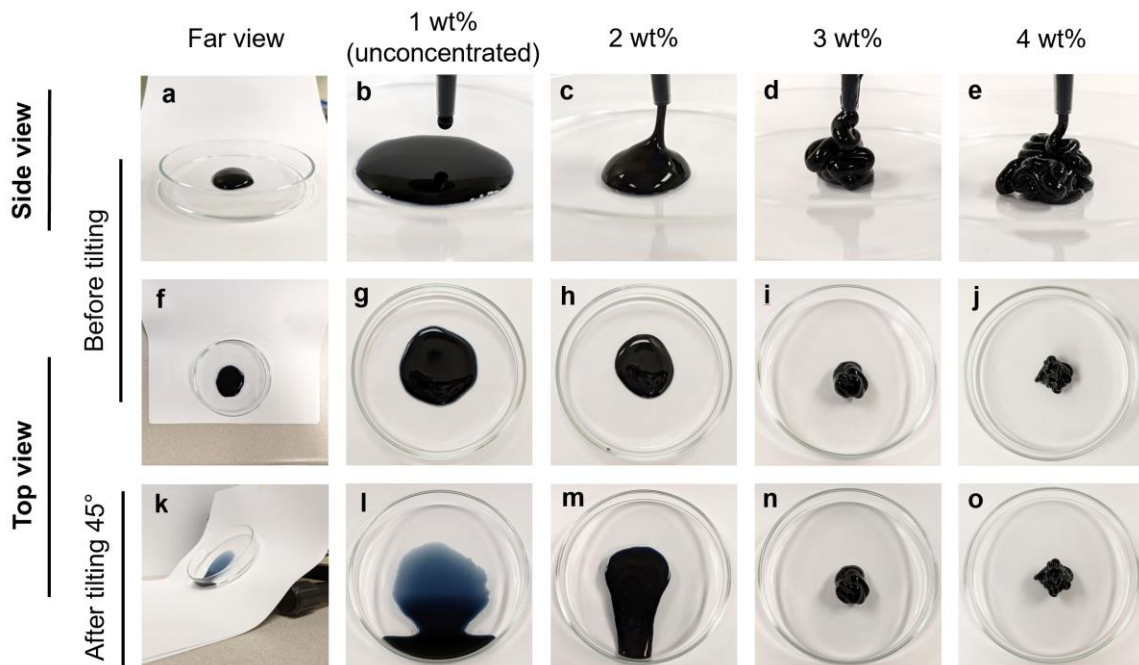


Figure 2.6. Images of extruded PEDOT:PSS inks at concentrations of 1, 2, 3, and 4 wt % (a-e) viewed from the side, (f-j) top view of samples on a level surface, and (k-o) after tilting the samples 45°.

The PEDOT:PSS dispersions with 2, 3, and 4 wt % concentrations all show significantly increased low-shear steady-state viscosity and exhibit consistent shear thinning behavior across the entire applied shear rate regime (Figure 2.7a). Oscillatory amplitude sweeps show that all three inks are viscoelastic, and the storage and loss moduli (G' and G'' , respectively) both increase with increasing PEDOT:PSS concentration (Figure 2.7b). The yield stress of an ink is defined by the crossover between G' and G'' . Retaining self-supportive 3D structural integrity typically requires a yield stress of above 100 Pa to overcome structural distortions caused by capillary forces that arise from the curved surfaces of the filaments.²⁵ Both the 3 and 4 wt % inks meet this criterion as they exhibit yield stresses of 140 and 143 Pa, respectively. These rheological observations are also reflected in the hand extrusion tests, where both the 3 and 4 wt % inks appear as viscous paste and lead to stackable filaments (Figure 2.6). The 4 wt % ink generates the best defined filaments, whereas minor line spreading upon nozzle exit is observed for the 3 wt % ink. However, the 4 wt % ink displayed a sizable amount of aggregates even after filtration and caused frequent clogging during printing. Conversely, the minor line widening from the 3 wt % ink can be easily corrected through commonly used parameter optimization strategies in DIW printing. As a result, the 3 wt % ink was chosen for this study.

2.4.3 Rheology Experimental Method

2.4.3.1 Rheological characterization for PEDOT:PSS ink

The gap size between the upper and lower plates of the rheometer was set at 1 mm. For steady-state tests, a pre-shear at 1 s^{-1} was applied for 10 s, followed by a 300 s resting period prior to steady-state shear testing. Samples for oscillatory amplitude tests were subject to a pre-shearing condition of 1% strain with an angular frequency of 10 rad/sec for 10 seconds, followed by a relaxation stage of 300 s prior to data collection.

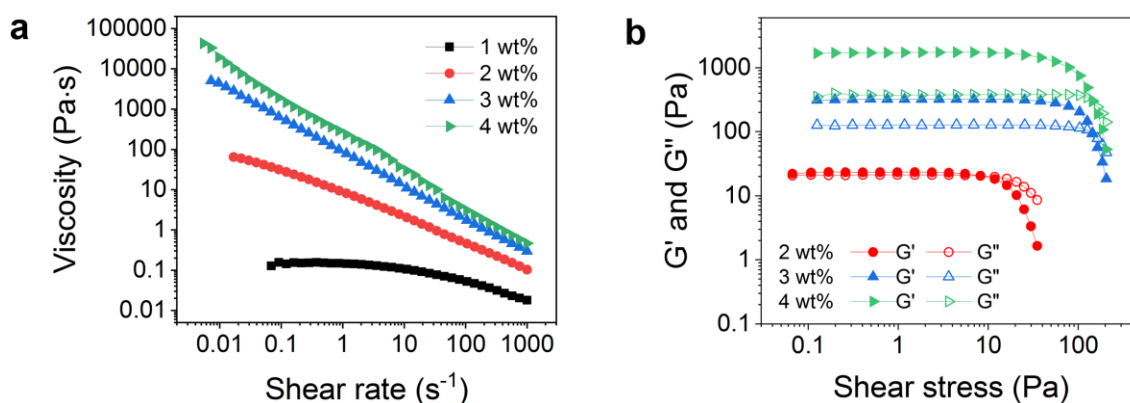


Figure 2.7. Rheology data for PEDOT:PSS inks of various concentrations collected under (a) steady-shear and (b) oscillatory conditions.

2.4.3.2 Time-dependence of the rheological properties for PEDOT:PSS ink

One challenge with this ink formulation is that the yield stress of the ink slowly increases with time, from 125 to 192 Pa within 5 h of paste preparation, likely due to the formation of more extended hydrogen bonding networks (Figure 2.8), but remains printable. Past this duration, the ink would occasionally clog the nozzle. The lifetime of the ink can be extended by re-homogenizing the aged ink followed by filtration, which removes most aggregates. Because of the time-dependence of the ink yield stress, a piston-based DIW setup is more suitable than the more commonly used pneumatic mechanism.²⁶ The air pressure of a pneumatic setup needs to be periodically adjusted to facilitate high quality printing of an ink with time-dependent yield stress, making the process manually tedious albeit feasible. Conversely, the piston mechanism depresses the volume of the ink at a specific rate with displacement controlled by a mechanical motor, making it significantly less sensitive to small changes in yield stress of the ink. As a result, optimized computerized settings would lead to high quality prints of our PEDOT:PSS ink without manual adjustments. The usage of piston-based DIW setup has led to good printing resolution and feature fidelity, highlighting the importance of tailoring the extrusion method to material characteristics.

Because of the strong focus of this work on enhancing the conductivity of PEDOT:PSS, we considered trading off ink shelf-life as an acceptable compromise. In future work, ink shelf life may be extended by incorporating a suitable inhibitor to delay or prevent physical crosslinking. To provide context for the sizes of structures for which such endeavors will be necessary, the printing time for the films used in conductivity measurements (Figure 2.14d), the hand (Figure 2.30c), and the encased spring (Figure 2.31a,b) were 12 sec, 9.5 min, and 35.5 min, respectively.

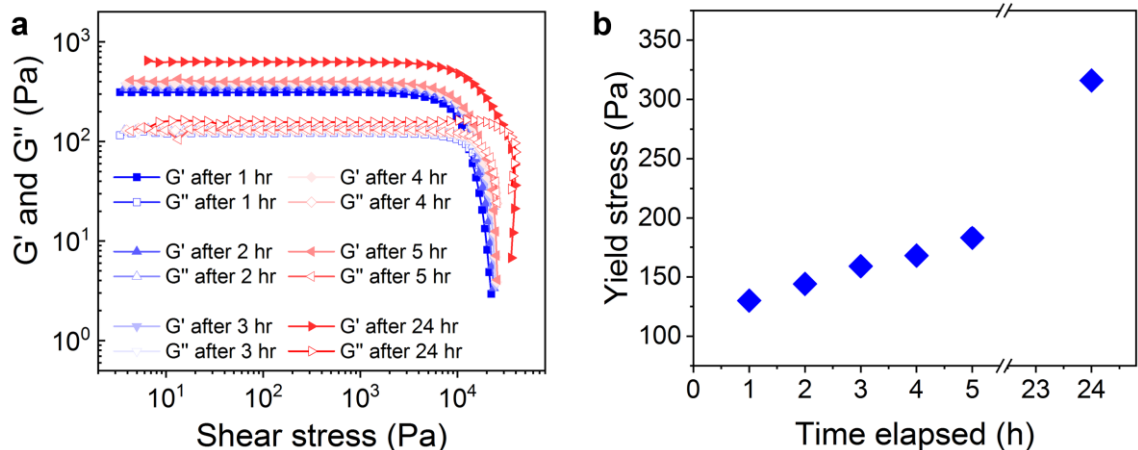


Figure 2.8. (a) Measurements of storage (G') and loss (G'') moduli from oscillatory amplitude sweeps and (b) Yield stresses of PEDOT:PSS inks that are 1, 2, 3, 4, 5, and 24 hours after preparation.

2.5 Printing Parameter Optimization and 3D Printing

2.5.1 Experimental for 3D Printing Parameter Tuning

In a typical print, the PEDOT:PSS ink was loaded into a 20 mL luer-lok syringe (Kinesis), which was inserted into the external carriage of the Discov3ry extruder. The syringe and an extrusion nozzle (Subrex) of select gauge size was connected by a ca. 230 mm-long Tygon tubing (Thermo Scientific, 3.175 mm inner diameter) using male and female hosebarb adapters (Cole-Parmer, 3.2 mm inner diameter; part numbers: male: EW-30800-24 and female: EW-30800-08). A print speed of 16 mm/s was used for most prints unless otherwise stated.

Structures shown in Figures 2.12a,b were printed on a fluorinated ethylene propylene (FEP) sheet and wax paper, respectively, and adhered to a build plate at room temperature. Structure in Figures 2.12c,d was printed onto a sheet of Ecoflex 00-30 silicone (Smooth-On). Upon drying of the PEDOT:PSS, a thin layer of uncured Ecoflex 00-30 was poured on top of the print to encapsulate it. Individual lines and 10 line-wide films were printed on glass slides (Fisher Scientific) with the

print bed heated to different temperatures. Samples printed at room temperature were left to dry for 36 hours. For all remaining samples, after the completion of printing, they were immediately transferred to a hotplate (Chemat Technology, Inc.) set to the same heating temperature as the build plate and left there until dried. Samples printed at 50 °C typically require approximately 2 hours of heating time for drying, whereas the 80-130 °C samples become dried in about 20 min. Finally, all samples were annealed at 130 °C for 10 minutes to remove trace residual solvents prior to conductivity measurements. Dimensions of the line were measured using a FLIR Grasshopper®3 camera through a Nikon MSB50040 achromatic lens, and analyzed using ImageJ image analysis software.

2.5.2 3D Printing Parameter Tuning

Different nozzle diameters can lead to different printed filament sizes, requiring the extrusion rate to be adjusted against nozzle diameters. However, the resolution and print quality from each given nozzle is greatly influenced by the rate of extrusion and printhead travel speed. The combination of these two factors can greatly influence the printing resolution, including creating discontinuous lines or thinning of lines if the extrusion rate is too low, or if the rate is too high, die swelling or coiling.²⁷ When a fixed extrusion rate is used for printing with different nozzle sizes, the nozzle size does not effectively control the printing resolution (Figure 2.9a). The smallest nozzles used in this test extrudes much wider lines than their respective nozzle widths because of the high extrusion rate, as well as die swelling effects (Figure 2.9c), the latter of which is caused by ink relaxation after being elongated by high nozzle shear.²⁸ The ink exerts increasing normal force at increasing shear rates (Figure 2.9**Error! Reference source not found.**b) that is indicative of die swelling.²⁸ More material is extruded when larger nozzles are used, but extruded line dimensions are still less than their inner diameters. Printing with a relatively low extrusion rate for a particular nozzle size can result in discontinuous lines, unless the nozzle-to-build plate distance is decreased, which will further increase the line width to height ratio. We demonstrated that changing the extrusion rate for a given nozzle size is an effective way of tuning the printed dimensions (Figure 2.9d). Setting the extrusion rate too low or too high results in printed line dimensions that are smaller or larger than the ideal dimensions of the nozzle inner diameter, respectively. After optimizing the extrusion rates for each nozzle (Figure 2.9f), we were able to effectively control the printing resolution (Figure 2.9e). This not only allows us to preserve printing resolution, but to minimize the effect of normal forces, a variable that changes with nozzle sizes, on the structure-property relations of DIW printed PEDOT:PSS.

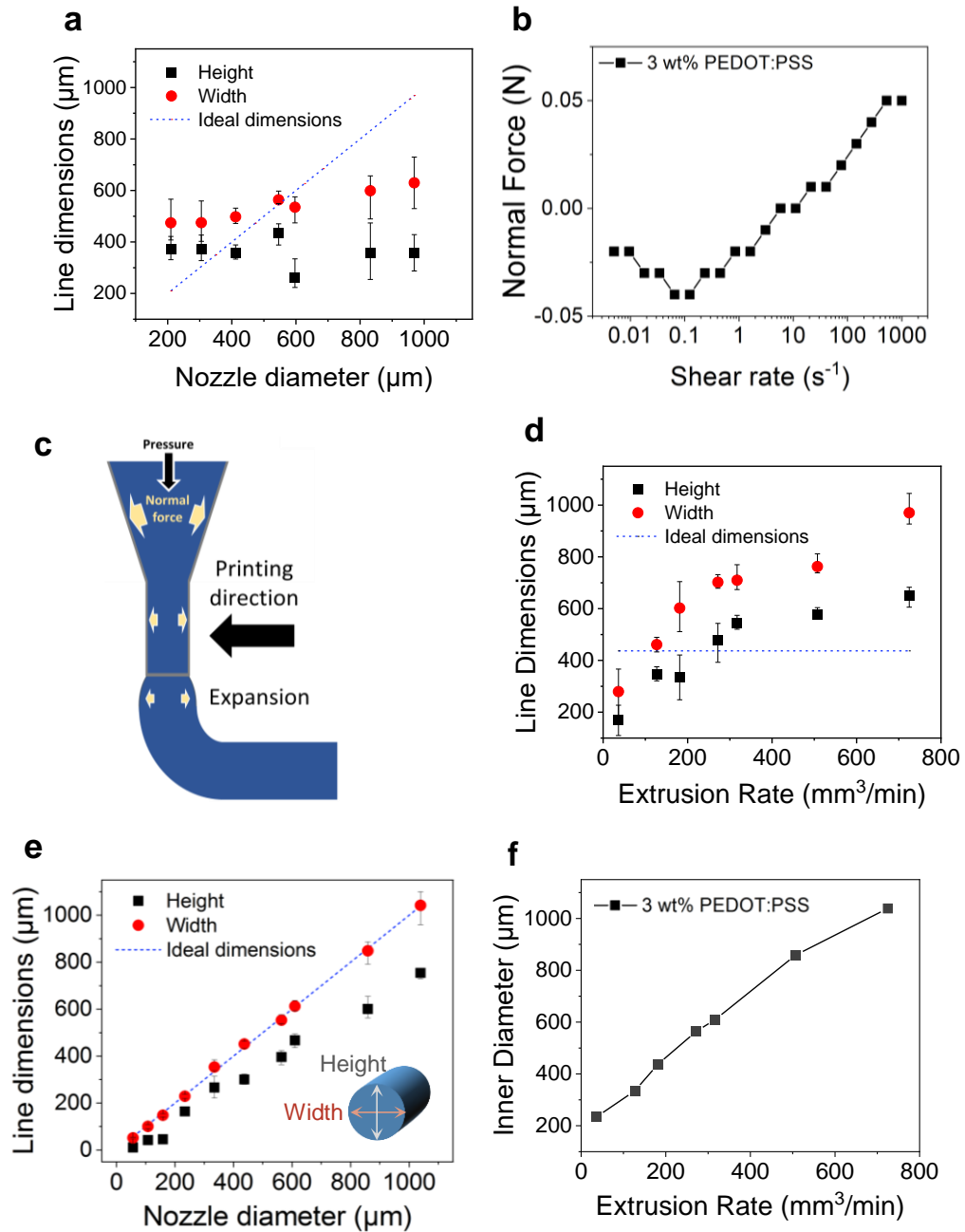


Figure 2.9. (a) Graph of printed line dimensions of PEDOT:PSS using different nozzle diameters while keeping printing parameters unvaried. (b) Normal force exerted by PEDOT:PSS ink when increasing the applied shear rate. (c) Diagram of die swelling when ink is extruded with high pressures. (d) Plot of printed line dimensions when using different extrusion rates and a 437 μm inner diameter nozzle. (e) Plot of printed dimensions when using optimized extrusion rates for each nozzle. (f) Optimized extrusion rates for each nozzle inner diameter that is used in our study.

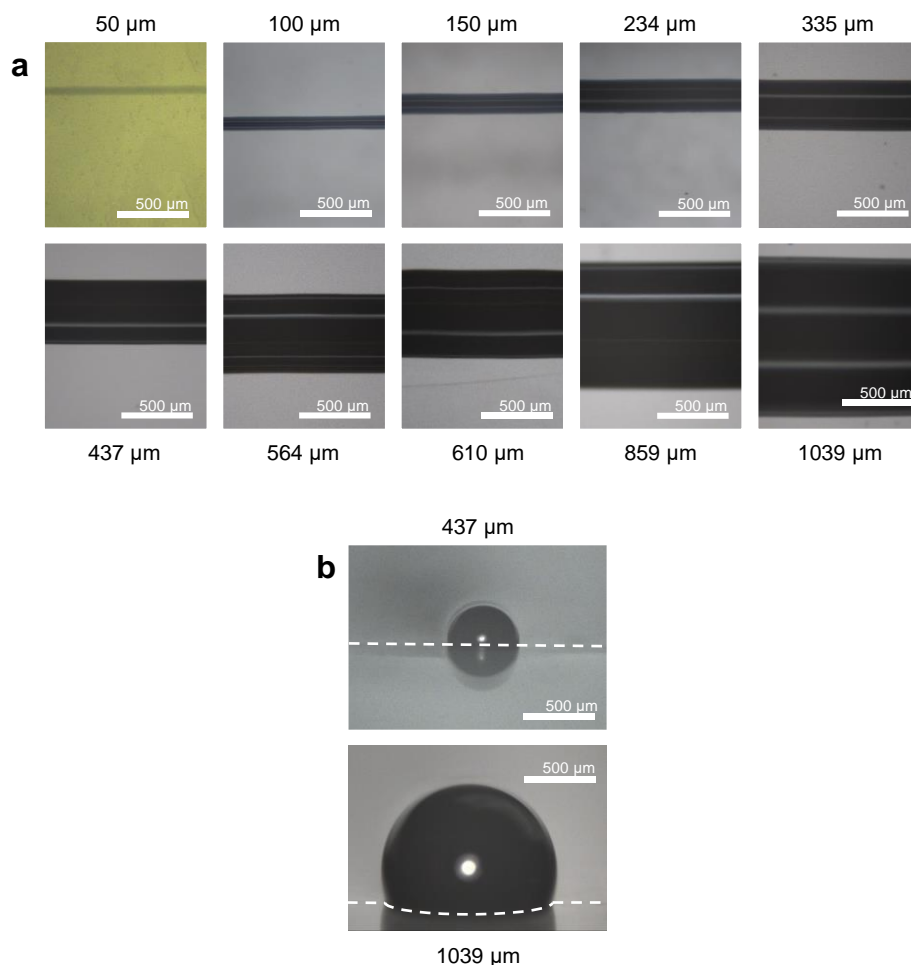


Figure 2.10. (a) Optical microscope images of freshly printed PEDOT:PSS filaments (i.e., 3 wt % solid, hydrated state) printed using nozzles with different inner diameters, each printed with their respective optimal extrusion rates. The filament printed with the 50 μm inner diameter nozzle was printed on a Kapton substrate, and the other samples were printed on a fluorinated ethylene propylene (FEP) substrate. The filaments were printed with their optimized print parameters and had uniform, smooth surfaces that often reflected light, which gave their surfaces the appearance of having horizontal white lines along the print direction. Each frame contains only one filament. (b) Representative cross-sections of printed filaments, showing their semi-circular shapes.

2.5.3 Scanning Electron Microscopy

In order to observe if the printed filaments have good interfilament connectivity, we carried out scanning electron microscopy (SEM) characterization

for morphology and interfaces between printed filaments of 3D printed PEDOT:PSS films.

PEDOT:PSS films printed on silicon wafers were used for SEM. The film cross-section was obtained by cleaving the silicon wafer substrate perpendicular to the printing direction of the PEDOT:PSS film. The PEDOT:PSS film breaks along the silicon wafer fracture, leading to a pristine cross-section. SEM images were collected on a Zeiss Gemini 500 with an accelerating voltage of 3 kV.

The printed film surfaces appear smooth when examined with the naked eye, but interfaces can be seen under illumination from certain angles (Figure 2.11a). Upon closer examination using SEM, the filaments appear to overlap at the edges that lead to good inter-filament connectivity. A minor ridge is formed where the adjacent filaments overlap, leading to two shallow valleys to the sides of the ridges (Figure 2.11c-e). No distinguishable interfaces or any other morphological heterogeneity can be identified within any given 3 mm-wide scanning window of the film cross-section, which contains multiple overlapping filaments.

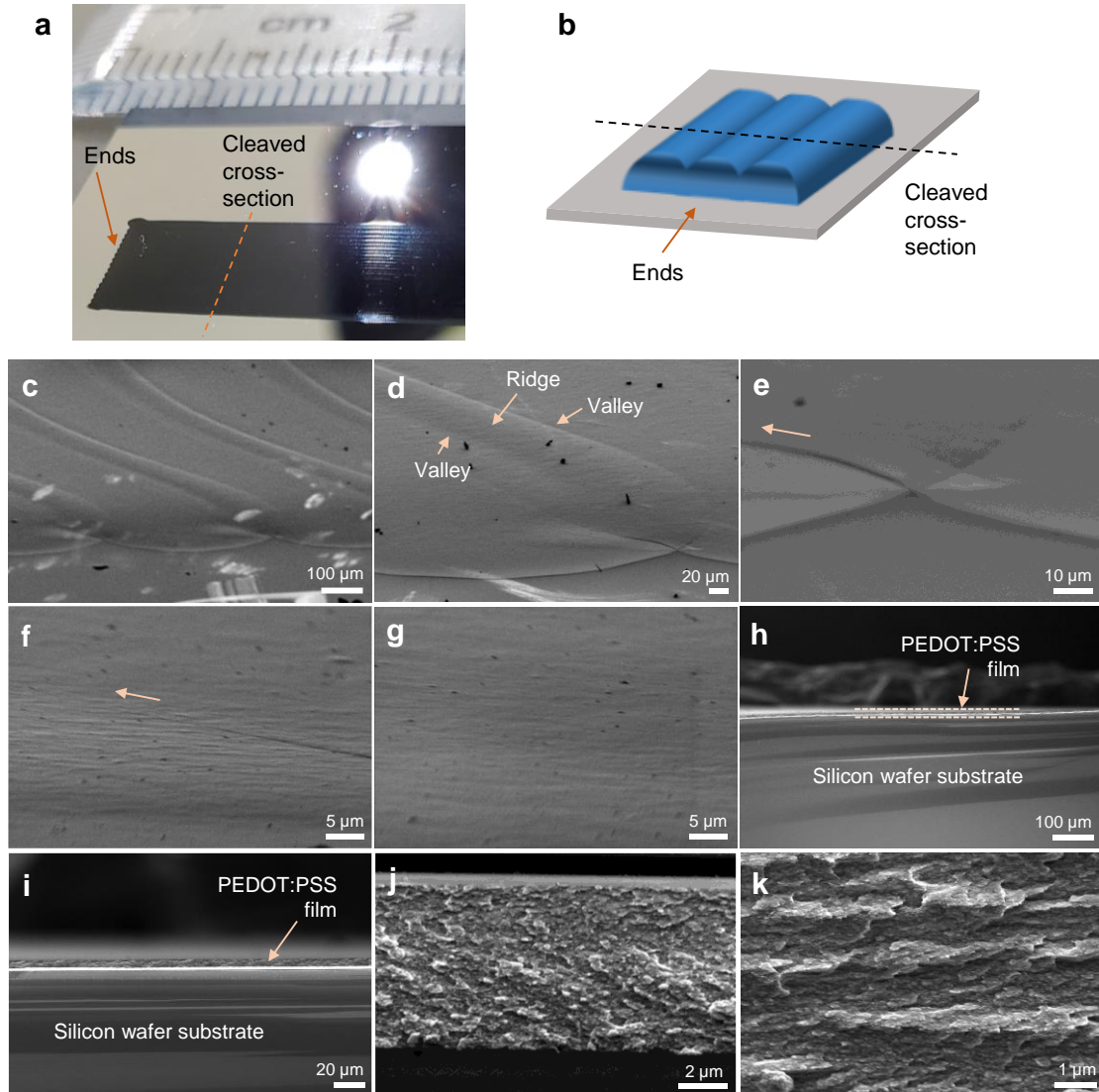


Figure 2.11. Filament interfaces within DIW printed PEDOT:PSS films. (a) Photograph showing the individual filaments within films. (b) Schematic diagram showing the two different viewing angles for the SEM images in (c-k). (c-g) SEM images of various magnifications showing the ends of the films. (c-e) Interface between individual filaments can be clearly visualized at a tilted angle. The arrow on (e) indicates the scanning direction leading to the frame in (f). (f) Approximately 2-3 mm from the ends of the films, adjacent printed filaments appear to fuse completely with no distinguishable interfaces beyond a shallow valley. The arrow on (f) indicates the scanning direction for obtaining (g), at/beyond which point, only the shallow valley is observable. (h-k) Cross-sectional SEM images of various magnifications showing uniform morphology, indicating the lines are indeed fully fused together.

2.5.4 3D Printing of PEDOT:PSS

With parameter optimization (Figure 2.9), we were able to demonstrate good resolution control for printed lines where their widths are nearly identical with the nozzle inner diameter for nozzle sizes ranging from 50 to 1039 μm (Figures 2.9e and 2.10). Six to ten layers of this ink can be stacked to form a variety of freestanding or encapsulated 3D structures (Figure 2.12a-d). Drying of the printed specimen leads to solid PEDOT:PSS. Scanning electron microscopy (SEM) images of a single-layer, solid PEDOT:PSS film show that adjacent filaments are merged together with no distinguishable interfaces along the cross sections (Figure 2.11). This is likely a result of the high water content of the PEDOT:PSS ink and the slow drying rate, which provides sufficient mobility and time for chains to diffuse and merge at the interfaces between adjacent filaments.

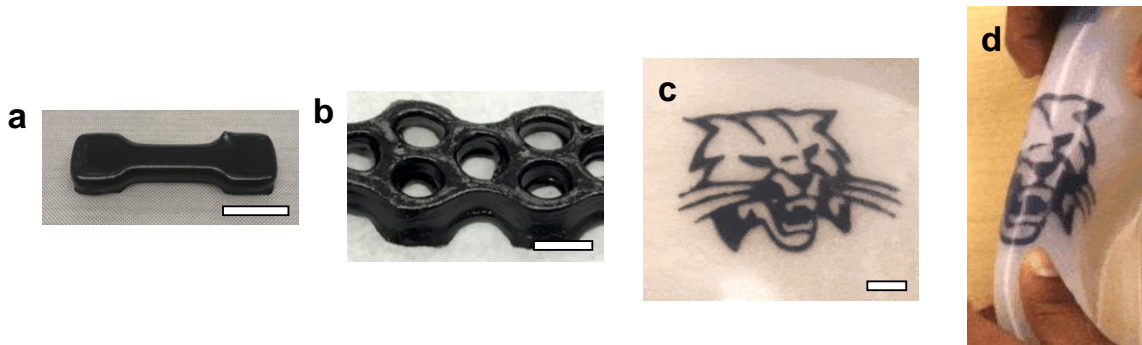


Figure 2.12. Photographs of 3D printed PEDOT:PSS: dog bone (a), connected wells (b), and bobcat embedded in silicone (c). Scale bar for (c-d): 10 mm.

2.6 Electrical Conductivity Characterization

2.6.1 Experimental

A Keithley 2450 SMU SourceMeter with a Keithley Model 5806 Kelvin Clip Lead Set was used to measure the four-terminal resistances of two-lead samples.

2.6.2 Comparison Between 2-Point and 4-Point Measurements

The average values are similar, with a barely 2.5% difference in conductivity between the two measurement methods. Four-point measurements eliminate contact resistance, which typically leads to higher conductivity values than when a two-point geometry is used. However, the Kelvin clamps are four-wire, two-contact measurement probes that are designed to minimize the resistance from contact transitions and measurement leads or supply cables. The differences in measured values between these two methods are small for our materials. Due to the small

width of the printed single filaments (hundreds of micrometers in width), it is challenging to carry out four-probe measurements along the direction perpendicular to the printing direction. Given the small difference in conductivity between 2-contact Kelvin clamp and 4-probe measurements along the parallel (\parallel) direction, we concluded that it is reasonable to use the 2-contact Kelvin clamp method for all measurements in this work (i.e., along directions parallel and perpendicular to the printing direction, single filament and films) for consistency and comparability.

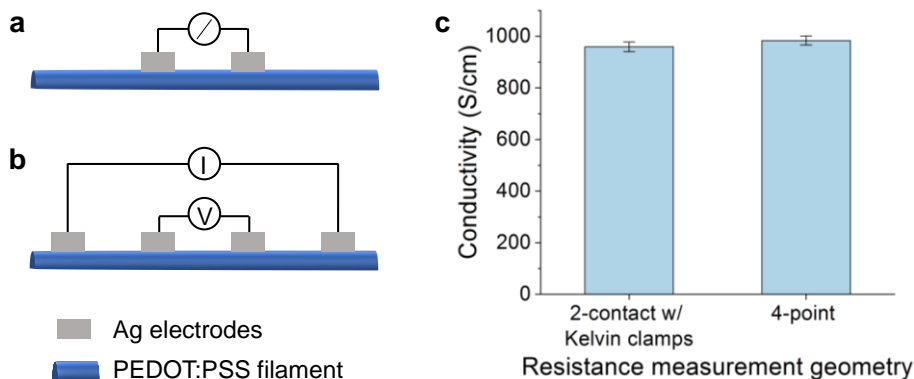


Figure 2.13. Comparison between two-contact resistance measurement using (a) Keithley 5806 Kelvin clamps and (b) four-point resistance measurement geometries. (c) Comparison between conductivity values of single printed filaments, measured along the direction \parallel to printing direction, obtained from the 2-contact Kelvin clamp measurements and the 4-point resistance measurements.

2.6.3 Anisotropic Conductivity of Printed Filament

To thoroughly understand the processing–structure–electrical property relations of the 3D printed PEDOT:PSS, we carried out a series of conductivity measurements based on the following rationale. (1) Since shear-based directional processing is often associated with anisotropic physical properties,^{29–32} conductivities were measured in the directions parallel (\parallel) and perpendicular (\perp) to the printing direction, denoted as σ_{\parallel} and σ_{\perp} , respectively (Figure 2.14a). (2) DIW 3D printing involves the extrusion of 1D filaments arranged into 2D layers, which are then vertically stacked into 3D structures. To understand the effect of this additive nature on the electrical properties of PEDOT:PSS, the conductivity anisotropy was analyzed for both single extruded lines and films that comprise ten slightly overlapping parallel lines. (3) During DIW extrusion, the ink experiences shear thinning, which is associated with domain alignment and/or chain extension or alignment.³³ A smaller nozzle diameter results in a higher shear force. Therefore, conductivity is measured for PEDOT:PSS extruded using a range of nozzle sizes.

Finally, (4) substrate temperature has been shown to influence the degree of crystallinity and phase separation in solution-processed CPs.³⁴ Hence, to investigate the relationship between substrate temperature and CP conductivity, the printing process was performed using different print bed temperatures. The results from these measurements are shown in Figure 2.14b-d.

Conductivity of the single extruded filaments best represents the electrical properties directly induced by the extrusion process (Figure 2.14b,c). Significant conductivity anisotropy between σ_{\parallel} and σ_{\perp} is observed for all printed filaments. Interestingly, the conductivity values, regardless of measurement directions, have negligible correlation with nozzle diameter. Also, both σ_{\parallel} and σ_{\perp} exhibit a minor dependence on print bed temperature. The σ_{\parallel} increases from ca. 576 to 851 S/cm and σ_{\perp} , from ca. 91 to 120 S/cm as the print bed temperature increases from 25 to 130 °C. We emphasize that the higher end of σ_{\parallel} for our printed PEDOT:PSS approaches the benchmark value of 1000 S/cm even in the as-printed form. These results demonstrate that high conductivity can be achieved in 3D printed CPs through ink preparation methods that mimic the conditions leading to high conductivity in 2D processing.

For DIW-printed films composed of ten parallel, slightly overlapping lines, the anisotropy between σ_{\parallel} and σ_{\perp} largely diminishes, but σ_{\parallel} remains consistently higher than σ_{\perp} within each film (Figure 2.14b,d). The σ_{\parallel} for each film is lower than the single filament counterpart, whereas the σ_{\perp} follows the opposite trend. Films printed with the high print bed temperature exhibit less conductivity anisotropy than those from low print bed temperature.

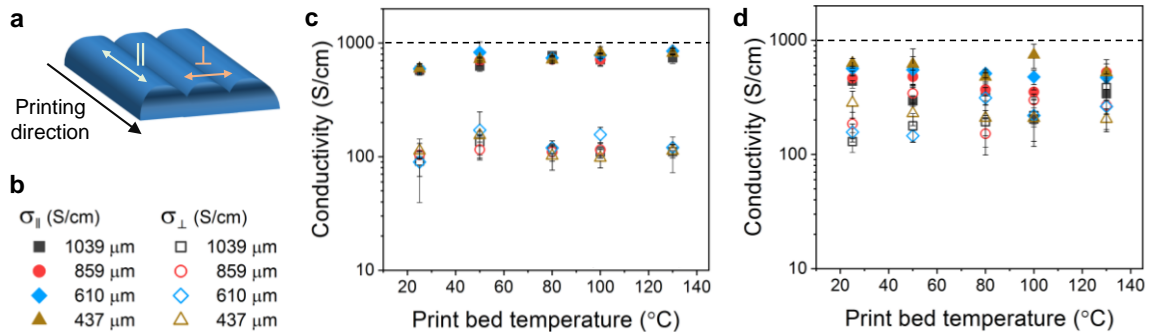


Figure 2.14. (a) Schematic illustration showing the parallel (\parallel) and perpendicular (\perp) directions with respect to the printing direction. (b) Legend for conductivity plots of printed (c) single lines and (d) films (composed of 10 lines). Dashed lines on (c) and (d) denote the benchmark 1000 S/cm conductivity for spin-coated PEDOT:PSS.

2.7 Mechanistic Investigation

To uncover the source of these conductivity trends, we investigate how printing parameters impact the key factors that influence electrical properties of PEDOT:PSS: (1) chain alignment, (2) nanoscopic morphology, (3) crystallinity, and (4) phase separation.

2.7.1 Probing Chain Alignment Through Rheology Simulation

In order to understand the response of PEDOT:PSS ink to shear flow fields and the cascade effects of this response on the structure-property relations of PEDOT:PSS in solid-state, we designed rheological experiments to simulate the DIW extrusion process.

2.7.1.1 Shear rate calculation for rheology simulation:

The shear-induced viscosity changes of the printing process were calculated using the Hagen-Poiseuille equation (eq. 1),³⁵ where $\dot{\gamma}$ is shear rate (s^{-1}), V is the resulting displacement volume (m^3) from each nozzles' optimized extrusion rate of radius R (m) in a print of known time t (s).

$$\dot{\gamma} = \frac{4V}{\pi R^3 t} \quad (\text{eq. 2.1})$$

Optimal extrusion rates were found for each nozzle size, so that the extruded filament matched the inner diameter of nozzles for consistent printing performance. These optimal extrusion rates were found by printing a 2D path, and modifying the extrusion rate, while keeping the print time and distance constant, resulting in different total extrusion volumes for each nozzle. The total print volumes were too small to directly measure, so instead, each nozzle's print volume was calculated by using the measured extrusion amount from a large print of a known extrusion rate.

The syringe displacement is controlled by a NEMA 17 stepper motor with known rotational parameters that allow us to convert from the total number of motor microsteps taken and the total extrusion volume. The stepper motor moves 200 steps per rotation with 16 microsteps per step:

$$\text{Microsteps} = (\text{Motor Rotations}) \left(\frac{200 \text{ Steps}}{\text{Motor Rotations}} \right) \left(\frac{16 \text{ Microsteps}}{\text{Steps}} \right) \quad (\text{eq. 2.2})$$

Each extrusion nozzle has an optimal extrusion rate, which is controlled by a nozzle-specific M92 E command value. The extrusion motor moves one microstep for every mm³ of the extrusion command in the G-code, multiplied by the nozzle-specific M92 E command value (eq. 2.3).

$$\text{Microsteps} = (\text{M92 E})(G - \text{Code Print Volume (mm}^3)) \quad (\text{eq. 2.3})$$

Equation 2.3 was used to calculate the total number of motor microsteps for a large test print which had an M92 E command value of 2000 and a programmed print volume of 8476.46 mm³ (eq. 2.4). The real extrusion volume was measured to derive a conversion factor that allows for the conversion of total number of microsteps to real extrusion volume:

$$\text{Microsteps} = (2000)(8476.46) \quad (\text{eq. 2.4})$$

$$= 1.6952920 \times 10^7$$

$$\frac{\text{Microsteps}}{\text{Real Extrusion Volume (m}^3)} = \frac{1.6952920 \times 10^7}{1.661 \times 10^{-5}} \quad (\text{eq. 2.5})$$

$$\frac{\text{Microsteps}}{\text{Real Extrusion Volume (m}^3)} = 1.02065 \times 10^{12}$$

$$\text{Microsteps} = 1.02065 \times 10^{12} \text{ Real Extrusion Volume (m}^3)$$

Substituting the value for microsteps in eq. 2.5 for microsteps in eq. 2.3 gives a new equation for the real extrusion volume when printing using any nozzle-specific M92 E command value (eq. 2.6).

$$1.02065 \times 10^{12} \text{ Real Extrusion Volume (m}^3) = (\text{M92 E})(G - \text{Code Print Volume (mm}^3))$$

$$Real\ Extrusion\ Volume\ (m^3) = \left(\frac{(M92\ E)(G\text{-Code}\ Print\ Volume\ (mm^3))}{1.02065 \times 10^{12}} \right) \quad (eq. 2.6)$$

Substituting equation 2.6 for extrusion volume in eq. 2.1 allows us to calculate each nozzle's shear rate by using nozzle inner diameter, G-code print volume, and nozzle-specific M92 E value.

$$\dot{\gamma} = \frac{4 \left(\frac{(M92\ E)(G\text{-Code}\ Print\ Volume\ (m^3))}{1.020645 \times 10^{12}} \right)}{\pi R^3 t} \quad (eq. 2.7)$$

The calculated nozzle shear rates for a variety of nozzles are summarized in Figure 2.15a. Viscosity values of the PEDOT:PSS ink for these shear rates can be extracted from the steady-state flow curves (Figure 2.15b).

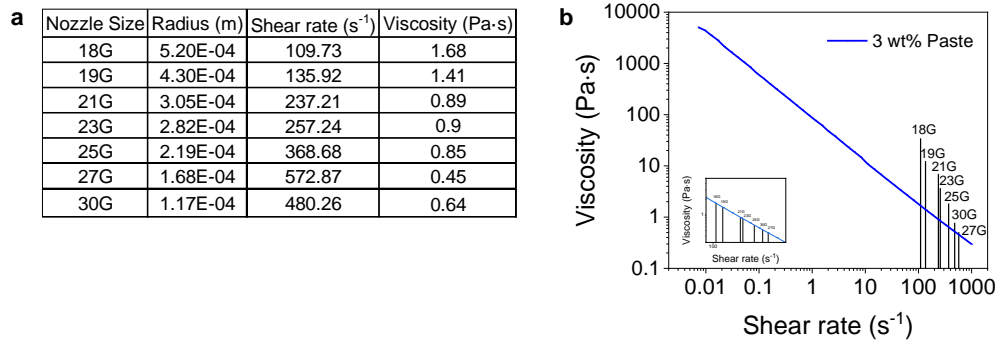


Figure 2.15. (a) Calculated shear rates and viscosities of PEDOT:PSS ink while extruded through nozzles of different inner diameters. (b) Calculated nozzle shear rates plotted on a 3 wt% PEDOT:PSS ink viscosity curve.

2.7.1.2 Rheology simulation

Two complementary rheological simulation studies were carried out to simulate the various stages of ink flow during and post DIW printing (Figure 2.16a). First, a rotational simulation test that monitors the viscosity changes of the PEDOT:PSS ink through various stages of flow was performed using parameters shown in Figure 2.16b. These shear rate values and time durations were calculated based on the parameters used for the printing. The simulation results are shown in Figure 2.16. Second, a combination of rotational shear and oscillatory shear, termed “O-R-O”, were carried out to study the storage modulus recovery of the ink. Parameters used for this test are shown in Figure 2.16c, and are chosen

to reflect the actual printing conditions. The results are shown in Figure 2.16d; an expanded view of the nozzle shear region of the plot is provided in Figure 2.16e.

Processing methods that involve directional shear flow are often reported to induce a certain degree of polymer chain or nanoscopic domain alignment.³³ This led us to investigate whether the shear from DIW printing induces polymer chains or domains to uncoil and/or deform and reorient along the flow direction, leading to anisotropic conductivity. To probe this hypothesis, we carried out rheological experiments to simulate the extrusion process.³⁶ We found that the viscosity and storage moduli recover rapidly within approximately 20 s for all nozzle diameters, which is faster than the time it takes for the printed ink to dry (Figure 2.16). From this, we can conclude that shear-induced alignment is not a significant contributor to the observed anisotropic conductivity,³⁷ which explains the lack of dependence of conductivity on nozzle diameter.

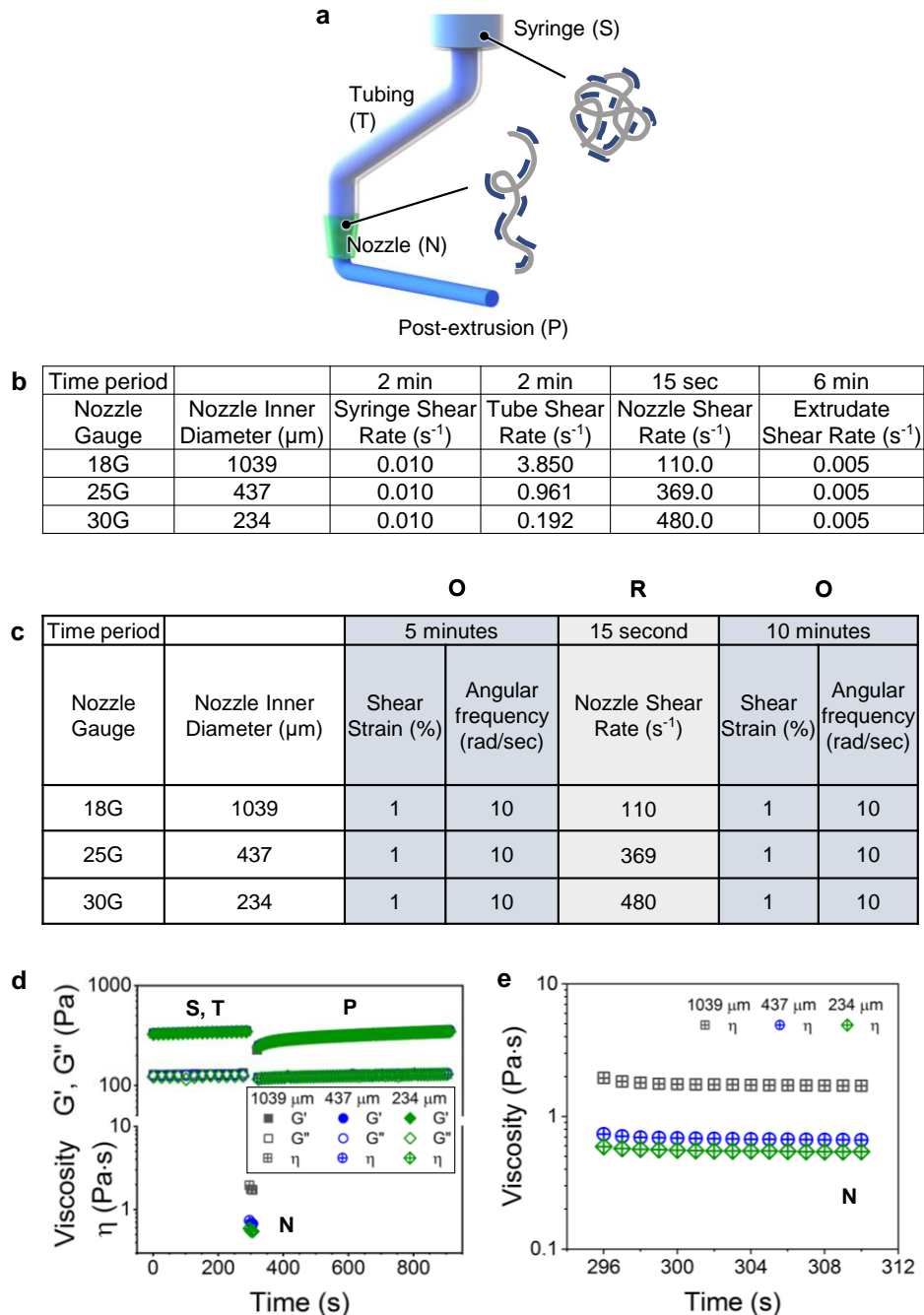


Figure 2.16. (a) Schematic illustrations of the travel path of PEDOT:PSS ink and the associated conformational changes of PEDOT:PSS complexes under flow. (b) Viscosity changes of the PEDOT:PSS ink through various stages of flow. (c) Summary of parameters used for simulating the rheological behavior of PEDOT:PSS ink during different stages in the extrusion printing process using three representative nozzle sizes. O and R represent the test in oscillatory shear and steady-state rotational shear modes, respectively. (d) Printing rheology simulations with PEDOT:PSS ink using parameters from (c), simulating when ink

is in the syringe (S), feed tube (T), print nozzle (N) and post-extrusion (P). (e) An expanded view of the nozzle (N) shear rate section in (d).

2.7.2 Wide Angle X-Ray Scattering

The WAXS spectra shown in this manuscript were collected at Beamline 7.3.3 of the Advance Light Source (ALS), Lawrence Berkeley National Lab (LBNL). Preliminary data (not shown here) were collected on Beamline 11-3 at the Stanford Radiation Lightsource, SLAC National Accelerator Laboratory. A transmission geometry was used with the printing direction of the films aligned along the vertical (q_z) direction. The beam energy used for experiments conducted at ALS and SLAC were 10 keV and 12.7 keV, respectively. For the ALS experiments, samples were analyzed in an argon environment, and an exposure time of 10 s was used. Igor Pro Nikka Irena packages were used to analyze the 2D spectra and to extract 1D spectra of integrated intensity vs. scattering wave vector (q). The q_x and q_z curves were obtained by integrating a 20 deg sector of the 2D spectra along the direction perpendicular and parallel to the printing direction, respectively. Crystal sizes were determined by applying the Scherrer equation to the PEDOT (020) π - π stacking peak ($q = 1.84 \text{ \AA}^{-1}$). 1D WAXS spectra integrated from 20 deg sectors along the directions parallel (q_z) and perpendicular (q_x) to the printing direction for films printed using two different nozzle sizes, each at a bed temperature of 25 °C and 100 °C, are shown in Figure 2.17.

Wide angle X-ray scattering (WAXS) was employed to further elucidate the origins of the weak dependence of PEDOT:PSS conductivity on substrate temperature and the lack of correlation between nozzle size and conductivity. Higher print bed temperature leads to an increase in PEDOT π - π stacking peak intensity ($q \approx 1.8 \text{ \AA}^{-1}$), and hence a higher PEDOT-to-PSS peak ratio, and crystallite size (Figure 2.18b). This is consistent with those from prior literature which illustrated that elevated solvent evaporation rates, resulting from higher substrate temperature, improves the ordering of solution processed CPs, thus increasing conductivity.³⁷ However, little difference in PEDOT π - π peak intensity, and hence PEDOT-to-PSS peak ratio, is observed between PEDOT:PSS printed using different nozzle sizes (Figure 2.18a,b), nor is there any anisotropy in peak intensity or crystallite sizes (Figures 2.17 and 2.18c).

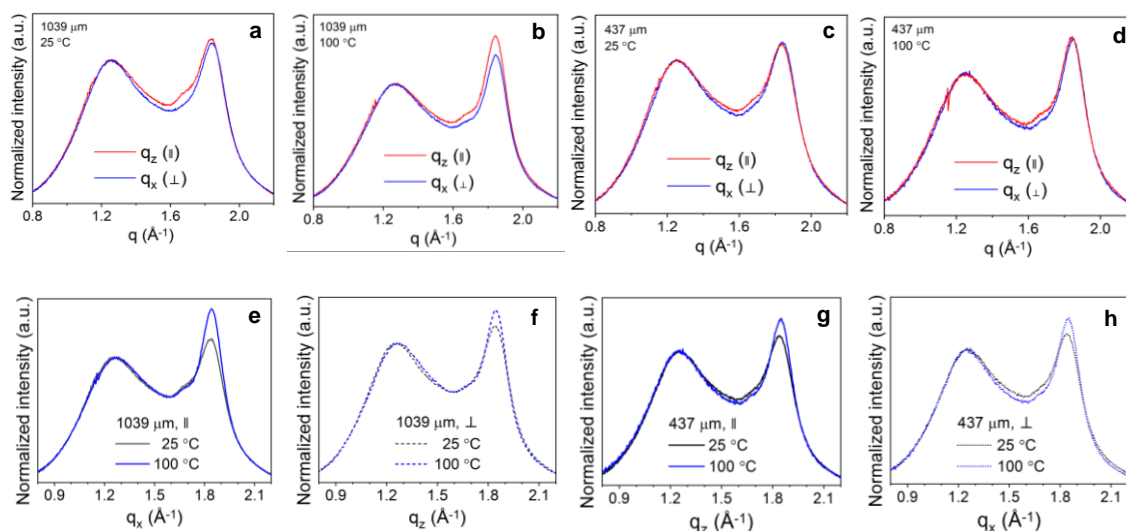


Figure 2.17. Integrated 1D intensities of WAXS spectra along the directions parallel and perpendicular to the printing direction under conditions indicated on each plot. Plots (a-d) compare spectra along the two directions. Plots (a-b) compare spectra when printing with a 1039 μm nozzle and bed temperatures of 25 $^{\circ}\text{C}$ (a) and 100 $^{\circ}\text{C}$ (b), respectively. Plots (c-d) compare spectra of samples printed with a 437 μm nozzle at bed temperatures of 25 $^{\circ}\text{C}$ (c) and 100 $^{\circ}\text{C}$ (d), respectively. Plots (e-h) compare spectra of samples printed with bed temperatures of 25 $^{\circ}\text{C}$ and 100 $^{\circ}\text{C}$. Plots (e-f) compare spectra of samples printed using a 1039 μm nozzle, plotted along the parallel (e) and S-18 perpendicular (f) directions, respectively. Plots (g-h) compare spectra printed using a 437 μm nozzle, plotted along the parallel (g) and perpendicular (h) directions, respectively.

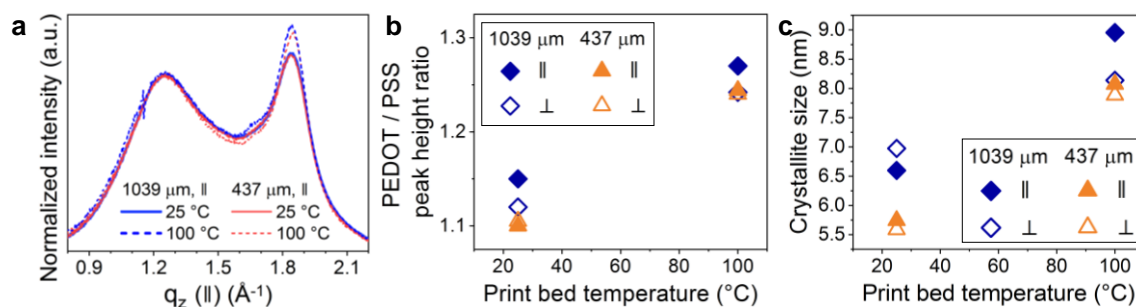


Figure 2.18. (a) Integrated 1D intensities of WAXS spectra along the parallel direction of films printed using different nozzle diameters. (b) Height ratios of the PEDOT (020) ($q \approx 1.8 \text{ \AA}^{-1}$) and PSS ($q \approx 1.2 \text{ \AA}^{-1}$) peaks from integrated 1D intensities of WAXS spectra along the parallel direction of films printed using different nozzle diameters. (c) Calculated PEDOT crystallite sizes along the parallel and perpendicular directions for films printed with different bed temperatures and nozzle diameters.

2.7.3 Atomic Force Microscopy

Experimental: The AFM samples were prepared by printing PEDOT:PSS on highly doped silicon wafers (UniversityWafer, 1113), followed by the same drying procedure detailed in a previous section. The samples were annealed at 130 °C for 10 min before AFM imaging to remove surface moisture. AFM images were collected on a Park NX10 AFM using PPP-NCHR (Nanosensors) tips at the Imaging and Manipulation of Nanostructures Lab of the Molecular Foundry, Lawrence Berkeley National Lab (LBNL). Phase and height images were obtained using tapping mode at a 512 × 512 pixel density and processed using Gwyddion.

PEDOT:PSS films typically have a grain- or fiber-like morphology comprised of PEDOT-rich domains encompassed by PSS-rich shells.^{20,38} Compared to the relatively spherical grain morphology in spin-coated films (Figure 2.19a)^{20,38}Error! Bookmark not defined. the grains from DIW-printed samples are more interconnected and hence larger in size (Figure 2.19c,e). However, the arrangement of these grains do not show clear directionality at the nanoscopic domain scale, evidenced by the near-spherical fast Fourier transform (FFT) patterns of the AFM images (Figure 2.19c,e). These results are consistent with the findings of rheological simulation, which indicated that the chains or domains relax back to the isotropic state rapidly after shear force is removed. Previous reports on shear-based 2D processing such as solution shearing or brush painting have illustrated that shear force can induce aggregation and merging of PEDOT:PSS micelles in solution, leading to larger grain sizes or fiber-like morphologies in solid-state.^{29,32,38} Our results demonstrate that the shear force in DIW-extrusion leads to similar morphological effects in our 3D printed films.

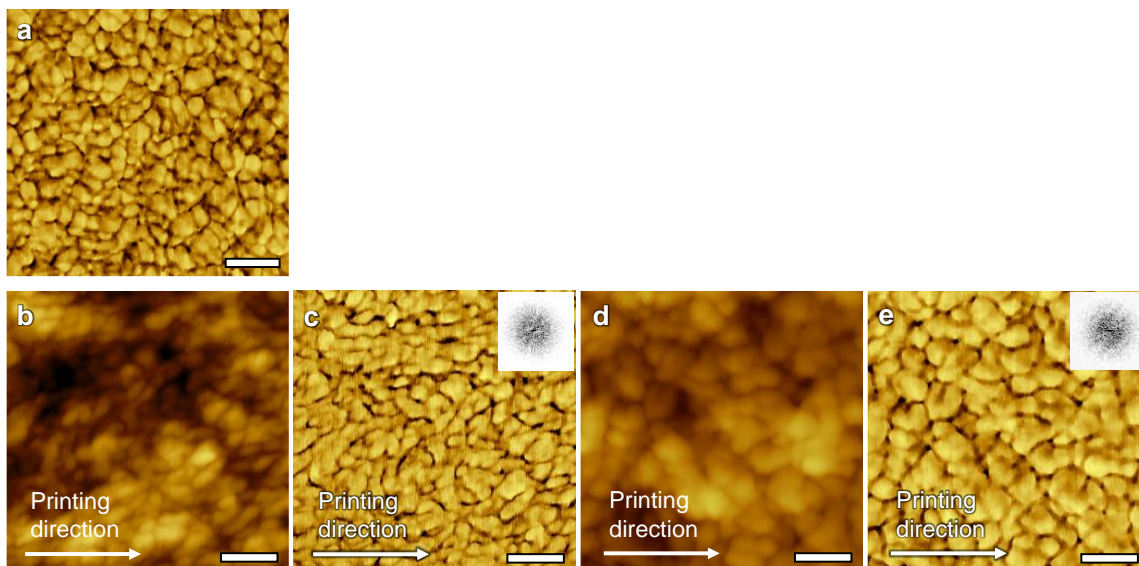


Figure 2.19. (a) AFM phase image of spin coated PEDOT:PSS film as a reference for comparison. AFM height (b) and (d) and phase (c), (e) images for films printed with a bed temperature of 100 °C using nozzles with inner diameters of 1039 μm (b, c) and 437 μm (d, e). Scale bars: 100 nm.

2.7.4 Phase Separation

The minor crystallographic and morphological anisotropies cannot account for the significant conductivity anisotropy, with a difference as large as 730 S/cm between σ_{\parallel} and σ_{\perp} (Figure 2.14c). We noticed that one distinct feature of these DIW-printed PEDOT:PSS is that they have unusually strong phase separation. Transparent outlines around the printed specimen can often be visibly observed, particularly around corners where the capillary force is especially strong. Some of these transparent outlines are large enough (3-5 mm in width) to be isolated for WAXS and X-ray photoelectron spectroscopy (XPS) analyses, both of which confirm its identity as PSS (Figure 2.20).^{38,39}

To understand the effect of phase separation on sample conductivity, XPS was employed to probe the chemical composition at different locations of the printed filaments (Figure 2.21) and films (Figure 2.22). For PEDOT:PSS, two sets of distinct peaks are observed in XPS: doublets at 163.7 eV and 165.4 eV, arising from the S 2p_{1/2} and S 2p_{3/2} of the thiophene in PEDOT, and the higher binding energy peak centered at around 167.8 eV, which is the sum of the 167.6 eV (S 2p_{1/2}) and 168.9 eV (S 2p_{3/2}) constituents of the sulfonate sulfur in PSS.^{39,40} For single printed lines, XPS revealed different chemical composition at the middle, edge, and outline (i.e., area immediately adjacent to the filament edge), denoted as M, E, and O, respectively (Figure 2.21a). Each filament is surrounded by a pure

PSS outline on the sides. The absence of the inductive effects from positively charged PEDOT causes the PSS peak in the outline to appear at a higher binding energy (168.6 eV) than that in PEDOT:PSS, confirming that the PSS chains in the outline are unbound to PEDOT.⁴¹ Integrating the areas under peaks reveal that the PEDOT content is slightly higher in the middle of the filament (ca. 35%) than near the edges (ca. 31%) (Figure 2.21).

2.7.4.1 Identity of the transparent film around the prints

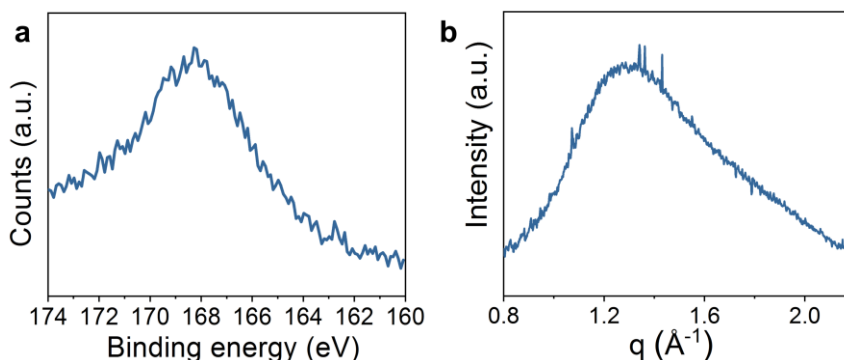


Figure 2.20. (a) XPS and (b) WAXS spectra of the phase separated pure PSS around the outline of the printed PEDOT:PSS lines that can be seen in Figure 2d,e. The XPS peak centers at around 168.4 eV, characteristic of the sulfonate S 2p binding energy from free PSS. The broad peak in WAXS centers at 1.28 \AA^{-1} , coincides with the repeating distance between PSS chains.^{32,37,39}

2.7.4.2 XPS peak fitting

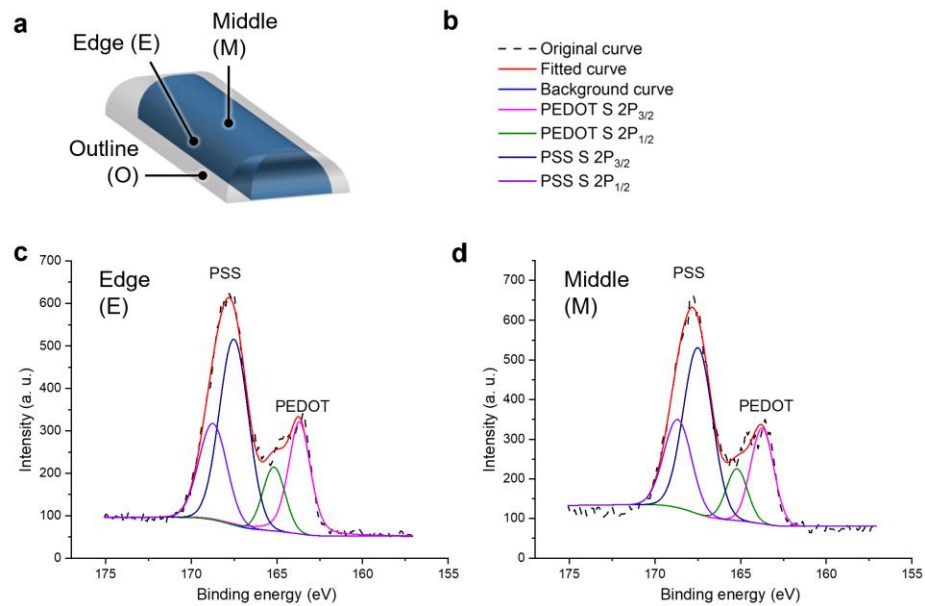


Figure 2.21. (a) Schematic drawing showing the different regions of a single printed line. (b) Legend for (c) and (d). (c) Peak fitting for the XPS spectra collected at the edge and (d) middle of a single printed line.

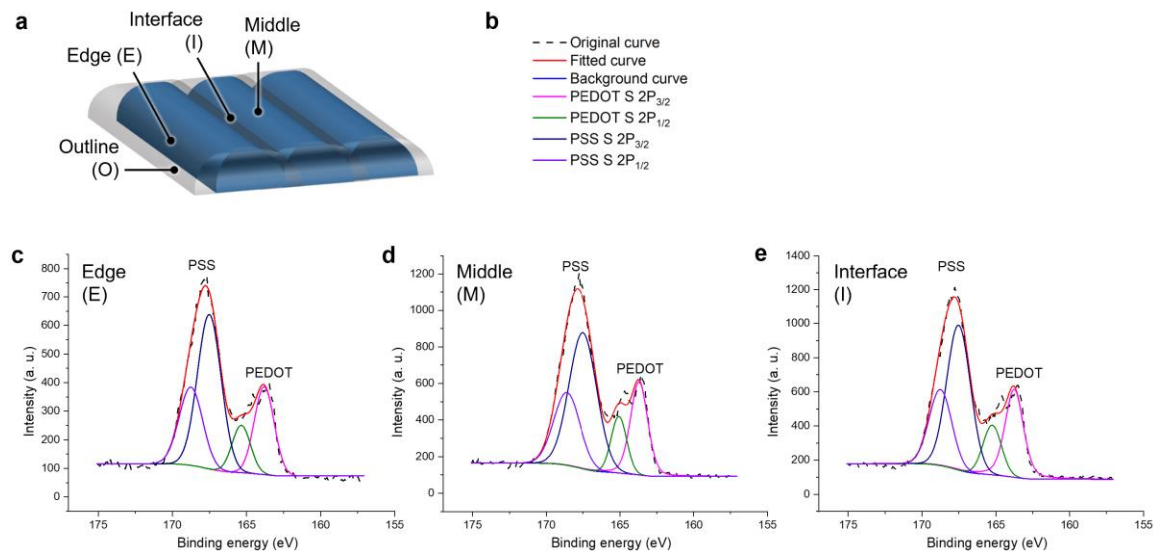


Figure 2.22. (a) Schematic drawing showing the different regions of a printed film (10 parallel lines). (b) Legend for (c-e). (c) Peak fitting for the XPS spectra collected at the edge of the film, (d) middle of a line within the film, and (e) interface between two adjacent lines within the film.

The likely cause of this strong lateral phase separation is the drying kinetics of the printed specimen. While the shear-based DIW 3D printing mechanism bears resemblance to brush painting or solution shearing, the drying kinetics of the 3D printed PEDOT:PSS is similar to drop casted films. The nozzle diameters used in our study varied from 50 to 1039 μm , leading to filaments of PEDOT:PSS paste of width similar to the nozzle diameters (because the bottom of the filaments are pinned to the substrate), but shrinking in the height direction to 25 to 35 μm upon complete drying. This thickness range is similar to that of drop casted films, but diverges significantly from the spin coated, brush painted, or solution sheared counterparts, which have thickness of tens to hundreds of nanometers. As a result, the time scale for drying is significantly longer for 3D printed samples than those from 2D shear-based methods. The as-purchased PEDOT:PSS formulation has a PEDOT-to-PSS ratio of 1-to-2.2 because excess PSS is necessary to offset the poor water-solubility of PEDOT to create a stable colloidal dispersion. Previous work has shown that $\sim 73\%$ of PSS is associated with PEDOT through electrostatic interaction, indicating the presence of a substantial amount of free PSS.⁴² Prior to concentrating the ~ 1 wt % PEDOT:PSS aqueous dispersion to a 3 wt % printable ink, 5 vol % of DMSO was added for conductivity enhancement. DMSO has a low vapor pressure and does not form azeotropes with water.⁴³ Therefore, as water evaporates, the DMSO concentration in solvent consistently increases. Hence, the 3 wt % PEDOT:PSS aqueous ink likely has a DMSO concentration of ~ 17 vol %. As the extruded filament dries, the DMSO concentration gradually increases due to the decrease in water content. The PEDOT:PSS electrostatic complex can be swelled by, but cannot be dissolved in the DMSO-rich solvent.⁴³ On the other hand, the free PSS is soluble in this solvent environment and can be extracted to concentrate in this phase. As a result of this solid-liquid phase separation, PEDOT:PSS complexes precipitate out while the free PSS accumulates in the DMSO-rich solvent on the periphery of the printed lines, leading to strong phase separation, evidenced by the observed chemical compositional differences across the filament width (Figure 2.21). This proposed mechanism is in agreement with previous findings demonstrating that drying drop-casted PEDOT:PSS containing over 10 vol % DMSO leads to significant radial phase separation, with unbound PSS forming a border around the PEDOT:PSS film.⁴³

2.7.5 Relationship Between Phase Separation and Conductivity

The lateral phase separation of DIW-printed PEDOT:PSS has a strong effect on the value and anisotropy of its conductivity. In this section, we first explain (i) the electrode configuration for σ_{\parallel} and σ_{\perp} measurements, then discuss (ii) how

the phase separation in combination with electrode configuration have led to the strongly anisotropic conductivity shown in Figure 2.14.

2.7.5.1 Electrode configuration

To measure the σ_{\parallel} for a single line, silver electrodes were painted perpendicular to the printing direction across the widths of the printed lines approximately 1 cm apart from each other perpendicular to the printing direction (Figure 2.23a).

To measure the σ_{\parallel} for a printed film, two silver electrodes were painted perpendicular to the printing direction across the widths of the printed film. The electrodes were approximately 1.3 cm from each other (Figure 2.23b).

To measure the σ_{\perp} for a single line, a narrow strip of cellophane tape (Scotch Magic Tape, 3M) was cut to a width of approximately half of a printed line's width. It was then aligned along the length of the line and adhered with gentle force to the middle section of the line to act as a mask for silver paste electrode deposition on both sides. Silver paste electrodes were painted over the exposed sides of the printed PEDOT:PSS line and allowed to dry at room temperature for 20 minutes. The tape mask was then peeled off, leaving a gap between the electrodes. Subsequently, the sample was heated to 130 °C for 10 minutes to remove remaining solvents in silver electrodes, followed by being cut into segments that are approximately 1 mm wide (Figure 2.23c).

To measure the σ_{\perp} for multi-line films, Scotch Magic Tape was cut into narrow strips to act as a mask that ensures the electrode is only painted on the outer lines. Two narrow strips of tape were applied to a sample along the printing direction, each with one of their edges masking the inner half of the outermost printed lines on either side of the sample. Silver paste electrodes were painted over the exposed outer sides of the PEDOT:PSS samples and then allowed to dry at room temperature for 20 minutes. The tape was then peeled off, and the samples were heated to 130 °C for 10 minutes to finish drying. The samples were then cut perpendicular to the printing directions to make rectangular samples that were approximately 3 mm wide (Figure 2.23d).

2.7.5.2 Effect of phase separation on conductivity

This strong lateral phase separation is likely the cause of the strong conductivity anisotropy in printed filaments (Figure 2.14c). For σ_{\parallel} measurement, the entire width of the printed line is wrapped within the electrodes (Figure 2.22a). Despite the strong lateral phase separation, efficient charge transport is facilitated by the direct contact of the PEDOT-rich middle section of the line with the

electrodes. Conversely, in σ_{\perp} measurements, the electrodes are largely in contact with the PSS outline, so the PSS outline and PSS-rich line edges act as barriers that impede efficient charge transport (Figure 2.23c), leading to substantially lower measured conductivity values.

To probe whether inter-filament interfaces in DIW-printed PEDOT:PSS films form resistive barriers between adjacent lines, we analyzed the chemical composition at the interface (I) between adjacent lines in addition to the middle and edge of lines and the outline of the film (Figure 2.22a). As shown in the stacked XPS spectra and the integrated atomic composition plot (Figure 2.22), a pure PSS outline is observed at the periphery of the film. The PEDOT composition at the line edge and the interface between adjacent lines are similar, 32 and 31%, respectively, which is slightly lower than the 35% PEDOT content at the middle of the line. Considering the drying time for filaments is likely on the order of hundreds of seconds,³⁷ and the printing speed is 16 mm/s for printing structures that are typically 20-60 mm in length, the newly extruded filament is likely deposited on a hydrated previously deposited filament. The absence of a significantly more PSS-rich region at the line interfaces suggest that the adjacent lines merge while they are still hydrated before the lateral phase separation could occur within individual filaments, meaning less PSS separates into its own phase. Consequently, we conjecture that the printed PEDOT:PSS films contain more free PSS across its volume, beyond the surface depth that XPS can profile, than the single printed lines. This could explain the weaker conductivity anisotropy in films where their σ_{\parallel} are lower than those in their respective single-line counterparts (Figure 2.14d).

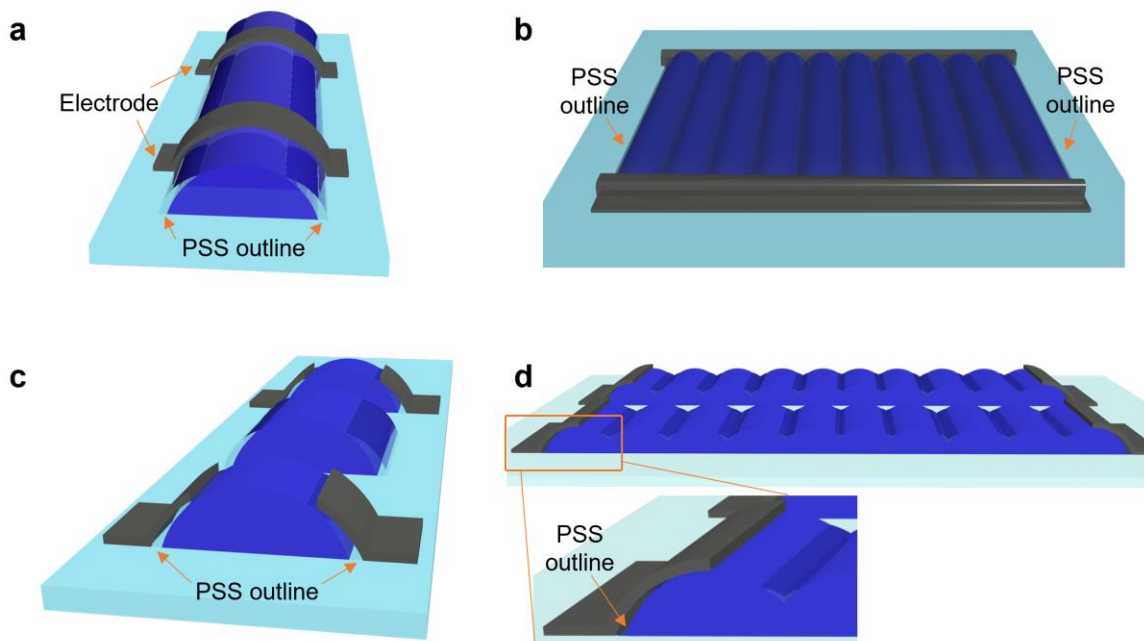


Figure 2.23. Schematic illustration depicting the electrode configuration and measurement geometry for $\sigma_{||}$ (a) for single line, (b) for film and σ_{\perp} (c) for single line, (d) for film. For σ_{\perp} measurements (c), (d), the printed single lines or films are isolated into sections that share the same length as the electrode width. Each film is comprised of 10 lines deposited parallel to each other. The σ_{\perp} for films are higher than those measured in single-line samples likely due to the larger contact areas between electrodes and the filaments forming the edges of films, facilitating more efficient charge transport between the more PEDOT-rich areas and electrodes. The film σ_{\perp} values remain lower than their $\sigma_{||}$ counterparts likely because of the multiple inter-filament junctions and line edges, both of which have slightly higher PSS content compared to the middle of the lines.

2.8 Post-Printing DMSO Treatment to Improve Conductivity

With the knowledge that strong phase separation is the main cause for lowered conductivity and strong anisotropy in DIW 3D printed PEDOT:PSS films, we carried out a post-printing solvent treatment to remove the PSS outline. A number of polar organic solvents, including short-chain alcohols or their mixtures, DMSO, ethylene glycol, and aqueous acid solutions, have been shown to be effective solvents in removing unbound PSS.²⁰ We chose DMSO as the rinsing solvent to be consistent with the solvent additive incorporated in the initial DIW ink preparation to avoid additional variables.

Using the 1039 μm nozzle as a case-study, XPS analyses confirm the complete removal of the pure PSS outline at the filament and film periphery and

some unbound PSS within the PEDOT:PSS (Figures 2.27 and 2.28). The anisotropic conductivity data for as-printed single lines and films printed using the 1039 μm nozzle are isolated in Figure 2.25a, where the different sets of values are scattered across a nearly one order of magnitude range. In stark contrast, after DMSO treatment, the σ_{\parallel} for single lines and films and the σ_{\perp} for films all converged to the ca. 1000 S/cm region (Figure 2.25b). Notably, the σ_{\parallel} for the DMSO-treated single lines, regardless of print bed temperature, are all above the benchmark 1000 S/cm value, with values as high as ca. 1200 S/cm. WAXS and AFM also confirm that the mechanism for this increase in conductivity and decrease in anisotropy is the removal of free-PSS through DMSO-rinsing (Figures 2.24, 26, and 27).

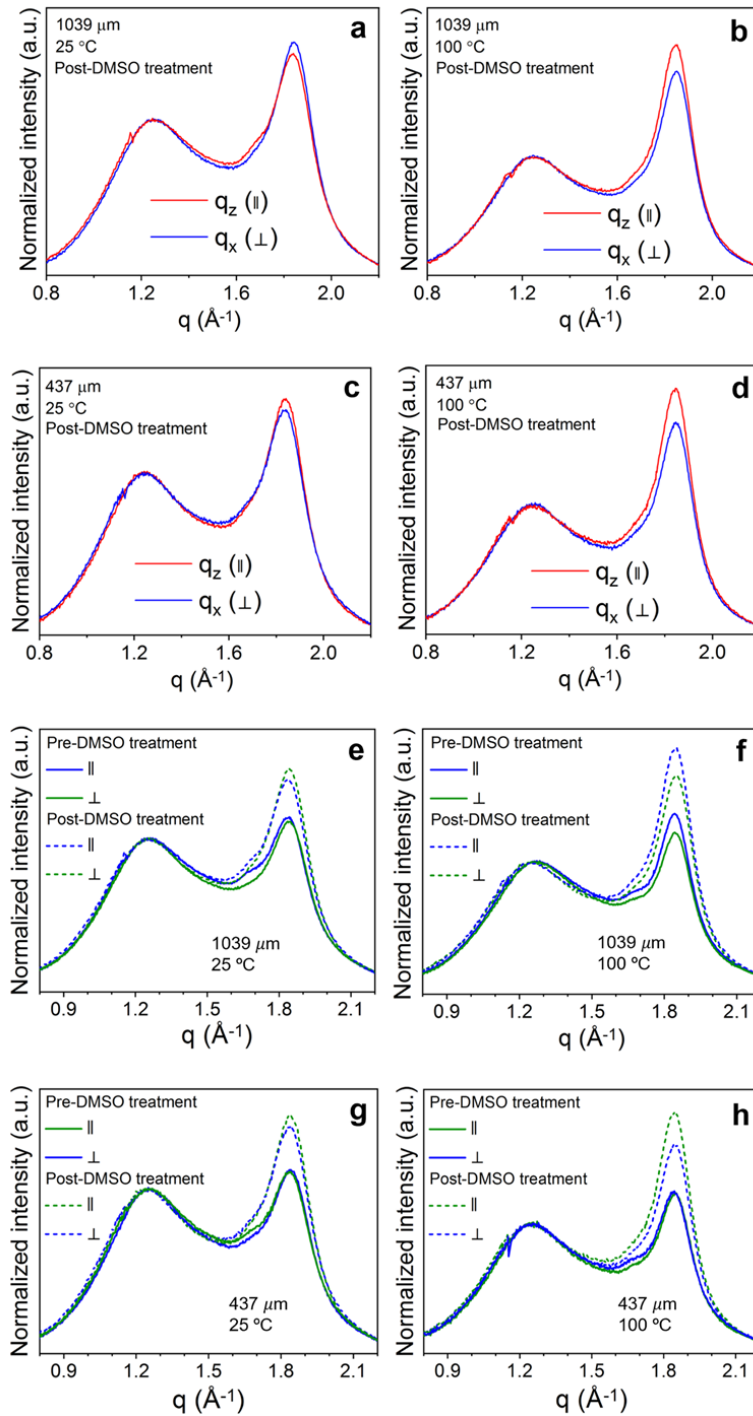


Figure 2.24. Integrated 1D intensities of WAXS spectra along the parallel and perpendicular directions of films under conditions specified on each plot.

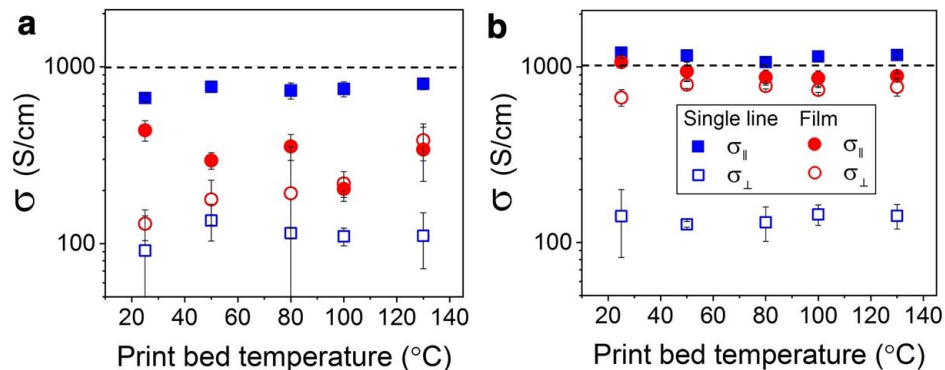


Figure 2.25. (a) Conductivity along the parallel and perpendicular directions for as-printed dried PEDOT:PSS single lines and films extruded using a 1039 μm nozzle. (a) shares the same legend as (b). (b) Conductivity for PEDOT:PSS single lines and films printed using a 1039 μm nozzle after DMSO treatment.

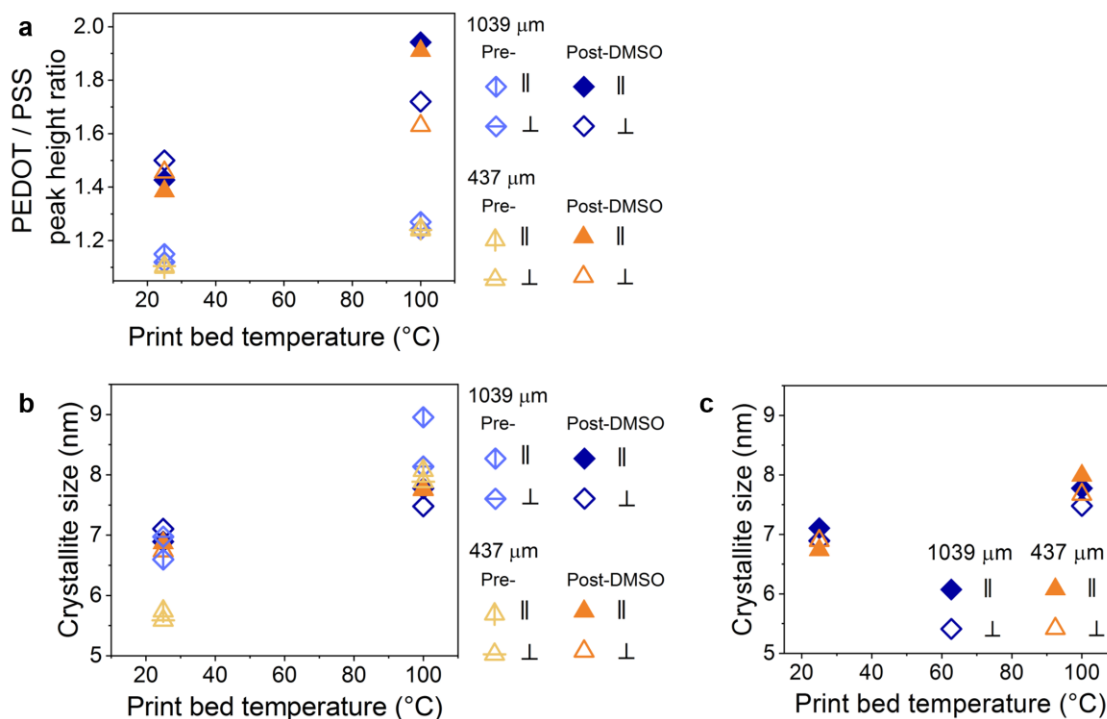


Figure 2.26. (a) Height ratios of the PEDOT (020) ($q \approx 1.8 \text{ \AA}$) and PSS ($q \approx 1.2 \text{ \AA}$) peaks and (b) calculated PEDOT crystallite sizes based on the PEDOT (020) peak along the parallel and perpendicular directions for films printed with different bed temperatures and nozzle diameters, before and after DMSO treatment. The crystallite sizes after the DMSO treatment are isolated in (c) for clarity.

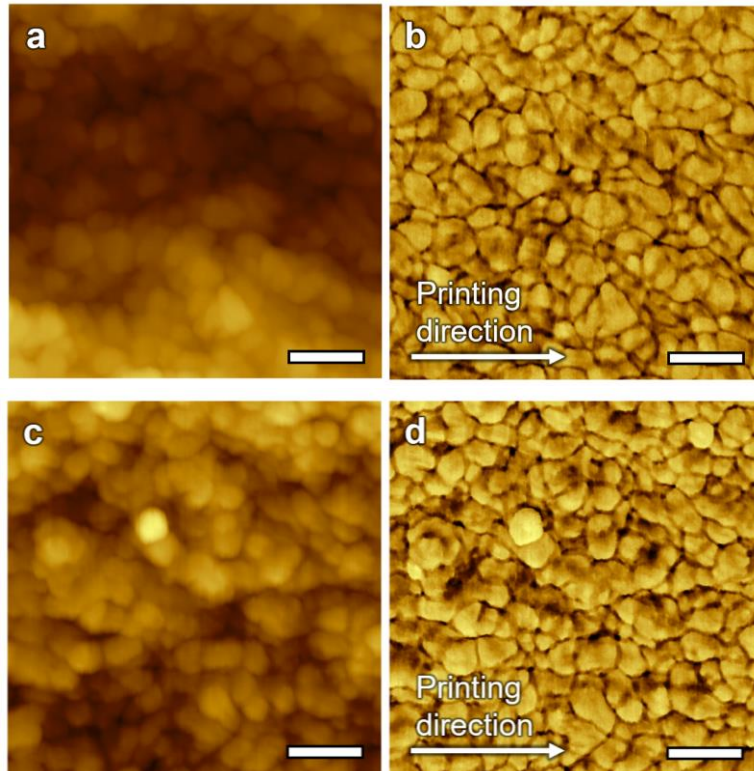


Figure 25.27. AFM height (a, c) and phase (b, d) images for post-DMSO-treated PEDOT:PSS films printed with a bed temperature of 100 °C using nozzles with inner diameters of 1039 μm (a, b) and 437 μm (c, d). Scale bars for (a)-(d): 100 nm.

2.8.1 Additional data on the effect of DMSO treatment on phase separation

We hypothesized that the PSS concentrated at the interfaces of printed filaments were the cause of the observed anisotropic conductivity. XPS analysis was used to investigate whether the DMSO treatment decreased the anisotropy by removing these PSS interfaces.

After the DMSO treatment, the pure PSS outline is removed from both single lines and films. In films, the thiophene (from PEDOT) to sulfonate (from PSS) S 2p peak ratios become significantly higher compared to the as-printed samples (Figure 2.22), which is also reflected by the higher PEDOT content: 48% at line edges, 51% at the middle of the lines, and 46% at interfaces between adjacent lines. Similar to as-printed films, the slightly higher σ_{\parallel} compared to σ_{\perp} is likely a result of the slightly more resistive inter-filament junctions with higher PSS content. The spherical nozzle geometry and the line-by-line deposition mechanism lead to a slight dip in height between adjacent lines. It is possible that small amount

of the PSS that was extracted from the PEDOT:PSS film by the DMSO treatment was redeposited in these gaps during the drying step, leading to the higher PSS content in these regions. The PSS sulfonate S 2p peak for post-DMSO treated samples appear at 167.5 eV as opposed to those in as-printed counterparts (167.8 eV). This 0.3 eV peak shift to lower binding energy further corroborates the removal of free PSS, for which the peak appears at a higher binding energy due to the absence of electrostatic effects from the positively charged PEDOT.^{38,39}

Interestingly, the σ_{\perp} for post-DMSO treated single lines remain approximately the same as the as-printed samples. This can be attributed to the mostly unchanged PEDOT-to-PSS ratio at line edges (2.25a and 2.28). The higher PSS content at edges could be a result of the higher edge-to-volume ratio in single lines compared to films. This causes the PSS-containing DMSO to collect at filament edges due to the higher capillary force, which may have resulted in the dissolved PSS to be reabsorbed into the edges during drying. Additional rinsing steps with fresh DMSO or other solvents may alleviate this lateral compositional difference. Given that the emphasis of this study is to identify the source of low conductivity and reach the 1000 S/cm benchmark conductivity in DIW-printed PEDOT:PSS, we elected not to focus on post-treatment optimization.

Interestingly, the σ_{\perp} and PEDOT-to-PSS ratio for post-DMSO treated single lines remain approximately the same as in the as-printed samples (Figures 2.25a,b and 2.28). XPS positional analysis reveals that the PEDOT content in the middle of the single line increases to 51%, but the content remains approximately the same as the as-printed counterparts at the line edges (30%) (Figures 2.28 and 2.29). This compositional difference could explain the observation that DMSO treatment leads to σ_{\parallel} increase for single lines, but not for σ_{\perp} as the more resistive PSS-rich line edges are the areas in direct contact with electrodes in σ_{\perp} measurements (Figure 2.30). The reason for the higher PSS content at edges could be a result of the higher edge-to-volume ratio in single lines compared to films. The PSS-containing DMSO may collect at the single filament edges due to the higher capillary force, which may have resulted in the PSS dissolved in the DMSO to be reabsorbed into the line edges during drying. Additional rinsing steps with fresh DMSO or other solvents may alleviate this lateral compositional difference. Given the emphasis of this study is to understand processing-structure-property relations for DIW 3D printed PEDOT:PSS and to reach the 1000 S/cm benchmark conductivity, we elected not to focus on optimization of the post-treatment step. It will be a subject of future investigations.

2.8.1.1 XPS spectra and peak fitting

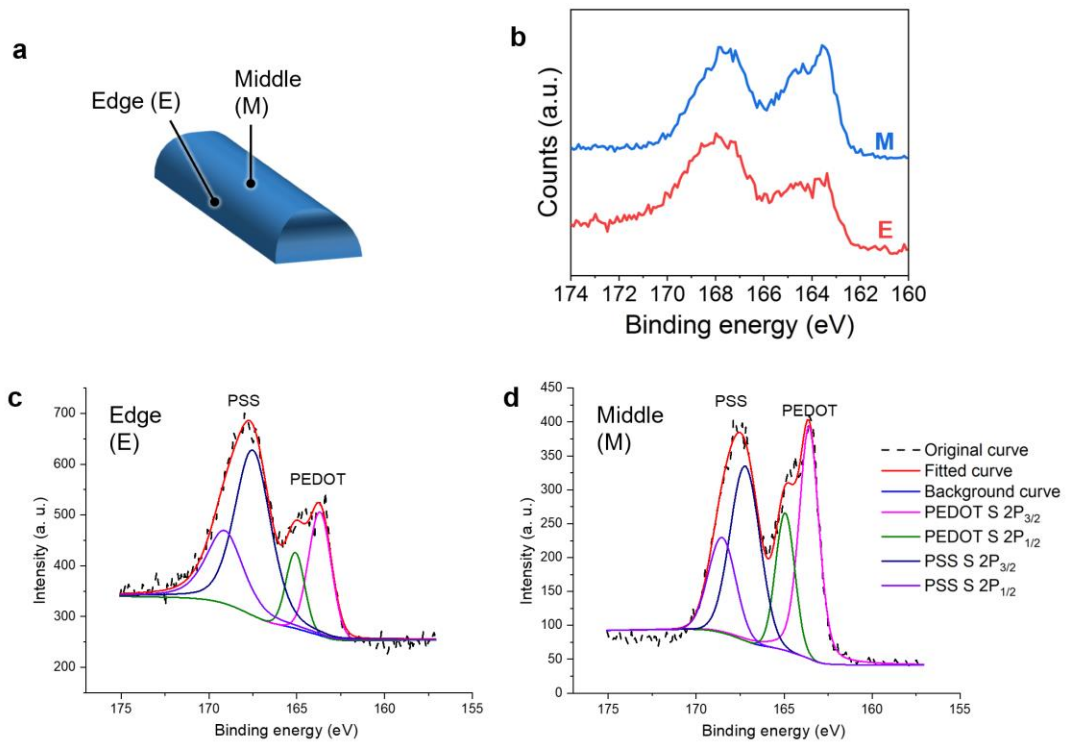


Figure 2.28. (a) Schematic drawing showing the different regions of a single printed line after DMSO-treatment. (b) XPS spectra for the different regions within the film. (c) Peak fitting for the XPS spectra collected at the edge and (d) middle of a single printed line after DMSO treatment. (c) and (d) share the same legend which is shown on (d).

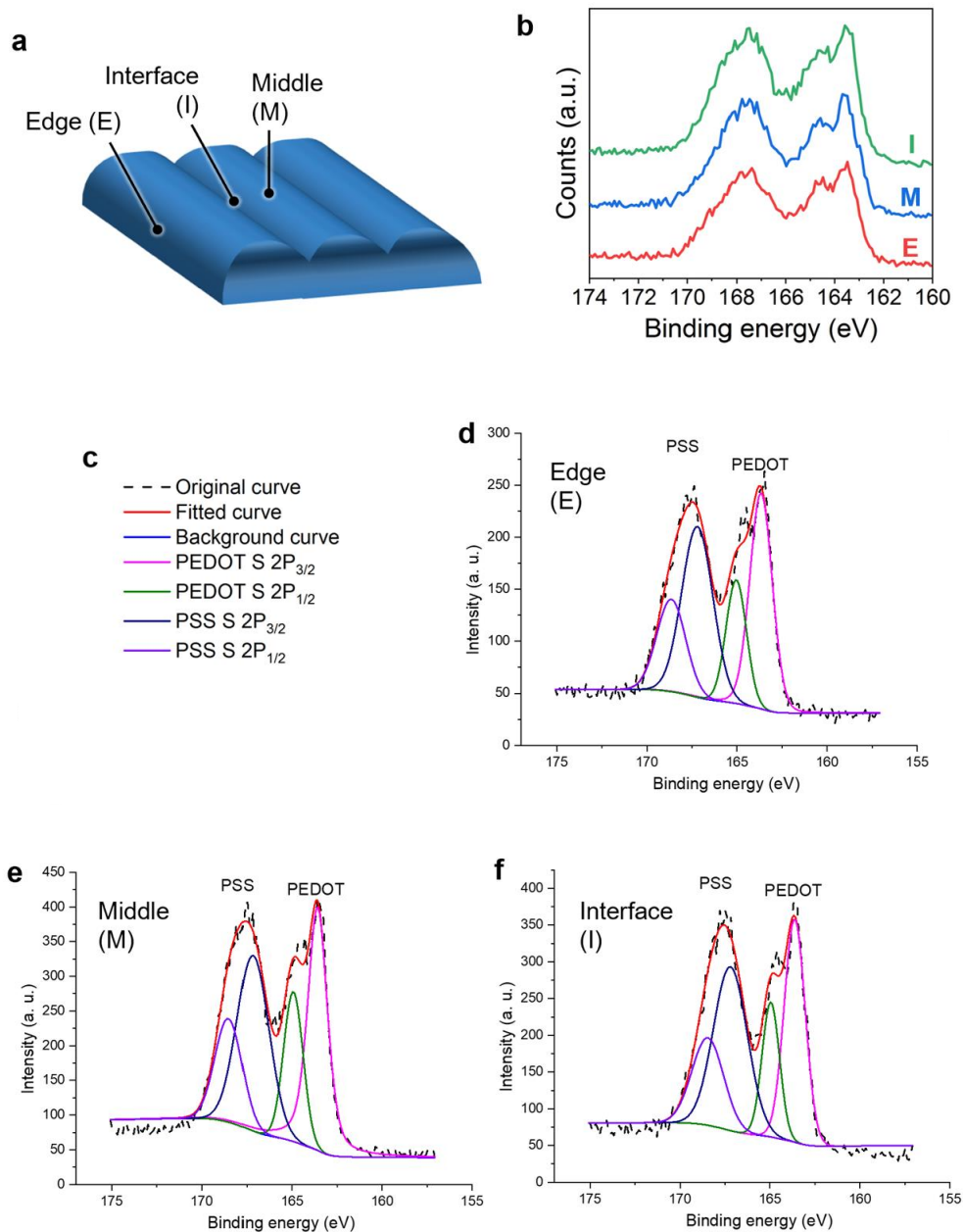


Figure 2.29. (a) Schematic drawing showing the different regions of a printed film (10 parallel lines) after DMSO treatment. (b) XPS spectra for the different regions within the film. (c) Legend for (d-f). Peak fitting for the XPS spectra collected at (d) the edge of the film, (e) middle of a line within the film, and (f) interface between two adjacent lines within the film.

Collectively, WAXS, AFM, and XPS all confirm that the mechanism for this increase in conductivity and decrease in anisotropy is the removal of free-PSS

through DMSO-rinsing (Figures 2.24-29). For samples printed with two different nozzle diameters, the PEDOT π - π to PSS peak ratios in WAXS spectra become 1.38-1.50 at 25 °C and 1.63-1.94 at 100 °C after the DMSO treatment, as compared to their pre-treatment values of 1.12-1.15 and 1.24-1.27, respectively (Figures 2.24 and 2.26). The crystallite sizes estimated from the PEDOT π - π scattering peak ($q = 1.8 \text{ \AA}$) for post-DMSO treated samples converged to a much narrower region, 6.7-7.1 nm and 7.5-8.0 nm for print bed temperature of 25 °C and 100 °C, respectively, compared to the as-printed samples, indicating polymer chain relaxation and rearrangement to a less anisotropic state while they are swelled by DMSO during the treatment (Figure 2.26b,c). AFM images reveal that the DMSO treatment has also led the PEDOT-rich grains to be better defined and to have a thinner PSS-rich shell (Figure 2.27).

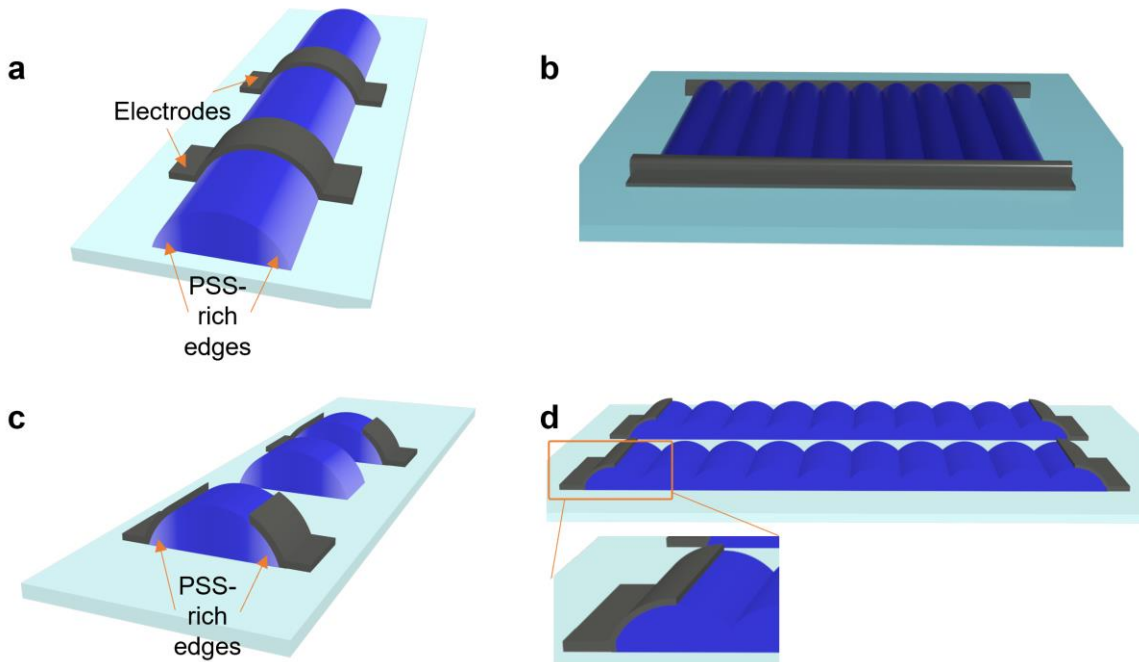


Figure 2.30. Schematic illustration depicting the electrode configuration and measurement geometry for σ_{\parallel} : (a) for single line and (b) for film, and σ_{\perp} : (c) for single line and (d) for film. Compared to the as-printed samples (Figure 2.23), the phase separated pure PSS outline has been removed by the DMSO treatment. For σ_{\perp} measurements (c, d), the printed single lines or films are isolated into sections that share the same length as the electrode width.

2.9 Demonstration for 3D Applications

The 3D printing of PEDOT:PSS with conductivity surpassing 1000 S/cm in the solid-state opens new opportunities in several previously inaccessible applications. We demonstrate such prospects with two examples (Figure 2.31-36).

Printing parameters for pneumatically extruding the PEDOT:PSS ink were first determined using a line test. A series of straight lines was printed with a printhead travel speed of 20 mm/s using a Subrex 19G (859 μm) nozzle. The line widths were measured to determine at which pressure the line width most closely corresponded to the nozzle diameter. Images of the lines were taken with a FLIR Grasshopper[®]3 camera through a Nikon MSB50040 achromatic lens. Line widths were analyzed using ImageJ image analysis software. With this method it was determined that the optimal pressure for PEDOT:PSS was 11 kPa at room temperature, and F-127 was 36 kPa at 30°C to ensure F-127 does not undergo a gel-sol transition near its lower critical gel temperature at around 16.5 °C.⁴⁴ These parameters produced line widths of 932 μm and 847 μm , respectively. Due to software limitations, the line width for F-127 was used preferentially to the PEDOT:PSS line width, as preserving the printing accuracy of the more viscous support material produced prints with better resolution.

Due to the gradual rheological changes of the PEDOT:PSS ink, the extrusion pressure was manually increased in 1.0 kPa steps during the print when needed to ensure consistency in dispensing. The final printing pressure did not exceed 15 kPa. F-127 was noted to have consistent printability throughout and did not require manual pressure adjustment.

2.9.1 3D Scanning and Printing

3D printing, in combination with 3D scanning, has led to replicas of physiologically accurate organs and limbs that can serve as surgical practice objects, tissue engineering platforms, and bespoke prosthetics.⁴⁵⁻⁴⁷ The high conductivity and low impedance of PEDOT:PSS have rendered it a sought-after material in cell culture platforms or probes for stimulation, sensing, and recording for electro-responsive cells such as neurons or cardiomyocytes.⁴⁷⁻⁴⁹ To demonstrate the prospect of combining these two fields, we 3D scanned a hand and used DIW to print the output CAD file into a PEDOT:PSS replica (Figures 2.31). This demonstration illustrates the potential to create electro-responsive artificial organs and personalized functional organic prosthetics.

A Sense 3D Scanner (3D Systems) was used to scan the hand of a volunteer. The scanned file was subsequently exported as an STL file using the manufacture software. Blender was then used to improve the surface smoothness of the scan by averaging the angles between the polygon faces of the model.

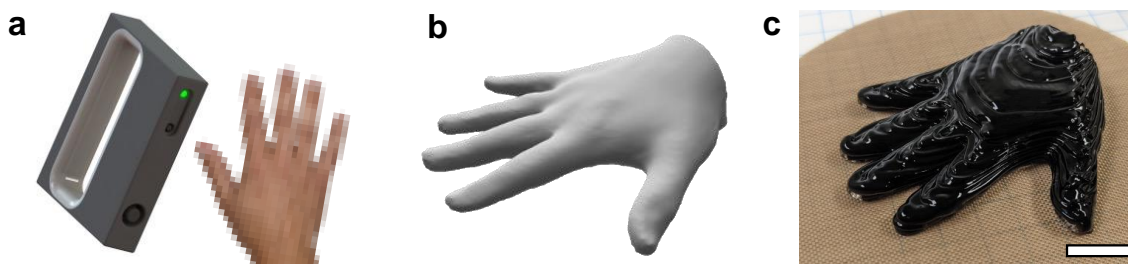


Figure 2.31. (a–c) Demonstration showing the prospect for 3D scanned, personalized organic bioelectronics. (a) and (b) the 3D scanned hand during various stages of the printing using PEDOT:PSS ink. (c) Top-down view of a completed printed hand. Scale bar for (c) is 10 mm.

2.9.2 The 3D printing, processing, characterization, and applications of PEDOT:PSS springs

Stretchable and wearable electronics is another area where highly conductive, 3D printed PEDOT:PSS can create new opportunities. These electronics need to retain electrical functions under mechanical deformation such as stretching and flexing, ideally omnidirectionally.^{50,51} CPs are one of the main classes of materials for such *de novo* electronics.^{52,53} However, the intrinsically brittle CPs such as PEDOT:PSS need to be chemically modified or blended with an additive to become stretchable.^{52,53} Aside from their often inferior conductivity in the unstrained state resulting from these modifications, the conductivity of these materials is often also heavily strain-dependent because polymer chains or nanoscopic domains need to deform to accommodate strain.

3D printing brings the capability to create structures that can accommodate mechanical deformation through 3D geometry, which effectively decouples materials' electrical properties from its response to mechanical deformation.^{11,54} We utilize multi-material DIW to print PEDOT:PSS springs with the support of a sacrificial material, Pluronic F-127 hydrogel (Figure 2.32a-c).⁵⁵ Support removal followed by dehydration produces solid PEDOT:PSS springs (Figure 2.32d-f). These solid-state springs typically exhibit some defects such as edge rippling. We note that the isotropic dehydration and shrinking of hydrogel structures is a challenge in the 3D printing field and the subject of several recent standalone, notable studies.^{56–58} Protocols for uniformly dehydrating PEDOT:PSS hydrogels with complex 3D shapes have not been reported to the best of our knowledge. Hence, our dehydration process focuses on general shape retention rather than perfecting the retention of geometry and resolution.

To demonstrate this prospect, we 3D printed a PEDOT:PSS spring using multi-material DIW printing. Unsupported, overhanging entities such as the curly wire that comprises a spring is not feasible to print directly using DIW because the soft, hydrated filament would collapse from its own weight. As a result, such geometry has not been realized for PEDOT:PSS to the best of our knowledge.

To improve printability and ensure stability through the drying process, springs were designed with an elliptical cross section (length = 3.05 mm, width = 5.70 mm) with three complete turns and a pitch of 6.75 mm. Spring models were sliced using PrusaSlicer at 20% infill density with full autogenerated supports. Within each layer, the F-127 support component was printed first, followed by PEDOT:PSS build material. The structure was printed on PTFE mesh sheet adhered to the build plate. The mesh allows for solvent evaporation from the bottom, promoting even drying across the entire structure during the later dehydration process. When printing was complete (Figure 2.32), the structure and the PTFE substrate were removed together from the printer build plate and then taped to an aluminum drying rack. Each encased spring was covered with an upside-down beaker to slow down the evaporation rate of the exposed sides to ensure even drying across the print surfaces. The covered prints were then transferred to a convection oven and heated at 30 °C for 12 hours. Subsequently, the beakers were removed, the oven temperature was raised to 50 °C, and the encased springs were allowed to continue drying for approximately 53 hours. The encased springs were then removed from the oven and allowed to sit for one hour, followed by removal of the PTFE mesh sheet substrate.

A series of heated solvent washes were used to remove the dried F-127 support. The first wash was comprised of 50 mL of DMSO heated to 100 °C in a 150 mL beaker. Each dried spring encased in F-127 support was placed into its own beaker of DMSO bath, covered and gently stirred at 50 rpm for 15 minutes, which removed most of the support. The liberated springs were transferred to a second covered solvent bath of 50 mL of fresh DMSO at 100 °C, and again gently stirred at 50 rpm for 20 minutes (Figure 2.32d). To facilitate rapid drying, DMSO was removed from the springs by submerging them in 50 mL of acetone, covered, and stirred gently at 50 rpm for 15 minutes. The process was repeated with 50 mL of fresh acetone. Subsequently, the PEDOT:PSS springs were removed from the solvent and let dry at room temperature for 10 minutes, followed by 10 minutes of heating at 50 °C in a convection oven to remove remaining acetone. The dried springs were then rehydrated in deionized water for 5 min, then fitted onto a customized SLA-printed spring brace (Figure 2.32e) and dried in a convection oven at 80 °C for 20 minutes. Finally, upon uncoiling from their braces, free-standing, solid-state PEDOT:PSS springs were materialized (Figure 2.32f). They were stored in tightly closed plastic jars until they were ready for characterizations or applications.

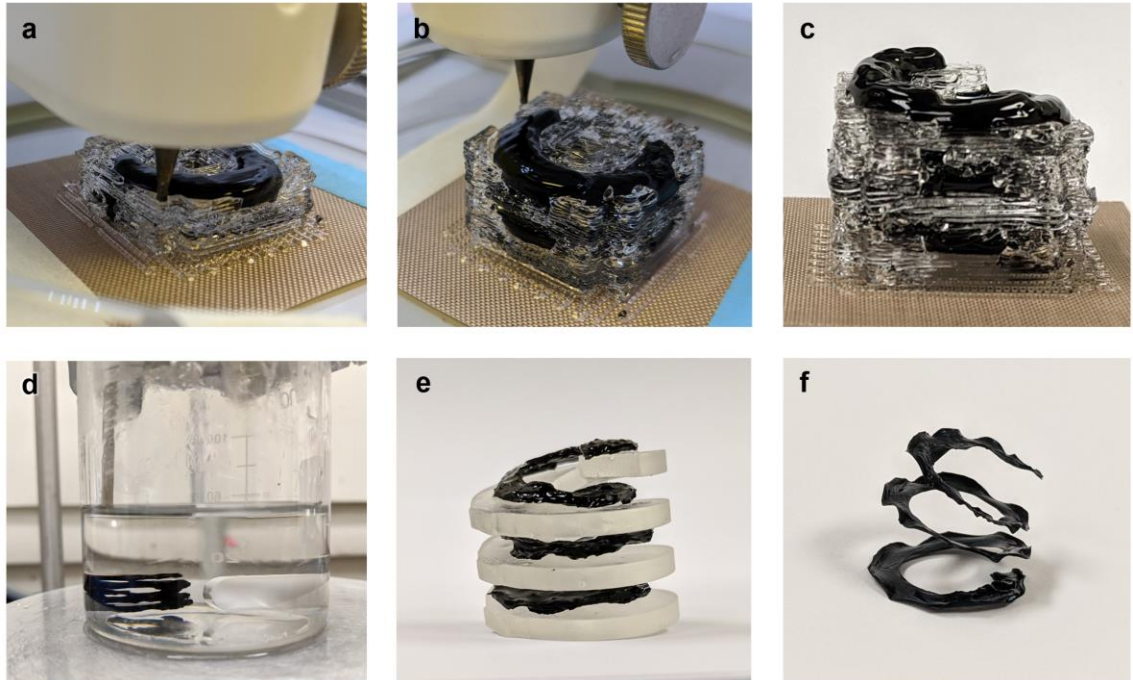


Figure 2.32. (a) and (b) Photographs showing the various stages of the printing of a PEDOT:PSS spring (dark gel) supported by F-127 (clear gel). (c) Side view of an as-printed three-turn spring hosted within the F-127 support. (d) PEDOT:PSS hydrogel floating in DMSO with the dissolution of the F-127 support structure. (e) The PEDOT:PSS spring hydrogel resting on a SLA-printed spring replica brace to promote uniform drying and shrinking. (f) Photograph of the fully dehydrated PEDOT:PSS spring.

3D printed springs were compressed to -65% strain (compressive strain is denoted as negative strain), allowed to return to the original height, and stretched until failure. Very little force is required to compress the spring to -55% strain and stretched to 450% strain as a result of the geometric freedom of the spring, resulting in a near-plateau region in the stress-strain curve. The Young's modulus for this near-plateau region of the spring is merely 31 Pa compared to the ~ 1.2 GPa for the PEDOT:PSS constituent (Figure 2.33), illustrating the powerful property tunability through geometric design enabled by 3D printing. Since the geometric deformation of the spring accommodates the compressive and tensile strains within this lengthy plateau region, little stress is exerted on the polymer chains or domains. As a result, the normalized resistance is nearly unchanged, with merely some minor fluctuations of $< 3\%$, within this strain region. The compressive stress increases rapidly between -55% and -65% strain, indicating the onset of densification. In the tensile region, when the spring is elongated beyond 450% strain, the twisting of the ribbon that forms the spring, reflected by the minor stress drop at around 460% and 640% strain, allows for additional elongation. Both stress and resistance increase rapidly at strain above 640% until the spring ruptures at

~700% strain. Upon breakage, the spring bounces back to its original shape as a result of the geometry-induced elasticity even though PEDOT:PSS is intrinsically brittle.

The geometry-induced elasticity and stress-resistance plateau region in a broad compressive and tensile strain range provide outstanding cycling stability for PEDOT:PSS springs. As shown in Figure 2.34c, the resistance of the spring remains unchanged for the first 100 cycles loaded and unloaded between -40% (compression) and 400% (tension) strain (Figure 2.34c), and increased by merely 4.4% after 1500 loading cycles in this strain range. For each cycle, the resistance values remain constant between -40% and 400% strain, demonstrating the remarkable electrical stability and fatigue resistance imbued by even relatively simple 3D geometries.

To highlight the drastic differences in stiffness, stress-strain behavior, and elongation at break that 3D geometry has induced in springs compared to those intrinsic to the constituting material, a stress-strain curve for a representative PEDOT:PSS dog bone specimen is plotted with that of a spring in Figure 2.33. Expanded views of stress-strain curves for the dog bone and spring are shown in Figure 2.33b and c, respectively. The compressive portion of the stress-strain curve for the spring is enlarged in Figure 2.33d.

The PEDOT:PSS dog bones are prepared using the following procedure. 5 vol % of DMSO was added to the as-purchased PEDOT:PSS dispersion (Clevios PH1000) and stirred at 300 rpm for 5 hours. 20 mL of the solution is then poured into a custom-made PTFE mold (110 mm length × 32mm width × 25mm height). The solution was left to dry for approximately 24 h under ambient conditions. The solid film was then released from the mold and cut into identical specimen with a custom-made dog bone-shaped master stamp. The samples were annealed at 100 °C under vacuum overnight and then annealed at 130 °C on a hotplate for 4 hours to remove residue solvent prior to tensile testing.

To illustrate the remarkable fatigue resistant properties of the PEDOT:PSS springs, they were subjected to 1500 loading and unloading cycles between -40% (compression) and 400% where the highest device stability can be achieved. Representative cycles of the stress-strain curves are shown in Figure 2.34a. The stress-strain curves have nearly no hysteresis, demonstrating their elastic nature. The overall shape of the stress-strain curves is retained through all cycles, but the stress for all data points decreased by ca. 0.22 kPa over the course of the 1500 cycles. This could be caused by water-absorption over the day-long testing duration due to the slightly hygroscopic nature of PEDOT:PSS, or polymer chain rearrangements, nanoscopic domain elongation, and/or the formation of micro-cracks. Data for the first 100 cycles are plotted in Figure 2.34c. The resistance of the spring only increased by less than 0.3% after being cycled across the 440%

strain range (-40% compressive strain and 400% tensile strain) for 100 cycles, demonstrating the remarkable geometry-induced mechanical characteristics for an otherwise intrinsically brittle material.

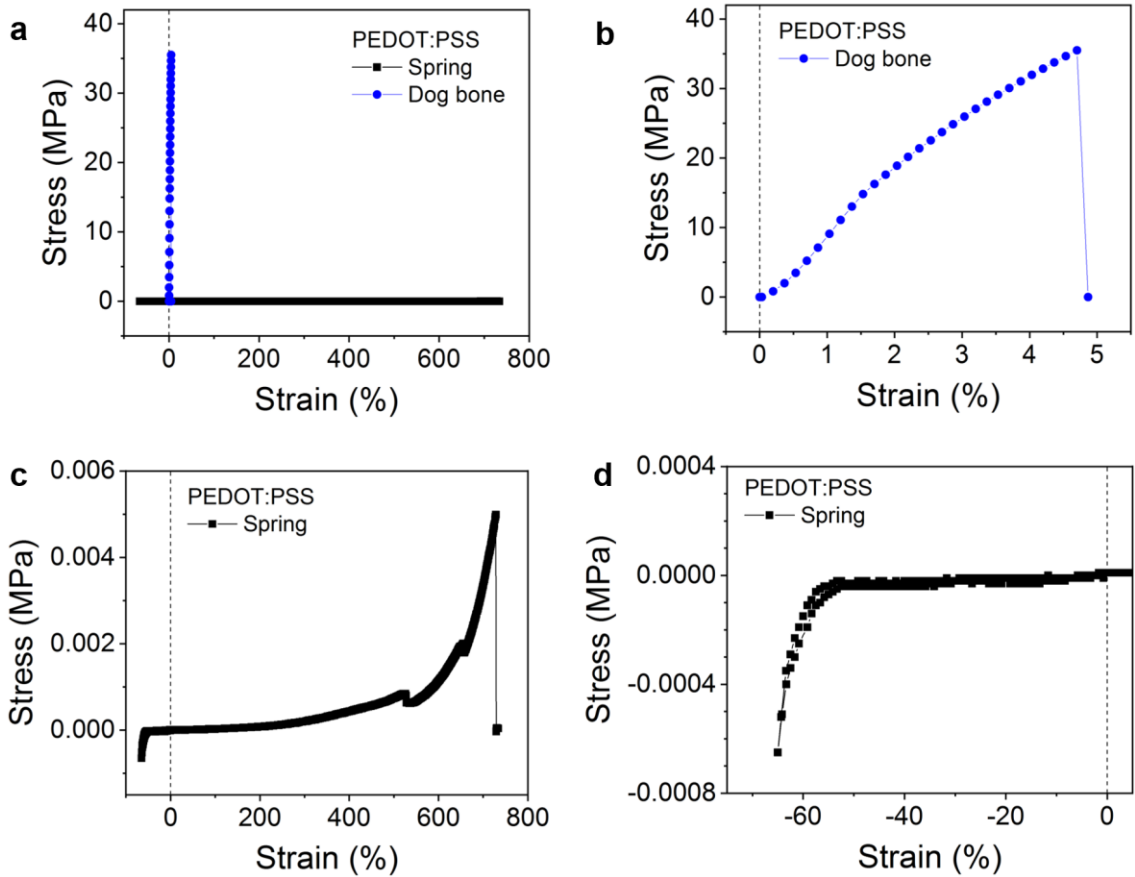


Figure 2.33. Stress-strain behavior of (a) 3D printed PEDOT:PSS spring compared to drop casted dog bone, (b) expanded view of the dog bone, (c) expanded view of the spring, and (d) expanded view of the compression region of the spring. The vertical dashed line in all plots marks 0% strain.

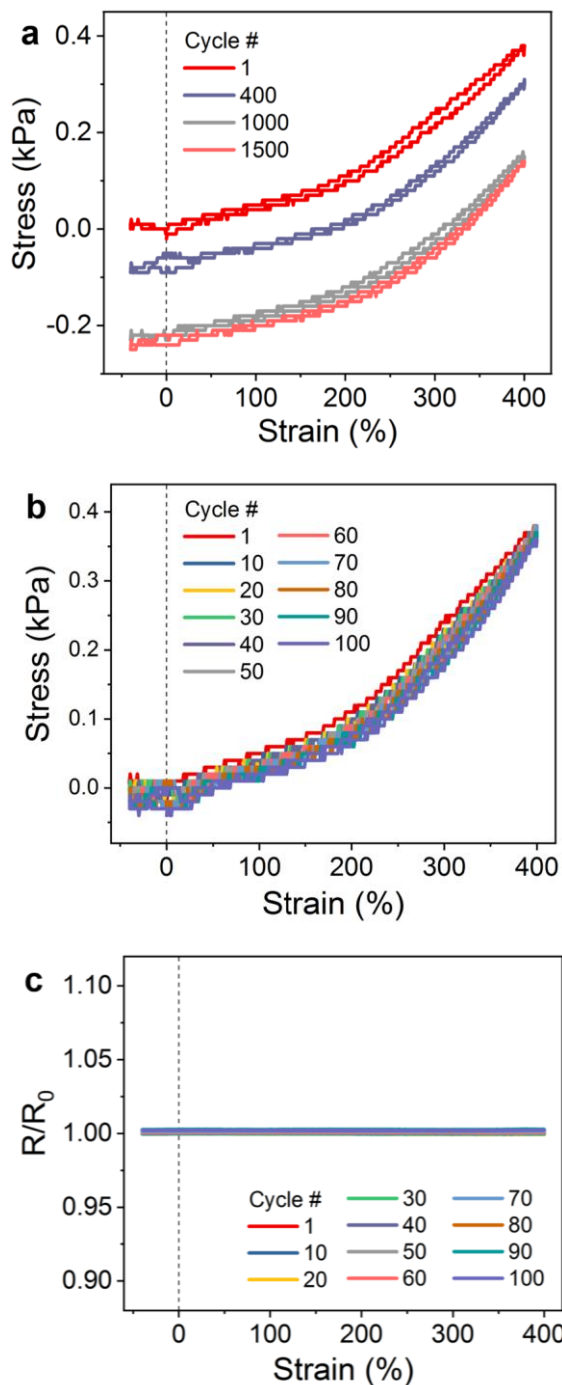


Figure 2.34. (a) Stress-strain curves for PEDOT:PSS spring during various cycle numbers when loaded/unloaded between 40% compression and 400% tensile strains. (b) Stress-strain curves at an incremental cycle # of ten for the first 100 cycles and (c) the corresponding normalized resistance curves.

2.9.3 3D printed PEDOT:PSS omnidirectional LED device

The electrical-mechanical correlations of the 3D printed PEDOT:PSS spring are further illustrated through a highly omnidirectionally deformable LED device that retains light intensity through compression, stretching, bending and twisting (Figures 2.35 and 2.36). The advantageous attributes of 3D-shaped PEDOT:PSS are in stark contrast to previous work that rely on chemical modification, additives, or composites, which exhibit resistance change starting at as low as 5% tensile strain and by several folds when elongated to 50-100% strain.^{52,53} The ability to process CPs in 3D provides the flexibility and opportunity to access more elaborate and tunable geometry-stress-strain-electrical property relations, such as those associated with complex 3D architected metamaterials,^{11,54} providing a new approach for creating mechanically deformable or reconfigurable organic electronic materials.

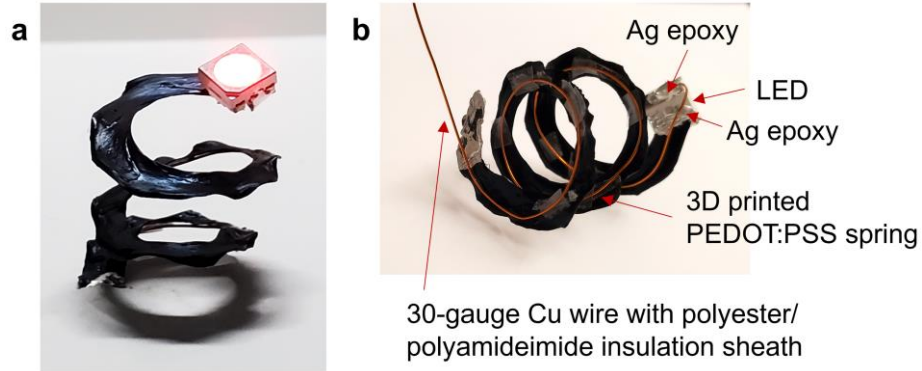


Figure 26. (a) Picture of the PEDOT:PSS spring LED device. (b) Electrode configuration for the device.

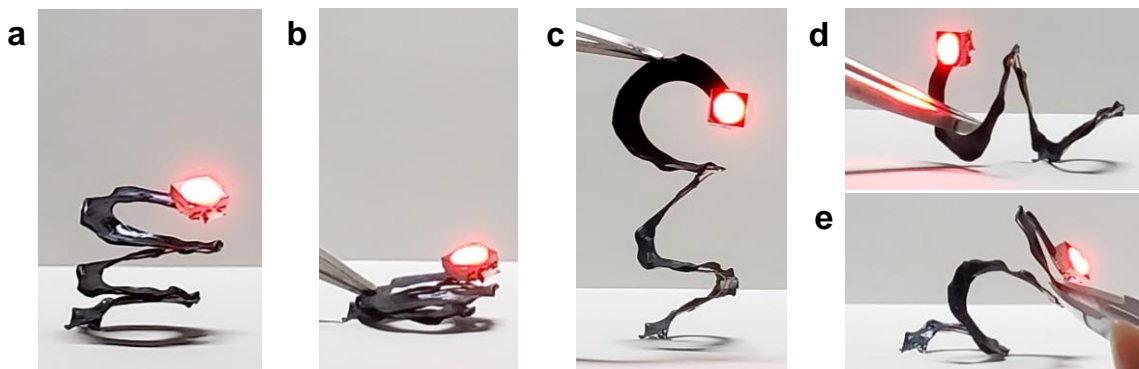


Figure 27. (a-e) An LED electronic device using the PEDOT:PSS spring as an interconnect being compressed, stretched, and flexed in various directions while retaining its emission intensity.

2.10 Conclusions and Outlook

The findings from this chapter have unveiled a number of fundamental insights for the DIW 3D printing of PEDOT:PSS, in particular, that the cause for its low conductivity associated with DIW processing is the strong lateral phase separation. We demonstrated that conductivity as high as 1200 S/cm can be achieved in 3D-printed PEDOT:PSS by (1) formulating DIW ink under conditions that resemble conventional 2D processing and (2) removing the free PSS at filament periphery from the lateral phase-separation. PEDOT:PSS-based electronics with new form factors have been achieved as a result of our study.

Our investigation has also offered a number of other fundamental insights for creating highly conductive 3D PEDOT:PSS. First, for both single lines and films, σ_{\parallel} is consistently higher than σ_{\perp} even after DMSO rinsing, albeit the difference is small in films. This feature indicates that if achieving the lowest possible resistance is paramount to an application, the printing direction should be aligned with the direction of current flow. Second, the conductivity dependence on print bed temperature is also mostly removed after DMSO treatment. Therefore, DIW printing can be carried out at room temperature to achieve high conductivity for process simplicity. Third, we found that the conductivity of DIW printed PEDOT:PSS is largely independent of nozzle diameter. After the post-printing solvent treatment, single line conductivity is still slightly higher than their film counterparts. Therefore, for the printing of an electrode or interconnect of a certain width, it is advantageous to print using a nozzle that matches the line width rather than printing multiple overlapping lines using smaller nozzles. Applying these insights can potentially lead to more efficient charge transport in 3D printed organic electronics containing PEDOT:PSS.

2.11 References

- (1) Zhou, L. Y.; Fu, J.; He, Y. A Review of 3D Printing Technologies for Soft Polymer Materials. *Adv. Funct. Mater.* **2020**, *30* (28), 1–38. <https://doi.org/10.1002/adfm.202000187>.
- (2) Kamyshny, A.; Magdassi, S. Conductive Nanomaterials for 2D and 3D Printed Flexible Electronics. *Chem. Soc. Rev.* **2019**, *48* (6), 1712–1740. <https://doi.org/10.1039/C8CS00738A>.
- (3) MacDonald, E.; Wicker, R. Multiprocess 3D Printing for Increasing Component Functionality. *Science* (80-.). **2016**, *353* (6307). <https://doi.org/10.1126/science.aaf2093>.
- (4) Jordan, R. S.; Wang, Y. 3D Printing of Conjugated Polymers. *J. Polym. Sci. Part B Polym. Phys.* **2019**, *57* (23), 1592–1605. <https://doi.org/10.1002/polb.24893>.
- (5) Edition, S. *Handbook of Thermoplastics*.
- (6) Jørgensen, M.; Norrman, K.; Krebs, F. C. Stability/Degradation of Polymer Solar Cells. *Sol. Energy Mater. Sol. Cells* **2008**, *92* (7), 686–714. <https://doi.org/10.1016/j.solmat.2008.01.005>.
- (7) Louis, B.; Caubergh, S.; Larsson, P. O.; Tian, Y.; Scheblykin, I. G. Light and Oxygen Induce Chain Scission of Conjugated Polymers in Solution. *Phys. Chem. Chem. Phys.* **2018**, *20* (3), 1829–1837. <https://doi.org/10.1039/c7cp07347j>.
- (8) Xia, Y.; M. Wiesinger, J.; G. MacDiarmid, A.; J. Epstein, A. Camphorsulfonic Acid Fully Doped Polyaniline Emeraldine Salt: Conformations in Different Solvents Studied by an Ultraviolet/Visible/Near-Infrared Spectroscopic Method. *Chem. Mater.* **2002**, *7* (3), 443–445. <https://doi.org/10.1021/cm00051a002>.
- (9) Zhang, W. J.; Feng, J.; MacDiarmid, A. G.; Epstein, A. J. Synthesis of Oligomeric Anilines. *Synth. Met.* **1997**, *84* (1), 119–120. [https://doi.org/https://doi.org/10.1016/S0379-6779\(97\)80674-1](https://doi.org/https://doi.org/10.1016/S0379-6779(97)80674-1).
- (10) Lopez-Larrea, N.; Criado-Gonzalez, M.; Dominguez-Alfaro, A.; Alegret, N.; del Agua, I.; Marchiori, B.; Mecerreyes, D. Digital Light 3D Printing of PEDOT-Based Photopolymerizable Inks for Biosensing. *ACS Appl. Polym. Mater.* **2022**, *4* (9), 6749–6759. <https://doi.org/10.1021/acsapm.2c01170>.
- (11) Jordan, R. S.; Frye, J.; Hernandez, V.; Prado, I.; Giglio, A.; Abbasizadeh, N.; Flores-Martinez, M.; Shirzad, K.; Xu, B.; Hill, I. M.; Wang, Y. 3D Printed Architected Conducting Polymer Hydrogels. *J. Mater. Chem. B* **2021**, *9* (35), 7258–7270. <https://doi.org/10.1039/D1TB00877C>.
- (12) Zhang, S.; Chen, Y.; Liu, H.; Wang, Z.; Ling, H.; Wang, C.; Ni, J.; Çelebi-

- Saltik, B.; Wang, X.; Meng, X.; Kim, H. J.; Baidya, A.; Ahadian, S.; Ashammakhi, N.; Dokmeci, M. R.; Travas-Sejdic, J.; Khademhosseini, A. Room-Temperature-Formed PEDOT:PSS Hydrogels Enable Injectable, Soft, and Healable Organic Bioelectronics. *Adv. Mater.* **2020**, *32* (1). <https://doi.org/10.1002/adma.201904752>.
- (13) Fantino, E.; Roppolo, I.; Zhang, D.; Xiao, J.; Chiappone, A.; Castellino, M.; Guo, Q.; Pirri, C. F.; Yang, J. 3D Printing/Interfacial Polymerization Coupling for the Fabrication of Conductive Hydrogel. *Macromol. Mater. Eng.* **2018**, *303* (4), 1–8. <https://doi.org/10.1002/mame.201700356>.
- (14) Wu, Y.; Chen, Y. X.; Yan, J.; Yang, S.; Dong, P.; Soman, P. Fabrication of Conductive Polyaniline Hydrogel Using Porogen Leaching and Projection Microstereolithography. *J. Mater. Chem. B* **2015**, *3* (26), 5352–5360. <https://doi.org/10.1039/c5tb00629e>.
- (15) Joo, H.; Cho, S. Comparative Studies on Polyurethane Composites Filled with Polyaniline and Graphene for DLP-Type 3D Printing. *Polymers (Basel)*. **2020**, *12* (1). <https://doi.org/10.3390/polym12010067>.
- (16) Mire, C. A.; Agrawal, A.; Wallace, G. G.; Calvert, P.; In Het Panhuis, M. Inkjet and Extrusion Printing of Conducting Poly(3,4- Ethylenedioxythiophene) Tracks on and Embedded in Biopolymer Materials. *J. Mater. Chem.* **2011**, *21* (8), 2671–2678. <https://doi.org/10.1039/c0jm03587d>.
- (17) Yuk, H.; Lu, B.; Lin, S.; Qu, K.; Xu, J.; Luo, J.; Zhao, X. 3D Printing of Conducting Polymers. *Nat. Commun.* **2020**, *11* (1), 4–11. <https://doi.org/10.1038/s41467-020-15316-7>.
- (18) Lu, B.; Yuk, H.; Lin, S.; Jian, N.; Qu, K.; Xu, J.; Zhao, X. Pure PEDOT:PSS Hydrogels. *Nat. Commun.* **2019**, *10* (1). <https://doi.org/10.1038/s41467-019-09003-5>.
- (19) Wei, H.; Lei, M.; Zhang, P.; Leng, J.; Zheng, Z.; Yu, Y. Orthogonal Photochemistry-Assisted Printing of 3D Tough and Stretchable Conductive Hydrogels. *Nat. Commun.* **2021**, *12* (1), 2082. <https://doi.org/10.1038/s41467-021-21869-y>.
- (20) Ouyang, J. “Secondary Doping” Methods to Significantly Enhance the Conductivity of PEDOT:PSS for Its Application as Transparent Electrode of Optoelectronic Devices. *Displays* **2013**, *34* (5), 423–436. <https://doi.org/10.1016/j.displa.2013.08.007>.
- (21) Kroon, R.; Mengistie, D. A.; Kiefer, D.; Hynynen, J.; Ryan, J. D.; Yu, L.; Müller, C. Thermoelectric Plastics: From Design to Synthesis{,} Processing and Structure–Property Relationships. *Chem. Soc. Rev.* **2016**, *45* (22), 6147–6164. <https://doi.org/10.1039/C6CS00149A>.
- (22) Shi, H.; Liu, C.; Jiang, Q.; Xu, J. Effective Approaches to Improve the

- Electrical Conductivity of PEDOT:PSS: A Review. *Adv. Electron. Mater.* **2015**, *1* (4), 1–16. <https://doi.org/10.1002/aelm.201500017>.
- (23) Zhang, P.; Aydemir, N.; Alkaisi, M.; E. Williams, D.; Travas-Sejdic, J. Direct Writing and Characterization of Three-Dimensional Conducting Polymer PEDOT Arrays. *ACS Appl. Mater. & Interfaces* **2018**, *10* (14), 11888–11895. <https://doi.org/10.1021/acsami.8b02289>.
- (24) Kee, S.; Haque, M. A.; Corzo, D.; Alshareef, H. N.; Baran, D. Self-Healing and Stretchable 3D-Printed Organic Thermoelectrics. *Adv. Funct. Mater.* **2019**, *29* (51). <https://doi.org/10.1002/adfm.201905426>.
- (25) Kokkinis, D.; Schaffner, M.; Studart, A. R. Multimaterial Magnetically Assisted 3D Printing of Composite Materials. *Nat. Commun.* **2015**, *6* (1), 8643. <https://doi.org/10.1038/ncomms9643>.
- (26) Liu, J.; Yan, C. 3D Printing of Scaffolds for Tissue Engineering. In *3D Printing*; Cvetković, D., Ed.; IntechOpen: Rijeka, 2018. <https://doi.org/10.5772/intechopen.78145>.
- (27) Yuk, H.; Zhao, X. A New 3D Printing Strategy by Harnessing Deformation, Instability, and Fracture of Viscoelastic Inks. *Adv. Mater.* **2018**, *30* (6). <https://doi.org/10.1002/adma.201704028>.
- (28) Sun, J.; Phan-Thien, N.; Tanner, R. I. Extrudate Swell through an Orifice Die. *Rheol. Acta* **1996**, *35* (1), 1–12. <https://doi.org/10.1007/BF00366548>.
- (29) Wang, G.; Huang, W.; Eastham, N. D.; Fabiano, S.; Manley, E. F.; Zeng, L.; Wang, B.; Zhang, X.; Chen, Z.; Li, R.; Chang, R. P. H.; Chen, L. X.; Bedzyk, M. J.; Melkonyan, F. S.; Facchetti, A.; Marks, T. J. Aggregation Control in Natural Brush-Printed Conjugated Polymer Films and Implications for Enhancing Charge Transport. *Proc. Natl. Acad. Sci. U. S. A.* **2017**, *114* (47), E10066–E10073. <https://doi.org/10.1073/pnas.1713634114>.
- (30) Worfolk, B. J.; Andrews, S. C.; Park, S.; Reinspach, J.; Liu, N.; Toney, M. F.; Mannsfeld, S. C. B.; Bao, Z. Ultrahigh Electrical Conductivity in Solution-Sheared Polymeric Transparent Films. *Proc. Natl. Acad. Sci. U. S. A.* **2015**, *112* (46), 14138–14143. <https://doi.org/10.1073/pnas.1509958112>.
- (31) Wang, Y.; Sun, L.; Wang, C.; Yang, F.; Ren, X.; Zhang, X.; Dong, H.; Hu, W. Organic Crystalline Materials in Flexible Electronics. *Chem. Soc. Rev.* **2019**, *48* (6), 1492–1530. <https://doi.org/10.1039/c8cs00406d>.
- (32) Hinckley, A. C.; Andrews, S. C.; Dunham, M. T.; Sood, A.; Barako, M. T.; Schneider, S.; Toney, M. F.; Goodson, K. E.; Bao, Z. Achieving High Thermoelectric Performance and Metallic Transport in Solvent-Sheared PEDOT:PSS. *Adv. Electron. Mater.* **2021**, *7* (3), 1–9. <https://doi.org/10.1002/aelm.202001190>.
- (33) Mezger, T. G. *The Rheology Handbook*; Vincentz Network Hannover, 2012;

Vol. 10.

- (34) Kim, S. S.; Na, S. I.; Jo, J.; Tae, G.; Kim, D. Y. Efficient Polymer Solar Cells Fabricated by Simple Brush Painting. *Adv. Mater.* **2007**, *19* (24), 4410–4415. <https://doi.org/10.1002/adma.200702040>.
- (35) Malkin, Alexander Ya; Isayev, A. I. Liquids. In *Rheology: Concepts, Methods, and Applications*; 2017; pp 129–232.
- (36) Schaffner, M.; Rühls, P. A.; Coulter, F.; Kilcher, S.; Studart, A. R. 3D Printing of Bacteria into Functional Complex Materials. *Sci. Adv.* **2017**, *3* (12). <https://doi.org/10.1126/sciadv.aao6804>.
- (37) Palumbiny, C. M.; Liu, F.; Russell, T. P.; Hexemer, A.; Wang, C.; Müller-Buschbaum, P. The Crystallization of PEDOT:PSS Polymeric Electrodes Probed in Situ during Printing. *Adv. Mater.* **2015**, *27* (22), 3391–3397. <https://doi.org/10.1002/adma.201500315>.
- (38) Lee, Y.-Y.; Choi, G. M.; Lim, S.-M.; Cho, J.-Y.; Choi, I.-S.; Nam, K. T.; Joo, Y.-C. Growth Mechanism of Strain-Dependent Morphological Change in PEDOT:PSS Films. *Sci. Rep.* **2016**, *6* (1), 25332. <https://doi.org/10.1038/srep25332>.
- (39) Greczynski, G.; Kugler, T.; Salaneck, W. R. Characterization of the PEDOT-PSS System by Means of X-Ray and Ultraviolet Photoelectron Spectroscopy. *Thin Solid Films* **1999**, *354* (1), 129–135. [https://doi.org/https://doi.org/10.1016/S0040-6090\(99\)00422-8](https://doi.org/https://doi.org/10.1016/S0040-6090(99)00422-8).
- (40) Yemata, T. A.; Zheng, Y.; Kyaw, A. K. K.; Wang, X.; Song, J.; Chin, W. S.; Xu, J. Modulation of the Doping Level of PEDOT:PSS Film by Treatment with Hydrazine to Improve the Seebeck Coefficient. *RSC Adv.* **2020**, *10* (3), 1786–1792. <https://doi.org/10.1039/c9ra07648d>.
- (41) Park, H.; Lee, S. H.; Kim, F. S.; Choi, H. H.; Cheong, I. W.; Kim, J. H. Enhanced Thermoelectric Properties of PEDOT:PSS Nanofilms by a Chemical Dedoping Process. *J. Mater. Chem. A* **2014**, *2* (18), 6532–6539. <https://doi.org/10.1039/c3ta14960a>.
- (42) Diah, A. W. M.; Quirino, J. P.; Belcher, W.; Holdsworth, C. I. Investigation of the Doping Efficiency of Poly(Styrene Sulfonic Acid) in Poly(3,4-Ethylenedioxythiophene)/Poly(Styrene Sulfonic Acid) Dispersions by Capillary Electrophoresis. *Electrophoresis* **2014**, *35* (14), 1976–1983. <https://doi.org/10.1002/elps.201400056>.
- (43) Ouyang, L.; Musumeci, C.; J. Jafari, M.; Ederth, T.; Inganäs, O. Imaging the Phase Separation Between PEDOT and Polyelectrolytes During Processing of Highly Conductive PEDOT:PSS Films. *ACS Appl. Mater. & Interfaces* **2015**, *7* (35), 19764–19773. <https://doi.org/10.1021/acsami.5b05439>.
- (44) Pandit, N. K.; Kisaka, J. Loss of Gelation Ability of Pluronic® F127 in the

- Presence of Some Salts. *Int. J. Pharm.* **1996**, *145* (1–2), 129–136. [https://doi.org/10.1016/S0378-5173\(96\)04748-5](https://doi.org/10.1016/S0378-5173(96)04748-5).
- (45) Zhang, Y. S.; Yue, K.; Aleman, J.; Mollazadeh-Moghaddam, K.; Bakht, S. M.; Yang, J.; Jia, W.; Dell'Erba, V.; Assawes, P.; Shin, S. R.; Dokmeci, M. R.; Oklu, R.; Khademhosseini, A. 3D Bioprinting for Tissue and Organ Fabrication. *Ann. Biomed. Eng.* **2017**, *45* (1), 148–163. <https://doi.org/10.1007/s10439-016-1612-8>.
- (46) Martelli, N.; Serrano, C.; Van Den Brink, H.; Pineau, J.; Prognon, P.; Borget, I.; El Batti, S. Advantages and Disadvantages of 3-Dimensional Printing in Surgery: A Systematic Review. *Surg. (United States)* **2016**, *159* (6), 1485–1500. <https://doi.org/10.1016/j.surg.2015.12.017>.
- (47) S. Mannoor, M.; Jiang, Z.; James, T.; Lin Kong, Y.; A. Malatesta, K.; O. Soboyejo, W.; Verma, N.; H. Gracias, D.; C. McAlpine, M. 3D Printed Bionic Ears. *Nano Lett.* **2013**, *13* (6), 2634–2639. <https://doi.org/10.1021/nl4007744>.
- (48) Mawad, D.; Stewart, E.; Officer, D. L.; Romeo, T.; Wagner, P.; Wagner, K.; Wallace, G. G. A Single Component Conducting Polymer Hydrogel as a Scaffold for Tissue Engineering. *Adv. Funct. Mater.* **2012**, *22* (13), 2692–2699. <https://doi.org/10.1002/adfm.201102373>.
- (49) Kaur, G.; Adhikari, R.; Cass, P.; Bown, M.; Gunatillake, P. Electrically Conductive Polymers and Composites for Biomedical Applications. *RSC Adv.* **2015**, *5* (47), 37553–37567. <https://doi.org/10.1039/c5ra01851j>.
- (50) Ling, Y.; An, T.; Yap, L. W.; Zhu, B.; Gong, S.; Cheng, W. Disruptive, Soft, Wearable Sensors. *Adv. Mater.* **2020**, *32* (18), 1–13. <https://doi.org/10.1002/adma.201904664>.
- (51) Ma, Y.; Zhang, Y.; Cai, S.; Han, Z.; Liu, X.; Wang, F.; Cao, Y.; Wang, Z.; Li, H.; Chen, Y.; Feng, X. Flexible Hybrid Electronics for Digital Healthcare. *Adv. Mater.* **2020**, *32* (15), 1–23. <https://doi.org/10.1002/adma.201902062>.
- (52) Kleinschmidt, A. T.; J. Lipomi, D. Stretchable Conjugated Polymers: A Case Study in Topic Selection for New Research Groups. *Acc. Chem. Res.* **2018**, *51* (12), 3134–3143. <https://doi.org/10.1021/acs.accounts.8b00459>.
- (53) Kayser, L. V.; Lipomi, D. J. Stretchable Conductive Polymers and Composites Based on PEDOT and PEDOT:PSS. *Adv. Mater.* **2019**, *31* (10), 1–13. <https://doi.org/10.1002/adma.201806133>.
- (54) Greer, J. R.; Deshpande, V. S. Three-Dimensional Architected Materials and Structures: Design, Fabrication, and Mechanical Behavior. *MRS Bull.* **2019**, *44* (10), 750–757. <https://doi.org/10.1557/mrs.2019.232>.
- (55) Hinton, T. J.; Jallerat, Q.; Palchesko, R. N.; Park, J. H.; Grodzicki, M. S.; Shue, H. J.; Ramadan, M. H.; Hudson, A. R.; Feinberg, A. W. Three-

Dimensional Printing of Complex Biological Structures by Freeform Reversible Embedding of Suspended Hydrogels. *Sci. Adv.* **2015**, *1* (9). <https://doi.org/10.1126/sciadv.1500758>.

- (56) Gong, J.; Schuurmans, C. C. L.; Genderen, A. M. van; Cao, X.; Li, W.; Cheng, F.; He, J. J.; López, A.; Huerta, V.; Manríquez, J.; Li, R.; Li, H.; Delavaux, C.; Sebastian, S.; Capendale, P. E.; Wang, H.; Xie, J.; Yu, M.; Masereeuw, R.; Vermonden, T.; Zhang, Y. S. Complexation-Induced Resolution Enhancement of 3D-Printed Hydrogel Constructs. *Nat. Commun.* **2020**, *11* (1), 1–14. <https://doi.org/10.1038/s41467-020-14997-4>.
- (57) Oran, D.; Rodrigues, S. G.; Gao, R.; Asano, S.; Skylar-Scott, M. A.; Chen, F.; Tillberg, P. W.; Marblestone, A. H.; Boyden, E. S. 3D Nanofabrication by Volumetric Deposition and Controlled Shrinkage of Patterned Scaffolds. *Science* (80-.). **2018**, *362* (6420), 1281–1285. <https://doi.org/10.1126/science.aau5119>.
- (58) Dickey, M. D. Stretchable and Soft Electronics Using Liquid Metals. *Adv. Mater.* **2017**, *29* (27), 1–19. <https://doi.org/10.1002/adma.201606425>.

Chapter 3

Pure PEDOT with complex architectures via 3D printing-assisted casting

3.1 Abstract

Achieving highly complex 3D geometries with conducting polymers is achievable using vat photopolymerization (VP) methods, but results in low conductivity performance, due to the limited amount of conductive polymer that can be integrated into printed objects. For instance, the conductive polymer poly(3,4-ethylenedioxythiophene):poly(styrenesulfonate) (PEDOT:PSS) added to a VP resin has been shown to achieve conductivity of only 0.1 S/cm, which is four orders of magnitude lower than what is achievable by solution cast PEDOT:PSS. To address this shortcoming, we developed a 3D printing-assisted casting method to balance shape complexity and high conductivity. To achieve this, we produced complex 3D geometry cavities with VP-printed casts that serve as templates to fill with a melt-processable PEDOT precursor. After removal of the cast with water, the precursor undergoes a solid-state polymerization into the conductive PEDOT while retaining its original casted 3D shape, including octet, truncated octahedron, and trees with intricate and overhanging structures, not achievable previously with 3D printed PEDOT. Additionally, the flowable nature of the PEDOT precursor can act as a carrier for more conductive materials, such as silver flakes, capable of improving the electrical conductivity to as high as 7000 S/cm. This work has led to an improved understanding of the processing-structure-property relationships of 3D printed conducting polymers as well as new methods for the additive manufacturing the chemically temperamental electronic materials, opening doors to new applications.

3.2 Introduction

The additive manufacturing (AM) of conjugated, electrically conductive polymers (CPs) has grown considerably in recent years.¹⁻⁴ The shape customizability, 3D patterning, and versatility of processing a wide range of CPs makes this a valuable fabrication method in wide range of electronic applications, including energy storage devices, neurosensors,⁵ flexible OLED devices,⁶ wearable electronics with tailored geometries to fit the human body. AM provides new benefits to CPs including ad hoc patterning, 3D patterning, and producing lower waste than subtractive methods. This is largely from the advantageous solution processability of CPs that makes is compatible with a wide range of AM methods.

Each AM method has its own advantages and limitations when fabricating with CPs, where there is often a tradeoff between material versatility and architectural complexity. One of the most versatile AM methods for processing CPs is direct ink writing (DIW), where pressurized inks are extruded onto a surface in a 2D pattern, moved along the z-axis, and repeated to build up a 3D object. This process requires that the ink can flow out of the extrusion nozzle under applied pressure and hold its desired shape after extrusion.⁷ These simple requirements make many solution-processable CPs, including PEDOT:PSS aqueous inks, well-suited for manufacturing a variety of conductive structures using DIW, including soft neural probes,^{5,8} electromagnetic shielding,⁹ free-standing conductive springs,¹⁰ photochemical cells,¹¹ and wearable organic thermoelectric devices.¹² However, formulating inks to allow them to flow under pressure can decrease its yield stress, limiting the number of printable layers of ink without collapsing, as well as the amount of structural overhanging, and the geometric complexity of DIW CPs. One method of overcoming this limitation is by extruding a removable secondary support material during the printing of CPs to enable the printing of overhanging structures, such as springs.¹⁰ However, removal of the support material results in lateral deformation of the structures that do not accurately replicate the intended printed object.

The resolution and print fidelity limitations can be overcome by using vat polymerization (VP) 3D printing techniques, which use a pattern of UV light to cure a thin layer of UV-curable resin. The layer of cured resin is moved along the z-axis to allow for the curing of an additional layer of resin, and the process is repeated to build a 3D object.¹³ However, it is not feasible to polymerize CPs from their monomers using VP, as the conducting polymers strongly absorbs UV light.¹⁴ One method to overcome this limitation is to incorporate a PEDOT:PSS suspension into UV-curable resin to print conductive 3D objects.¹⁵⁻¹⁸ However, resin modifications are required for printing, due to the strong light absorbance of the conducting

polymer. Because of this, only a small amount of the conducting polymer component can be added, resulting printed objects bearing low conductivity.

Instead of relying on only one method of fabrication, approaches that combine the high resolution and throughput of VP with other manufacturing methods can achieving complex 3D architectures with desirable conductive and mechanical behavior. One instance is to use VP printed architected hydrogel templates that can be used to grow conductive polymer polyaniline (PANI) in the hydrogel.¹⁹ By incorporating negatively charged monomers into the hydrogel resin, the hydrogel acts as a template for growing positively charged PANI and act as a dopant to improve its conductivity. However, by using this approach, only a small amount of PANI can be incorporated into the hydrogels, resulting in a low conductivity. Similarly, using two-photon lithography (2PP) of PEG-MWNT hydrogels with complex 3D architectures were soaked in a PEDOT:PSS solution for interpenetrating with PEDOT for improving conductivity.²⁰ However, only a small amount of conductive polymer could be incorporated, leading to only an increase in weight of only 1.3 wt%, and a improvement in conductivity from 1.0×10^{-3} S/cm to only 0.43 S/cm.

In contrast to 3DP, a higher amount of the desired material can be manufactured into a desired shape by polymer-injection molding, which is compatible with a broad range of materials from a flowable fluid. These materials are made into a flowable material by heating above their glass transition temperature (T_g), then injecting into a multi-part mold containing their desired shape. Once the part has become solidified by cooling below its T_g , the mold components are separated, and the polymeric object is removed. This is widely used to rapidly produce polymeric objects. However, the repeatable use of these molds limits the geometric complexity of injection-molded components. A similar method has been used for filling hollow VP-printed 3D molds with functional liquid materials to produce metamaterials, such as with low melting point molten gallium²¹ to produce self-healing tough materials, or using ferrofluid to create flexible magneto responsive materials.²² However, these require the use of their outer 3D printed shells and the fluids inside and do not allow for the materials of interest to be in their pure state while retain their desired 3D shapes. These geometric limitations are overcome by using molds that fully disintegrate after the infilled part has cooled and solidified. This method differs from injection molding in that the molten material flows freely when heated, allowing for filling the cavity using gravity, rather than pressurized injection filling. Additionally, the mold comes apart uniformly with agitation, or soaking in a specialized caustic solution that degrades the mold.

However, using these approaches with conductive polymers is not feasible, due to the degradation of CPs when heated at high temperatures. To overcome

this limitation, we designed a method of casting of a CP precursor, DBEDOT, that can undergo a solid-state polymerization reaction under mild heating conditions to produce pure PEDOT structures with good conductivity. We found that highly complex 3D architected casting molds can be made from a VP printed gel that when dried, acts as a casting structure for molten DBEDOT, and disintegrates when added to water, revealing the complex 3D structured DBEDOT inside. With this method, highly complex 3D objects can be made with free-standing overhanging structures including truncated octahedron and octet lattice shapes. Additionally, the DBEDOT can act as a carrier for casting highly conductive silver flakes, to achieve highly conductive 3D shapes, such as springs. Additionally, the morphology of PEDOT from cast DBEDOT was found to have a variety of structures, including organized plate-like structures, indicating the possibility of using these as high surface area electronics. These findings pave the way for the casting of other castable pure materials into shapes previously not accessible with 3D printing methods.

3.3 Experimental

DBEDOT purification

2,5-Dibromo-3,4-ethylenedioxythiophene (DBEDOT; Tokyo Chemical Industry Co., Ltd.) was purified by filtering over a plug of silica eluting first with hexane (Fisher Scientific), then dichloromethane (Fisher Scientific) to produce a pale-yellow liquid. The product was then dried *in vacuo* to produce a white solid product. The product was confirmed using ^1H NMR and ^{13}C NMR.

UV-curable resin preparation

200 mL of dimethyl sulfoxide (DMSO; Fisher Scientific), 136.06 mg of 4-methoxyphenol (Alfa Aesar), and 93.20 g of 2-acrylamido-2-methyl-1-propanesulfonic acid (AMPSA; Sigma-Aldrich) was added to an aluminum foil-wrapped 1000 mL Kimble GL45 media bottle, followed by sonication. Then, 62.06 mg of quinoline yellow (Acros Organics), 10.80 g acrylamide (AAM; Fisher Scientific), 6 g N,N'-methylenebisacrylamide (MBAA; Alfa Aesar) were added, followed by sonication to dissolve. Then 5.37 mL of ethyl (2,4,6-trimethylbenzoyl)phenylphosphinate) (TPO-L; Oakwood Chemical) was added, then dissolved by swirling the container. Storage and mixing steps were performed in a dark room to avoid premature polymerization.

Many of dried hollow molds had minor structural holes that if not repaired, would lead to unwanted ingress of oil and leakage of molten DBEDOT during the filling process. A 'patch' resin was made to repair these holes, and was made by modifying the SLA resin to have no dye to achieve rapid polymerization,

substituting DMSO with a lower boiling point 1:1 mixture of deionized water and 1,4-dioxane (Alfa Aesar), and scaling the formulation down by 90% as only small quantities were needed. For this resin, 6.80 mg 4-methoxyphenol was initially mixed with 10 mL of 1:1 volume mixture of 1,4-dioxane:water in a 20 mL scintillation vial to avoid premature polymerization from trace peroxides in 1,4-dioxane. Then 4.66 g of AMPSA was added to the mixture and dissolved by sonication, followed by adding 0.54 g AAM and 0.19 g MBAA, then contents were dissolved by sonication. Then, 0.27 mL of TPO-L was added and the vial was stirred to dissolve. All mixing steps were performed in a dark room, and the vial was covered with foil when not in the dark room to avoid premature polymerization.

Hollow molds and trays preparation

Cone sprue adapter and tray models were made using Autodesk Tinkercad, tree and lattice models were made using Rhinoceros 3D and the integrated graphical algorithm editor, Grasshopper. After models were prepared, they were exported as an .stl file, then prepared and sliced using ChituboxPro slicer software. To hollow objects in ChituboxPro, objects were tilting 22.5 degrees, then the hollowing function was performed with 0% density, and 0.50 mm wall thickness settings. Then the topmost part of the molds for filling with molten DBEDOT were merged with cone sprue adapters made in Tinkercad, then a hole was made to connect the inside of the two merged structures in ChituboxPro.

Post-printing processing

There were two processing methods for printing objects; one using heat and the other using a solvent exchange method. Objects dried using heat had excellent shape retention and could stick to a glass slide while it was hot, allowing tray samples to stay flat and have a stable surface to stick to. However, this method caused large hollow objects to become fragile and break during heating, which is why we used a solvent exchange method for processing these.

For heating, samples were first rinsed twice with DMSO to remove excess unreacted resin. After rinsing, excess DMSO was poured off and soaked up with a paper towel. Samples were then placed onto a PTFE sheet-covered hot plate set to 140 °C. The samples were periodically turned as they curled and dried over the course of an hour, at which point they stopped shrinking in size. The samples were then placed into ethyl acetate for 10 minutes to remove remaining DMSO and were quickly dried again on the same hot plate. Samples were used within the same day, or stored in an air-tight plastic jar to avoid absorbing ambient water.

Freshly-printed samples were placed into a beaker containing enough isopropanol (IPA; Fisher Scientific) to submerge them. The beaker was covered in aluminum foil, then then heated to 100 °C for an hour. Over time, DMSO, quinoline yellow, and other remaining unpolymerized resin components became dissolved

in the IPA wash, turning it yellow, at which time, the solvent was discarded and replaced. The process was repeated until the samples had very little yellow color left. Samples were then removed, and the supports were cut off, followed by one more heated IPA wash. Samples were then removed, and placed in a 60 °C overnight to dry. Once dry, samples were stored in an air-tight plastic jar to avoid absorbing ambient water.

For filling objects with molten DBEDOT, a glass pipette was cut on the stem above the tapered region to remove its narrow tip. The tip was fire polished with a propane torch to remove the sharp edge. Then, a two-part epoxy (Gorilla Clear Epoxy) was applied to approximately 1 cm of the smoothed tip, and heated with a heat gun to decrease the curing time. Once hardened, patch resin was coated over the epoxy and cured with a handheld UV laser. More patch resin was applied to the tip, attached to the cone-shaped opening of the mold, then cured using the handheld UV laser. More resin was applied and cured to secure the rod in place. The sample was then placed in the oven at 60 °C for at least an hour to dry. Once dry, the cavity was filled with acetone to check for leaks. To find the locations of leaks, the sample was placed into a beaker of acetone, then air pressure was applied through the opening of the glass tube to gently blow bubbles out of the location(s) of the leak(s). The sample was then dried, and patched with patch resin and UV light, tested for leaks again, then dried in the oven at 60 °C, followed by one more leak test, then drying in the oven.

The spring mold was prepared using the same procedure, but instead of attaching a glass rod, a male hosebarb adapter (Cole-Parmer, 3.2 mm inner diameter; part number: EW-30800-24) was attached to each of the two ends of the spring cavity.

Casting of DBEDOT into hollow lattice molds

DBEDOT as a powder is difficult to load into the glass filling tube due to static charging of the glass and DBEDOT powder. To overcome this, the DBEDOT powder was poured onto a glass slide on a hot plate set to 110 °C, allowed to melt, then carefully removed and cooled on a room temperature table. This recrystallized DBEDOT was then scrapped off of the glass slide, and is easier to be poured into the glass filling tube due to its larger particle sizes.

Before filling, a vacuum oven was preheated to 130 °C, and silicone oil nearly filling a 250 mL beaker was preheated to 110 °C while mixing on a stir plate. Then, recrystallized DBEDOT was added to the glass filling tube of a hollow mold. After the oil and vacuum oven have preheated, the glass filling tube portion of the hollow mold apparatus is clamped to a weighted metal mesh cup to keep most of the buoyant hollow mold apparatus submerged in the hot oil, and the top of the glass tube above the oil. Then, the mold assembly on the support apparatus was

submerged in the hot oil bath, then two were placed into the vacuum oven, and the vacuum oven door was closed. After the DBEDOT was observed to be melting, high vacuum was applied to remove air from the inside of the mold and allow molten DBEDOT to flow inside. After DBEDOT was flowing inside, some air was allowed to enter to force more molten DBEDOT inside, followed by applying more vacuum to remove trapped air. Once DBEDOT completely filled the mold, the vacuum was released and the mold assembly/support apparatus is removed from the oil. DBEDOT shrinks considerably when it crystallizes which can form voids in the structure. To avoid this, the mold apparatus was slowly submerged into room-temperature oil to crystallize the contracting DBEDOT from the bottom-up, which pulls in molten DBEDOT from the sprue at the top of the filling apparatus.

Casting of Ag/DBEDOT composite

To prepare the Ag/DBEDOT mixture, 2 g purified DBEDOT, 3 g Ag flake (APS 4-8 micron, 99.9%; Thermo Scientific and Alfa Aesar) was combined with approximately 10 mL ethyl acetate (Fisher Scientific) in a 20 mL glass vial. The mixture was sonicated for one minute to help disperse the silver flakes, then dried in vacuo. A metal spatula was then used to grind up the solid mixture into a powder and stored in the freezer until needed.

3 g of the dry Ag/DBEDOT mixture was poured into a 10 mL BioX printing cartridge with a syringe tip cap. A 1 L mason jar was filled to approximately 3.5 cm below the rim with silicone oil (Thermo Scientific) was slowly mixed and heated to 110 °C on a heated stir plate. Subsequently, the screw mold assembly was prepared first by attaching 30 cm of Tygon tubing (Thermo Scientific, 3.175 mm inner diameter) to a female hosebarb adapter (Cole-Parmer, 3.2 mm inner diameter; part number: EW-30800-08) which was screwed into one of the male hosebarb adapters on the hollow spring mold assembly. A loop was made with this hose and was held in place with a binder clip. The BioX printing cartridge with the Ag/DBEDOT flake mixture was then placed over half way into the oil and mixed with a straightened-out paperclip until the mixture was melted. The cartridge was then removed from the silicone oil, wiped with a paper towel, then placed into the Thinky mixture, which had an adapter to hold the cartridge, then mixed for 10 seconds, then removed and screwed onto the male hosebarb adapter at the free end of the spring mold, followed by plunging into the hot silicone oil, making sure that the Tygon tube outlet and the top of the cartridge are held above the oil. After the contents are melted, the plunger is pushed into the cartridge using a makeshift plunger from a 1 mL syringe (Norm-Ject; manufacturer number: NJ-9166017-02). Constant pressure is applied to the plunger until all of the melted content fills the entire spring mold. Then the mold apparatus is removed and rapidly cooled by plunging into room temperature silicone oil, and disassembling of the spring attachments.

Mold removal

A cotton-tipped applicator (Fisher) was used to apply deionized water to the shell to make it absorb water to become a soft hydrogel. A razor was used to remove the hydrogel. After all of the shell was removed, it was submerged in deionized water to remove any remaining hydrogel, then set to rest on a paper towel and any remaining water was absorbed with a paper towel. Once dry, the sample was kept in a plastic jar lined with a Kimwipe at -4 °C until it was ready to polymerize in the oven.

Hall samples preparation

To prepare the substrate for casting Hall samples, a rectangular piece of aluminum foil (approximately 2.5 x 2.5 cm) was attached to a silicon wafer substrate using a thin layer of vacuum grease. The foil was pressed to produce a uniform, flat surface. Ag/DBEDOT or DBEDOT powder was poured onto the foil substrate, then melted at 120 °C on a hot plate, then pressed flat with a disk of aluminum foil adhered with vacuum grease to a round glass coverslip. Once the sample was fully melted, a drop of isopropanol was dropped onto the center of the aluminum foil cover to facilitate shrinking from recrystallization to occur radially from the center to the edges and prevent gaps from forming in the sample. The casting apparatus was then removed from the hot plate and set on a table to cool, followed by an additional drop of isopropanol being placed on the center of the cover. Once fully cooled, any remaining isopropanol was soaked up using a paper towel. The sample was removed by first peeling off the aluminum foil cover, followed by removal of the aluminum foil substrate by sliding it off of the wafer, then peeling it off from the sample. Samples needing to be heated were heated in an oven at 24 hours at 60 °C, and those needing no heating were stored at -4 °C. Samples needing a further annealing step were first placed on a fluorinated ethylene propylene (FEP) sheet adhered to a piece of silicon wafer. A piece of a porous PTFE sheet was cut into a ring to cover and hold down the sample edges to prevent the sample from curling, as well as allow for gases to freely escape during the extra heating step. Then the samples were heated to 150 °C for 10 minutes on a hot plate.

Nanoindentation samples preparation

AMPSA shallow square tray molds were printed with a final dry cavity size of 1x1x0.2 cm (length x width x height) with rim and bottom thicknesses of the mold of 1 mm. After printing, they were processed using the heat drying method. Each sample tray was placed on a glass slide, heated to 110 °C on a hot plate, then pressed to adhere the sample to the glass to make the sample flat and rigid. Trays were filled with an excess of Ag/DBEDOT or DBEDOT powder, which was then melted by placing the glass slide on a hot plate set to 110 °C. For Ag/DBEDOT

samples, the molten mixture was mixed with a paperclip for uniform melting, followed by carefully tapping the sample apparatus on a table to evenly distribute the sample in the tray. The filling process was repeated until each tray was filled. Samples were removed from AMPSA trays by soaking them in DI water, then patted dry with a paper towel, then processed using the appropriate heating conditions, or stored at -4 °C if no heating steps were needed.

WAXS and SEM samples preparation

Shallow rectangular AMPSA trays were used as molds for casting molten DBEDOT. After printing the molds, they were processed using the heat drying method. Each sample tray was placed on a glass slide, heated to 110 °C on a hot plate, then pressed to adhere the sample to the glass to make the sample flat and rigid. Trays were filled with an excess of DBEDOT powder, which was then melted by placing the glass slide on a hot plate set to 110 °C. The filling process was repeated until each tray was filled. Samples were removed from AMPSA trays by soaking them in DI water, then patted dry with a paper towel, then processed using the appropriate heating conditions, or stored at -4 °C if no heating steps were needed.

CAD for the hollow lattices

The hollow lattice structures were designed using Rhinoceros 3D with the Grasshopper plugin. The design process began by defining the lattice geometry and subsequently adjusting the model's thickness. This approach enabled efficient iteration and customization of the lattice parameters such as thickness and hollowness. Leveraging Grasshopper's "Pipe Variable" and "Solid Difference" functions, the dimensions of the lattice were programmatically adjustable to vary the size and hollow characteristics of the model as required. Following this, the designs were further refined within Rhinoceros 3D to ensure both manufacturability and structural integrity. Final adjustments were made to optimize the mechanical properties of the lattice for its intended application.

CAD of the tree model

Creating the tree model involved using a few basic features of the 3D design software AutoDesk Fusion 360. While the tree branches could be made with simple sketch lines, the "Fit Point Spline" feature was necessary to bring more texture to the tree sketch, facilitating a smoother transition between each groove of the branches. Key features such as "Offset Plane" and "Sweep" were utilized to mimic the classic curvature of the tree trunk. The most important step was attaching the tree trunk components to the three individual branches, achieved using the "Loft" feature, which allowed for a unique connection to each tree branch.

Solid-state NMR

Solid state CP-MAS ^{13}C NMR spectra were obtained on a Bruker AV600 using a 3.2 mm zirconia rotor spinning at 10 kHz with a cross-polarization contact time of 2.5 ms. To achieve a good signal to noise ratio, 4096 scans were collected for each sample.

Synchrotron X-ray scattering

Synchrotron wide-angle X-ray scattering (WAXS) experiments were carried out at Beamline 7.3.3 of the Advance Light Source (ALS), Lawrence Berkeley National Lab (LBNL). Briefly, DEBDOT and PEDOT bulk rectangular strips (20 mm (length) \times 7 mm (width)) with thicknesses of approximately 200 and 300 μm , respectively, were prepared and mounted to the sample holder. WAXS spectra were collected in transmission geometry at 10 keV with an average exposure time of 2 s at ambient temperature. “Empty” exposures were collected for creating mask and background file for data analysis. Igor Pro Nikka Irena packages were used to process and obtain the 2D WAXS pattern by applying the mask file after background subtraction.

X-ray photoelectron spectroscopy (XPS) characterization

XPS characterizations were done by using a Nexsa X-Ray Photoelectron Spectrometer System (Thermo Fisher Scientific). Samples were loaded onto silicon wafer pieces which were stabilized onto the sample holder by metal clips. A spot size of 400 μm was selected. The spectrum of sulfur was collected in the range of 160~170 eV with scan cycles of 40. Characterization had been done on multiple spots on the same sample to ensure generality. “XPSPeak 4.1” software was used to fit the collected curves. The specific area ratio between S 2p $_{1/2}$ and S 2p $_{3/2}$ peaks had been set to a constant 0.5. The sulfur atomic percentages of PSS and PEDOT were calculated by taking the area ratios of 2p peaks of PSS to those of PEDOT.

Scanning Electron Microscope (SEM) characterization

The morphology of DBEDOT and PEDOT samples was observed with the help of Scanning Electron Microscope (Zeiss Gemini 500, ZEISS Company, Germany). Samples were directly glued onto the SEM pin mount without any sputtering. Cross-section samples were placed onto the 90° mounts to examine the surface. An accelerating voltage of 3 kV was applied; working distance was adjusted and optimized for the best quality of the pictures. For high magnification images, Frame Integration mode coupled with a decreased scanning speed was being used to take fine pictures.

3.4 Results and Discussion

DBEDOT underwent a self-catalyzing polymerization at 60 °C heating for 24 hours (Figure 3.1a). This unusual solid-state polymerization was enabled by the close packing of DBEDOT in its crystalline state. Additionally, bromine was released over the course of the reaction, which was trapped inside the material, and assisted in oxidizing and doping PEDOT, making it more conductive.^{23,24} The reaction was visibly noticeable when performed on pure, transparent and colorless DBEDOT crystals obtained from crystallizing DBEDOT from a methanol solution. After heating at 60 °C for 24 hours, they became dark blue/black from the formation of PEDOT (Figure 3.1b). Although DBEDOT polymerized when heated for extended periods of time, its melting point of around 95 °C allowed it to be rapidly cast into molds of different shapes, then solidified by cooling before polymerization could occur (Figure 3.1c). The cast DBEDOT objects were then heated at 60 °C for 24 hours, which caused them to have the same color change that was observed in the single crystal DBEDOT, indicating that cast DBEDOT underwent the same solid-state polymerization into PEDOT.

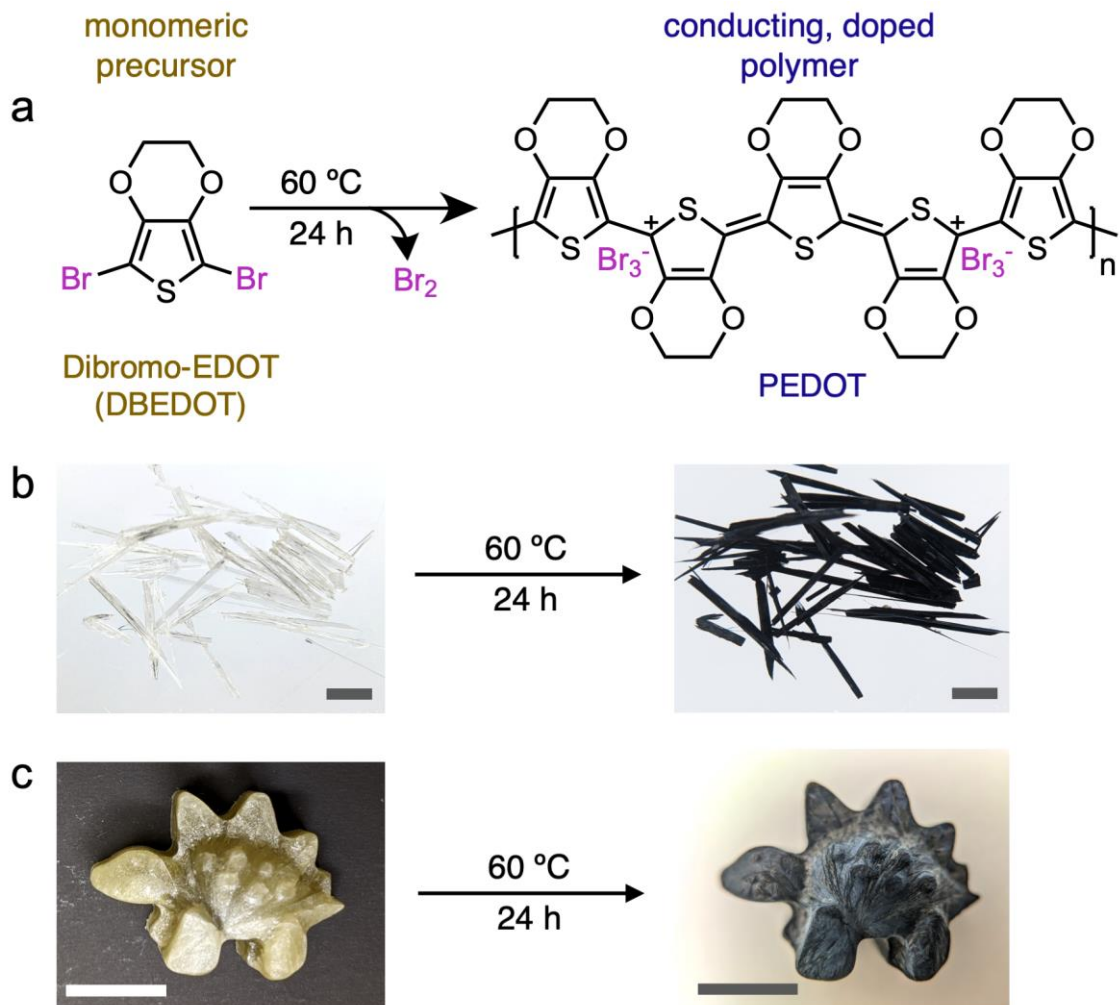


Figure 3.1. Solid-state polymerization of DBEDOT to PEDOT. (a) Chemical reaction; (b)-(c) Photographs of (b) single crystals of DBEDOT and (c) casted polycrystalline DBEDOT polymerized into PEDOT under mild heating. Scale bar: 5 mm.

To enable casting DBEDOT into 3D shapes, we developed a 3D printable mold that can be removed using a simple water solution. We achieved this by designing a resin which contains sulfonic acid side chains in the polymer that absorbs water and become a superabsorbent polymer, making it brittle, and causing it to disintegrate. To perform the filling process, we found that the molds must be kept uniformly heated to prevent DBEDOT from cooling, which was accomplished by submersion in a heated silicone oil bath (Figure 3.2). The molds are able to be filled with the molten DBEDOT monomer, which flows into the empty space of the molds and solidified by cooling to room temperature (Figure 3.3a and b). The molds were then swelled and made brittle by exposed them to water,

making the molds disintegrate, revealing the 3D DBEDOT structure inside that matched the cavity structure inside the molds. The versatility in design freedom of VP allowed us to design and cast a variety of shapes and sizes with overhanging structures, including octet lattices, truncated octahedron, or arbitrary structures such as a tree (Figure 3.3c-f). The pure DBEDOT structures then underwent the solid-state polymerization step by heating at 60°C for 24 hours to transform into pure PEDOT. This transformation in the DBEDOT structures was confirmed by the color change from white/pale green of DBEDOT to the dark blue/black color of PEDOT (Figure 3.3g-j).

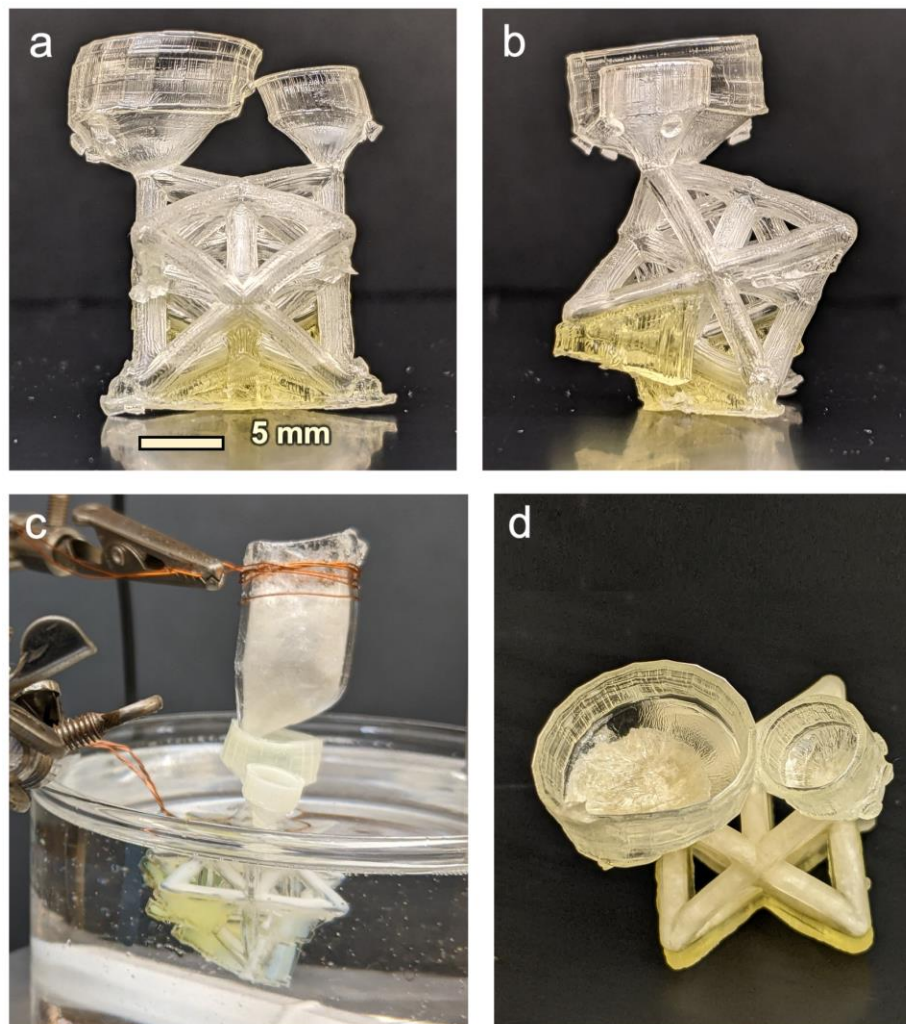


Figure 3.2. Photographs of (a) and (b) dried mold with inlet and outlet funnels attached, (c) set up for melting and filling DBEDOT precursor, and (d) mold with DBEDOT after DBEDOT solidification at room temperature.

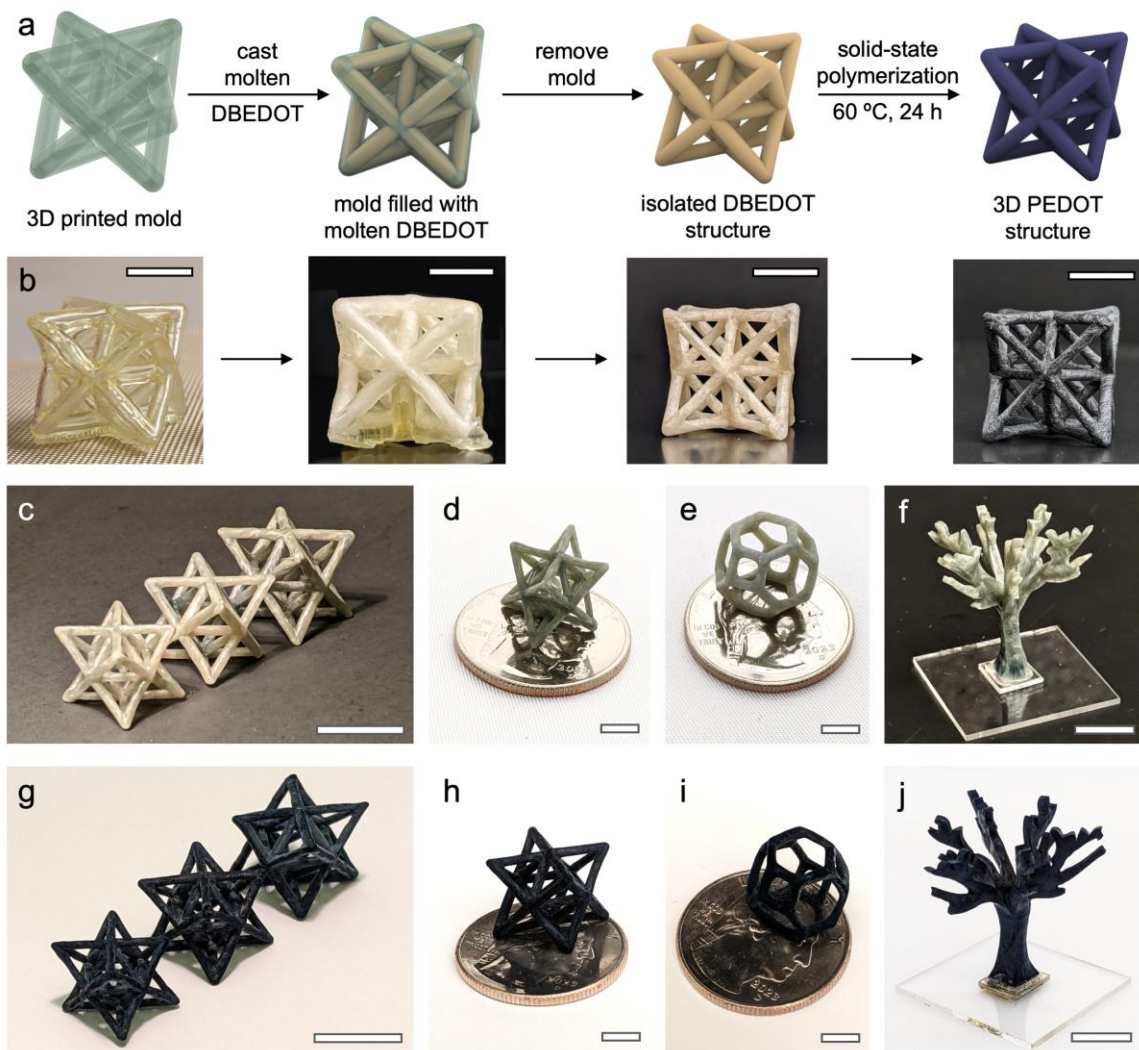


Figure 3.3. 3D-printing assisted casting of PEDOT. (a) Schematic diagram and (b) the corresponding photographs of the process flow. (c)-(f) Photographs of isolated DBEDOT structures after mold removal. (g)-(j) Pure, doped PEDOT structures after the solid-state polymerization of (c)-(f), respectively. Scale bar: 5 mm.

3.4.1 DBEDOT and SSP-PEDOT Characterization

Previous studies on the properties of PEDOT polymerized in the solid-state from DBEDOT were performed on isolated single crystals of DBEDOT that were crystallized from an ethanol solution. In contrast, our casting method used melt-processed DBEDOT, which motivated us to determine the processing-structure-properties of our melt-processed DBEDOT and subsequently formed PEDOT, and compare it with the previously found properties of DBEDOT and PEDOT from literature.

3.4.1.1 NMR Analysis of DBEDOT Polymerization

3.4.1.1.1 DBEDOT

The as received DBEDOT appeared light blue/grey from trace amounts of PEDOT formed from the spontaneous solid-state polymerization. However, the small quantity of impurities were undetectable by ^1H or ^{13}C NMR (Figures 3.4 and 3.5). Additionally, the presence of Br_2 from the byproduct of the polymerization can catalyze the polymerization of DBEDOT, and shorten the available working time when casting molten DBEDOT. These impurities could be removed using column chromatography, as indicated by the product having a white/pale yellow color. When purified DBEDOT was melt-cast, it appeared to form many crystals when cooled, yet remained chemically identical after casting as indicated by ^1H and ^{13}C NMR (Figures 3.4 and 3.5).

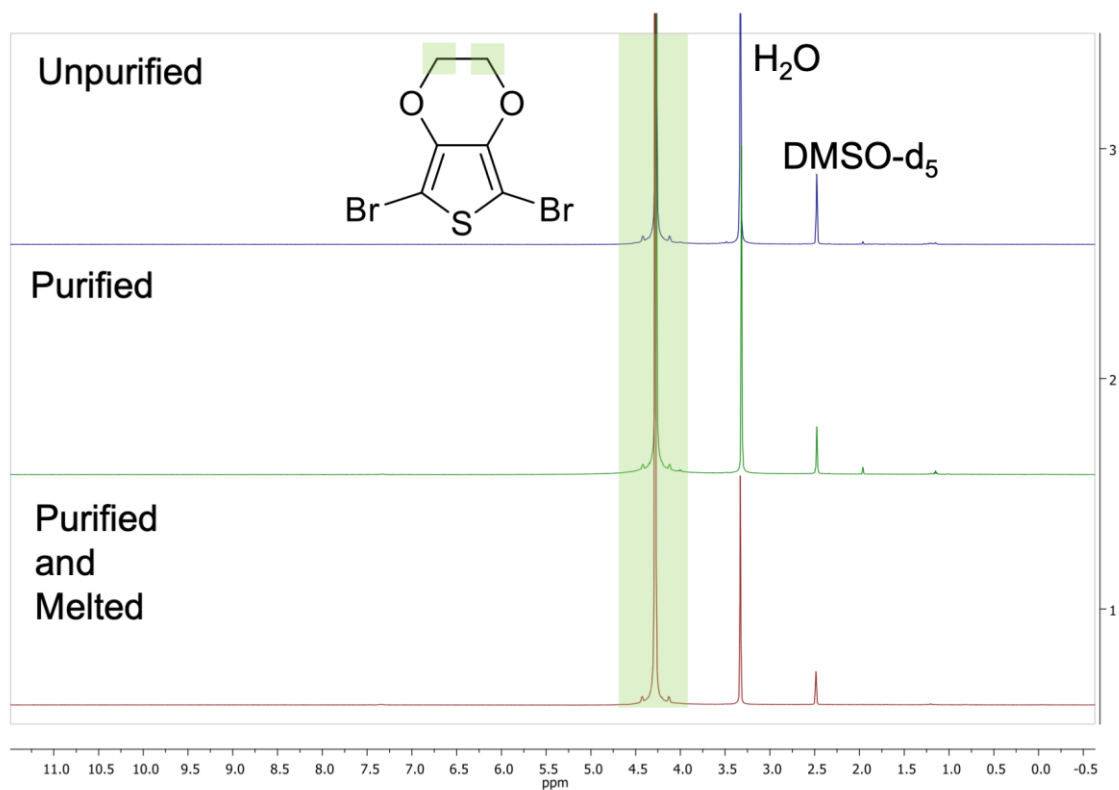


Figure 3.4. ^1H NMR of DBEDOT that was as-received (unpurified), purified, and resolidified from melting of the purified powder.

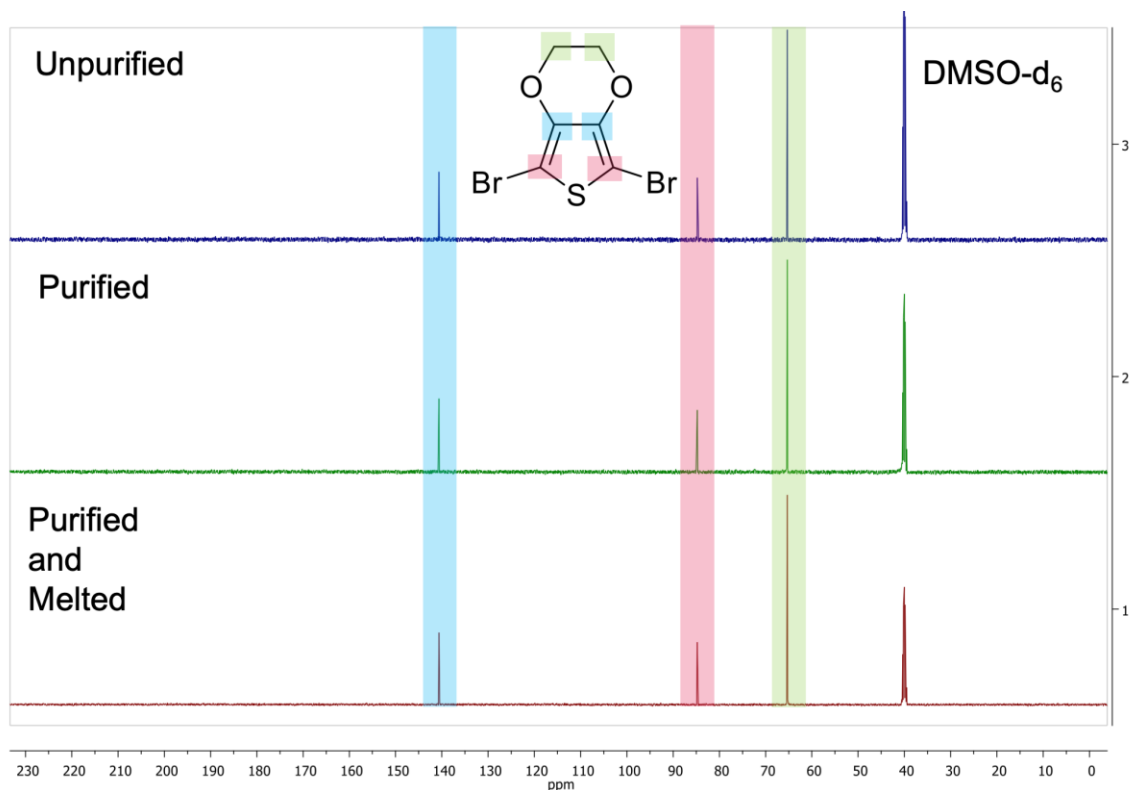
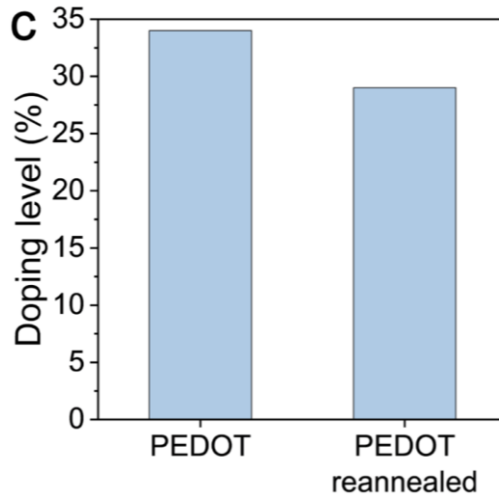
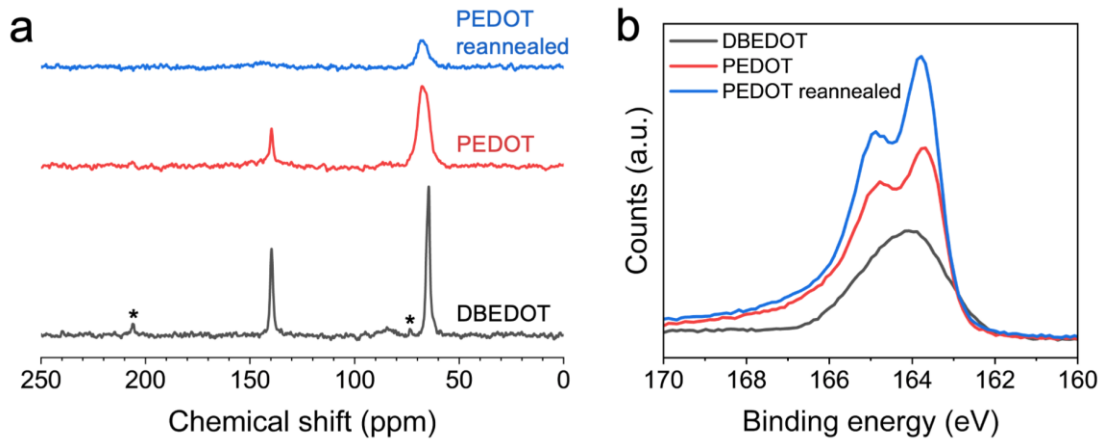


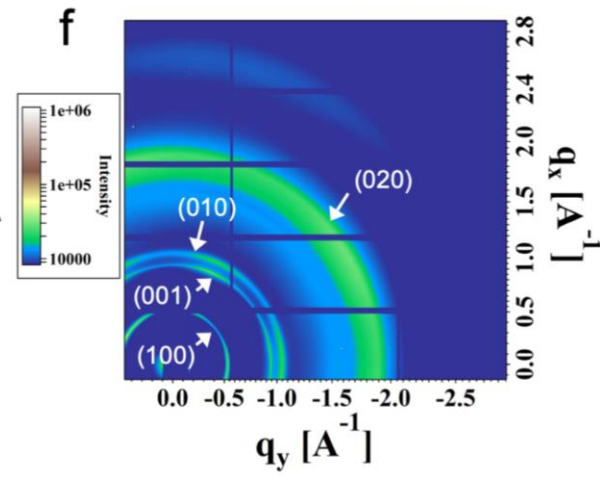
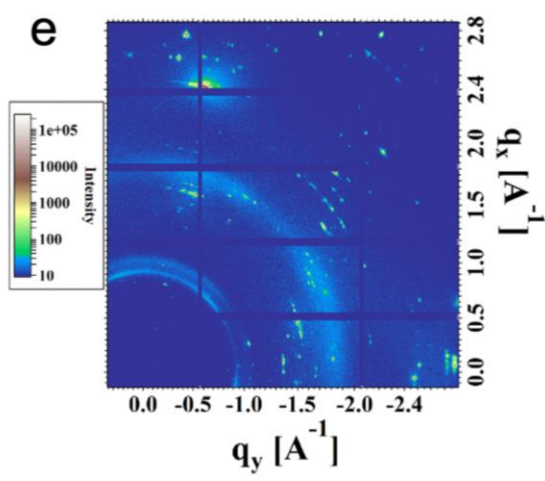
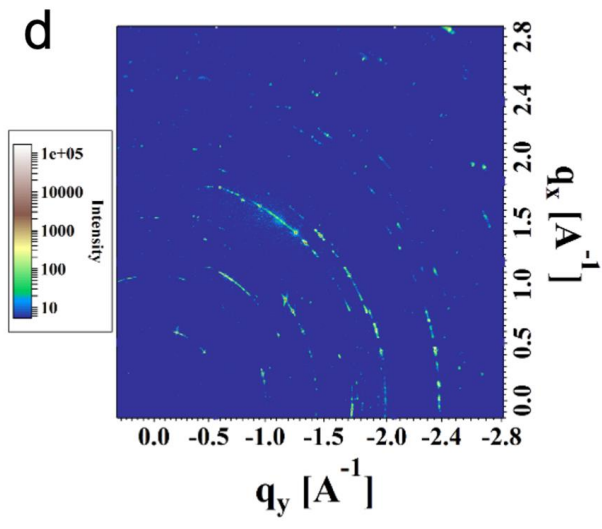
Figure 3.5. ^{13}C NMR of DBEDOT that was as-received (unpurified), purified, and resolidified from melting of the purified powder.

3.4.1.1.2 SSNMR

Solid state CP-MAS ^{13}C NMR spectroscopy was used to characterize the structure of the monomeric precursor (DBEDOT) as well as the resulting polymer (PEDOT) after solid-state polymerization (Figure 3.3a). DBEDOT showed a strong peak at 65 ppm corresponding to the carbons of the oligoether bridge, a broad peak at 85 ppm corresponding to the 2,5-thiophene ring carbons, and strong peak at 139 ppm corresponding to the 3,4-thiophene ring carbons. To our surprise, the resulting spectra of solid-state polymerization of the sample at 60 °C showed a mixture of both DBEDOT and PEDOT. This result differs from previous findings that single crystals of DBEDOT monomer are completely consumed with these conditions. The peak centered at 68 ppm in the aliphatic region is slightly broader due to the presence of both the monomer and the polymer, and the sharp peak at 139 ppm suggests the presence of remaining DBEDOT. Subsequent experiments showed that a subsequent annealing step at 150 °C for 10 minutes completely eliminated the remaining monomer and left behind PEDOT, as indicated by the

broadened peak at 150 ppm and the peak at 68 ppm. Paramagnetic broadening greatly affected the NMR signals from the polymeric backbone due to spurious radicals present from polaron formation.





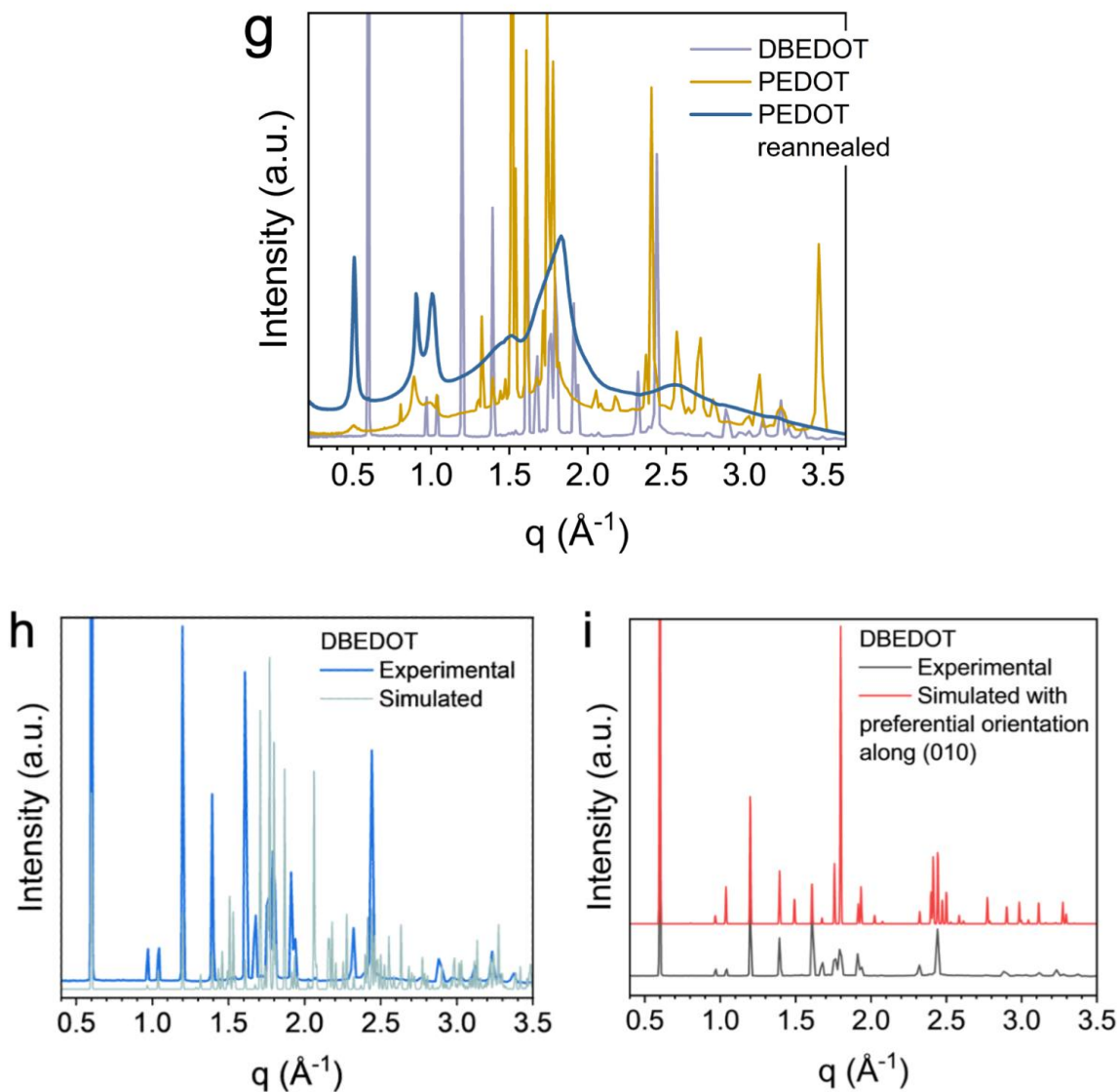


Figure 3.6. Chemical and structural characterization. (a) Solid-state ^{13}C NMR and (b) XPS of DBEDOT, PEDOT, and reannealed PEDOT. (c) Doping levels of PEDOT and reannealed PEDOT obtained through the S 2p peak from XPS. (d)-(f) 2D WAXS scattering spectra of DBEDOT, PEDOT, and reannealed PEDOT, respectively. The combined 1D linear plots of these WAXS scattering patterns are shown in (g). (h)-(i) 1D WAXS spectrum of DBEDOT compared to (h) the simulated pattern based on the single crystal structure of DBEDOT and (i) the simulated pattern with a preferential orientation along (010).

3.4.1.2 Characterization of Cast Material

3.4.1.2.1 WAXS

The surface of melt-cast DBEDOT appeared to have many crystals formed after cooling, which led to the many scattering peaks seen in wide-angle X-ray scattering (WAXS) of melt-cast DBEDOT samples (Figure 3.6d). After annealing, broad peaks from PEDOT formation appeared, but the strong scattering peaks remained from remaining DBEDOT crystals (Figure 3.6e). After reannealing, only PEDOT signal remained (Figure 3.6f), confirming the results seen from ^{13}C NMR analysis. However, each sample of melt-crystallized DBEDOT had unique crystal growth patterns and crystal orientations, resulting in different scattering peaks between samples (Figure 3.6g).

To confirm the crystal structure identity of our melt-cast DBEDOT, we compared its 1D WAXS spectrum to that of simulated DBEDOT crystal scattering (Figure 3.6i and 3.8) with the simulated crystal packing structure shown in Figure 3.7. The scattering patterns of melt-processed DBEDOT shared most of the most prominent scattering peaks of simulated scattering of single-crystal DBEDOT. Melt-cast DBEDOT displayed a much closer peak correspondence to simulated DBEDOT scattering of a single DBEDOT crystal with preferential orientation along the (010) plane (Figure 3.6i), indicating that much of the melt-cast DBEDOT grew along this plane.

Monoclinic
Space group: Cc

$a = 25.2700 \text{ \AA}$

$b = 5.0127 \text{ \AA}$

$c = 15.6670 \text{ \AA}$

$\alpha = 90^\circ$

$\beta = 123.9590^\circ$

$\gamma = 90^\circ$

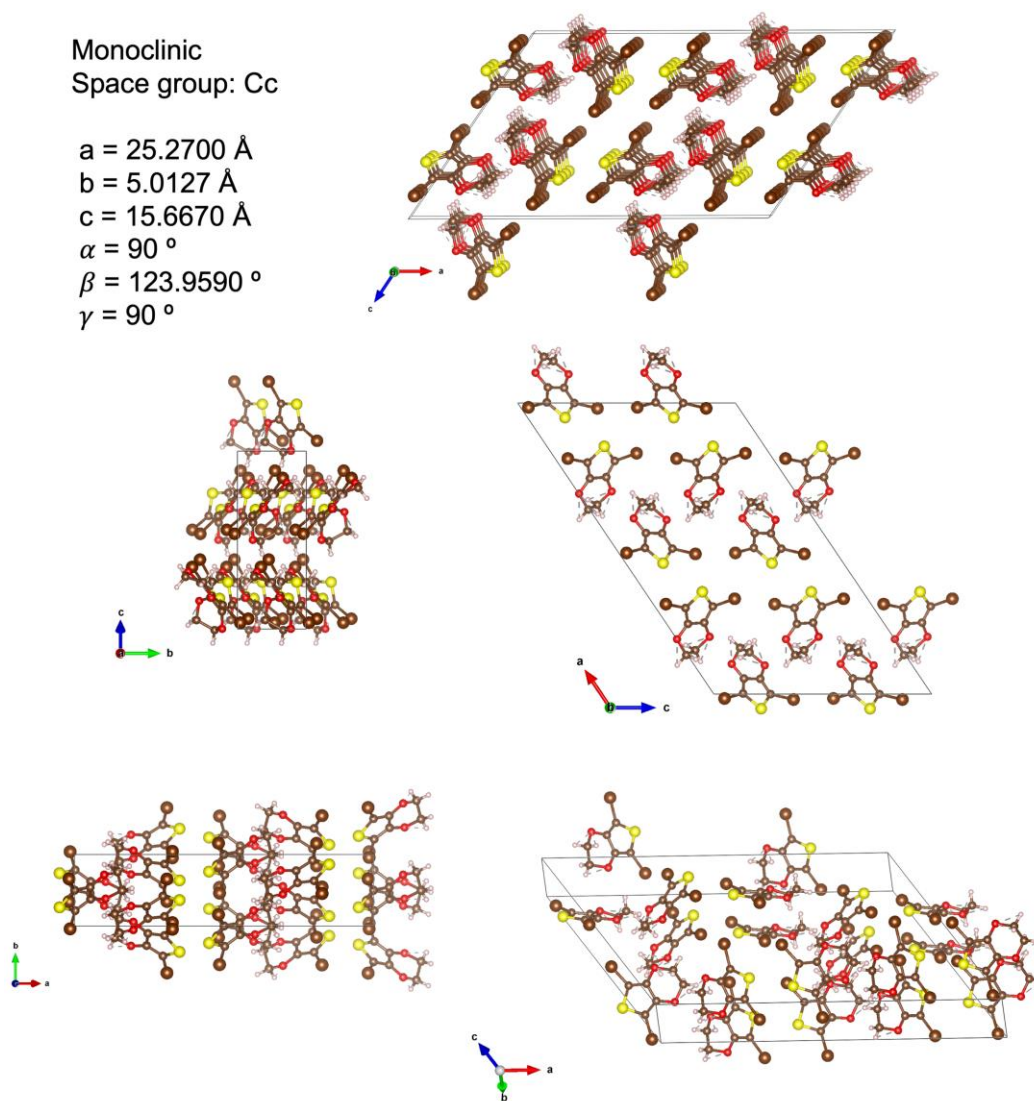


Figure 3.7. Crystal packing arrangement of DBEDOT.

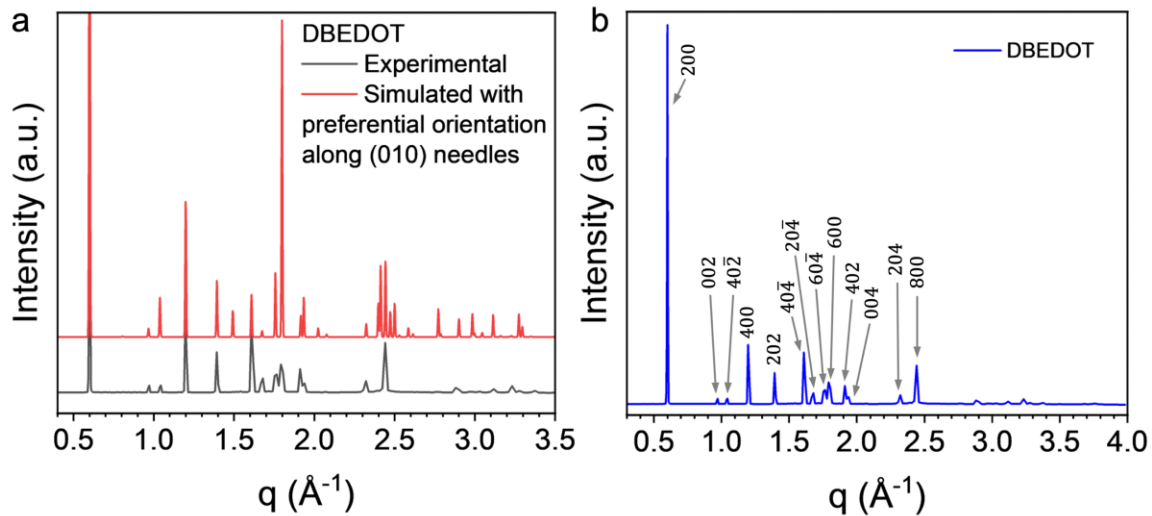
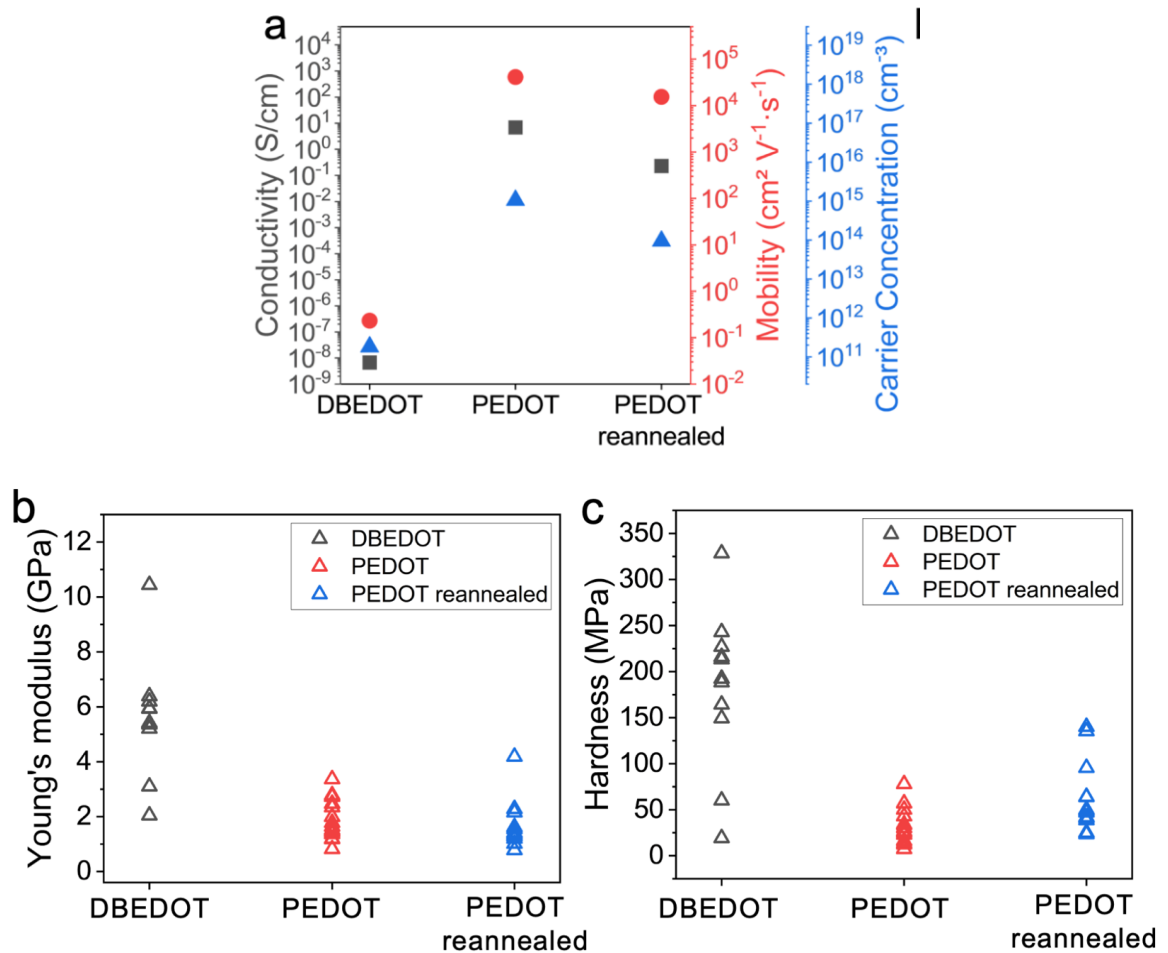


Figure 3.8. (a) Experimental diffraction spectrum of DBEDOT overlaid with simulated spectrum with preferential orientation using the single crystal data of DBEDOT. (b) Peak indexing of the experimental DBEDOT diffraction spectrum.

3.4.1.2.2 Electrical and Mechanical Characterization

To gain a better understanding of the processing-structure-conductivity relationship of PEDOT from melt-cast DBEDOT, we used Hall measurements to measure carrier mobility and charge carrier concentration. As expected, melt-cast DBEDOT was electrically insulating, and became conductive when PEDOT formed from the initial heating step (Figure 3.9a). Surprisingly, the reannealing step decreased the conductivity of PEDOT, even though this process removed the insulating DBEDOT component. Initially, PEDOT had a high charge carrier concentration and charge mobility, but each of these decreased by approximately an order of magnitude after reannealing. To investigate the cause of this, we first determined why the charge carrier concentration decreased. By using XPS, we could determine the change in charged moieties of PEDOT (Figures 3.6b and 3.10). Interestingly, we found that the concentration of doped PEDOT decreased from 34% to 29% from the reannealing step (Figures 3.6c and 3.10). During the solid-state polymerization of DBEDOT, Br₂ is generated as a byproduct and becomes trapped, resulting in doping of PEDOT. However, given that Br₂ has a boiling point of 58.8 °C, heating to 150 °C can effectively evaporate excess bromine and decrease the doping level of PEDOT, resulting in lower conductivity. The decrease in charge mobility was unexpected, due to the potential increase in PEDOT formation and decreased amount of insulating DBEDOT from the extra annealing step. The decrease in charge carrier mobility could be attributed to structural changes that occurred during the extra annealing step. To better understand these changes, we carried out a study of the morphology using scanning electron microscopy (SEM). DBEDOT appeared to have a smooth surface with many visible crystal interfaces (Figure 3.11a), but was rough from different crystal orientations at the sub-micron scale (Figures 3.9d and 3.11c). However, the morphology appeared dramatically different after the first solid-state polymerization step, with multiple layers of stacked plates on the surface and throughout the material (Figures 3.9e and h, 3.12), and columns with different orientations (Figure 3.9f and g). In all PEDOT samples, there was a noticeable amount of empty space, likely due to the loss of Br₂ from the reaction, and a decreased volume from the DBEDOT monomer to PEDOT. However, after the reannealing step, we found that new PEDOT features appeared, most notably spikes (Figure 3.13d), as well as a rougher surface on the stacked platelets (Figure 3.13j and k). Most of the stacked plates and columns remained intact, indicating that there were no noticeable structural changes that would account for the change in charge mobility. Instead, there may have been small structural changes that changed the mobility between the conductive PEDOT structures. One source of these small changes could be from the noticeable volume expansion that we observed upon melting DBEDOT. Since the reannealing step was done at a much higher temperature than the melting point of DBEDOT, this expanding DBEDOT

when located between PEDOT, structures could have caused them to separate and decrease the charge mobility. Another possibility is that as DBEDOT melted, its surface tension between PEDOT structures caused them to become permanently dislocated, leading to their decreased mobility. These structural changes also influenced the material's mechanical properties as well. Measurements of the Young's modulus and hardness of DBEDOT were found to have a wide range of values, due their numerous crystal orientations (Figure 3.9b and c). After the solid-state reaction, these values decreased, likely due to the decreased density. After the reannealing, the Young's modulus and hardness both increased, likely from the formation of new PEDOT structures and small rearrangements that occurred when DBEDOT melts.



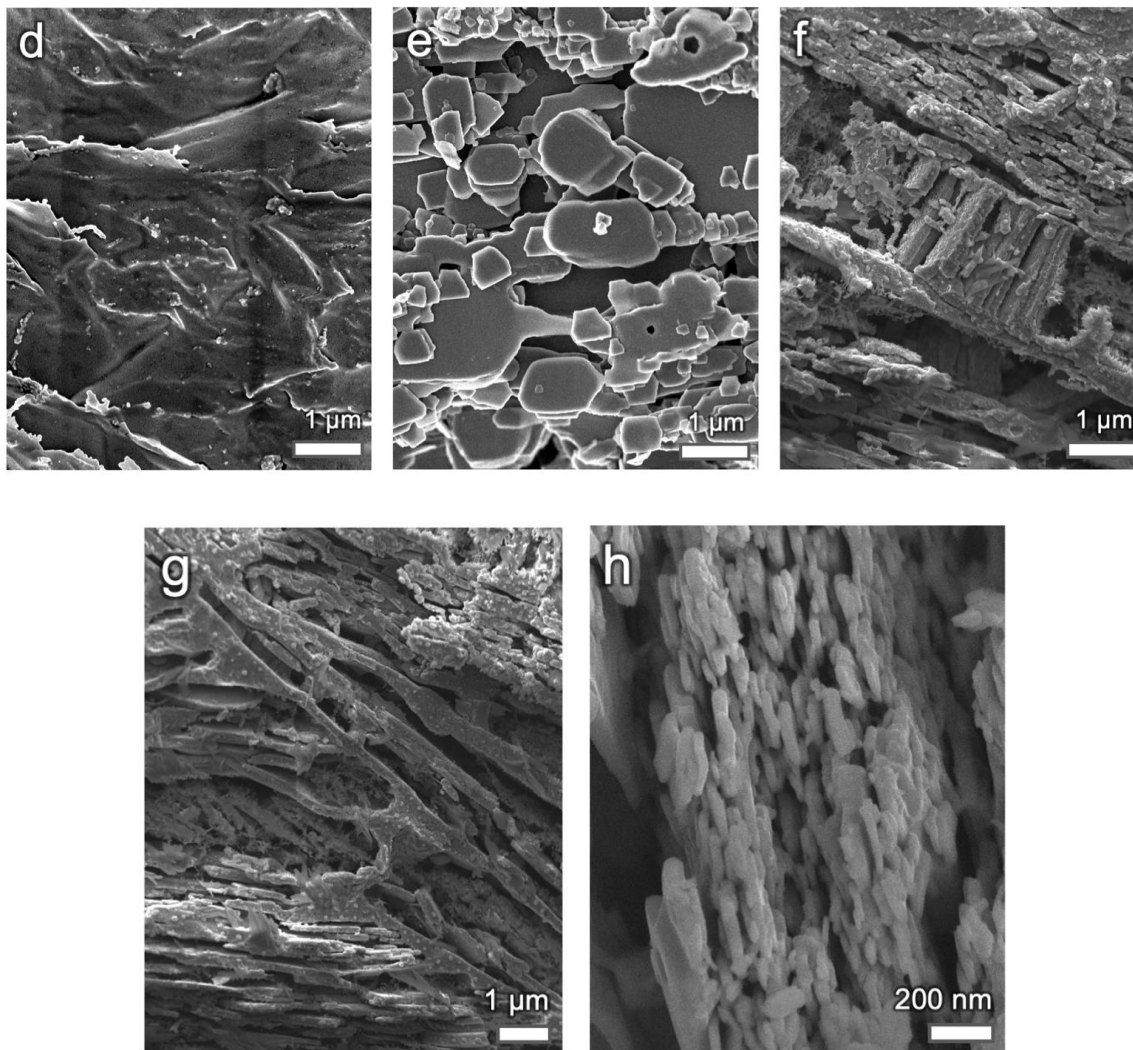
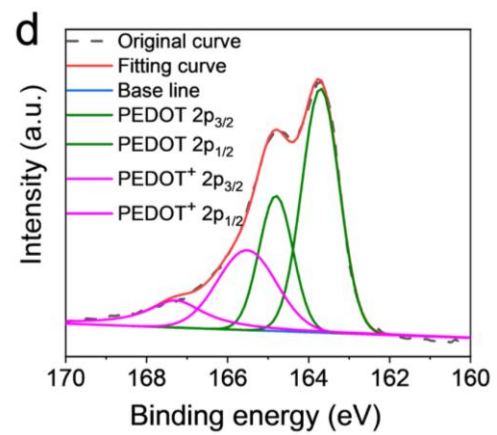
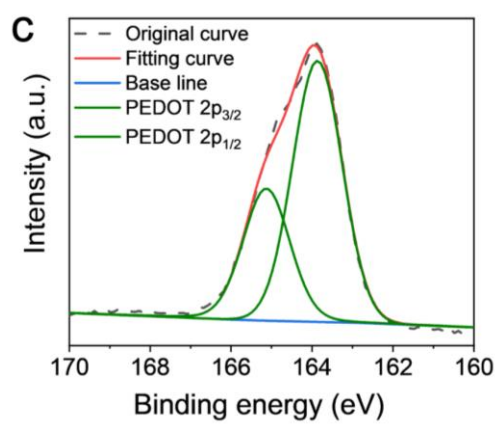
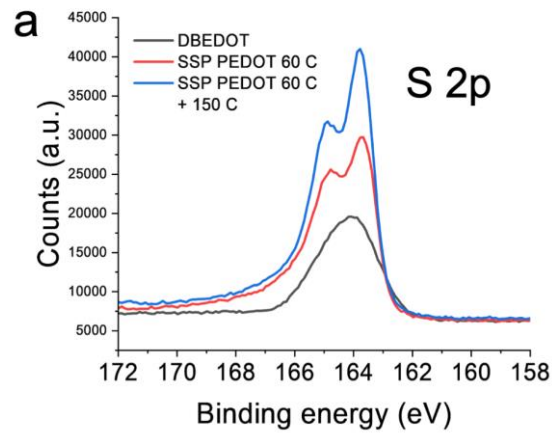


Figure 3.9. Electrical and mechanical characterization. (a) The conductivity, mobility, and carrier concentration values obtained through Hall measurements. (b) Young's modulus and (c) hardness values obtained through nanoindentation studies. (d)-(h) SEM images of (d) DBEDOT, (e) top view of PEDOT, (f)-(h) different cross-sectional views of PEDOT.



b

	PEDOT	PEDOT ⁺	Doping level
SSP PEDOT (60 C)	66%	34%	34%
SSP PEDOT reannealed (60 C+150 C)	71%	29%	29%

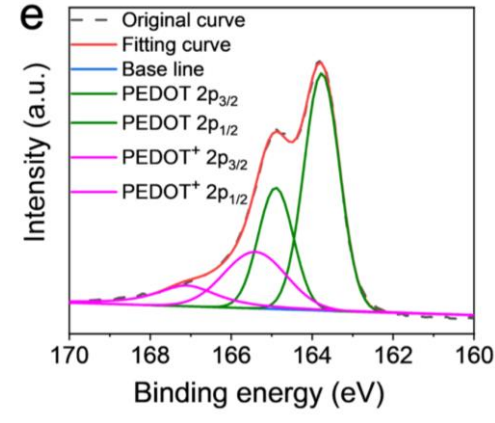


Figure 3.10. (a) S 2p XPS of DBEDOT, PEDOT, and reannealed PEDOT. The peak fitting for these three spectra are shown in (c)-(e). Doping level calculations from integrated peak areas from (c)-(e) are tabulated in (b).

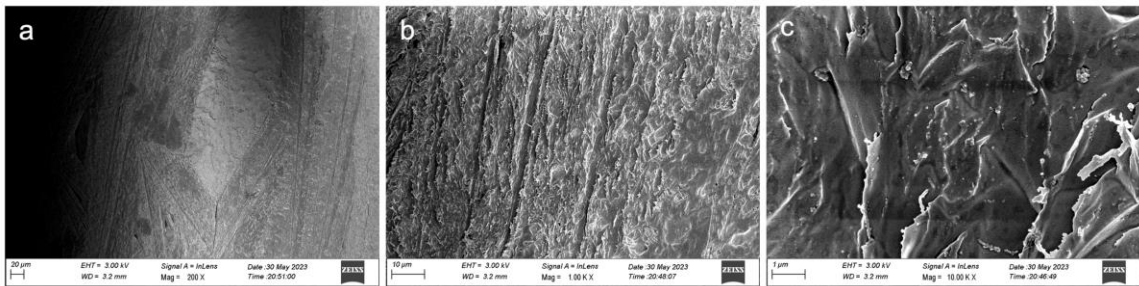


Figure 3.11. SEM images of solidified DBEDOT at various magnifications.

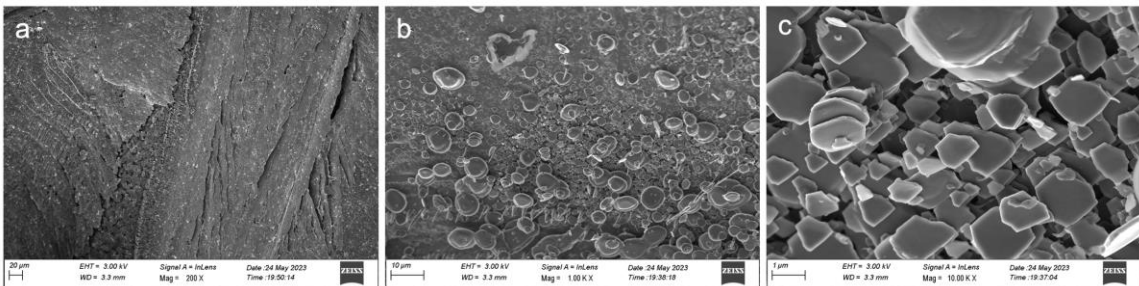


Figure 3.12. SEM images of PEDOT at various magnifications.

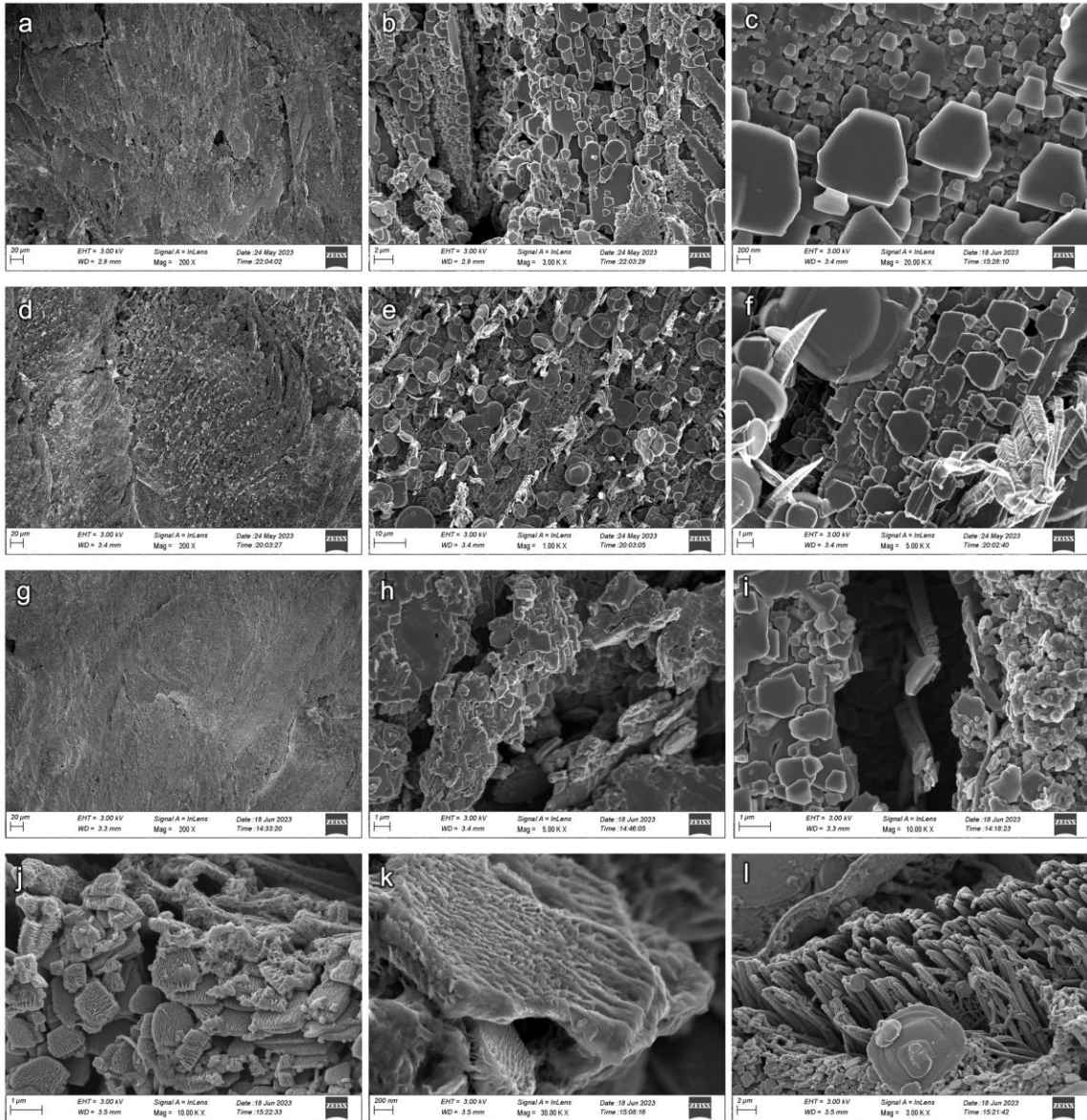


Figure 3.13. SEM images of reannealed PEDOT at various magnifications.

3.4.2 Molten DBEDOT as a Carrier for Highly Conductive Silver Flakes

The maximum conductivity of PEDOT was found to have good conductivity of nearly 10 S/cm. However, this value was lower than what had been previously achieved with solid-state polymerized PEDOT, and two orders of magnitude lower than what can be achieved with PEDOT:PSS. However, one advantage of using molten DBEDOT is that it can be used as a flowable carrier for fillers with much higher conductivity, such as silver flakes, resulting in the ability to make highly conductive complex 3D objects. To demonstrate this, we tested the conductivity of Ag-PEDOT with various amounts of silver flakes (Figure 3.14c). The addition of only 5 volume % of silver flakes dramatically increased the conductivity by over three orders of magnitude, and with the addition of 17 volume %, was able to achieve over 8000 S/cm, far higher than what can be achieved with PEDOT alone. A higher loading of silver flake was not used, as increasing the loading of silver flake in molten DBEDOT was found to increase the viscosity higher than what could be feasibly mixed and injected to molds using our existing casting methods. The high viscosity of the Ag-DBEDOT mixture required the use of positive pressure to inject the material into molds. By using this approach, we could successfully create free-standing objects, like a spring, of 17 volume % Ag-DBEDOT (Figure 3.14a and b). Additionally, this approach to use a conductive filler can effectively increase the conductivity with silver flakes at a lower loading level than what is needed when using other insulating fillers.

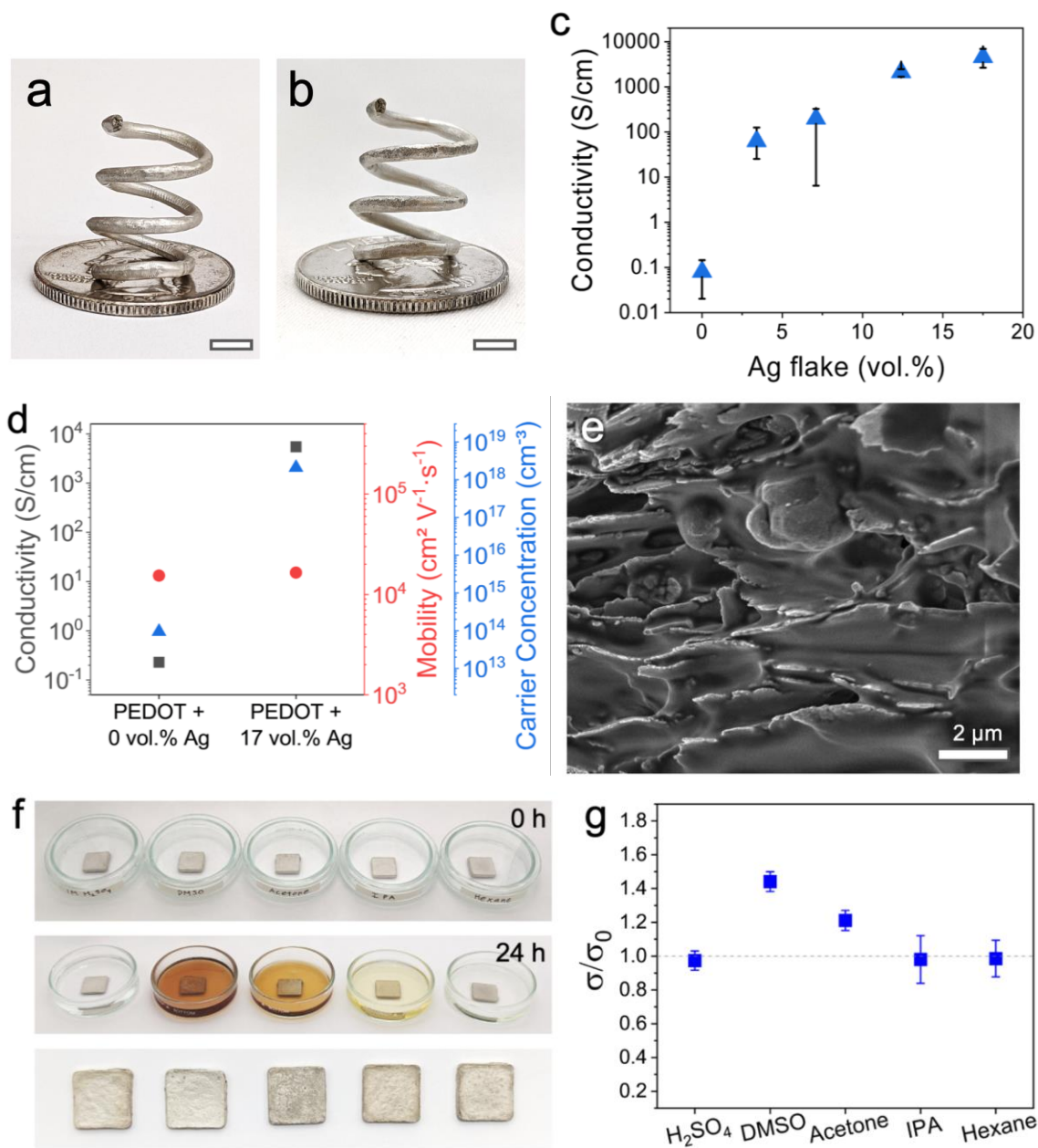


Figure 3.14. Ag-PEDOT composites. (a)-(b) Photographs of (a) 3DPAC Ag-DBEDOT and (b) Ag-PEDOT structures. (c) Conductivity of the composite at various loadings of Ag flakes. (d) Conductivity, mobility, and carrier concentration values of PEDOT and Ag (17 vol.%) - PEDOT composite obtained through Hall measurements. (e) SEM of the Ag (17 vol.%) - PEDOT composite. (f) Photographs showing the Ag (17 vol.%) - PEDOT composite soaked in various solvents at 0 h (top row), after 24 h of soaking (middle row), and the soaked specimens after drying (bottom row). From left to right: 1M H₂SO₄ (aq.) solution, DMSO, acetone,

IPA, hexane. (g) Normalized conductivity of the Ag (17 vol.%)–PEDOT composite after soaking in solvents. Scale bar for (a)–(b): 5 mm.

Because we were using this new approach for casting two different conductive components, we s to better understand how our processing method influenced its conductivity. We found that the mobility of charges remained low due to the dysconnectivity and voids from the structure (Figures 3.14e, 3.15). The silver flakes remain well distributed (Figure 3.15a and b), with PEDOT covering their surfaces and binding them together (Figure 3.15c–e). The increase in conductivity was mainly due to the higher carrier concentration of silver than PEDOT.

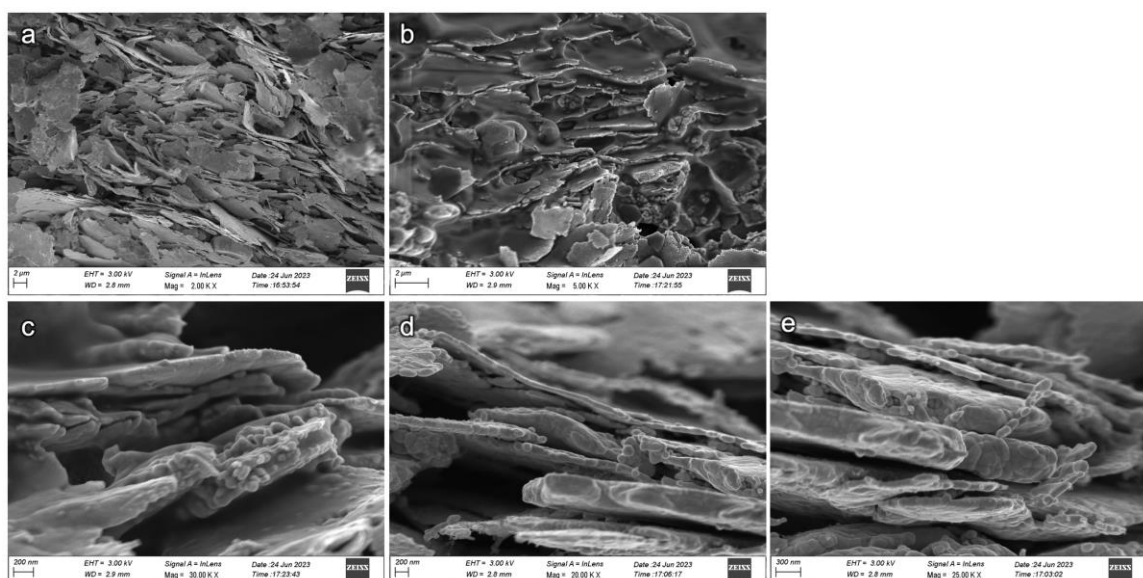


Figure 3.15. SEM images of the composite of PEDOT-reannealed with 17 vol.% Ag at various magnifications.

The insolubility of conductive polymers can often make this class of material difficult to process. However, our approach to using insoluble PEDOT as a filler allows us to have a fully conductive composite that is resistant to a variety of common solvents that could otherwise dissolve polymer structures. To demonstrate this, we exposed 17 volume % Ag–PEDOT to a 1M H_2SO_4 (aq.) solution, DMSO, acetone, isopropanol, and hexane for 24 hours (Figure 3.14f). The resulting DMSO and acetone solvents turned dark orange, likely from dissolving free bromine contained in the sample. In every case, the Ag–PEDOT remained intact, and did not decrease in conductivity performance (Figure 3.14g).

In some solvents, like DMSO and acetone, the conductivity was found to increase, likely from dissolving extra bromine that can oxidize the surface of silver flakes.

3.5 Summary and Outlook

In this work, we demonstrated a new method for making pure PEDOT into 3D shapes by facile casting of a molten PEDOT precursor into a water-removable hollow 3D mold, followed by solid-state polymerization by mild heating. This method is capable of producing a wide variety of shapes including octet and truncated octahedron unit cells, and arbitrary shapes like trees. Our detailed characterization found that DBEDOT monomer still remained after the solid-state polymerization, but could be removed after an additional heating step. We were surprised to find that the solid-state polymerized PEDOT had a variety of structures, including columns and stacked plate-like structures. The conductivity of PEDOT could be improved to over 8000 S/cm by adding highly conductive silver flakes to the DBEDOT monomer, which demonstrates the ability to use DBEDOT as a carrier for other useful materials to improve its performance. Additionally, PEDOT formed is solvent resistant, and retains its high conductivity even with the inclusion of silver flakes.

These findings are a significant improvement over previous efforts to make 3D PEDOT structures which faced tradeoffs between high 3D shape complexity or either high conductivity due to the limited PEDOT that could be incorporated into VP resins. The structures and understanding of their formation can possibly lead to the use for tougher electronics where the stacked PEDOT plates could act as sacrificial structures in a tough nacre-like material.

Additionally, this method can also be used with a variety of other materials that are difficult to form into 3D structures with traditional light-based or extrusion-based AM techniques, without sacrificing their desirable properties for printability. This includes soft materials, such as soft silicones, which are desirable for wearable electronics and biomaterials, which are difficult to manufacture with 3D printing methods due to their low yield stress.^{25,26} This would also be a valuable processing method for low melting point metals, such as gallium, for producing intricate 3D metal objects without complex casting requirements, to expand its use by decreasing turnaround time and decreasing production costs.

3.7 References

- (1) Criado-Gonzalez, M.; Dominguez-Alfaro, A.; Lopez-Larrea, N.; Alegret, N.; Mecerreyes, D. Additive Manufacturing of Conducting Polymers: Recent Advances, Challenges, and Opportunities. *ACS Appl. Polym. Mater.* **2021**, *3* (6), 2865–2883. <https://doi.org/10.1021/acsapm.1c00252>.
- (2) Martinelli, A.; Nitti, A.; Giannotta, G.; Po, R.; Pasini, D. 3D Printing of Conductive Organic Polymers: Challenges and Opportunities towards Dynamic and Electrically Responsive Materials. *Mater. Today Chem.* **2022**, *26*, 101135. <https://doi.org/https://doi.org/10.1016/j.mtchem.2022.101135>.
- (3) Jordan, R. S.; Wang, Y. 3D Printing of Conjugated Polymers. *J. Polym. Sci. Part B Polym. Phys.* **2019**, *57* (23), 1592–1605. <https://doi.org/10.1002/polb.24893>.
- (4) Ryan, K. R.; Down, M. P.; Hurst, N. J.; Keefe, E. M.; Banks, C. E. Additive Manufacturing (3D Printing) of Electrically Conductive Polymers and Polymer Nanocomposites and Their Applications. *eScience* **2022**, *2* (4), 365–381. <https://doi.org/https://doi.org/10.1016/j.esci.2022.07.003>.
- (5) Yuk, H.; Lu, B.; Lin, S.; Qu, K.; Xu, J.; Luo, J.; Zhao, X. 3D Printing of Conducting Polymers. *Nat. Commun.* **2020**, *11* (1), 4–11. <https://doi.org/10.1038/s41467-020-15316-7>.
- (6) Ruitao, S.; Hyun, P. S.; Xia, O.; Ih, A. S.; C., M. M. 3D-Printed Flexible Organic Light-Emitting Diode Displays. *Sci. Adv.* **2022**, *8* (1), eabl8798. <https://doi.org/10.1126/sciadv.abl8798>.
- (7) Lewis, J. A. Direct Ink Writing of 3D Functional Materials. *Adv. Funct. Mater.* **2006**, *16* (17), 2193–2204. <https://doi.org/10.1002/adfm.200600434>.
- (8) Zheng, Y.; Wang, Y.; Zhang, F.; Zhang, S.; Piatkevich, K. D.; Zhou, N.; Pokorski, J. K. Coagulation Bath-Assisted 3D Printing of PEDOT:PSS with High Resolution and Strong Substrate Adhesion for Bioelectronic Devices. *Adv. Mater. Technol.* **2022**, *7* (7), 1–11. <https://doi.org/10.1002/admt.202101514>.
- (9) Ghaderi, S.; Hosseini, H.; Haddadi, S. A.; Kamkar, M.; Arjmand, M. 3D Printing of Solvent-Treated PEDOT:PSS Inks for Electromagnetic Interference Shielding. *J. Mater. Chem. A* **2023**, *11* (30), 16027–16038. <https://doi.org/10.1039/d3ta01021j>.
- (10) Hill, I.; Hernandez, V.; Xu, B.; A. Piceno, J.; Misiaszek, J.; Giglio, A.; Junez, E.; Chen, J.; D. Ashby, P.; S. Jordan, R.; Wang, Y. Imparting High Conductivity to 3D Printed PEDOT:PSS. *ACS Appl. Polym. Mater.* **2023**, *5* (6), 3989–3998. <https://doi.org/10.1021/acsapm.3c00232>.
- (11) Jae Kim, Y.; Il Kim, S.; Kim, J.; Yun, J.; Hong, H.; Kim, J.; Ryu, W. 3D Printing of Thylakoid-PEDOT:PSS Composite Electrode for Bio-Photoelectrochemical Cells. *ACS Appl. Energy Mater.* **2023**, *6* (2), 773–781. <https://doi.org/10.1021/acsaem.2c03033>.
- (12) Kee, S.; Haque, M. A.; Corzo, D.; Alshareef, H. N.; Baran, D. Self-Healing and Stretchable 3D-Printed Organic Thermoelectrics. *Adv. Funct. Mater.* **2019**, *29* (51), 1905426. <https://doi.org/https://doi.org/10.1002/adfm.201905426>.

- (13) Ligon, S. C.; Liska, R.; Stampfl, J.; Gurr, M.; Mülhaupt, R. Polymers for 3D Printing and Customized Additive Manufacturing. *Chem. Rev.* **2017**, *117* (15), 10212–10290. <https://doi.org/10.1021/acs.chemrev.7b00074>.
- (14) Wynne, K. J.; Street, G. B. Conducting Polymers. A Short Review. *Ind. Eng. Chem. Prod. Res. Dev.* **1982**, *21* (1), 23–28. <https://doi.org/10.1021/i300005a005>.
- (15) Zhu, H.; Hu, X.; Liu, B.; Chen, Z.; Qu, S. 3D Printing of Conductive Hydrogel–Elastomer Hybrids for Stretchable Electronics. *ACS Appl. Mater. & Interfaces* **2021**, *13* (49), 59243–59251. <https://doi.org/10.1021/acsami.1c17526>.
- (16) Lopez-Larrea, N.; Criado-Gonzalez, M.; Dominguez-Alfaro, A.; Alegret, N.; del Agua, I.; Marchiori, B.; Mecerreyes, D. Digital Light 3D Printing of PEDOT-Based Photopolymerizable Inks for Biosensing. *ACS Appl. Polym. Mater.* **2022**, *4* (9), 6749–6759. <https://doi.org/10.1021/acsapm.2c01170>.
- (17) Scordo, G.; Bertana, V.; Scaltrito, L.; Ferrero, S.; Cocuzza, M.; Marasso, S. L.; Romano, S.; Sesana, R.; Catania, F.; Pirri, C. F. A Novel Highly Electrically Conductive Composite Resin for Stereolithography. *Mater. Today Commun.* **2019**, *19* (September 2018), 12–17. <https://doi.org/10.1016/j.mtcomm.2018.12.017>.
- (18) Scordo, G.; Bertana, V.; Ballezio, A.; Carcione, R.; Marasso, S. L.; Cocuzza, M.; Pirri, C. F.; Manachino, M.; Gomez, M. G.; Vitale, A.; Chiodoni, A.; Tamburri, E.; Scaltrito, L. Effect of Volatile Organic Compounds Adsorption on 3D-Printed Peda:Pedot for Long-Term Monitoring Devices. *Nanomaterials* **2021**, *11* (1), 1–15. <https://doi.org/10.3390/nano11010094>.
- (19) Jordan, R. S.; Frye, J.; Hernandez, V.; Prado, I.; Giglio, A.; Abbasizadeh, N.; Flores-Martinez, M.; Shirzad, K.; Xu, B.; Hill, I. M.; Wang, Y. 3D Printed Architected Conducting Polymer Hydrogels. *J. Mater. Chem. B* **2021**, *9* (35), 7258–7270. <https://doi.org/10.1039/D1TB00877C>.
- (20) Tao, Y.; Wei, C.; Liu, J.; Deng, C.; Cai, S.; Xiong, W. Nanostructured Electrically Conductive Hydrogels Obtained: Via Ultrafast Laser Processing and Self-Assembly. *Nanoscale* **2019**, *11* (18), 9176–9184. <https://doi.org/10.1039/c9nr01230c>.
- (21) Zhang, W.; Chen, J.; Li, X.; Lu, Y. Liquid Metal-Polymer Microlattice Metamaterials with High Fracture Toughness and Damage Recoverability. *Small* **2020**, *16* (46), 2004190. <https://doi.org/https://doi.org/10.1002/smll.202004190>.
- (22) Jackson, J. A.; Messner, M. C.; Dudukovic, N. A.; Smith, W. L.; Bekker, L.; Moran, B.; Golobic, A. M.; Pascall, A. J.; Duoss, E. B.; Loh, K. J.; Spadaccini, C. M. Field Responsive Mechanical Metamaterials. *Sci. Adv.* **2024**, *4* (12), eaau6419. <https://doi.org/10.1126/sciadv.aau6419>.
- (23) Meng, H.; Perepichka, D. F.; Wudl, F. Facile Solid-State Synthesis of Highly Conducting Poly(Ethylenedioxythiophene). *Angew. Chemie - Int. Ed.* **2003**, *42* (6), 658–661. <https://doi.org/10.1002/anie.200390181>.
- (24) Meng, H.; Perepichka, D. F.; Bendikov, M.; Wudl, F.; Pan, G. Z.; Yu, W.; Dong, W.; Brown, S. Solid-State Synthesis of a Conducting Polythiophene via an Unprecedented Heterocyclic Coupling Reaction. *J. Am. Chem. Soc.* **2003**, *125*

- (49), 15151–15162. <https://doi.org/10.1021/ja037115y>.
- (25) Zhou, L.; Gao, Q.; Fu, J.; Chen, Q.; Zhu, J.; Sun, Y.; He, Y. Multimaterial 3D Printing of Highly Stretchable Silicone Elastomers. *ACS Appl. Mater. Interfaces* **2019**, *11* (26), 23573–23583. <https://doi.org/10.1021/acsami.9b04873>.
- (26) Xie, R.; Mukherjee, S.; Levi, A. E.; Reynolds, V. G.; Wang, H.; Chabinyo, M. L.; Bates, C. M. Room Temperature 3D Printing of Super-Soft and Solvent-Free Elastomers. *Sci. Adv.* **2024**, *6* (46), eabc6900. <https://doi.org/10.1126/sciadv.abc6900>.

Chapter 4

Oligoaniline-Assisted Self-Assembly of Polyaniline Crystals

4.1 Abstract

The conductivity or charge transport mobility of conjugated polymers (CPs) is largely correlated with their degree of crystallinity, rendering the crystallization of CPs an important endeavour. However, such tasks can be challenging, especially in the absence of sidechain functionalization. In this study, we demonstrate that the incorporation of a small amount of oligomers, specifically tetraaniline, can induce crystallization of the parent polymer, polyaniline, through a single-step self-assembly process. The resulting crystals are compositionally homogeneous because oligomers and their parent polymer share the same repeating unit and are both electroactive. Mechanistic studies reveal that the tetraaniline forms a crystalline seed that subsequently guides the assembly of polyaniline due to their structural similarities. Applying this oligomer-assisted crystallization approach to polyaniline with defined molecular weights resulted in single crystalline nanowires for the 5,000 Da polyaniline, and nanowires with strong preferential chain orientation for those with molecular weights between 10,000 and 100,000 Da. Absorption studies reveal that the polymer chains are in an expanded conformation, which likely contributed to the high degree of packing order. Two-probe, single nanowire measurements show that the crystals have conductivity as high as 19.5 S/cm. This method is simple, general, and can potentially be applied to other CPs.

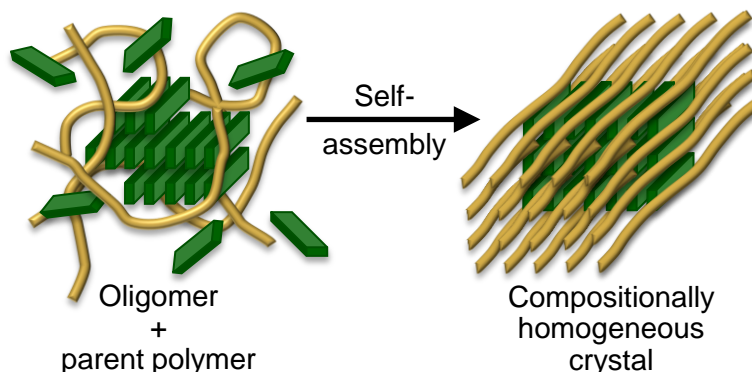


Figure 4.1. Summary figure for Oligoaniline-Assisted Self-Assembly of Polyaniline Crystals.

4.2 Introduction

Advancement in the understanding of the fundamental structure-property relationships of conjugated polymers (CPs), including conducting and semiconducting polymers, has fuelled the development of high performance organic electronics.^{1,2} Crystalline CPs, especially single crystals, are fundamentally important for understanding the charge transport properties in relation to packing arrangement and orientation. From an application-driven perspective, crystalline CPs are important for achieving high efficiency in organic electronics because they provide enhanced and directional conductivity or charge carrier mobility compared to their disordered or poorly crystalline counterparts³. Unfortunately, single crystals or crystals with strong preferential orientation of CPs are difficult to produce due to the rich free energy landscape compared to the soft chain polymer counterparts,^{4,5} but can be made possible through a few solution-based methods, such as side chain or backbone modification. Sidechain modification provides CPs with additional noncovalent interactions including van der Waals or solvophobic interactions through sidechain interdigitation or aggregation, thus leading to enhanced ordering.^{6,7} The steric effects from certain sidechains can also restrict the torsion angle between the repeating units along the polymer backbone, thus promoting ordered stacking. Directly increasing the backbone planarity such as by incorporating fused rings or alkyne groups can increase the persistence length of the polymer, and create enhanced intermolecular interactions.^{8,9} The same goal can be achieved by incorporating heteroatoms such as fluorine or sulfur along the polymer backbone to create additional intramolecular interactions that can “lock” the backbone conformation.^{10,11} In the absence of side chain or backbone engineering, ordered packing can be obtained by growing CPs from heterogeneous nucleation sites such as the surface of CNT.^{12,13} Due to the preferential π - π packing orientation of CPs on the π -conjugated surface of CNTs, CPs can pack in highly ordered fashion with the growth long axis perpendicular to the surface of the heterogeneous nucleation sites. Unfortunately, such methods only generate hetero-structures, essentially changing the chemical composition of the CPs.

Compared to sidechain-functionalized or backbone-modified CPs, crystallization of unmodified CPs such as polyaniline (PANI), polypyrrole (PPy), polythiophene (PT), or poly(3,4-ethylenedioxythiophene) (PEDOT) is especially challenging due to the high torsion angle between the adjacent repeating units and the limited noncovalent interactions beyond those offered by the π -faces.¹⁴ Vapor phase polymerization (VPP) has been the most successful in generating crystalline entities for such materials, but the resulting structures are usually semicrystalline with small crystallites embedded in disordered regions.^{15,16} It has been shown that VPP in combination with nanoconfinement within lithographically fabricated narrow channels can lead to single or polycrystalline PEDOT with very high conductivity.¹⁷

However, the degree of crystallinity is channel-width dependent. Also, channel fabrication requires multi-step lithography on a surface, limiting its scalability. Alternatively, through solution-based methods, crystals of unmodified CPs such as PANI can be synthesized through *in-situ* polymerization at the air-water interface in the presence of surfactants.¹⁸ The resulting 2D crystals can be scaled up to wafer-size by increasing the air-water interfacial area, but the scalability pales in comparison to bulk solution- or vapor-based methods. Regardless of the specific method, a major limitation to all *in-situ* polymerization approaches is that they do not offer the ability to separately control the degree of crystallinity and materials' chemical properties such as molecular weight or polydispersity. On the contrary, crystallization of pre-made CPs offer such explicit control because the chemical properties of the crystals are dictated through synthesis, whereas the packing order is controlled through crystallization.^{4,5} This distinct advantage makes post-synthetic crystallization approaches generally more favourable.

Here, we demonstrate a new concept on the crystallization of unmodified CPs. Using PANI as a model system, we achieve such feat through a simple, one-step self-assembly process in the presence of a small amount of oligomers of PANI, such as tetraaniline (TANI). The easily crystallizable TANI lowers the free energy barrier for the organization of PANI chains into ordered states through noncovalent intermolecular interactions. Both single crystals and crystals with strong preferential chain orientation have been obtained. Furthermore, due to the identical repeating units in oligomers and their parent polymer, the resulting crystals are compositionally homogeneous.

4.3. Experimental

4.3.1 Materials

Phenyl/amine-capped tetraaniline was synthesized via a previously reported procedure.¹⁹ Polyaniline without defined M_w was synthesized using a rapid mixing method²⁰ and purified by dialysis. Polyaniline of defined molecular weights (5,000, 10,000, 20,000, 50,000, 65,000, and 100,000 Da) in the emeraldine based form were purchased from Sigma-Aldrich. All organic solvents, acids, and dialysis tubing used in this study were obtained from Fisher Scientific.

4.3.2 Synthesis of phenyl/amine-capped tetraaniline (Ph/NH₂ TANI)

Ph/NH₂ TANI was synthesized following previously reported procedure with modified purification steps.¹⁹ 50 mmol of *N*-phenyl-1,4-phenylenediamine that was crushed using a mortar and pestle, was sonicated for 2 hours in a 250 mL 0.1 M HCl solution. A stoichiometric amount of iron(III) chloride was dissolved in a 50 mL 0.1 M HCl solution, and was rapidly added to the dimer mixture while being stirred

strongly with a mechanical stir rod. The mixture was allowed to react for 2 hours. Centrifugation was then used to wash the mixture with 300 mL 0.1 M HCl, followed by 450 mL 0.1 M NaOH to dedope tetraaniline and 3 L of deionized water. The crude product was dried under high vacuum. The dedoped crude product was reduced by dissolving it in 200 mL of 200 proof ethanol, followed by the addition of four equivalents of hydrazine monohydrate, which was allowed to stir overnight. The mixture was precipitated by adding 2 L deionized water, and the solid was collected using filtration. Impurities were removed by repeated mixing with 200 proof ethanol, centrifugation, and removal of the supernatant until the leucoemeraldine tetraaniline was isolated. Ethanol was then removed using high vacuum. The reduced tetraaniline was oxidized to the emeraldine base form by crushing and sonication in a 1 M HCl solution, followed by rapid addition of a solution of one equivalent of ammonium persulfate in 10 mL 1 M HCl, which was then stirred overnight. The mixture was dedoped by adding 1 M ammonium hydroxide, followed by repeated centrifugation with deionized water until the pH was neutral. The product was dried, then purified by filtering over a large plug of silica eluting with hexane, then ethyl acetate, and was repeated until the product was pure. The identity was confirmed using thin layer chromatography (TLC) and UV-vis-NIR (near-infrared) spectroscopy.

4.3.3 Self-assembly

Tetraaniline and polyaniline were ground into fine powder using agate mortar and pestle. In a typical process, 2 mg of powder comprised of TANI and PANI at the desired ratio were individually weighed out using a microbalance and then combined. The powder mixture is then added to a solvent mixture comprised of 1 mL of organic solvent such as THF and 4 mL of an aqueous acidic solution such as 0.1 M HClO₄. The mixture is swirled rapidly for a few seconds and left undisturbed for 5 days for the self-assembly process to occur. At the end of the process, dialysis was performed against deionized water for approximately 1 day to purify the products.

4.3.4 Electron microscopy

Scanning electron microscopy (SEM) analysis was performed using a JEOL JSM-6700 SEM or Zeiss Gemini 500 SEM on samples drop casted on silicon wafers. Transmission electron microscopy (TEM) samples were prepared by depositing a drop of the nanomaterial dispersion onto a TEM grid placed on top of filter paper. These samples were loosely covered and left to air dry overnight. Due to the high sensitivity of PANI to electron beam due to ionization and heating damage, cryogenic TEM and selected area electron diffraction (SAED) was performed. TEM samples were kept under dynamic vacuum overnight to completely remove moisture. They were rapidly frozen using liquid nitrogen and kept at liquid nitrogen temperature using a cryogenic sample holder during the

duration of imaging. TEM images and SAED patterns were collected on either a FEI/PHILIPS CM 120 TEM or a Talos F200C G2 TEM, operated under cryogenic conditions with an accelerating voltage of 200 kV. Au standards were used for SAED calibration.

4.3.5 Spectroscopic characterization

UV-vis-NIR of the dispersions were collected on a Shimadzu UV-3600 Plus. A quartz cuvette with a 1 mm path length was used to minimize water absorbance in the NIR region. ATR-IR spectra were obtained on a Bruker Vertex 70 spectrometer (ATR mode, diamond window).

4.3.6 Single wire measurement

Microelectrodes were fabricated via photolithography on a Si/SiO₂ wafer with 300 nm of SiO₂ layer followed by thermal evaporation of 5 nm of Cr and 90 nm of Au. A few drops of the dispersion were deposited on the microelectrode array. After a few seconds for the nanowires to settle, the wafer was tilted and the excess droplet was removed and blown dry by gently flowing nitrogen over the surface with a pressurized nitrogen gun. Measurements were carried out on freshly prepared samples using a Lakeshore semiconductor probe station under ambient conditions.

4.4 Chemical characterization of phenyl/amine-capped tetraaniline (Ph/NH₂ TANI)

The Ph/NH₂ TANI oligomer displayed FT-IR signals that are characteristic to polyaniline and many other aniline oligomers (Figure 4.2).²¹⁻²³ The characteristic peaks include the quinoid C=C stretching at around 1587 cm⁻¹, the benzoid C=C stretching at 1494 cm⁻¹, the C-N stretching of secondary aromatic amines at 1293 cm⁻¹, and the aromatic C-H out-of-plane bending at 831 and 744 cm⁻¹. A notable strong N-H stretching signal is present at 3372 cm⁻¹, which can be attributed to TANI's secondary amines, as well as the terminal primary amine groups. Although the sample was vacuum dried before analysis, there is still a trace amount of water which appears as a broad peak from the O-H stretching at 3324 cm⁻¹.

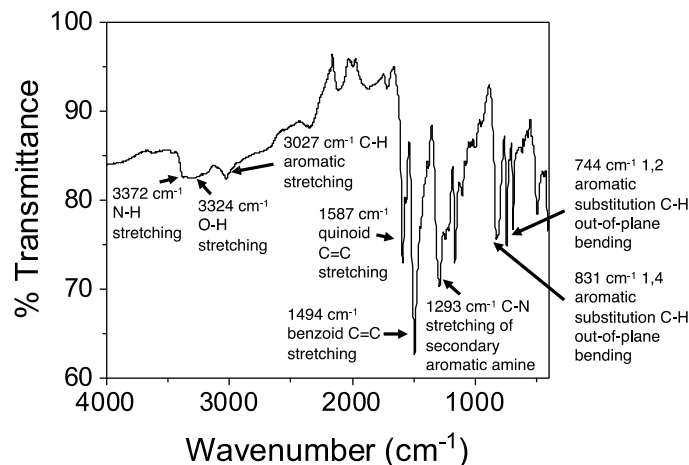


Figure 4.2. FT-IR spectrum with peak assignments of phenyl/amine-capped TANI.

4.5 Results and discussion

4.5.1 Conceptual demonstration

The rationale behind this project is the following. (1) The difficulty in crystallizing CPs, especially for unmodified CPs such as PANI, lies in their rich free energy landscape and the entropic barriers for chain rearrangement from disordered to ordered states. (2) Unlike CPs such as PANI, their oligomers such as TANI can easily crystallize into single crystals.^{19,24} This is because the free energy barrier for forming long-range order for oligomers is significantly lower than polymers owing to the short chain length of oligomers. (3) Oligomers and the parent polymers share the same chemical repeating units (e.g., TANI vs. PANI, shown in Figure 4.3a-b), so the intermolecular interactions between them would be identical to those between adjacent oligomers or adjacent polymer chains. Combining these rationales, we hypothesized that adding a small amount of oligomers to the crystallization of the parent polymers may decrease the free energy barrier for “straightening out” the polymer chains and facilitating their packing in a similar manner to the oligomers.

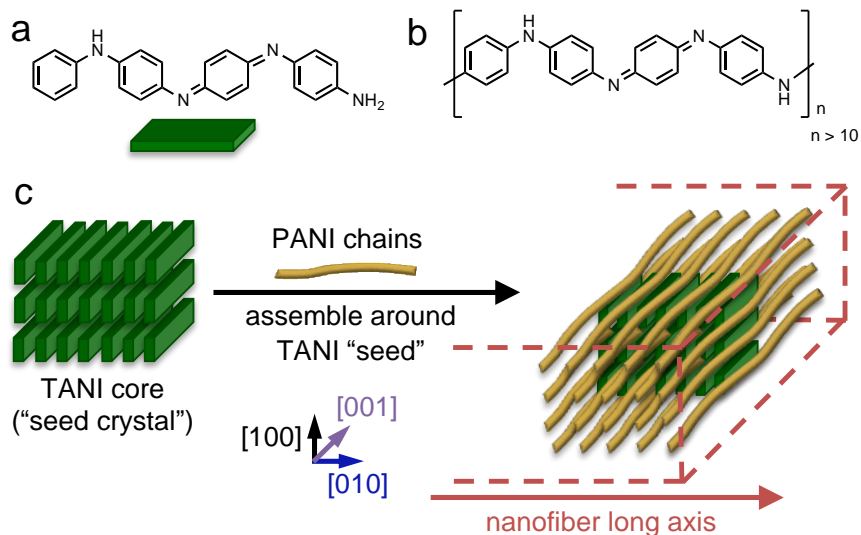


Figure 4.3. Chemical structures of (a) tetraaniline and (b) polyaniline. (c) Schematic diagram showing the mechanism behind TANI-assisted PANI assembly.

To probe this hypothesis, we mixed 20% of TANI into PANI, both in the dedoped, emeraldine base (EB) oxidation state, and added the mixture to a self-assembly solvent environment comprised of a 1:4 mixture of THF and 0.1 M HClO₄ (aq.). The mixture is left undisturbed to self-assemble over the course of 5 days. Prior to self-assembly, the as-used PANI powder in the EB form has a low aspect-ratio nanofibrous morphology (Figure 4.4c), and the TANI EB powder has an irregularly shaped, agglomerated morphology (Figure 4.11a). When TANI by itself is subjected to the self-assembly solvent environment, rigid and crystalline nanowires are obtained (Figure 4.4b), consistent with our previous findings. With the solid composition comprised of 80% PANI and 20% TANI, high aspect ratio, nonwoven nanowires are obtained (Figure 4.4c). The self-assembly process can be seen visually: the initial dark blue powder that settles at the bottom of the vial gradually turns green, indicative of TANI and/or PANI transitioning into the doped emeraldine salt (ES) form. The mixture slowly migrates into the surrounding medium through the self-assembly process, giving the precipitate a fluffy appearance. Upon purification via dialysis against deionized water, a stable dispersion can be formed by simple agitation (Figure 4.4f). The resulting nanowires are typically tens of microns long with an average diameter of 20-30 nm (Figure 4.7). (SAED) of these nanowires shows weak scattering arcs along the wire long axis, suggesting the preferential orientation of chains (Figure 4.5). The scattering arcs correspond to a d-spacing of 0.36 nm, characteristic to the intermolecular distance of π - π stacking along the [010] direction.⁴ This finding

indicates that π - π stacking could be a main driving force for the self-assembly of TANI/PANI, leading the nanowires to preferentially grow along this direction. Hydrogen bonding between amine groups has also likely aided in stabilizing the packing arrangement. We thereafter refer to these crystalline nanostructures as tetraaniline-assisted self-assembled polyaniline, abbreviated as TAS-PANI.

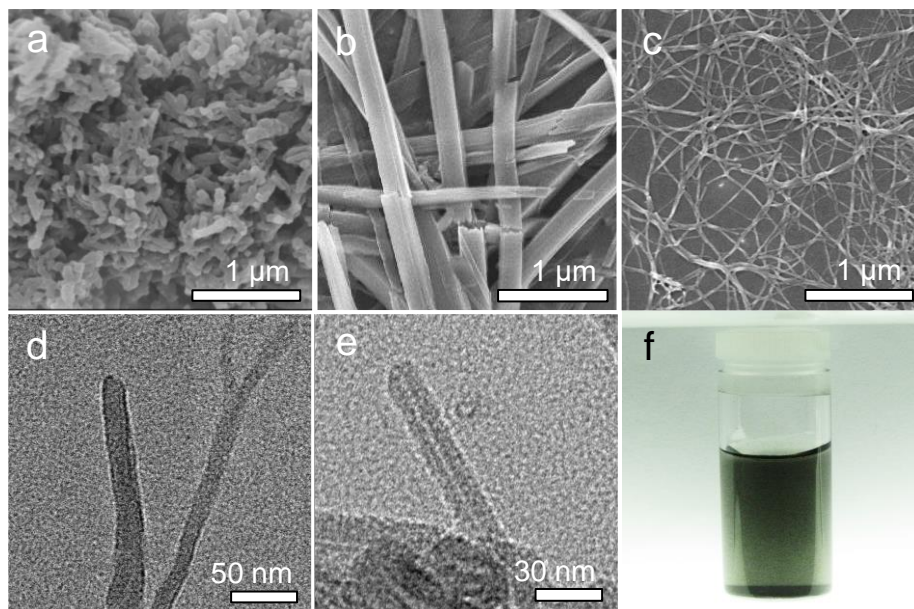


Figure 4.4. SEM images of (a) PANI nanofibers, (b) TANI nanowires, (c) self-assembled high aspect ratio PANI nanofibers containing 20% TANI (TAS-PANI). (d) TEM image of TAS-PANI. (e) TAS-PANI after acetone wash to remove TANI. (f) Photograph showing an aqueous dispersion of TAS-PANI.

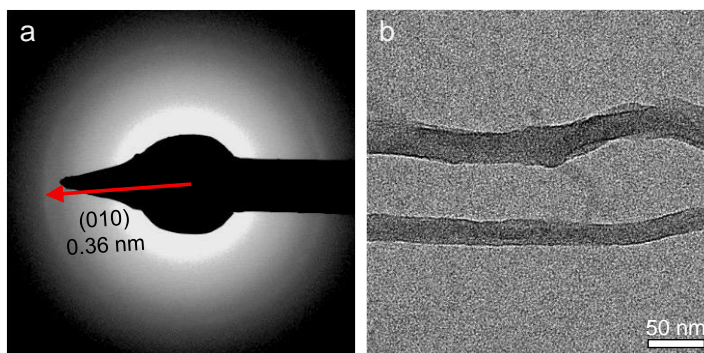


Figure 4.5. (a) Selected area electron diffraction (SAED) pattern and (b) the corresponding TEM image for self-assembled TAS-PANI-NF (PANI NF with 20% TANI). The packing diagram in Figure 4.3c is schematized based on the SAED data here. The scattering arcs have a spacing of 0.36 nm, corresponding to π - π stacking, indicating that TANI and PANI interact and assemble perpendicular to the long axis of the nanowires through π - π stacking. The weak scattering arcs indicate

that the degree of order is likely not strong. However, polymeric materials are sensitive to electron beams, so a certain level of beam damage may have also led to the weak scattering.

4.5.2 Mechanistic understanding

To understand the role of TANI in assisting the self-assembly of PANI, we soaked the isolated TAS-PANI nanowires in a copious amount of acetone overnight. TANI is soluble in acetone, but PANI has no solubility in it due to the significantly higher molecular weight. Therefore, the acetone wash would selectively remove the TANI component and leave behind PANI. Transmission electron microscopy (TEM) shows that the pristine TAS-PANI exhibits a solid interior (Figure 4.4d). However, a thin cavity can be clearly observed under TEM for the TAS-PANI nanowires after the solvent wash (Figure 4.4e). This result indicates that the small amount of TANI molecules likely first assemble into a crystalline core due to their propensity to crystallize (Figure 4.3c). PANI does not self-assemble in the absence of TANI (Figure 4.6i). Subsequently, due to the structural similarity between TANI and PANI, the disordered PANI chains would interact with the ordered TANI core, leading PANI chains to assemble along the same preferential stacking direction of TANI (Figure 4.3c).

With these experimental insights, the following self-assembly mechanism is unearthed. Neither TANI nor PANI is soluble in aqueous acidic solutions, but both can be doped in this environment. In the dedoped EB form, TANI is highly soluble whereas PANI is moderately soluble in polar organic solvents such as THF. Therefore, the solvent mixture used here offers partial solubility for PANI EB and TANI EB, which is generally considered a desirable condition for crystallization via self-assembly.²⁵ At the same time, the HClO₄ acid in the solvent mixture can dope PANI and TANI into their emeraldine salt (ES) forms, which have no and limited solubility in THF, respectively, and no solubility in water. Therefore, both PANI and TANI gradually lose solubility in the solvent mixture as increasing portions of them get protonated into the ES states, leading to interchain association due to solvophobic effects.

Due to the different solubilities of TANI and PANI in the EB states in the solvent mixture, there is likely a difference in the degree or rate of solvation and self-assembly, making the assembly of TANI and PANI sequential rather than concurrent. TANI has higher solubility in THF than PANI, so the 20% THF in the solvent mixture would first solvate mostly TANI. Once the TANI molecules are brought into the solvent mixture, they would get doped by the HClO₄ acid and transition into the protonated ES form that has marginal solubility in THF/water mixtures. Therefore, supersaturation is quickly reached, causing the TANI

molecules to aggregate through solvophobic, π - π , electrostatic, and hydrogen bonding interactions to minimize their interaction with solvent molecules.^{4,19,26} Ordered TANI cores are therefore formed and subsequently serve as nucleation centers for PANI assembly. Due to the lower solubility of PANI in THF, the same solvation-doping-precipitation-aggregation process occurs at a slower rate for PANI than that of TANI. As doped PANI chains are precipitated out from the solvent mixture, it is more energetically favourable for them to adhere to the existing heterogeneous nucleation centres of TANI “seed crystals” than spontaneously forming new homogenous nucleation centres. Therefore, PANI assembles around the TANI core. The π - π and other noncovalent interactions between the chemically identical oligomer and polymer leads PANI to adopt an extended chain conformation, facilitating PANI to stack along the same [010] long axis as TANI, leading to 1D nanowires with preferential ordering. We found that using other polar organic solvents such as dimethyl sulfoxide (DMSO) or other acids such as diluted nitric acid also leads to similar results (Figures 4.8 and 4.9). This proposed mechanism is analogous to that behind crystallization by self-seeding. Self-seeding is mostly used in the molten state for soft chain polymers such as polyethylene,²⁷ but has been applied to creating single crystals of poly(3-hexylthiophene) (P3HT) from its solution.²⁸ This process takes advantage of the slightly different solubility of amorphous versus crystalline domains of the same polymer in marginal solvents at elevated temperatures. When the solution is heated to such a temperature, the disordered domains of P3HT would dissolve in the solvent, but the highly ordered crystallites would remain intact because the ordered, tight packing makes solvent diffusion more difficult. Therefore, these undissolved crystallites serve as heterogeneous nucleation sites for crystal growth upon the cooling of the solution, leading to controlled growth of crystals. While mechanistically similar, our oligomer-assisted approach is conceptually and experimentally different. The addition of predetermined percentage of monodispersed oligomers allows our process to create such heterogeneous nucleation sites at room temperature using mostly water, an environmentally friendly solvent, and incorporate the dopant acid in the crystallization process. This is particularly useful for unmodified CPs like PANI or PEDOT because of their low solubility in common solvents.

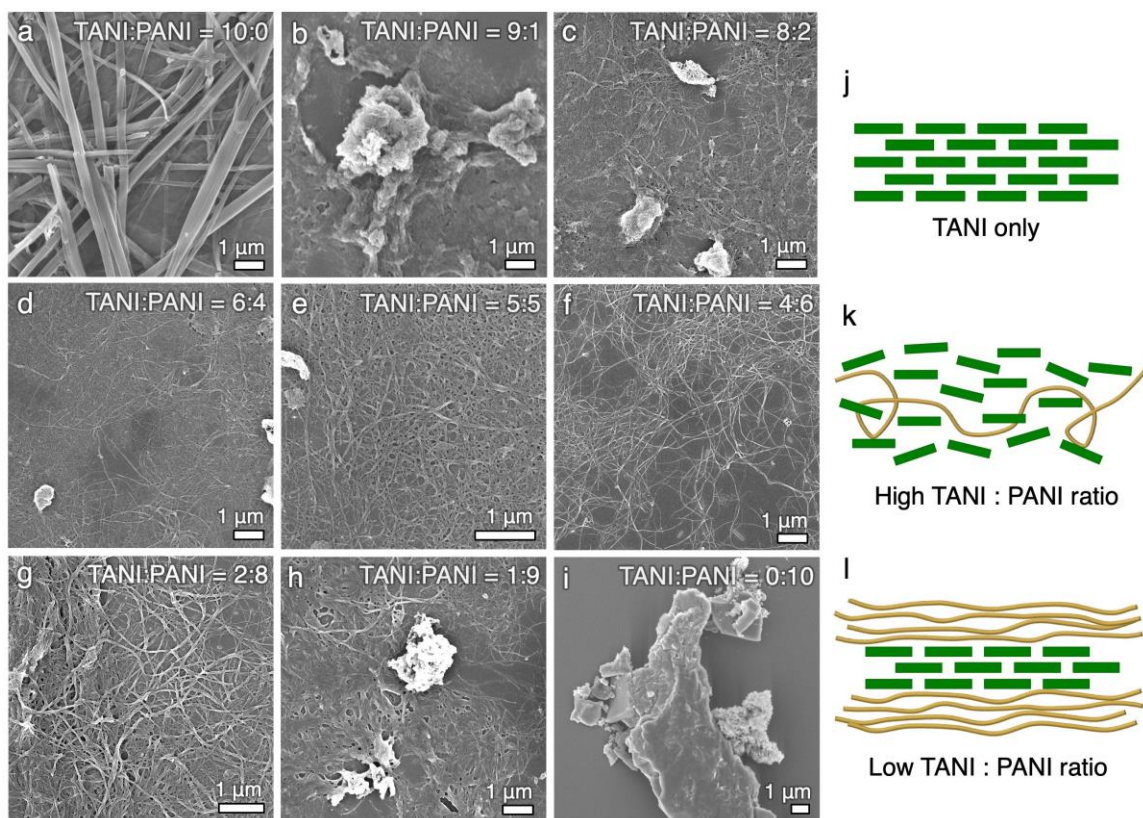


Figure 4.6. (a)-(i) SEM images of TANI and TAS-PANI self-assembled at different TANI:PANI ratio in a solvent mixture of 20% THF and 80% 0.1 M HClO₄. (j)-(l) Schematic diagrams illustrating the proposed mechanism behind the relationship between TANI:PANI ratio and the packing order.

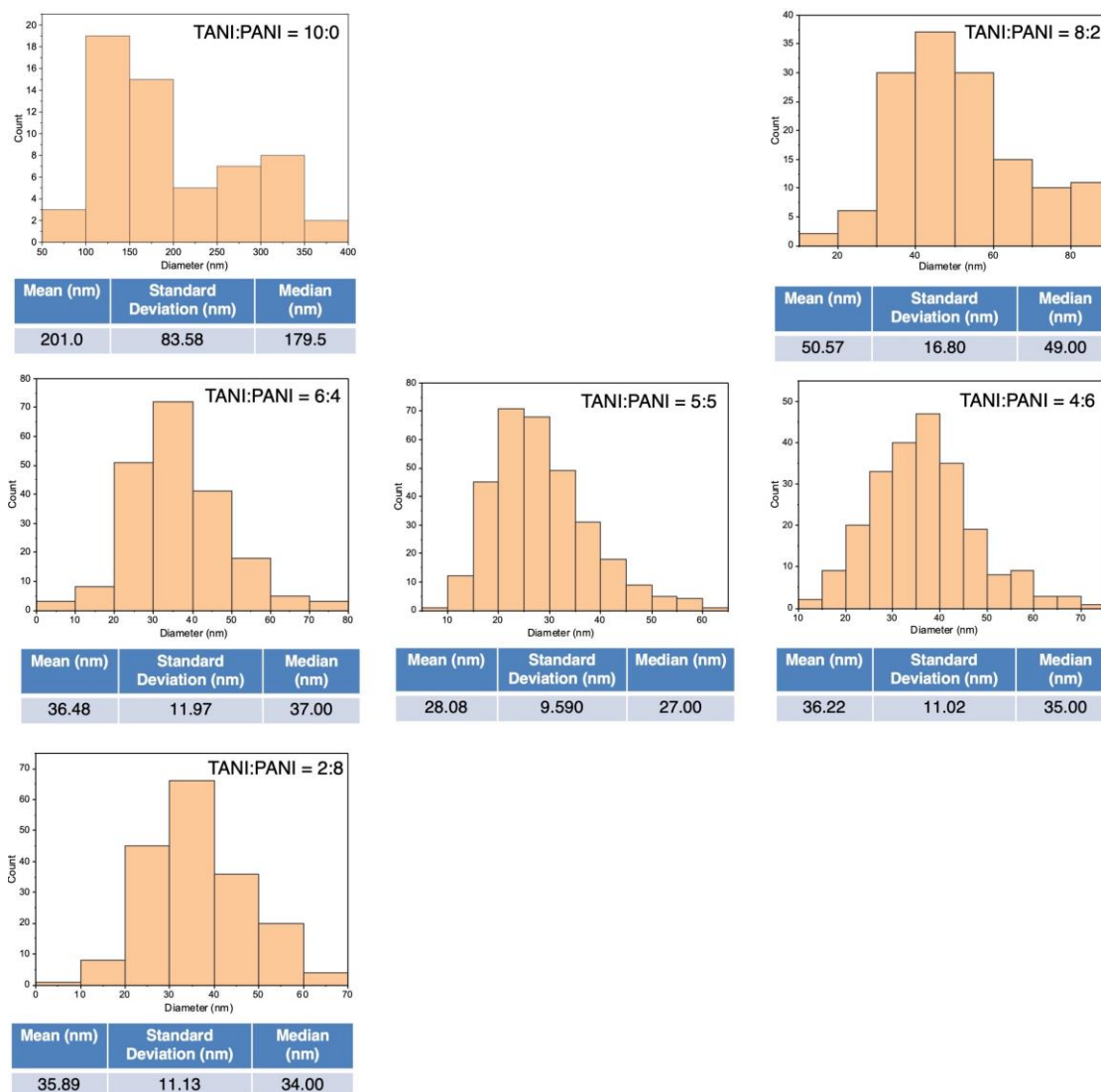


Figure 4.7. Diameter analysis of TAS-PANI self-assembled at different TANI:PANI ratios (Figure 4.6). Samples corresponding to TANI:PANI ratios of 9:1 (Figure 4.6b), 1:9 (Figure 4.6h), and 0:10 (Figure 4.6i) exhibit agglomerated morphology, so their diameter analyses are not included here.

To further understand the self-assembly mechanism, we systematically varied the ratio between TANI and PANI in the self-assembly process. We anticipated that a higher percentage of TANI would lead to better-defined structures due to TANI's high propensity to crystallize. To our surprise, the system with the highest TANI content (90% TANI and 10% PANI) only leads to irregularly shaped agglomerates (Figure 4.6b). The morphology of the nanowires gradually become better-defined as the PANI content is increased, with the 4:6 and 2:8

TANI:PANI ratio leading to morphologies that are the most well-defined (Figure 4.6f-g). Further increasing the PANI content to 90% generates agglomerates and poorly defined structures again (Figure 4.6h). The same trend is observed in TAS-PANI systems using other organic/acidic aqueous solvent combinations (Figures 4.8 and 4.9).

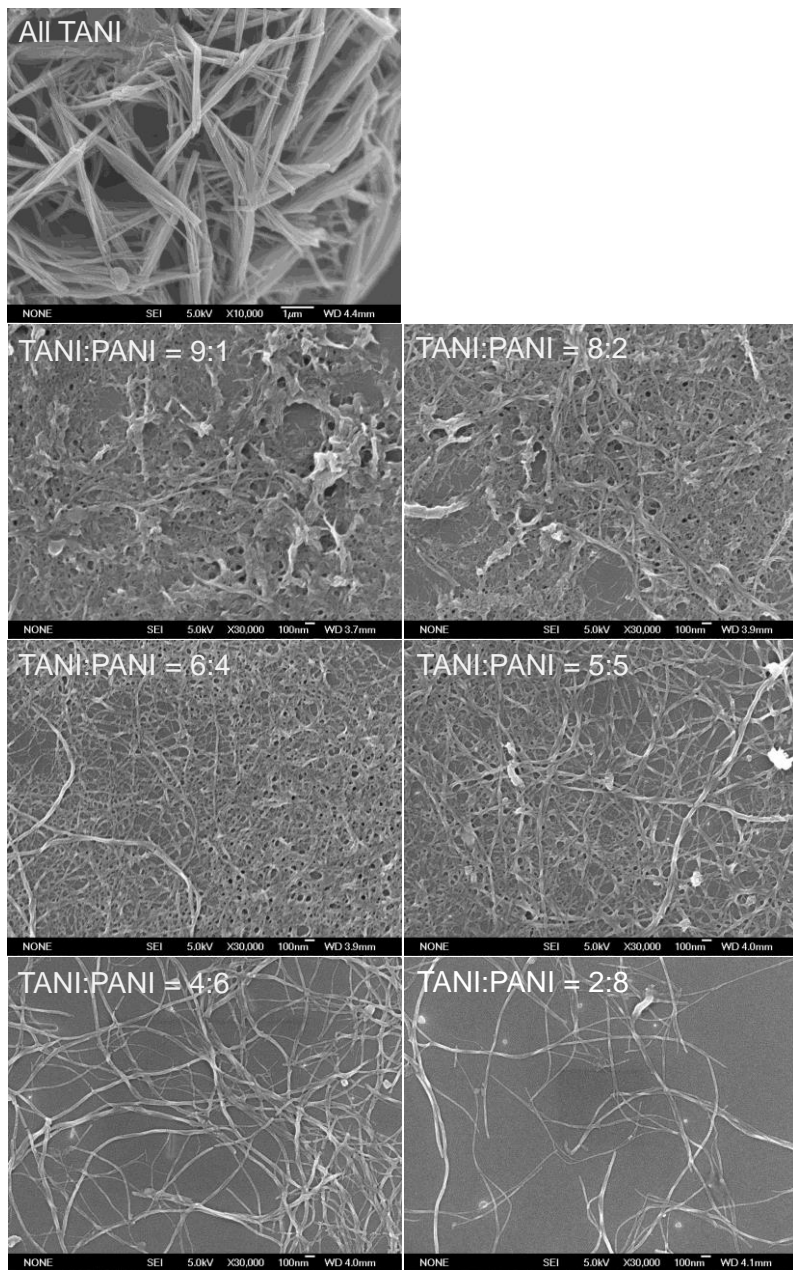


Figure 4.8. SEM images of TANI and TAS-PANI-NF self-assembly at different TANI:PANI ratio in a solvent mixture of 20% DMSO and 80% 0.1 M HClO₄.

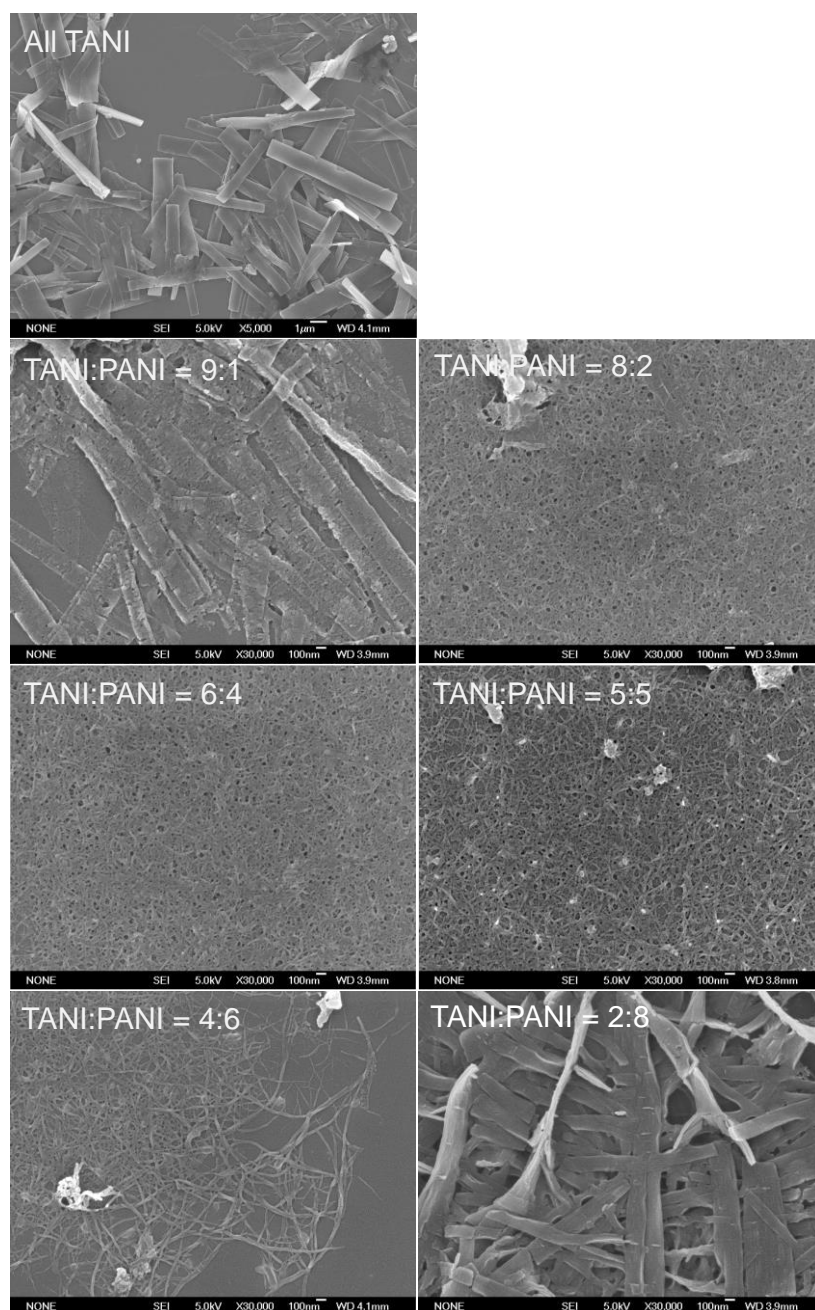


Figure 4.9. SEM images of TANI and TAS-PANI-NF self-assembly at different TANI:PANI ratio in a solvent mixture of 20% ethanol and 80% 0.1 M HClO₄.

Based on these observations, we conjecture that when there is a low concentration of PANI and a high concentration of TANI (e.g., 9:1 TANI:PANI ratio, Figure 4.6b), PANI serves as “impurities” that drastically increases the

polydispersity of TANI, thus disrupting the packing of TANI, leading to disordered structures with no defined supramolecular morphology (Figure 4.6k). On the contrary, when PANI content is beyond a certain concentration (i.e., beyond 50%), PANI becomes the major phase rather than impurities to TANI, which allows TANI to self-assemble into the “seed crystals” through the aforementioned mechanism, facilitating the ordered assembly of PANI (Figure 4.6l). Furthermore, it is possible that in addition to TANI cores serving as heterogeneous nucleation sites for PANI assembly, TANI is playing a more direct role in “straightening out” PANI chains. Unlike TANI, which can easily rotate and adopt to lattice sites, the doped PANI chains have to overcome a cascade of free energy barriers such as disentanglements and intramolecular interactions in order to transition to an extended chain conformation to form crystals.^{4,5} With the addition of a small amount of TANI, some of the TANI molecules that are still in solution can interact with PANI through π - π and other noncovalent interactions. This interaction essentially “dilutes” the PANI chains, shielding them from intramolecular interactions, leading to a more expanded chain conformation through disentanglement. The TANI-decorated segments of PANI would also lead the resulting complexes to become more rigid than PANI due to the increased segmental rigidity and diameter of the complexes. In fact, in examining the TEM images of TAS-PANI nanowires made using a 2:8 TANI:PANI ratio that have been washed with acetone post-assembly (Figure 4.4e), the diameter ratio between the cavity left by the removal of TANI to the remaining PANI shell is about 1:8, supporting our proposed mechanism that some of the TANI forms the nucleation centre, while some other TANI molecules “solubilize” the PANI chains and may have been co-crystallized with PANI in the nanowire shells, facilitating their ordered packing. This mechanism is analogous to work in parallel fields such as using graphene oxide to disperse carbon nanotubes (CNT) or surfactants to induce the assembly of molecular semiconductors.^{29,30} However, unlike these studies, no impurity is introduced in our system due to structure identity between TANI and PANI.

The most well-defined nanowires with the highest aspect ratios are obtained with TANI:PANI ratios of 4:6 and 2:8 (Figure 4.6f-g). Since the goal of this project is to use TANI to assist the crystallization of PANI, we use the 2:8 TANI:PANI ratio for the subsequent studies to maximize the PANI content in the system.

4.5.3 TANI-assisted crystallization of PANI with defined molecular weights

Compared to other methods, such as vapor phase polymerization, that can generate crystalline structures for unmodified CPs,¹⁵⁻¹⁷ the most significant advantage of using self-assembly to achieve crystalline structures is that we can separately control the chemical properties and the degree of crystallinity of the polymers. The former can be controlled through synthesis, whereas the latter can

be tuned by the assembly or crystallization process. As a proof-of-concept, we choose molecular weight (MW) as an example of chemical property.

PANI with relatively well-defined weight average molecular weight (M_w) of 5,000, 10,000, 20,000, 50,000, 65,000, and 100,000 Da are commercially available in the EB form. Subjecting them to the self-assembly process with the same solvent environment in the absence of TANI only yields large, irregularly shaped agglomerates (Figure 4.11, insets to Figure 4.10). However, when 20% of TANI is incorporated into the system, PANI of all six M_w self-assemble into well-defined 1D nanostructures (Figure 4.10). These TANI-assisted self-assembled nanostructures are abbreviated as TAS-PANI-5k, TAS-PANI-10k, TAS-PANI-20k, TAS-PANI-50k, TAS-PANI-65k, and TAS-PANI-100k, with the last component in the acronym indicating the average M_w of PANI.

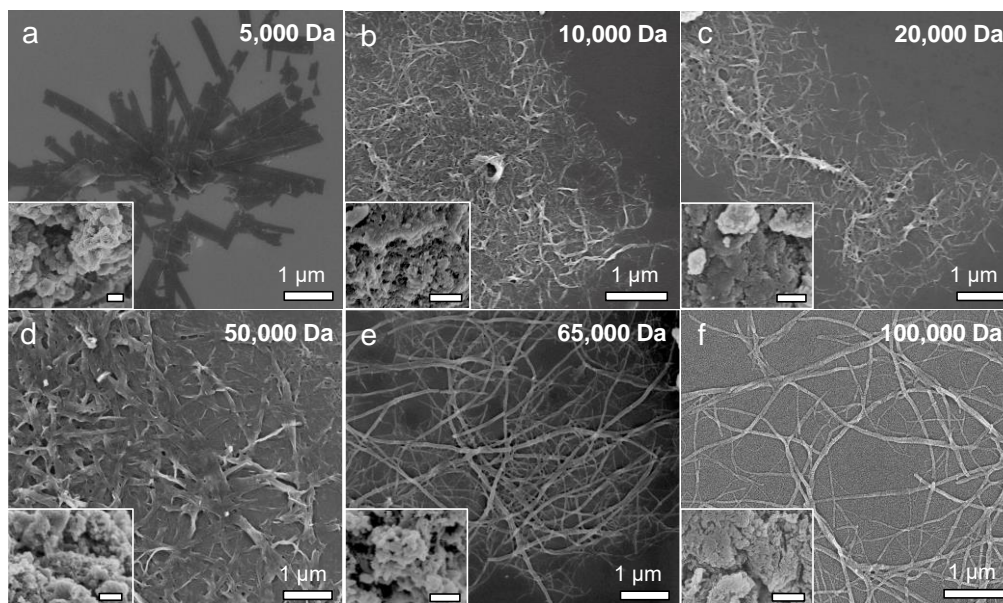


Figure 4.10. SEM images of 20% TANI-assisted self-assembled nanostructures of PANI with defined molecular weight: (a) 5,000 Da, (b) 10,000 Da, (c) 20,000 Da, (d) 50,000 Da, (e) 65,000 Da, (f) 100,000 Da. The inset to each SEM shows PANI of the same molecular weight subjected to identical self-assembly environment in the absence of TANI. The scale bars in the insets are 1 μm .

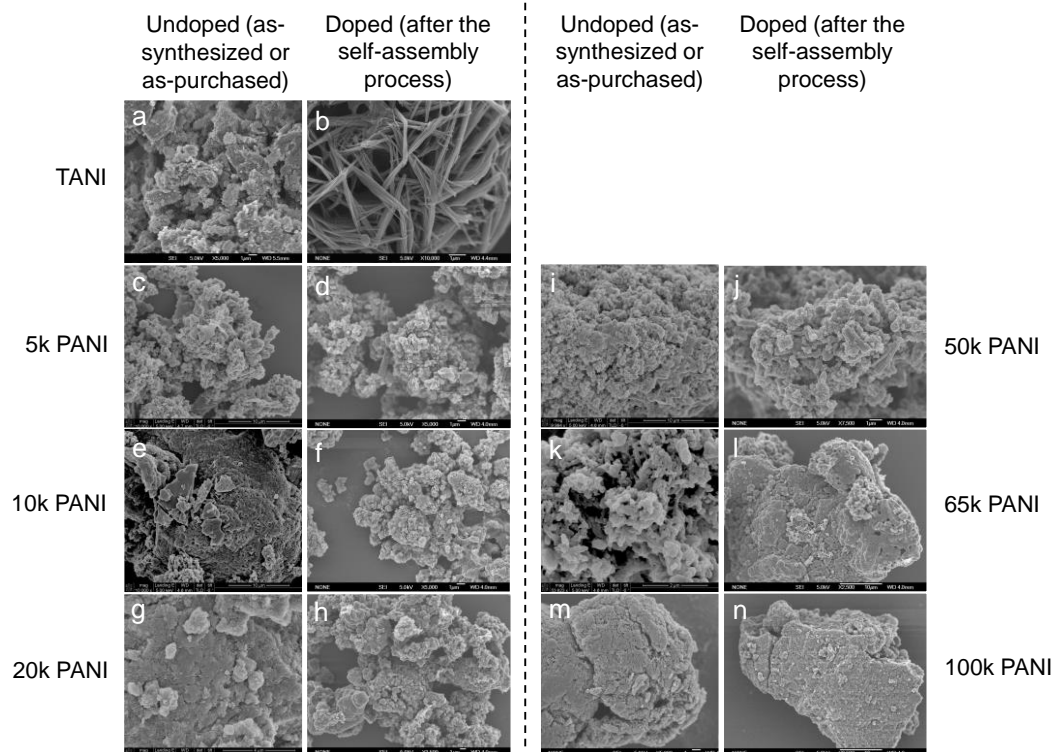


Figure 4.11. SEM images of TANI and PANI with various molecular weights in the as-synthesized (TANI) or as-purchased (PANI) forms vs. after self-assembly in a solvent mixture of either 20% THF and 80% water (the undoped columns) or 20% THF and 80% 0.1 M HClO₄ (the doped columns).

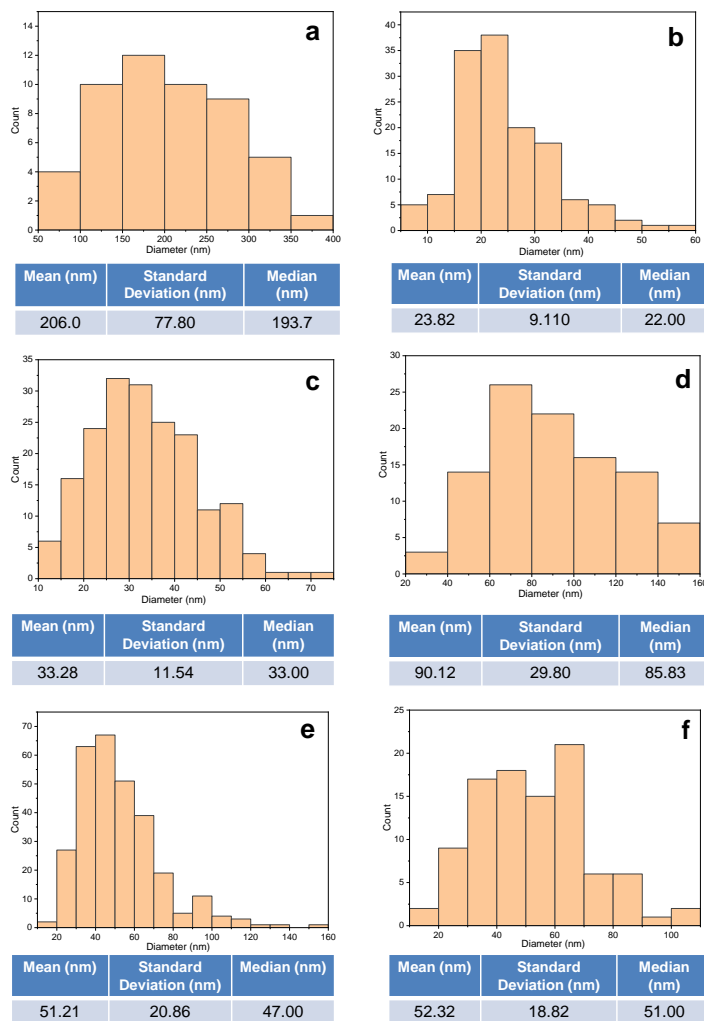


Figure 4.12. Diameter analysis of 20% TANI-assisted self-assembled nanostructures of PANI with defined molecular weight (Figure 4.10): (a) 5,000 Da, (b) 10,000 Da, (c) 20,000 Da, (d) 50,000 Da, (e) 65,000 Da, (f) 100,000 Da.

To better understand the correlation between the M_w of PANI and crystallinity of the nanostructures, SAED was performed on each sample (Figure 4.13). CPs are known to be electron-beam sensitive and typically suffer from heating damage during SAED collection.^{31,32} Doped CPs such as PANI in this study are positively charged, making them additionally prone to ionization damage from the negatively charged electron beam. Such radiation damage would cause bond breakage, which in turn result in radical formation and loss of packing periodicity.^{31,32} Unsurprisingly, our initial attempts in collecting SAED on the TAS-PANI samples under ambient conditions did not generate any diffraction patterns. To overcome electron beam damage, cryogenic condition was employed

in combination with low dose exposure in the imaging and diffraction of TAS-PANI nanostructures of all molecular weights. The samples remain beam sensitive under such conditions, but the diffraction pattern would last for a few seconds before gradually fading away, which is sufficient for data collection.

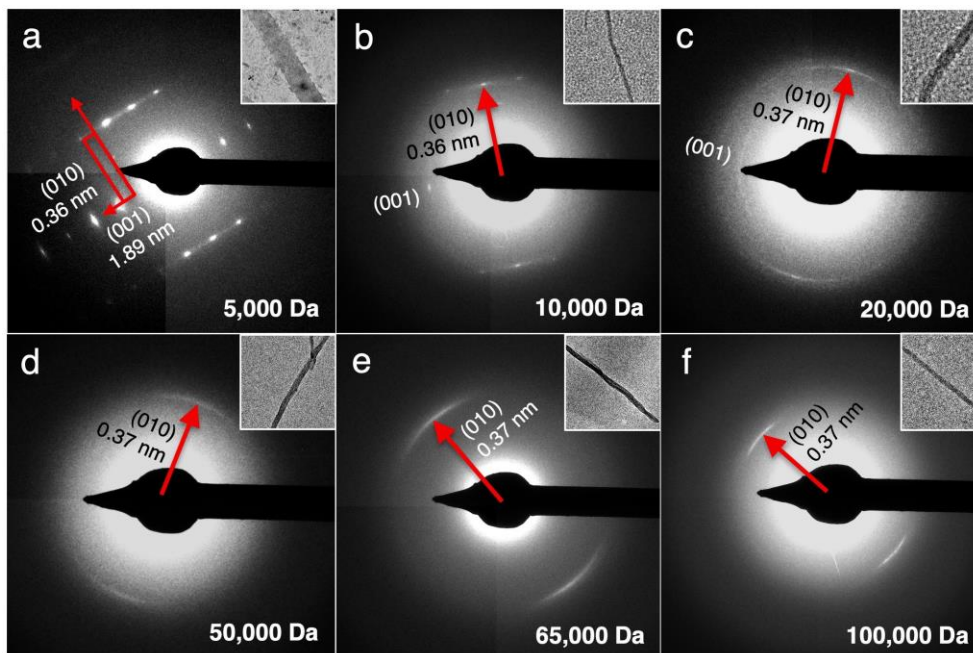


Figure 4.13. Select area electron diffraction (SAED) patterns of 20% TANI-assisted self-assembled nanostructures of PANI with defined molecular weight: (a) 5,000 Da, (b) 10,000 Da, (c) 20,000 Da, (d) 50,000 Da, (e) 65,000 Da, (f) 100,000 Da. These patterns are collected under cryogenic conditions. The inset to each SAED shows the TEM image of the nanoribbon/nanowire that corresponds to the SAED.

Comparison of the SAED patterns to their corresponding bright-field TEM images in the insets reveals that the preferential crystal growth direction, regardless of PANI M_w , is always along the [010] direction, indicating that the growth rate is the fastest along this facet. The spacing along [010] corresponds to π - π stacking,²⁴ suggesting that the π - π interaction between the repeating aniline units is likely a main mechanism in driving the self-assembly process. The π - π stacking distance increases slightly from 0.36 to 0.37 nm with increasing PANI M_w , likely due to the increasing entropic barriers to rearrange longer polymer chains, thus making the intermolecular packing less efficient. Most notably, clearly defined Bragg diffraction spots along both the (010) and (001) planes are observed in the SAED pattern for the TAS-PANI-5k nanoribbons, indicating that they are single crystalline with consistent and regular packing conformation (Figure 4.13a). SAED patterns collected over larger areas containing

multiple TAS-PANI-5k nanoribbons show spotty ring patterns (Figure 4.14), which is a result of overlapping Bragg spot patterns in various orientations. This further confirms the single crystalline nature of the TAS-PANI-5k nanoribbons. The d-spacing between the (00 l) planes is 1.89 nm, corresponding to the approximate length of 4 repetitions of aniline units along the PANI backbone.²⁰ The systematic odd absences along the (00 l) planes are consistent with glide symmetry, which indicates a possible alternating packing arrangement of the repeating units.

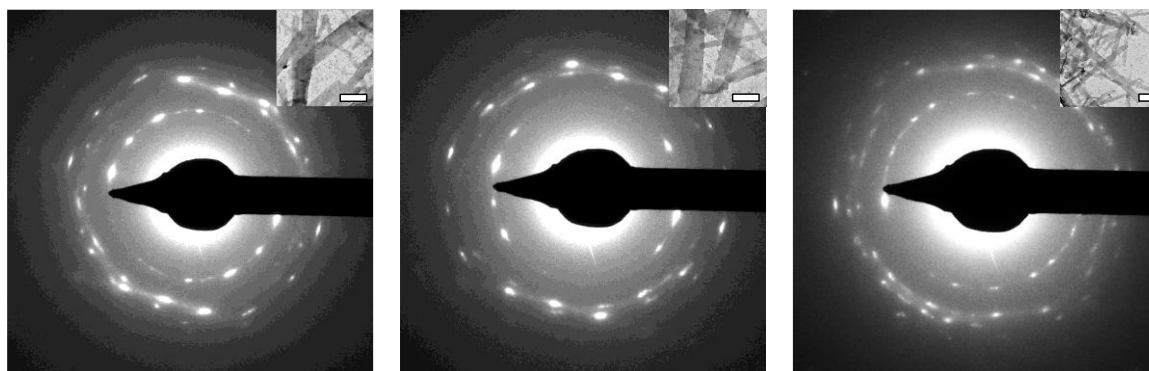


Figure 4.14. Select area electron diffraction (SAED) patterns of clusters of TAS-PANI-5k nanoribbon from different areas and samples. Insets show the corresponding TEM images. Scale bar = 500 nm. The SAED for a single TAS-PANI-5k nanoribbon is shown in Figure 4.13a, which indicates that these nanoribbons are single crystals. Similar results are obtained for over ten nanoribbons across multiple samples. To further confirm the representativeness of such results, we collected SAED patterns over large areas that contain multiple overlapping TAS-PANI-5k nanoribbons (insets in this figure). In all these SAED patterns, spotty rings are observed, which are results of the overlapping diffraction patterns of individual nanostructures. The discrete diffraction spots in these patterns confirm that a very high percentage, if not all, of the TAS-PANI-5k nanoribbons are single crystalline.

With increasing PANI MW, the SAED patterns gradually transition from Bragg diffraction spots to diffraction arcs, indicative of preferential orientation of polymer chains.^{4,5} For TAS-PANI-10k, Bragg diffraction spots for (010) are still present, but the intensity is streaked between the adjacent spots, indicating some degree of disorder in an otherwise well-packed crystal. As the PANI M_w is increased to 20,000 Da, spotty arcs are observed, suggesting that packing within TAS-PANI-20k is less ordered than the 10k counterpart. An increase in π - π stacking spacing from 0.36 to 0.37 nm along (010) is also observed between the M_w weight transition here, further corroborating the decreasing degree of packing order. With additional increase in PANI M_w to 50k or beyond, only diffraction arcs

are observed (Figure 4.13d-f). These results indicate a decrease in crystallinity of these nanostructures compared to the lower M_w PANI counterparts. However, these sharp arcs reveal a high degree of long range, preferential orientation of the repeating aniline units along the π - π stacking direction that forms the crystal long axis. The decrease in crystallinity with increasing PANI M_w is consistent with the general finding that the free energy barrier to reorganizing the conformations of polymer chain into ordered states increases with increasing polymer M_w .³³

In addition to packing orientation and degree of crystallinity, previous studies have suggested that the diameters of well-ordered polymer crystals can be additional indications of chain conformation such as fully extended or folded. TAS-PANI-5k forms well-defined nanoribbons with an average diameter around 200 nm, whereas the other samples with a PANI M_w of 10k, 20k, 50k, 65k, and 100k Da form nanowires with average diameter of around 25, 33, 90, 50, and 50 nm, respectively (Figure 4.12). Previous studies on the CP crystallization have noted a relationship between CP M_w and crystal diameter.³³ A fully extended PANI chain of 5k Da would be approximately 20-25 nm in length,^{34,35} which is significantly smaller than 200 nm, meaning the nanoribbons are comprised of many PANI chains along the width direction. Interestingly, earlier work has shown that lower MW P3HT (i.e., 6k Da) have fully extended chains in their crystals, and nanofibers with diameter consistent with the length of the P3HT chains would transform into nanoribbons, likely to minimize surface energy.³³ Previous studies on the crystal packing of oligoanilines has shown similar results possibly due to Oswald ripening.²⁴ It was found that the higher order structures are formed from the merging of smaller structures, i.e., nanoplates are the result of merged stacks of nanoribbons, and nanoribbons are the result of merged parallel arrays of nanowires. The nanowire diameter for TAS-PANI with PANI M_w between 10k and 100k Da are significantly smaller than the length of fully extended polymer chains, indicating the presence of chain folding in the nanowires. It is interesting that TAS-PANI-65k and TAS-PANI-100k exhibit smaller diameter than the TAS-PANI-50k counterpart. This could suggest that PANI chains of higher MW folds more,³³ likely due to the higher entropic barriers associated with “straightening out” longer chains, which typically have more entanglements and intramolecular interactions over extended distances.³⁶

4.5.4 Spectroscopic and electrical characterization

To gain further insights into the effect of crystallographic ordering on the relationship between chain conformation and conductivity of the TAS-PANI nanowires, UV-vis-near infrared (NIR) spectroscopy was employed. Figure 4.15a shows the solution UV-vis-NIR spectra of TANI and PANI of various M_w subjected to the same self-assembly environment as TAS-PANI, whereas Figure 4.15b shows those for the TAS-PANI nanowire dispersions. Three peaks centred at

around 280 nm, 470 nm, and 780 nm can be observed in both collections of spectra, characteristic of doped polyaniline or oligoaniline.^{19,37} The 280 nm peak can be assigned to the $\pi \rightarrow \pi^*$ transition, the 470 nm peak to the polaron $\rightarrow \pi^*$ transition, and the 780 nm peak to the $\pi \rightarrow$ polaron transition.^{19,37} The 780 nm peak for all the PANI-containing samples in both collections of spectra is highly asymmetrical and steadily increases into the NIR region, indicative of expanded PANI chain conformation and more ordered interchain packing.^{37,38} The intensity of the free carrier tail is associated with the delocalization of the polaron band, making it spread across the gap between the π and polaron bands^{33,34} As a result, a decrease in intensity of the 280 nm peak typically accompanies the formation of the free carrier tail. Note that oligoanilines such as TANI do not exhibit free carrier tails despite the relative chain linearity and high crystallographic order because its chain length is not sufficiently long for extensive charge delocalization along the backbone to occur.³⁹

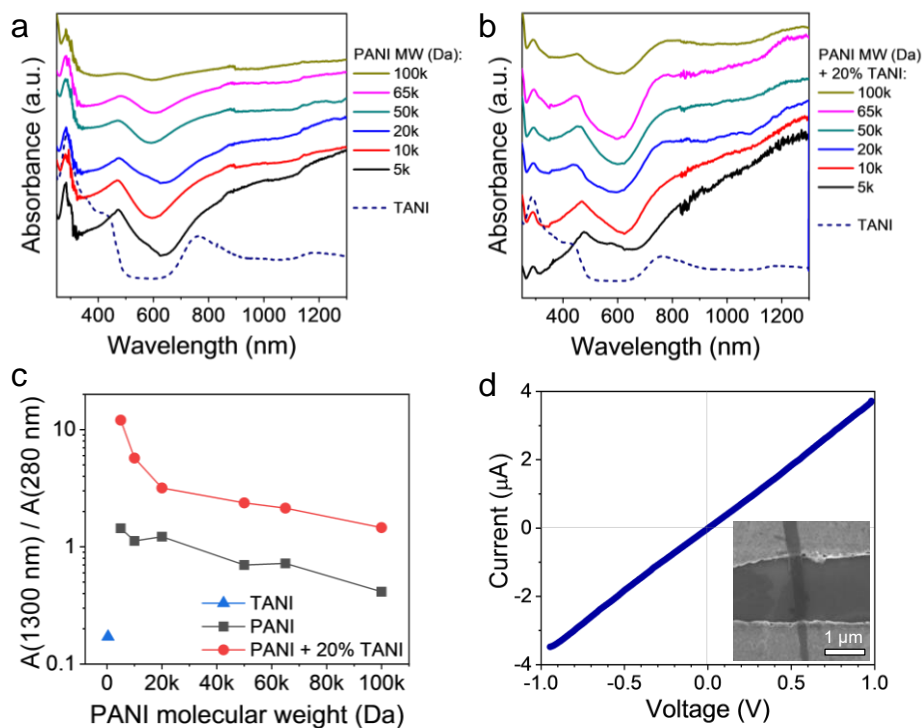


Figure 4.15. UV-vis-NIR spectra of (a) self-assembled TANI and PANI of different molecular weights, and (b) TAS-PANI of different PANI molecular weights. (c) The absorbance peak ratio between the ca. 1300 nm free-carrier tail and the ca. 280 nm $\pi \rightarrow \pi^*$ transition for TAS-PANI with different PANI molecular weights, extracted from the spectra in (a) and (b). (d) Current-voltage curve of a two-probe, single nanowire device of TAS-PANI-5k. Inset shows the SEM image of a representative device.

For the control experiments of PANI with various M_w subjected to the same self-assembly environment as TAS-PANI (Figure 4.15a), despite the presence of the free-carrier tail, the 280 nm peak that corresponds to the $\pi \rightarrow \pi^*$ transition exhibits high intensity for all PANI M_w . As a result, the absorbance ratio between the 1300 nm free-carrier tail and the 280 nm peaks is around or below 1 for all these samples (Figure 4.15c), indicating a high degree of compact coil chain conformation and strong aggregation.^{19,34} This result is consistent with the SEM observations for these samples where only agglomerates are observed (Figure 4.11). The results here suggest that the self-assembly solvent environment alone is effective in doping PANI and partially expanding some coil conformation; however, the extent of such functions is limited and most of the chains remain in the highly coiled and aggregated state.

In contrast, the 280 nm peak associated with $\pi \rightarrow \pi^*$ transition in the TAS-PANI samples show significantly decreased intensity compared to the other peaks. This decrease is accompanied by an increase in the intensity of the 1300 nm free-carrier tail peaks (Figure 4.15b). The collective effect of these changes in intensities is the significantly higher absorbance ratios between the 1300 nm and the 280 nm peaks (Figure 4.15c), confirming the nature of expanded chain conformation in TAS-PANI, which leads to the delocalization of the polaron band and thus charges.^{38,39} This “straightening out” of the PANI chain conformation facilitates ordered interchain packing, and thus leads to crystallization of the PANI chains in the TAS-PANI nanowires (Figures 4.10, 4.13). In particular, TAS-PANI with the lowest M_w , 5000 Da, exhibits a very intense free carrier tail, leading to a 1300-to-280 nm peak ratio of over 12, suggesting a high degree of chain linearity and hence interchain ordering. This is consistent with the SAED data of TAS-PANI-5k, which shows discrete diffraction spots, indicative of the single crystalline nature of these nanowires (Figure 4.13a). As the PANI M_w increases, the free-carrier tail weakens consistently. This is not only reflected by the gradually decreasing ratios between the 1300-to-280 nm peaks (Figure 4.15c), but also the more obvious appearance of the localized 780 nm peak from TANI in the UV-vis-NIR spectra of TAS-PANI with PANI M_w above 20,000 Da (Figure 4.15b). However, even with the highest M_w PANI of 100,000 Da, a 1300-to-280 nm peak ratio of 1.5 is obtained, significantly higher than the counterparts without TANI (Figure 4.15c), illustrating the effectiveness of TANI in shaping PANI into more extended chain conformation, promoting their preferential ordering (Figure 4.13f).

The presence of a steadily increasing free-carrier tail in the NIR region is characteristic of highly conductive polymers with expanded chain conformation. It has been shown that a strong free-carrier tail is typically associated with metallic materials⁴⁰ and correlates directly with high conductivity in conducting polymers.

Hence, the UV-vis-NIR results (Figure 4.15b) qualitatively suggest that the TAS-PANI nanowires have high conductivity.

Bulk conductivity measurements such as those based on casted films or pressed pellets do not offer meaningful assessment of the conductivity of crystalline nanostructures because the values are more reflective of the high contact resistance between the numerous nanostructure-nanostructure junctions rather than the intrinsic conductivity of the nanostructures.^{19,41} Therefore, we attempted single wire measurements for the TAS-PANI nanostructures by depositing them across two-contact microelectrodes with a gap size of 2-5 μm . Due to the tangled, web-like structure of the TAS-PANI nanowires with PANI M_w between 10,000 and 100,000 Da (Figure 4.10b-f), it was challenging to isolate enough of these MWs for reproducible measurements. However, the straight nanoribbon morphology of TAS-PANI-5k allowed us to isolate over 10 nanoribbons and bridge them across bottom-contact, Cr/Au microelectrodes for current-voltage (I-V) measurements.

Figure 4.15d shows a representative I-V curve, with the SEM image of a representative device shown in the inset. The linearity of the I-V curve indicates ohmic contact between the nanoribbons and the microelectrodes. Conductivity values ranging from 4.3 to 19.5 S/cm are obtained from these devices. Given the very intense free carrier tail observed in the UV-vis-NIR spectra, the conductivity values of the TAS-PANI-5k nanoribbons are likely much higher than our results indicate here. The apparent conductivity from our measurements is limited by the following factors: (1) The short length of the nanoribbons only allowed us to carry out 2-point probe measurements rather than 4-point probe measurements, meaning the measured resistance values include contributions from contact resistance. (2) These are bottom-contact devices, meaning the contact quality between the nanostructures and the electrodes are not optimal. Solvents or other impurities are often trapped between the sample and electrodes, impeding charge transport. Potentially fabricating top-contact devices may solve this issue, but such feats are challenging given the small nanoribbon size and conducting polymers' high sensitivity to the processing conditions required for lithography. These factors revolving around contact quality have likely also resulted in the spread of the measured conductivity values across the 4.3 to 19.5 S/cm range. Since the focus of this work is on demonstrating a new concept in crystallizing conjugated polymers, not on device optimization, we reserve more elaborate measurements for future studies.

Despite the likely underestimation of the conductivity of TAS-PANI, it is worth emphasizing that these values are much higher than typical PANI processed from water, which generally has a conductivity around 1 S/cm.⁴² Similarly intense free carrier tails from UV-vis-NIR and conductivity on the order of 10^1 S/cm or

above typically require large dopant acids such as camphorsulfonic acid in combination with harsh and toxic “secondary dopant” processing solvents like *m*-cresol,^{38,39} which are undesirable and not compatible with flexible or stretchable substrates required for next-generation organic electronics.

4.6 Conclusions and Outlooks

In summary, we have developed a simple, one-step self-assembly method towards highly crystalline PANI nanostructures with the assistance of a small amount of the corresponding, monodispersed oligomers such as tetraaniline. Since TANI and PANI share the same repeating units and are both electroactive, no impurities are introduced into the material through this process. Because the synthetic component that controls the chemical structures and the self-assembly process that dictates morphology and crystal packing are decoupled into separate steps in this approach, it can be applied to pre-made PANI with well-defined properties such as molecular weights, leading to their single crystals or crystals with preferential chain orientation. The presence of very strong free carrier tails in their UV-vis-NIR spectra indicate these materials are likely highly conductive.

The broader impact of this work lies in its simplicity and potential generality. The new concept demonstrated here is likely generally applicable to many other CPs or other polymers because oligomers of well-defined numbers of repeating units can be synthesized for each parent polymer. For the self-assembly of PANI, our preliminary results show that aniline dimer, which can also readily self-assemble into crystalline nanostructures, can play a similar role as TANI in assisting the self-assembly of PANI into ordered structures (Figure 4.16). This insight reveals that a variety of oligomers with different numbers of repeating units can potentially be used to induce the crystallization of their parent polymers, which will be the topic of a future study. Furthermore, being able to grow highly crystalline structures from a mostly aqueous solvent is environmentally friendly. Finally, even though this work focuses on crystalline nanostructures, we conjecture that the concept of oligomer-induced crystallization of the parent polymer can likely be extended to increasing the crystallinity of polymer thin films as well, potentially leading to enhanced performance in thin film electronics.

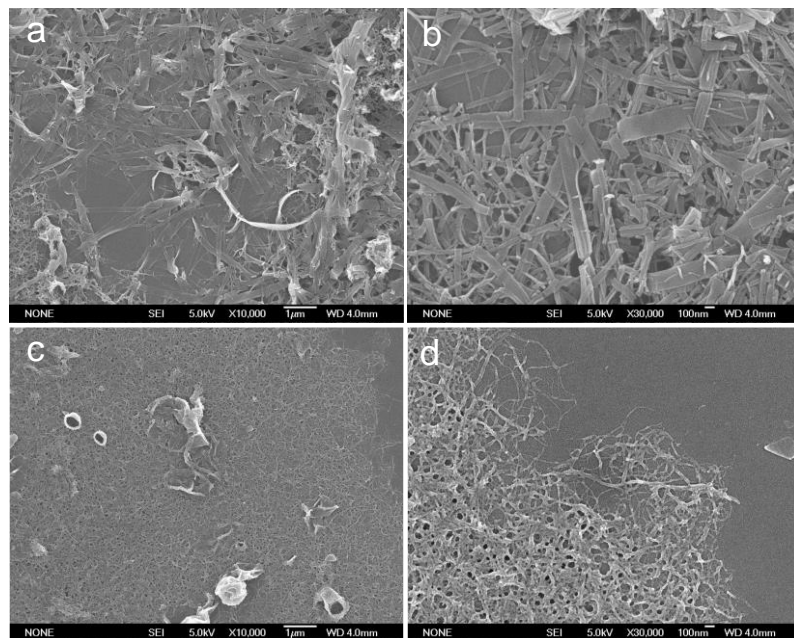


Figure 4.16. PANI-NF assembled with the assistance of aniline dimer. (a) and (b) SEM images of the assembled structure with a 60% PANI and 40% aniline dimer composition. (c) and (d) SEM images of the assembled structure with an 80% PANI and 20% aniline dimer composition.

4.7 Appendix

Table 4.1. Abbreviations

PANI	Polyaniline
TANI	Tetraaniline
TAS-PANI	Tetraaniline-assisted self-assembled polyaniline
TAS-PANI-5k	Tetraaniline-assisted self-assembled polyaniline ($M_w \sim 5k$ Da)
TAS-PANI-10k	Tetraaniline-assisted self-assembled polyaniline ($M_w \sim 10k$ Da)
TAS-PANI-20k	Tetraaniline-assisted self-assembled polyaniline ($M_w \sim 20k$ Da)
TAS-PANI-50k	Tetraaniline-assisted self-assembled polyaniline ($M_w \sim 50k$ Da)
TAS-PANI-65k	Tetraaniline-assisted self-assembled polyaniline ($M_w \sim 65k$ Da)
TAS-PANI-100k	Tetraaniline-assisted self-assembled polyaniline ($M_w \sim 100k$ Da)

4.8 References

- (1) Yao, Z. F.; Wang, J. Y.; Pei, J. High-Performance Polymer Field-Effect Transistors: From the Perspective of Multi-Level Microstructures. *Chem. Sci.* **2021**, *12* (4), 1193–1205. <https://doi.org/10.1039/d0sc06497a>.
- (2) Zhang, X.; Dong, H.; Hu, W. Organic Semiconductor Single Crystals for Electronics and Photonics. *Adv. Mater.* **2018**, *30* (44), 1–34. <https://doi.org/10.1002/adma.201801048>.
- (3) Kim, J.-Y.; Kwon, M.-H.; Kim, J.-T.; Kwon, S.; Ihm, D.-W.; Min, Y.-K. Crystallization Growth and Micropatterning on Self-Assembled Conductive Polymer Nanofilms. *J. Phys. Chem. C* **2007**, *111* (30), 11252–11258. <https://doi.org/10.1021/jp0683622>.
- (4) Lim, J. A.; Liu, F.; Ferdous, S.; Muthukumar, M.; Briseno, A. L. Polymer Semiconductor Crystals. *Mater. Today* **2010**, *13* (5), 14–24. [https://doi.org/10.1016/S1369-7021\(10\)70080-8](https://doi.org/10.1016/S1369-7021(10)70080-8).
- (5) Cao, X.; Zhao, K.; Chen, L.; Liu, J.; Han, Y. Conjugated Polymer Single Crystals and Nanowires. *Polym. Cryst.* **2019**, *2* (3). <https://doi.org/10.1002/pcr2.10064>.
- (6) Kim, D. H.; Han, J. T.; Park, Y. D.; Jang, Y.; Cho, J. H.; Hwang, M.; Cho, K. Single-Crystal Polythiophene Microwires Grown by Self-Assembly. *Adv. Mater.* **2006**, *18* (6), 719–723. <https://doi.org/10.1002/adma.200502442>.
- (7) Xiao, X.; Hu, Z.; Wang, Z.; He, T. Study on the Single Crystals of Poly(3-Octylthiophene) Induced by Solvent-Vapor Annealing. *J. Phys. Chem. B* **2009**, *113* (44), 14604–14610. <https://doi.org/10.1021/jp9064505>.
- (8) L. Briseno, A.; C. B. Mannsfeld, S.; J. Shamberger, P.; S. Ohuchi, F.; Bao, Z.; A. Jenekhe, S.; Xia, Y. Self-Assembly, Molecular Packing, and Electron Transport in n-Type Polymer Semiconductor Nanobelts. *Chem. Mater.* **2008**, *20* (14), 4712–4719. <https://doi.org/10.1021/cm8010265>.
- (9) Dong, H.; Jiang, S.; Jiang, L.; Liu, Y.; Li, H.; Hu, W.; Wang, E.; Yan, S.; Wei, Z.; Xu, W.; Gong, X. Nanowire Crystals of a Rigid Rod Conjugated Polymer. *J. Am. Chem. Soc.* **2009**, *131* (47), 17315–17320. <https://doi.org/10.1021/ja907015p>.
- (10) Huang, H.; Yang, L.; Facchetti, A.; J. Marks, T. Organic and Polymeric Semiconductors Enhanced by Noncovalent Conformational Locks. *Chem. Rev.* **2017**, *117* (15), 10291–10318. <https://doi.org/10.1021/acs.chemrev.7b00084>.
- (11) Zheng, Y. Q.; Lei, T.; Dou, J. H.; Xia, X.; Wang, J. Y.; Liu, C. J.; Pei, J. Strong Electron-Deficient Polymers Lead to High Electron Mobility in Air and Their Morphology-Dependent Transport Behaviors. *Adv. Mater.* **2016**, *28* (33), 7213–7219. <https://doi.org/10.1002/adma.201600541>.

- (12) Liu, J.; Moo-Young, J.; McInnis, M.; A. Pasquinelli, M.; Zhai, L. Conjugated Polymer Assemblies on Carbon Nanotubes. *Macromolecules* **2014**, *47* (2), 705–712. <https://doi.org/10.1021/ma401609q>.
- (13) Luo, Y.; A. Santos, F.; W. Wagner, T.; Tsoi, E.; Zhang, S. Dynamic Interactions between Poly(3-Hexylthiophene) and Single-Walled Carbon Nanotubes in Marginal Solvent. *J. Phys. Chem. B* **2014**, *118* (22), 6038–6046. <https://doi.org/10.1021/jp503128v>.
- (14) Agbolaghi, S.; Abbaspoor, S.; Abbasi, F. A Comprehensive Review on Polymer Single Crystals—From Fundamental Concepts to Applications. *Prog. Polym. Sci.* **2018**, *81*, 22–79. <https://doi.org/10.1016/j.progpolymsci.2017.11.006>.
- (15) M. D'Arcy, J.; F. El-Kady, M.; P. Khine, P.; Zhang, L.; Hwa Lee, S.; R. Davis, N.; S. Liu, D.; T. Yeung, M.; Yeol Kim, S.; L. Turner, C.; T. Lech, A.; T. Hammond, P.; B. Kaner, R. Vapor-Phase Polymerization of Nanofibrillar Poly(3,4-Ethylenedioxythiophene) for Supercapacitors. *ACS Nano* **2014**, *8* (2), 1500–1510. <https://doi.org/10.1021/nn405595r>.
- (16) Majumdar, S.; Sarmah, K.; Mahanta, D. A Simple Route to Prepare Polypyrrole-Coated Filter Papers via Vapor Phase Polymerization and Their Gas Sensing Application. *ACS Appl. Polym. Mater.* **2020**, *2* (5), 1933–1942. <https://doi.org/10.1021/acsapm.0c00147>.
- (17) Cho, B.; S. Park, K.; Baek, J.; S. Oh, H.; Koo Lee, Y.-E.; M. Sung, M. Single-Crystal Poly(3,4-Ethylenedioxythiophene) Nanowires with Ultrahigh Conductivity. *Nano Lett.* **2014**, *14* (6), 3321–3327. <https://doi.org/10.1021/nl500748y>.
- (18) Zhang, T.; Qi, H.; Liao, Z.; Horev, Y. D.; Panes-Ruiz, L. A.; Petkov, P. S.; Zhang, Z.; Shivhare, R.; Zhang, P.; Liu, K.; Bezugly, V.; Liu, S.; Zheng, Z.; Mannsfeld, S.; Heine, T.; Cuniberti, G.; Haick, H.; Zschech, E.; Kaiser, U.; Dong, R.; Feng, X. Engineering Crystalline Quasi-Two-Dimensional Polyaniline Thin Film with Enhanced Electrical and Chemiresistive Sensing Performances. *Nat. Commun.* **2019**, *10* (1), 1–9. <https://doi.org/10.1038/s41467-019-11921-3>.
- (19) Wang, Y.; D. Tran, H.; Liao, L.; Duan, X.; B. Kaner, R. Nanoscale Morphology, Dimensional Control, and Electrical Properties of Oligoanilines. *J. Am. Chem. Soc.* **2010**, *132* (30), 10365–10373. <https://doi.org/10.1021/ja1014184>.
- (20) Huang, J.; B. Kaner, R. A General Chemical Route to Polyaniline Nanofibers. *J. Am. Chem. Soc.* **2004**, *126* (3), 851–855. <https://doi.org/10.1021/ja0371754>.
- (21) D. Zujovic, Z.; Wang, Y.; A. Bowmaker, G.; B. Kaner, R. Structure of Ultralong Polyaniline Nanofibers Using Initiators. *Macromolecules* **2011**, *44*

- (8), 2735–2742. <https://doi.org/10.1021/ma102772t>.
- (22) Boyer, M.-I.; Quillard, S.; Rebourt, E.; Louarn, G.; Buisson, J. P.; Monkman, A.; Lefrant, S. Vibrational Analysis of Polyaniline: A Model Compound Approach. *J. Phys. Chem. B* **1998**, *102* (38), 7382–7392. <https://doi.org/10.1021/jp972652o>.
- (23) Wang, Y.; Tran, H. D.; Kaner, R. B. Template-Free Growth of Aligned Bundles of Conducting Polymer Nanowires. *J. Phys. Chem. C* **2009**, *113* (24), 10346–10349. <https://doi.org/10.1021/jp903583e>.
- (24) Wang, Y.; Liu, J.; D. Tran, H.; Mecklenburg, M.; N. Guan, X.; Z. Stieg, A.; C. Regan, B.; C. Martin, D.; B. Kaner, R. Morphological and Dimensional Control via Hierarchical Assembly of Doped Oligoaniline Single Crystals. *J. Am. Chem. Soc.* **2012**, *134* (22), 9251–9262. <https://doi.org/10.1021/ja301061a>.
- (25) Ma, Z.; Geng, Y.; Yan, D. Extended-Chain Lamellar Packing of Poly(3-Butylthiophene) in Single Crystals. *Polymer (Guildf)*. **2007**, *48* (1), 31–34. <https://doi.org/https://doi.org/10.1016/j.polymer.2006.10.034>.
- (26) Zang, L.; Che, Y.; S. Moore, J. One-Dimensional Self-Assembly of Planar π -Conjugated Molecules: Adaptable Building Blocks for Organic Nanodevices. *Acc. Chem. Res.* **2008**, *41* (12), 1596–1608. <https://doi.org/10.1021/ar800030w>.
- (27) Xu, J.; Ma, Y.; Hu, W.; Rehahn, M.; Reiter, G. Cloning Polymer Single Crystals through Self-Seeding. *Nat. Mater.* **2009**, *8* (4), 348–353. <https://doi.org/10.1038/nmat2405>.
- (28) Qian, J.; Guerin, G.; Lu, Y.; Cambridge, G.; Manners, I.; Winnik, M. A. Self-Seeding in One Dimension: An Approach To Control the Length of Fiberlike Polyisoprene–Polyferrocenylsilane Block Copolymer Micelles. *Angew. Chemie Int. Ed.* **2011**, *50* (7), 1622–1625. <https://doi.org/https://doi.org/10.1002/anie.201006223>.
- (29) Yan, Y.; Wang, R.; Qiu, X.; Wei, Z. Hexagonal Superlattice of Chiral Conducting Polymers Self-Assembled by Mimicking β -Sheet Proteins with Anisotropic Electrical Transport. *J. Am. Chem. Soc.* **2010**, *132* (34), 12006–12012. <https://doi.org/10.1021/ja1036447>.
- (30) Kim, J.; J. Cote, L.; Kim, F.; Yuan, W.; R. Shull, K.; Huang, J. Graphene Oxide Sheets at Interfaces. *J. Am. Chem. Soc.* **2010**, *132* (23), 8180–8186. <https://doi.org/10.1021/ja102777p>.
- (31) Greer, H. F.; Zhou, W. Electron Diffraction and HRTEM Imaging of Beam-Sensitive Materials. *Crystallogr. Rev.* **2011**, *17* (3), 163–185. <https://doi.org/10.1080/0889311X.2010.535525>.
- (32) Martin, D. C.; Thomas, E. L. Experimental High-Resolution Electron

- Microscopy of Polymers. *Polymer (Guildf)*. **1995**, 36 (9), 1743–1759. [https://doi.org/https://doi.org/10.1016/0032-3861\(95\)90922-O](https://doi.org/https://doi.org/10.1016/0032-3861(95)90922-O).
- (33) Liu, J.; Arif, M.; Zou, J.; I. Khondaker, S.; Zhai, L. Controlling Poly(3-Hexylthiophene) Crystal Dimension: Nanowhiskers and Nanoribbons. *Macromolecules* **2009**, 42 (24), 9390–9393. <https://doi.org/10.1021/ma901955c>.
- (34) P. Pouget, J.; E. Jozefowicz, M.; J. Epstein, A.; Tang, X.; G. MacDiarmid, A. X-Ray Structure of Polyaniline. *Macromolecules* **2002**, 24 (3), 779–789. <https://doi.org/10.1021/ma00003a022>.
- (35) Baughman, R. H.; Wolf, J. F.; Eckhardt, H.; Shacklette, L. W. The Structure of a Novel Polymeric Metal: Acceptor-Doped Polyaniline. *Synth. Met.* **1988**, 25 (2), 121–137. [https://doi.org/https://doi.org/10.1016/0379-6779\(88\)90348-7](https://doi.org/https://doi.org/10.1016/0379-6779(88)90348-7).
- (36) Sperling, L. H. *Introduction to Physical Polymer Science*, 4th ed.; Wiley-Interscience; Wiley: Hoboken, New Jersey, 2006.
- (37) Xia, Y.; M. Wiesinger, J.; G. MacDiarmid, A.; J. Epstein, A. Camphorsulfonic Acid Fully Doped Polyaniline Emeraldine Salt: Conformations in Different Solvents Studied by an Ultraviolet/Visible/Near-Infrared Spectroscopic Method. *Chem. Mater.* **2002**, 7 (3), 443–445. <https://doi.org/10.1021/cm00051a002>.
- (38) MacDiarmid, A. G.; Epstein, A. J. Secondary Doping in Polyaniline. *Synth. Met.* **1995**, 69 (1–3), 85–92. [https://doi.org/10.1016/0379-6779\(94\)02374-8](https://doi.org/10.1016/0379-6779(94)02374-8).
- (39) MacDiarmid, A. G.; Epstein, A. J. The Concept of Secondary Doping as Applied to Polyaniline. *Synth. Met.* **1994**, 65 (2–3), 103–116. [https://doi.org/10.1016/0379-6779\(94\)90171-6](https://doi.org/10.1016/0379-6779(94)90171-6).
- (40) Monkman, A. P.; Adams, P. Observed Anisotropies in Stretch Oriented Polyaniline. *Synth. Met.* **1991**, 41 (1–2), 627–633. [https://doi.org/10.1016/0379-6779\(91\)91146-2](https://doi.org/10.1016/0379-6779(91)91146-2).
- (41) Wang, Y.; A. Torres, J.; Z. Stieg, A.; Jiang, S.; T. Yeung, M.; Rubin, Y.; Chaudhuri, S.; Duan, X.; B. Kaner, R. Graphene-Assisted Solution Growth of Vertically Oriented Organic Semiconducting Single Crystals. *ACS Nano* **2015**, 9 (10), 9486–9496. <https://doi.org/10.1021/acsnano.5b03465>.
- (42) Li, D.; Huang, J.; B. Kaner, R. Polyaniline Nanofibers: A Unique Polymer Nanostructure for Versatile Applications. *Acc. Chem. Res.* **2008**, 42 (1), 135–145. <https://doi.org/10.1021/ar800080n>.

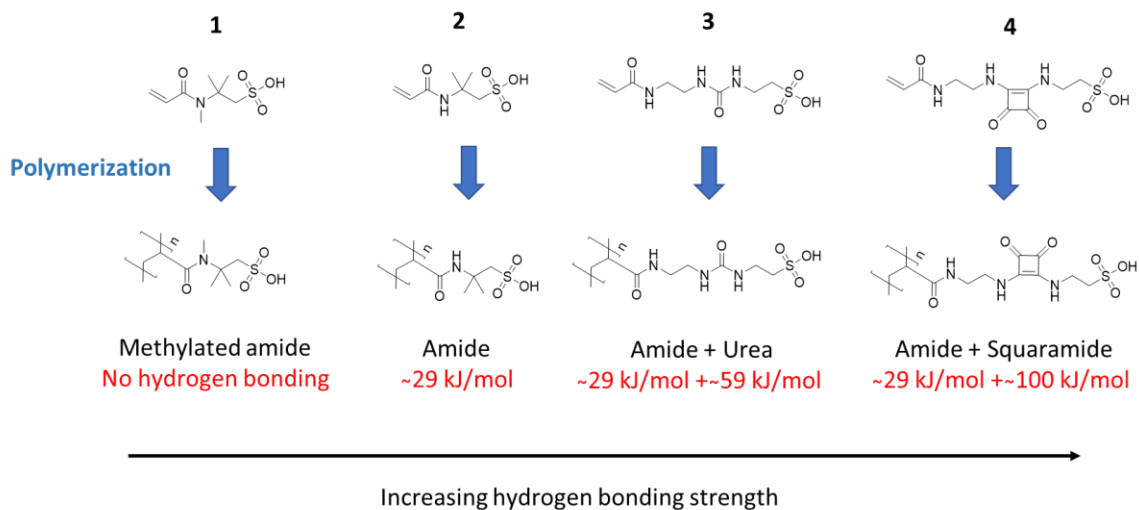
Chapter 5

Synthesis of modified PAMPSA for rate-adaptive polymers

5.1 Introduction

In a previous project, we designed an electrically conductive polymeric material with increasing toughness at higher strain rates, in contrast to that of classic viscoelastic material behavior.¹ Additionally, we investigated the fundamental structure-property relationships that give rise to this behavior. In our investigation, we found that the hydrogen bonding of one of its main polymeric components, poly(2-acrylamido-2-methyl-1-propanesulfonic acid) (PAMPSA), plays a crucial role in this strain rate-adaptive behavior. In this material, negatively charged side chains of PAMPSA act as a doping agent and polymerization template for the conductive polymer polyaniline (PANI) to form a solvophilic PANI:PAMPSA micelle.²⁻⁴ However, our investigation into the effect of hydrogen bonding was limited, as we only used PAMPSA as the hydrogen bonding polymer. Additionally, there were limited molecular weights of commercially available PAMPSA, limiting our investigation of the effect of polymer size on the mechanical properties.

We set out to synthesize the materials needed to bridge this knowledge gap. To help with investigating hydrogen bonding strength, AMPSA-based polymers of varying hydrogen bonding strength were synthesized, one with no hydrogen bonding (methylated AMPSA or MAMPSA) and two versions of stronger hydrogen bonding than PAMPSA (urea and squaramide monomers),⁵⁻⁷ which are depicted in Scheme 5.1. Additionally, we used two different polymerization methods to control the molecular weight of polymers formed from these monomers. Finally, we demonstrated the successful synthesis of polyaniline with one of these polymers, which is a key component of our conductive, strain-rate adaptive material.



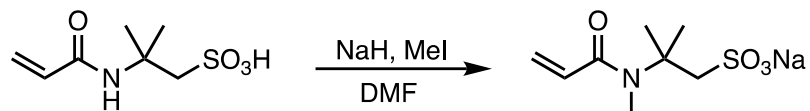
Scheme 5.1. AMPSA monomer and AMPSA monomer variants with different hydrogen bonding strengths.

5.2 MAMPSA Synthesis

5.2.1 Synthesis Procedure

The methylated AMPSA procedure was developed in our lab. To a flame dried 1000 mL round bottom flask, sodium hydride (NaH) was added, followed by 50 mL dry N,N-dimethylformamide (DMF) under N₂ flow. In flame-dried glassware, AMPSA was dissolved in 50 mL of dry DMF and transfer to a flame-dried addition funnel. The flask was placed on ice and AMPSA mixture was added dropwise via the addition funnel under N₂ to ensure that the reaction did not get out of control. Three equivalents of MeI was added to the reaction. Upon complete addition, the mixture was allowed to stir overnight at room temperature. The next morning, the reaction was checked using ¹H NMR to determine if all AMPSA had reacted, and additional NaH and MeI was added as needed. When complete, the mixture was carefully quenched by the slow, dropwise, addition of 25 mL of saturated NaHCO₃ to quench any leftover NaH. Then the mixture was evaporated to dryness *in vacuo* on the rotovap (bath temperature at 50-60 °C). The dried mixture was diluted with hexane to help precipitation. The solid was filtered and washed thoroughly with hexanes and diethyl ether. The precipitate was transferred to an Erlenmeyer flask and MAMPSA was extracted with acetone. The solids were filtered and extract again with acetone until the fractions no longer contained MAMPSA as determined via thin layer chromatography (TLC). The acetone extracts were pooled and concentrated *in vacuo* to yield a crude residue. To remove some of the NaI, the residue was dispersed in dichloromethane to precipitate NaI as a white solid, and filtered to collect dissolved MAMPSA. The crude product was extracted by filtering

over a large plug of silica eluting with a gradient of hexane to acetone (or can use acetonitrile) to 10% methanol in acetone. MAMPSA was passed through the silica plug again to remove remaining yellow impurities, then dry *in vacuo*. The product was dissolved in water, then filtered first through several 1 μm filters, then a 0.2 μm filter to remove dust and silica impurities.



Scheme 5.2. Reaction scheme for the amide methylation of AMPSA monomer.

Reagent	MW (g/mol)	eq.	mmol	mass (g)	vol (mL)	Density (g/mol)
AMPSA	207.24	1	144.6	30		
NaH	24	3	433.8	10.38		
MeI	141.94	3	433.8	61.8	27	2.28
DMF					200	

Table 5.1. Reaction quantities for AMPSA methylation reaction.

5.2.2 Results and Discussion

A large-scale reaction was performed using 30 g of AMPSA starting material. Not all AMPSA converted to MAMPSA, so an additional three equivalents of NaH and MeI were required, then an additional six equivalents of MeI to convert all AMPSA in the reaction, which was monitored using ^1H NMR (Figure 5.1). After performing the required steps of quenching, drying, washing, and extracting the MAMPSA product with acetone, the next step was to remove the NaI with a silica plug, which is a short version of column chromatography for separating molecules with a high R_f difference. However, we first believed that removing the very large amount of NaI with the silica plug was not feasible, so an extra step was taken to remove excess MeI by mixing the product with dichloromethane, resulting in NaI precipitation (Figure 5.2), which was removed by filtering the dissolved component. This step was found to not be necessary, and was omitted from the procedure in Section 5.2.1. Not all NaI was removed, but the removed precipitate contained no MAMPSA, based on TLC analysis (Figure 5.3). The crude product was purified with a silica plug in aliquots, using first hexane to remove mineral oil impurities and wet the crude product, acetone to remove NaI, and finally a 10% methanol/acetone

mixture to elute MAMPSA. MAMPSA was passed through the silica plug again to remove remaining yellow impurities (Figure 5.4). The product was then dissolved in water, then filtered first through several 1 μm filters, then a 0.2 μm filter to remove impurities that made the aqueous AMPSA solution cloudy (Figure 5.5).

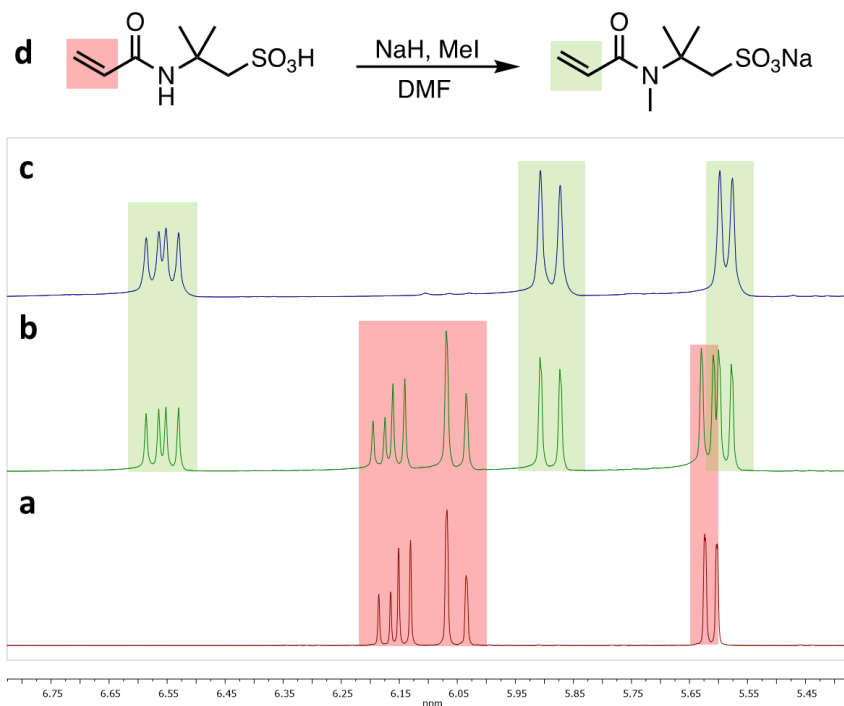


Figure 5.1. ^1H NMR spectra to monitor the functionalization of AMPSA monomer starting material (a) and product formed after addition of 3 equivalents (b) and 6 equivalents (c) of methyl iodide to starting material. Peaks monitored for reaction completeness are highlighted in red and green, which correspond to protons from starting material and product respectively with corresponding reaction scheme (d).



Figure 5.2. Crude MAMPSA product dissolved in DCM with NaI precipitate on bottom.



Figure 5.3. TLC plate with spot corresponding to pure MAMPSA monomer.

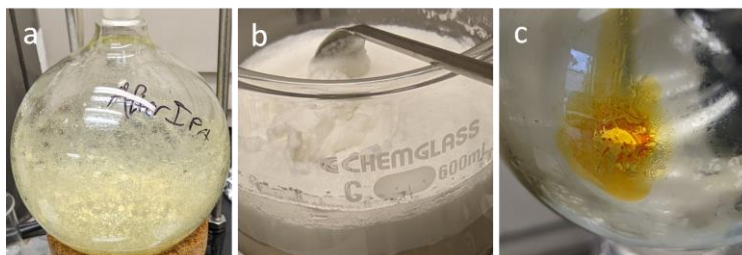


Figure 5.4. MAMPSA product before (a) and after purifying with additional elution through silica plug (b), and concentrated impurities (c).

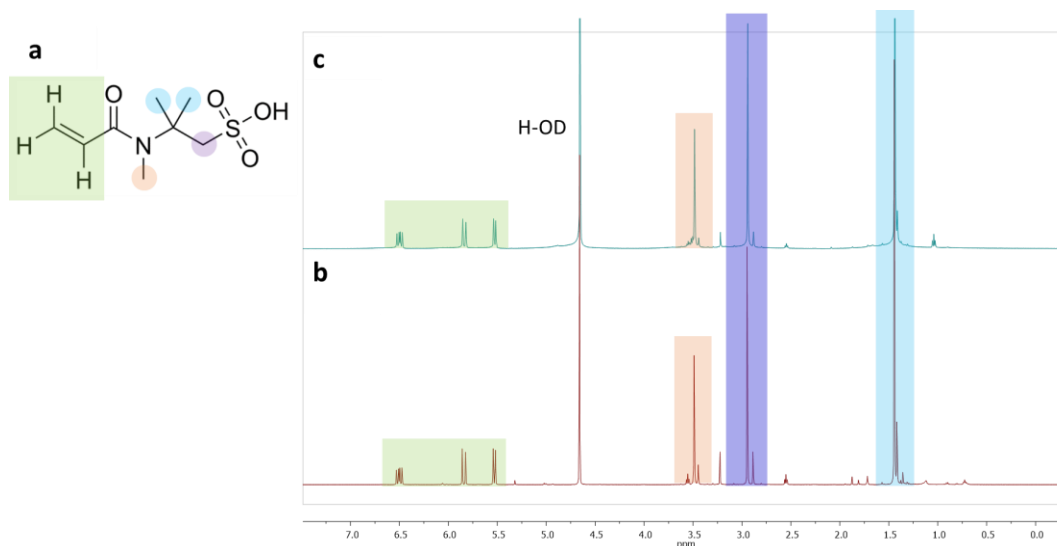
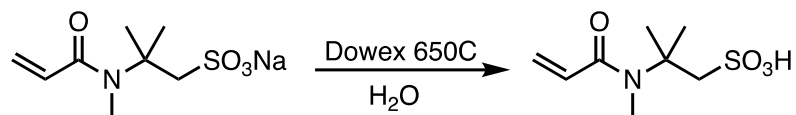


Figure 5.5. ^1H NMR spectra of MAMPSA monomer before (b) and after additional silica plug (c). Chemical structure of MAMPSA monomer (a) with peaks corresponding to their protons highlighted in green, orange, purple, and blue.

5.2.3 Ion Exchange Reaction for MAMPSA

5.2.3.1 Procedure

The following procedure was developed in our lab. The MAMPSA sodium salt was dissolved in 30 mL of deionized water. A column was prepared with a small amount of sand and approximately 40 mL of DOWEX 650C cation exchange resin beads. The column was pre-wet and washed with 40 mL of water; the pH of this eluent should be 5-6. The sodium salt solution was slowly added to the top of the column and the eluent was collected directly in a round bottom flask. The pH of the eluent was quickly changed to pH = 1 and was monitored with pH paper. Approximately 80 mL of water was used to wash the material off of the column, until the pH of the eluent had returned to 5-6. The aqueous solution was concentrated *in vacuo* (bath temp = 50 °C) to yield a light-yellow foam as the sulfonic acid.



Scheme 5.3. Reaction scheme for the cation ion exchange reaction of MAMPSA.

Reagent	MW (g/mol)	eq.	mmol or mmol/mL	mass (g)	vol (mL)
Na-MAMPSA	243.25	1	37.8 mmol	9.21	
DOWEX 650C		2	2 mmol/mL		40
Water					30

Table 5.2. Reaction quantities for the cation ion exchange reaction of MAMPSA.

5.2.3.2 Results and Discussion

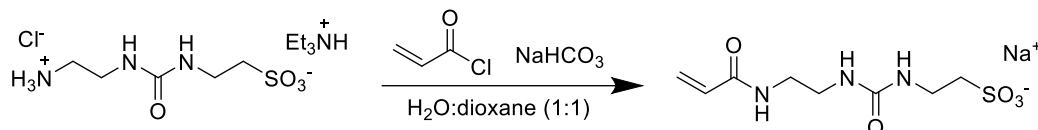
This procedure is simple to carry out and scale up if needed. When the MAMPSA salt is eluted through the column of ion exchange resin, sodium ions are exchanged for protons from the sulfonic acid-functionalized polymeric resin and become immobilized, leading to the elution of protonated MAMPSA. An excess of resin is used in order to ensure that all sodium is removed from the product.

5.3 Urea Monomer Synthesis

5.3.1 Synthesis Procedure

The following reaction procedure was developed in our lab. To perform the reaction depicted in Scheme 5.4, the urea bis-salt starting material was suspended in a 100 mL round bottom flask with 13 mL H₂O and 13 mL of 1,4-dioxane to form a white suspension. The suspension was cooled to 0 °C in an ice bath NaHCO₃ was added in small portions over 15 minutes to ensure the neutralization does not get hot and bubble over from gas formation. After complete addition of the mixture, it was warmed to room temp and allowed to stir for 30 min to ensure complete neutralization. The mixture was then cooled to 0 °C the acryloyl chloride was added dropwise as a solution in dioxane (3 mL) via an addition funnel over 20 min. A summary of the reactant quantities are shown in Table 5.3. Vigorous gas evolution occurred during the addition. Be careful not to add the acid chloride too fast as there seems to be an induction period. After complete addition, the mixture was allowed to react at 0 °C until gas evolution slowed significantly. The mixture was then warmed to room temperature and allowed to react for 1 hour. An additional equivalent of NaHCO₃ was added, followed by another one equivalent of acryloyl chloride in 3 mL dioxane slowly (1 drop/sec) at room temperature. The mixture was nearly clear. It was allowed to stir at room temperature. An aliquot was analyzed by ¹H NMR to confirm that the reaction had gone to completion, and additional

NaHCO₃ and acryloyl chloride was as needed. The crude solution was eluted through a column of cation exchange resin with three molar equivalents of resin to Na ions in solution. When complete, an organic extraction using ethyl acetate was used four times and the aqueous layers were kept. The aqueous mixture was concentrated *in vacuo* at 50 °C and dried under high vacuum overnight. When dry, it was stored in an air-tight container in a freezer at -4 °C.



Scheme 5.4. Reaction scheme for the conversion of urea bis salt to urea monomer.

Reagent	MW (g/mol)	eq.	mmol	mass (g)	vol (mL)	Density (g/mL)
Urea bis-salt	348.89	1	2.87	1		
Acryloyl chloride	90.51	2.1	6.03	0.55	0.49	1.12
NaHCO ₃	84.01	5.5	15.76	1.32		
Water					12.0	
1,4-Dioxane					6.0	

Table 5.3. Reaction quantities for conversion of urea bis salt to urea monomer.

5.3.2 Results and Discussion

The first attempt to synthesize the urea monomer was based on a procedure developed in our lab, as described in Section 5.3.1. However, several changes were needed to obtain the final desired product. First, three additional equivalents of acryloyl chloride were required, instead of the prescribed two to functionalize all the starting material (Figure 5.6). The original procedure then required drying *in vacuo*, washing the crude solid product with 50 °C MeOH, and drying the purified product. A small amount of the dried product was dissolved in D₂O for ¹H NMR analysis. Unexpectedly, the sample was a gel when mixed with the solvent (Figure 5.7), which was a result of the monomer polymerizing, based on ¹H NMR analysis (Figure 5.8).

Many attempts were made to avoid the premature polymerization, but all failed. The crude product was found to polymerize either during the drying process, or when dissolved after being dried. One potential workaround was to polymerize

the crude reactant solution after the functionalization was completed. However, the resulting polymer contains a large amount of sodium acrylate monomers as a byproduct of acryloyl chloride reacting with the aqueous sodium bicarbonate solution, leading the formation of an undesirable polymer. A new approach was taken to remove each component of the solution one at a time, starting with the sodium ions, by eluting the crude solution through a column of cationic exchange resin. This step was successful as indicated by pH paper indicating a pH of 1. The next component of the solvent to remove was 1,4-dioxane. Work by Alshaimi and coworkers demonstrated that organic extraction using ethyl acetate can effectively remove 1,4-dioxane from water.⁸ To carry this out, the crude product solution was washed with several additions of ethyl acetate. Upon inspection with ¹H NMR, it was found that the washes not only removed the 1,4-dioxane, but also the diethyl amine and acrylic acid byproducts, indicating that this was an effective method to remove undesirable byproducts (Figure 5.9). The organic washes were shown in ¹H NMR to contain none of the desired urea monomer, indicating that this method alone is sufficient to remove the reaction byproducts (Figure 5.10). This process does not remove acrylic acid if the ion exchange step is not first performed, due to its salt having higher water solubility. Most importantly, this procedure allows for the product to be dried and dissolved in D₂O without premature polymerization (Figure 5.11). The reaction was successfully scaled up to a 1 g scale, indicating that this method can be used for the future synthesis of the remaining urea monomer precursor.

The premature polymerization was likely due to reacting with trace amounts of radical-forming organic peroxides that spontaneously form in 1,4-dioxane.⁹⁻¹¹ These peroxides concentrate when drying the crude reaction mixture, increasing the reaction rate of the radical polymerization of the monomers in the mixture. Removing the 1,4-dioxane also likely removes these organic peroxides, and prevents premature polymerization.

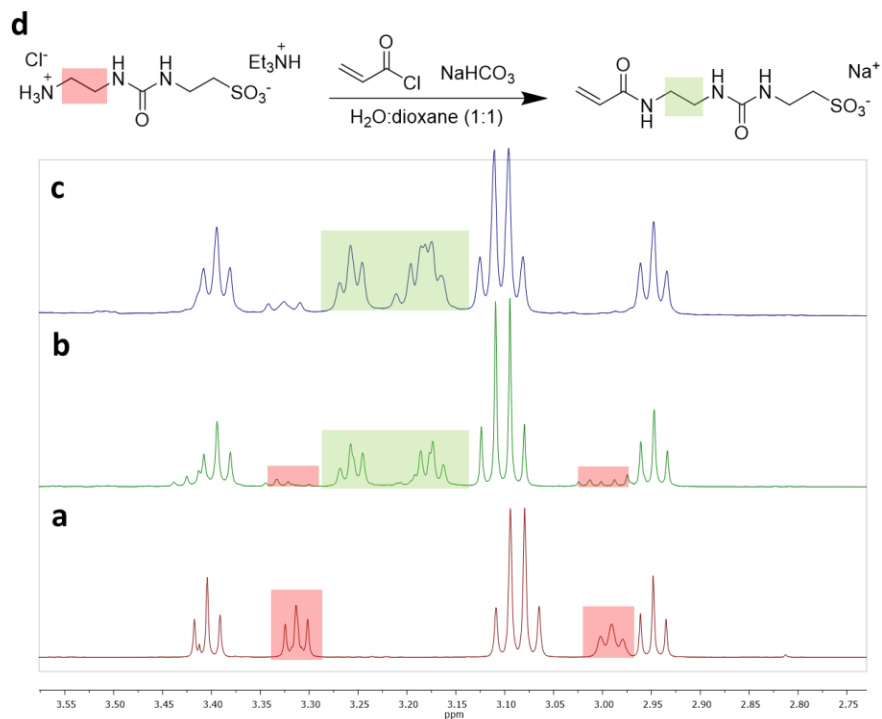


Figure 5.6. ^1H NMR spectra to monitor the functionalization of urea bis-salt starting material (a) and product formed after adding 2.1 equivalents (b) and 3.1 equivalents (c) of acryloyl chloride to starting material. Functionalization reaction scheme (d) with red and green highlighted regions corresponding to bis-salt starting material and monomer respectively.



Figure 5.7. Gelled solution from spontaneous polymerization of functionalized urea monomer product in D_2O .

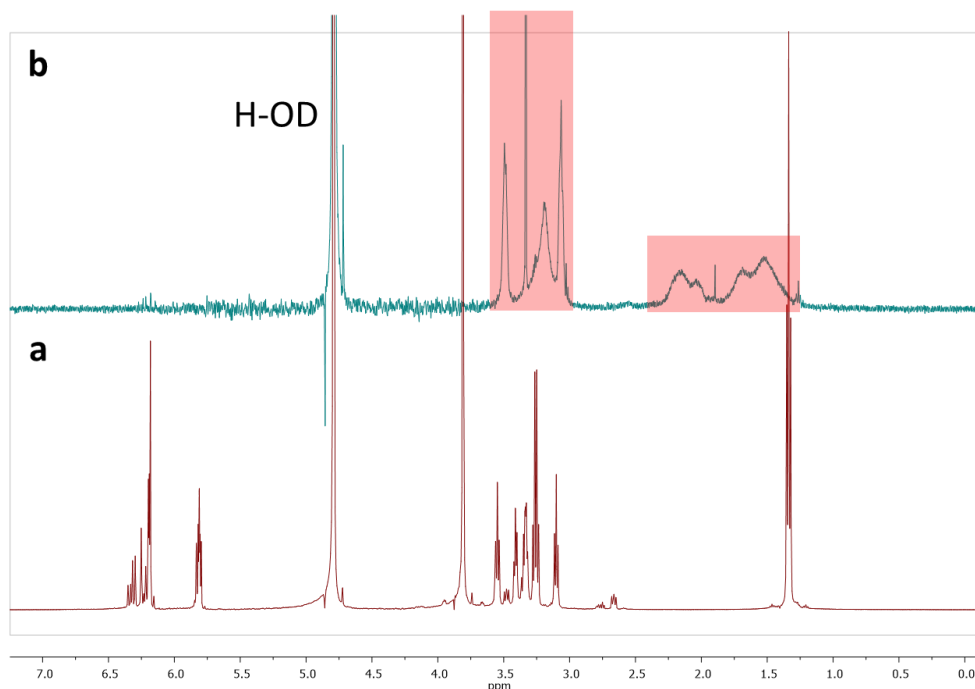


Figure 5.8. ¹H NMR spectra of functionalized urea monomer product before (a) and after workup (b). Peak broadening, highlighted in red, indicate polymer formation.

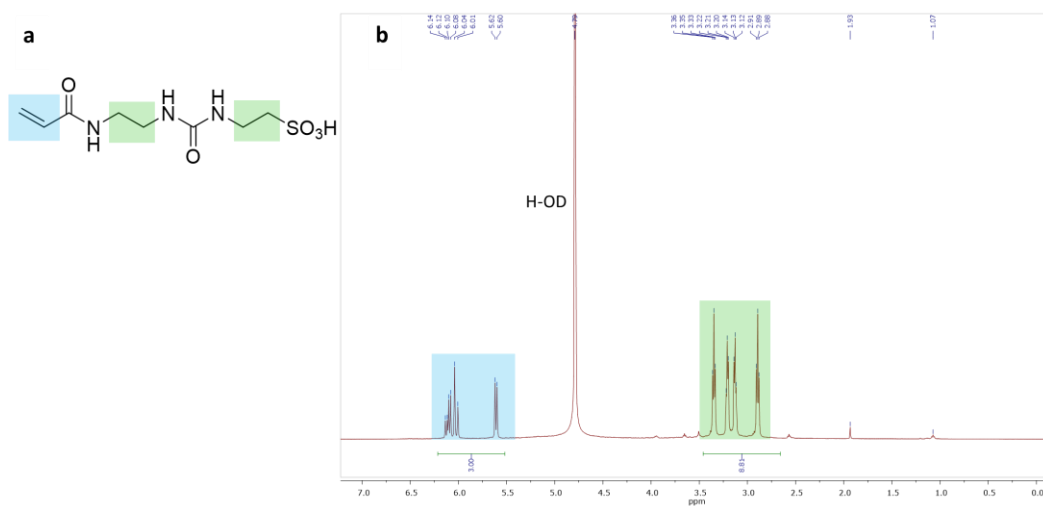


Figure 5.9. ¹H NMR spectrum of urea monomer product after ethyl acetate wash (b). Urea monomer structure (a) with peaks corresponding to vinyl and aliphatic groups of the product are highlighted in blue and green respectively.

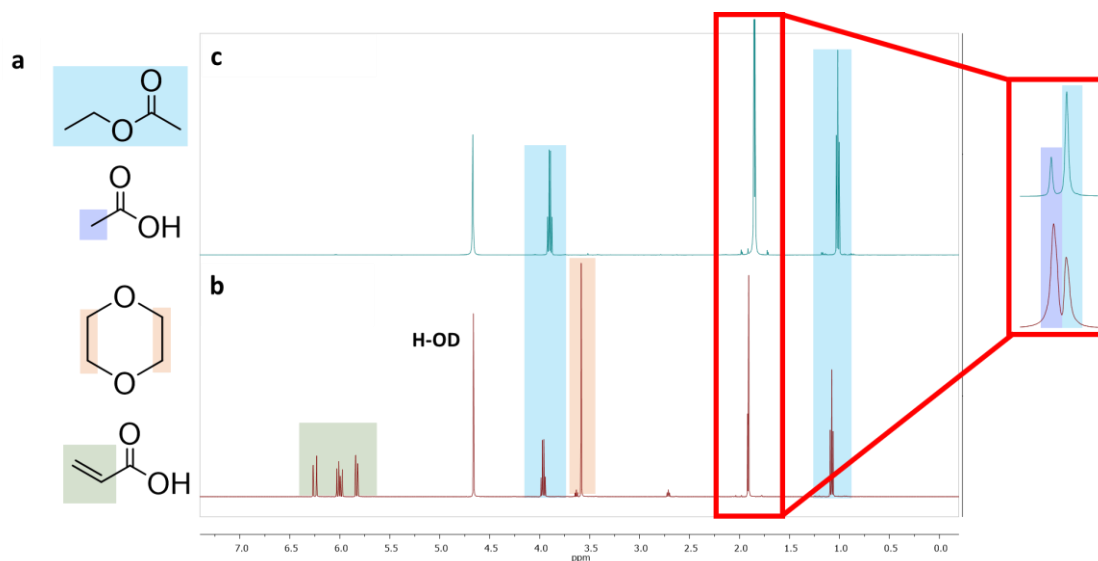


Figure 5.10. ^1H NMR spectra of byproducts removed in the first ethyl acetate wash (b) and after several washes (c). Chemical structures of solvents and reactants (a) with peaks corresponding to their protons highlighted in blue, purple, orange, and green, with a magnified view of region containing overlapping peaks.



Figure 5.11. No gelling of sample dissolved in D_2O , after washing with ethyl acetate.

5.4 AMPSA and AMPSA-Derivatives Polymerization

We use ultra-high molecular weight (UHMW) PAMPSA to make our electrically conductive impact-adaptive, PANI:PAMPSA-based material. To help us understand the effect of chain length on this material's mechanical properties, we will study the material when using different molecular weight average (MW) of PAMPSA. Our lab will achieve this in future work by synthesizing PAMPSA with

shorter MW and test their mechanical properties when used in PANI:PAMPSA-based material.

5.4.1 Free Radical Polymerization

We will start our study by polymerizing different MW AMPSA by using free radical polymerization, due to it being a simple chain growth polymerization that is initiated from a free radical active center to polymerize vinyl monomers. Each chain can either undergo propagation to grow from the addition of monomers to the chain, or terminate by deactivating the active centers, resulting in a dead chain. Since each chain grows from one active center formed from the initiator, the ratio of radical to monomer can be used to roughly predict and control polymer length.

5.4.1.1 PAMPSA Polymerization

The sources of our PAMPSA that we have used for our well-characterized PANI:PAMPSA-based materials are a 15 wt% aqueous solution from Sigma Aldrich, which claims a weight average MW of 2 MDa, and a 10 wt% PAMPSA solution from Fisher Scientific, which claims a weight average MW is 800 kDa. For our polymerization, we decided to produce three different length PAMPSA chains that are shorter than that, in particular, 1 kDa, 10 kDa, and 100 kDa. The resulting MW will be compared to their target MW by using gel permeation chromatography (GPC).

5.4.1.1.1 Procedure

The following procedure for the polymerization in Scheme 5.5 was developed in our lab. AMPSA monomer, water, and a magnetic stir bar was added to a 250 mL beaker and sonicated to dissolve. The solution was purged with N₂ for one hour. It was then stirred and heated in an oil bath on a magnetic stir plate set to 40 °C. Separately, 44 mg ammonium persulfate (APS) initiator was dissolved in N₂-purged water. The APS solution was rapidly added to the stirring AMPSA monomer solution, and covered with parafilm to react overnight. Quantities of reagents were used for each polymerization, and are listed in Table 5.4. When finished, it was removed from the oil bath and allowed to reach room temperature. A small quantity of sample was removed and analyzed using the GPC setup shown in Figure 5.12 with a 100 mM phosphate buffer solution with pH near 8.55. Calibration samples run through the GPC instrument were used to create a calibration curve as shown in Figure 5.13 and used to find the MW of polymerized PAMPSA.

100 kDa					
Reagent	Mass (g)	mmol	eq.	MW (g/mol)	mL
AMPSA	20	96.51	1.00	207.24	—
APS	0.044	0.193	0.002	228.18	—
Water	-	-	-	-	120

10 kDa					
Reagent	Mass (g)	mmol	eq.	MW (g/mol)	mL
AMPSA	20	96.51	1.00	207.24	—
APS	0.440	1.928	0.020	228.18	—
Water	-	-	-	-	120

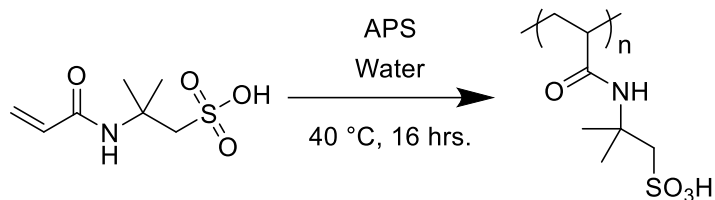
1 kDa					
Reagent	Mass (g)	mmol	eq.	MW (g/mol)	mL
AMPSA	20	96.51	1.00	207.24	—
APS	4.400	19.283	0.200	228.18	—
Water	-	-	-	-	120

Table 5.4. Reactant quantities and ratios used for polymerizing different weight PAMPSA.

6.4.1.1.2 Results and Discussion

Each solution became more viscous as the reaction proceeds. Viscosity appears to be higher in AMPSA with higher target MW. GPC results indicate that each polymer had different MW than what was expected, but that control over the amount of initiator was able to control which polymers would have the lowest, in-between, and highest MW. (Table 5.5). Surprisingly, the purchased PAMPSA that we used for making PANI:PAMPSA was much lower than their reported values, with the '2 MDa' PAMPSA measured to be 459,965 Da, and the '800 kDa' measured to be 471,427 kDa, indicating that either a problem with the procedure or their claimed MW are not accurate. These results indicate that the free radical

polymerization method is very limited at controlling MW, as the target and measured MW of synthesized PAMPSA could differ by two orders of magnitude.



Scheme 5.5. Reaction scheme for the free radical polymerization of AMPSA.

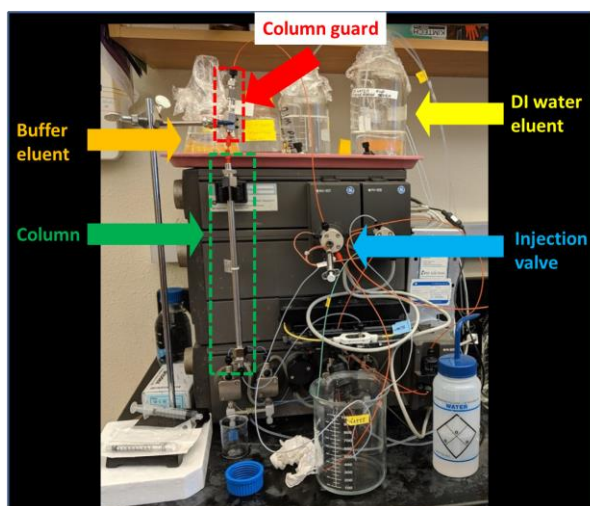


Figure 5.12. GPC machine used for PAMPSA MW characterization.

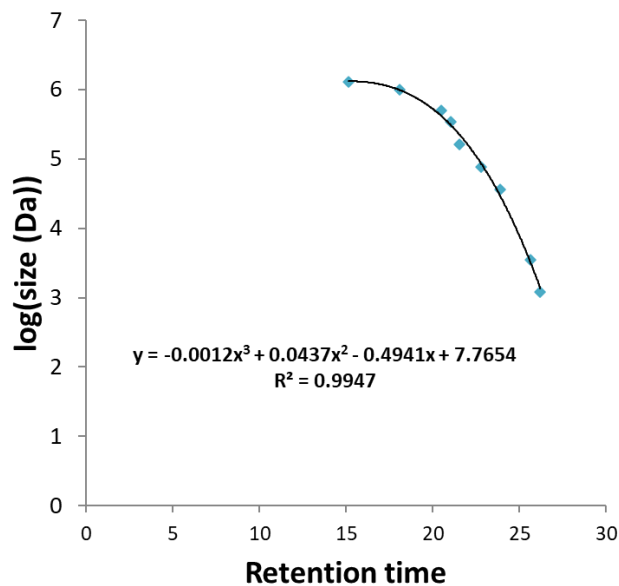


Figure 5.13. Calibration curve derived from GPC calibration standards.

PAMPSA Sample	Calculated Size (Da)
'1 kDa'	126,510
'10 kDa'	459,965
'100 kDa'	616,995
Thermal Fisher '800 kDa'	471,427
Sigma Aldrich '2 MDa'	459,965

Table 5.5. Sizes of polymers analyzed with GPC.

5.4.1.2 Squaramide Polymerization

Squaramide is the strongest hydrogen bonding AMPSA variant in our study. This monomer has been synthesized by our lab, but still requires conversion to its acidic form and needs to be polymerized.

5.4.1.2.1 Protonation with Cation Exchange Resin Procedure

To perform the ion exchange reaction of the squaramide monomer shown in Scheme 5.6, 0.25 g of squaramide monomer was dissolved in 1 mL deionized water and added to a column with 2 mL of washed cation exchange resin with deionized water. The quantities are summarized in Table 5.6. It was then eluted through column with deionized water until pH increases to about 5, then dried *in vacuo* and the product was stored at -4 °C.

Scheme 5.6. Reaction scheme for the cation ion exchange reaction of squaramide monomer.

Reagent	MW (g/mol)	Molar eq.	mmol	Mass or Volume
Squaramide Salt	339.3	1	0.737	250 mg
Cation Exchange Resin		3	2.210	1.105 mL

Table 5.6. Reactant quantities and ratios used for cation exchange reaction of squaramide monomer.

5.4.1.2.1.1 Observations

Product is light brown sticky viscous liquid while drying, and becomes a solid when fully dried. Monomer has good purity according to ¹H NMR (Figure 5.14b).

5.4.1.2.2 Squaramide Polymerization

Hydrogen bonding between polymer chains is an important factor influencing the mechanical properties of our conductive impact-adaptive material. To study this, we made an AMPSA-based polymer with a squaramide moiety, which forms strong hydrogen bonds. To carry this out, we used a squaramide monomer that was synthesized by our group, and polymerized it. However, we

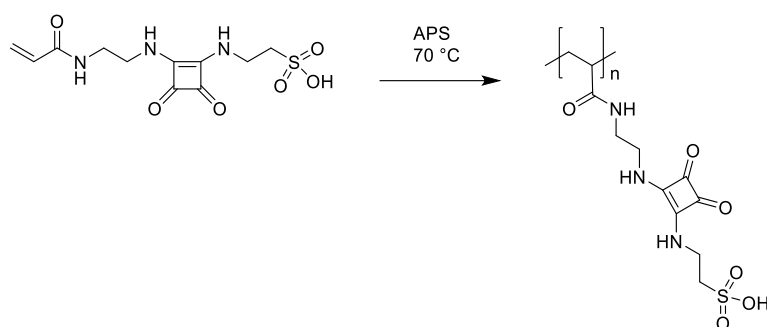
must first test it on a small scale. This test used the previously used free radical polymerization of AMPSA.

5.4.1.2.2.1 Procedure

To carry out the squaramide monomer polymerization depicted in Figure 5.7, deionized water was N₂-purged. 221 mg of squaramide monomer, a magnetic stir bar, and 1.25 mL water was added to a 20 mL glass vial. Separately, 4.44 mg of APS was dissolved in 1 mL water in a vial. The quantities are summarized in Table 5.7. Each solution was purged again for 10 minutes. The APS solution was added to the squaramide solution, covered, then mixed and heated at 70 °C overnight. ¹H NMR was used to check for reaction progress.

5.4.1.2.2.2 Results and Observations

After polymerizing overnight, ¹H NMR was used to check the reaction progress, but only 59% of the monomer had been consumed (Figure 5.14c). The presence of APS was checked with peroxide test strips, which indicated the absence of peroxide, and the consumption of the oxidizer. Because of this, a more robust method for polymerization is required to polymerize this monomer.



Scheme 5.7. Reaction scheme for the polymerization of squaramide monomer.

Reagent	MW (g/mol)	Molar eq.	mmol	Mass or Volume
Squaramide Monomer	317.32	1	0.696	221 mg
APS	228.18	0.028	0.019	4.44 mg
DI Water	18	-	-	1.25 mL

Table 5.7. Reactant quantities and ratios used for polymerizing the squaramide monomer.

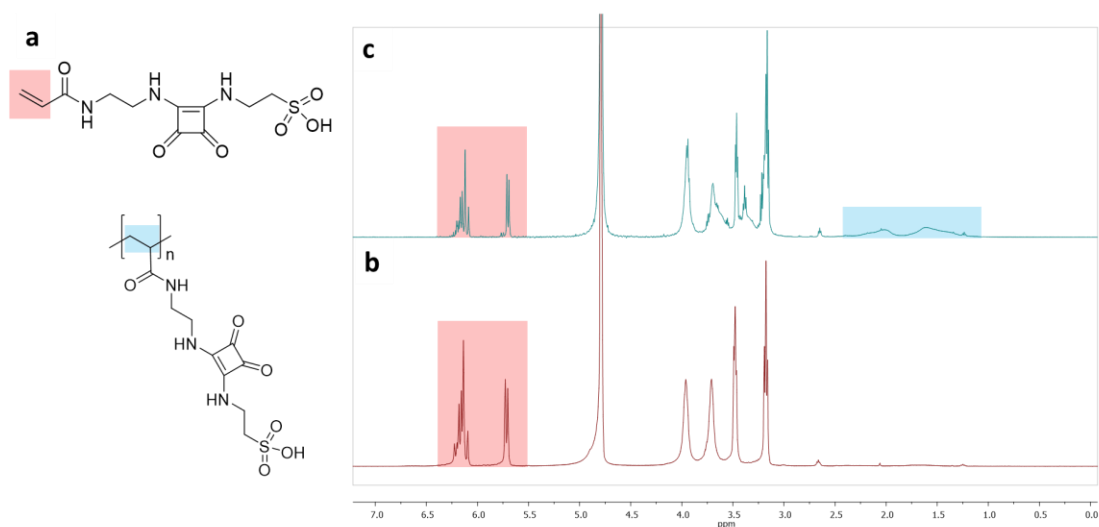


Figure 5.14. ^1H NMR spectrum of squaramide monomer (b) containing some formed polymer. Chemical structures of monomer and polymer (a) with peaks corresponding to their protons highlighted in red and blue. Mixture of monomer and polymer after polymerizing overnight (c).

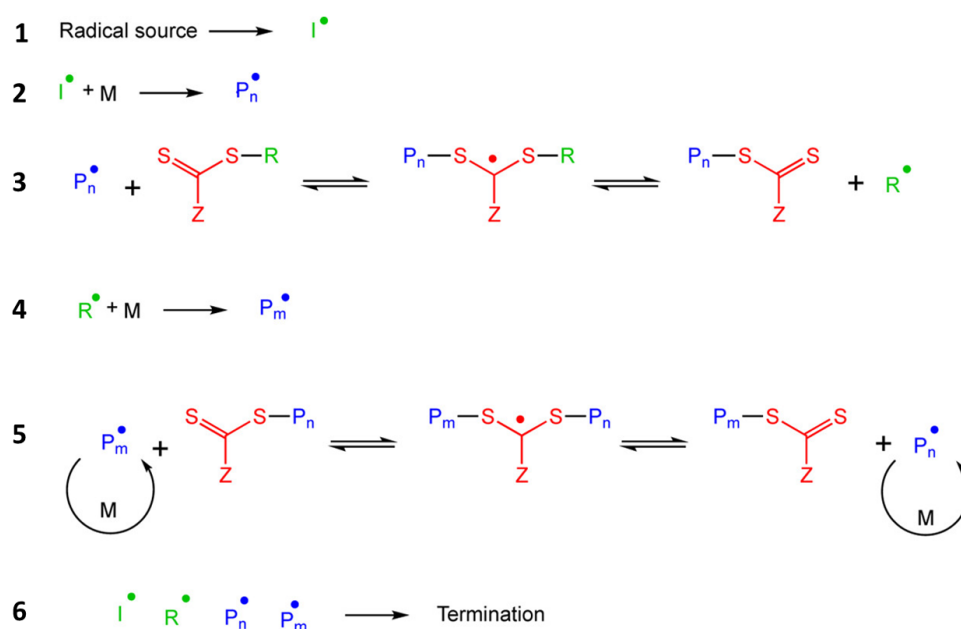
5.4.2 RAFT Polymerization

Our previous efforts to polymerize ultra-high molecular weight PAMPSA and the squaramide monomer using free radical polymerization either had low yield due to the early termination of radicals on growing chains, resulting in low yields¹² or uncontrolled molecular weight. Samples with low yield required prolonged heating over several days to polymerize remaining monomers. These two shortcomings led us to explore using alternative methods for polymerizing AMPSA and AMPSA-based monomers.

5.4.2.1 RAFT Mechanism and Advantage

Reversible deactivation radical polymerization (RDRP) or living radical polymerization methods are widely used, due to their ability to provide predictable, molecular weight and narrow size distribution, as well as a good tolerance for impurities. One of these methods is reversible addition-fragmentation chain transfer (RAFT) polymerization, which we chose for our polymerization of ultra-high molecular weight PAMPSA for its wide range of compatible polymers and the simplicity of the polymerization procedure. In a typical RAFT polymerization, there is a radical source, which is often a thermally-activated initiator, a RAFT agent, a monomer, and a solvent. The structure of a RAFT agent consists of a tiocarbonylthio group (Z-C(=S)S-R), a Z substituent that controls its reactivity and

solubility, and an R substituent which is a free radical leaving group capable of reinitiating polymerization.¹² When the initiator is activated, it decomposes into radical species, and each can bond with monomers in solution to produce active growing chains. An active chain will bond to the RAFT agent to become a dormant chain, and cause the RAFT agent to release an attached R substituent which becomes an active chain. The process repeats until monomers are fully consumed, or active chains undergo radical termination (Scheme 5.8).^{12,13} Typically, a small ratio of initiator to RAFT agent is used, which limits the number of active chains present in the reaction at any given time. This limits the number of chain termination events to allow it to reach ultra-high molecular weights.



Scheme 5.8. Mechanism of RAFT polymerization with activation (1), radical species adding to monomer (2), radical species adding to the RAFT agent and equilibrium between active and dormant chains (3), chain growth (4), equilibrium between active and dormant chains (5), and termination (6).¹²

5.4.2.2 AMPSA RAFT Polymerization Methods and Procedure

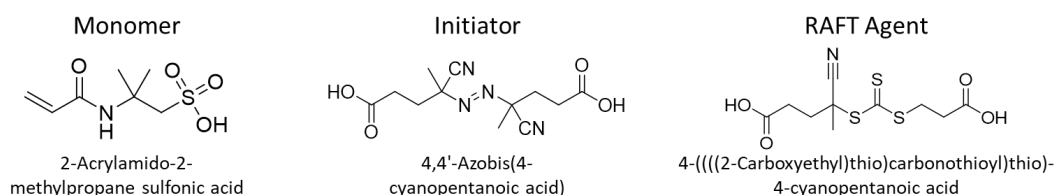
To design our procedure, we first determined the appropriate amounts of initiator and RAFT agent to use. For synthesizing our ultra-high molecular weight AMPSA-based polymers, we need to use a low ratio of initiator to RAFT agent to prevent premature termination of active chains. Work by Read and coworkers demonstrated that AMPSA copolymers could be polymerized to over 10^6 Da when

the initiator to RAFT ratio was 1:8.44 or less,¹⁴ leading us to use a 1:10 ratio. Additionally, the desired degree of polymerization can be easily calculated from the molar ratio of RAFT agent to monomer. For a target MW of 10⁶ Da, we used a RAFT agent to AMPSA ratio of 1:4825.32. Quantities and ratios of reactants are shown in Table 5.8.

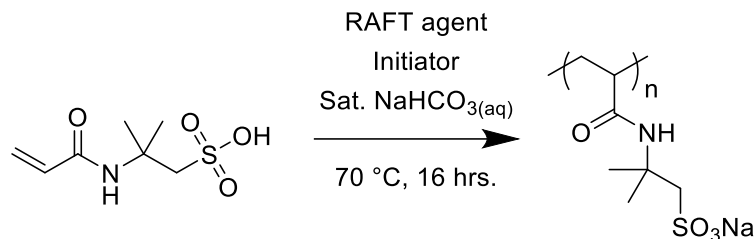
PAMPSA and PAMPSA-derivatives will later be polymerized with polyaniline, starting from a 15 wt% aqueous polymer solution. Using water as the solvent allows us to directly use the product for polymerizing with aniline after the PAMPSA and PAMPSA-derivatives are synthesized.

For our initiator and RAFT agent, we chose 4,4'-azobis(4-cyanopentanoic acid) and agent 4-(((2-carboxyethyl)thio)carbonothioyl)thio)-4-cyanopentanoic, respectively, each of which contain two carboxylic acid groups to improve water solubility (Scheme 5.9).

To perform the polymerization depicted in Scheme 5.10, approximately 100 mL of a saturated NaHCO₃ aqueous solution was N₂-purge for approximately 20 minutes. Serial dilution was used with the purged NaHCO₃ solution to get a 1.0 mL solution with 0.28 mg of initiator, and another 1.0 mL solution with 3.07 mg of RAFT agent. To a 500 mL round bottom flask, 10 g AMPSA monomer was added and dissolved in 56.67 mL of saturated NaHCO₃ solution. A summary of quantities is shown in Table 5.8. The RAFT agent and initiator solutions were added to the flask and stir briefly. The solution was frozen with a dry ice/acetone slurry, followed by five cycles of vacuum and backfilling with N₂. The Teflon mechanical stirrer and condenser column were attached while there is a strong flow of N₂ gas to prevent oxygen from entering the system, then the reaction was placed in a 70 °C oil bath, and stirred overnight. ¹H NMR was used to check the reaction progress and allowed to run longer if necessary. Once finished, it was removed from heat and stored in an air-tight container.



Scheme 5.9. Chemical structures and names of monomer, initiator, and RAFT agent used for AMPSA RAFT polymerization.



Scheme 5.10. Reaction of RAFT polymerization of AMPSA monomer.

Reagent	Mass (mg)	MW (g/mol)	mmol	mL
AMPSA	1.00E+04	207.24	48.25	
Initiator	0.280	280.28	0.001	
RAFT	3.074	307.41	0.010	
Sat. NaHCO ₃ Soln.				56.67

Table 5.8. Reactant quantities and ratios used for RAFT polymerization of AMPSA monomer.

5.4.2.2.1 Results and Discussion

When attempting to dissolve the initiator and RAFT agent in water, they were found to not be fully water soluble. To work around this problem, the polymerization solvent was changed to aqueous saturated sodium bicarbonate which converts the acidic moieties to sodium salts and increase their water solubility. This change was successful at fully dissolving all reaction components.

The first trial was run on a small scale with 10 % of the amount of reagents used in Table 5.8. We ran the experiment in a 20 mL vial capped with a rubber septum, stirred with a magnetic stir bar, and purged with N₂ and no vacuum was used. Polymerization occurred within 16 hours, but ¹H NMR indicated that only 78.5 % of the monomer had been converted to polymer (Figure 5.15). This was likely due to the fact that the small scale of the reaction caused much of the solvent to evaporate out of the reaction and condense on the reaction vial and slow the reaction rate. Trace oxygen contamination could have also terminated the reaction, due to the fact that it was not run under a constant input of fresh N₂. To address these issues, the reaction was scaled up to prevent water loss, and freeze-pump-thaw was used to remove all oxygen. Additionally, the resulting target 1 MDa PAMPSA solution would have a very high viscosity, and required the

continuous stirring with a mechanical stir paddle to ensure the reaction is thoroughly mixed until completion.

To do this, the reaction was scaled up tenfold, a three-neck flask was used with a Teflon stir paddle on a mechanical stirrer, a vacuum/nitrogen inlet on one side neck, and a condenser column. The condenser column was capped with a rubber stopper with a needle outlet which would force the reaction to run under positive pressure of N₂ and prevent oxygen from entering when assembling the mixture apparatus shown in Figure 5.16.

¹H NMR indicated that there was only a trace amount of monomer left in the reaction after 16 hours, and a nearly undetectable amount left after 8 more hours (Figure 5.17). These conditions were then chosen for the reaction conditions due to the complete polymerization.

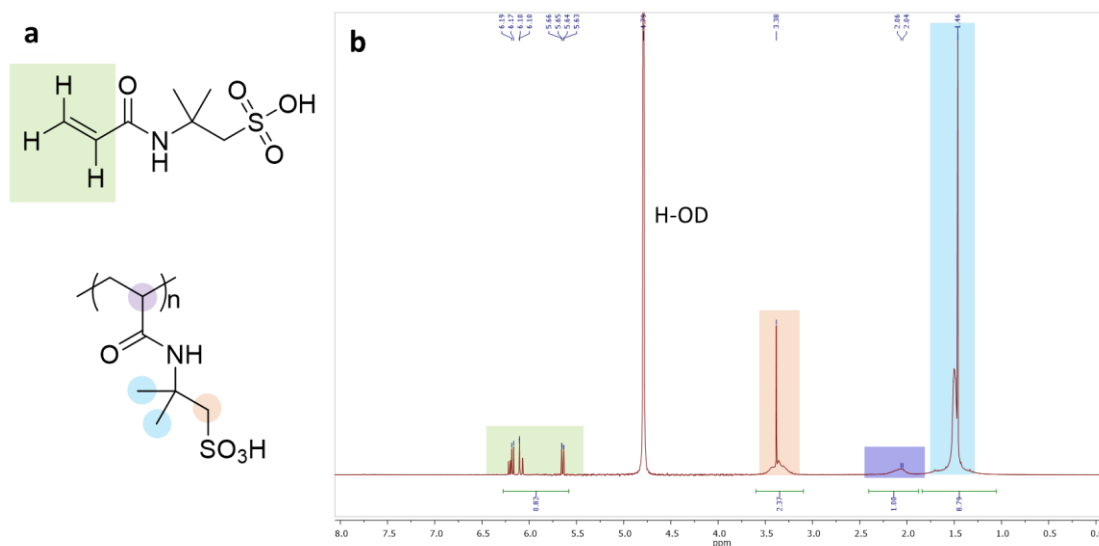


Figure 5.15 ¹H NMR spectrum of AMPSA RAFT polymerization in a vial after 16 hours (b). Chemical structures of monomer and polymer (a) with peaks corresponding to their protons highlighted in blue, green, purple, and orange.

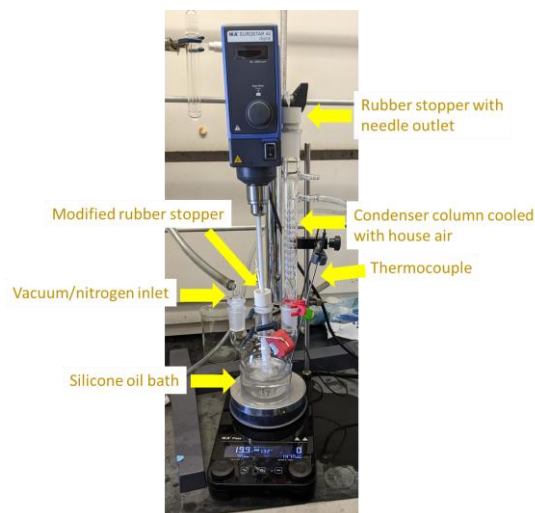


Figure 5.16. Large-scale AMPSA RAFT polymerization apparatus with labeled parts.

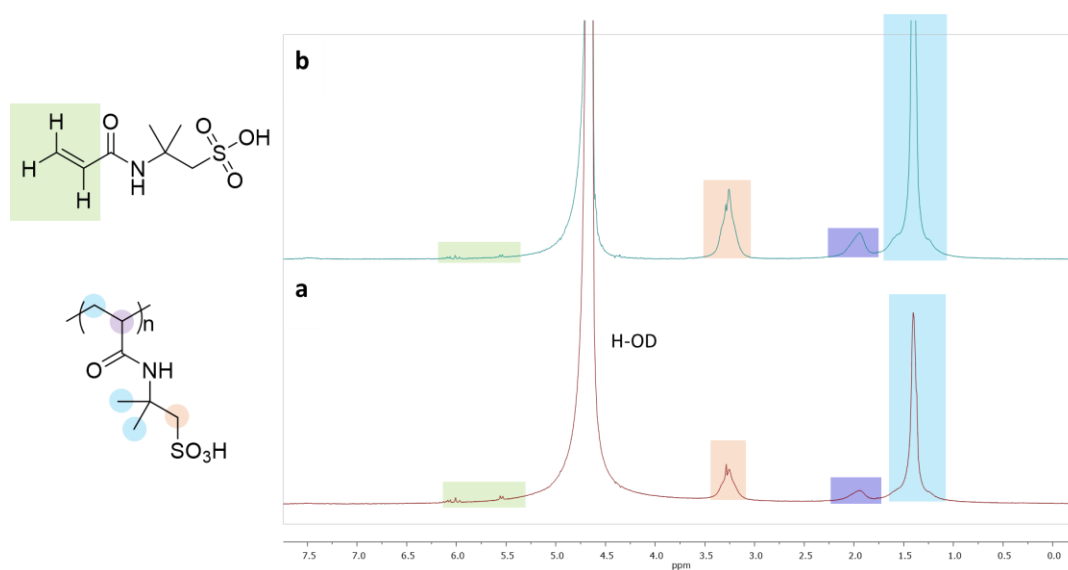


Figure 5.17. ^1H NMR spectrum of AMPSA polymerization after 16 hours (b) and 24 hours (c). Regions corresponding to monomer and polymer. Chemical structures of monomer and polymer (a) with peaks corresponding to their protons highlighted in blue, green, purple, and orange.

5.4.2.2.2 MAMPSA Polymerization

Our previous attempts to polymerize MAMPSA using free radical polymerization resulted in an uncontrolled polymerization with premature

termination of the active chains, and incomplete polymerization. We wanted to be able to polymerize ultra-high molecular weight PMAMPSA, which requires a more controlled polymerization method like RAFT. Since we successfully used the RAFT method with AMPSA, we set out to use this method to polymerize the MAMPSA monomer.

We started by using the polymerization method used for the RAFT polymerization of AMPSA (Table 5.8), but used the MAMPSA monomer and scaled the reaction down by 60 % to avoid using all of the synthesized monomer. After running the reaction for 24 hours, the monomer conversion was only 65.4 % (Figure 5.18). This may be from the smaller reaction being more influenced by the water condensing on the flask, and possibly some impurities poisoning the polymerization. Some impurities are in the sample based on TLC analysis (Figure 5.19), but ^1H NMR indicated the presence of a negligible amount of impurities (Figure 5.20).

The presence of some nucleophiles in the reaction can possibly hydrolyze the RAFT initiator, such as hydroxide ions from NaHCO_3 , and potentially deactivate the RAFT agent.¹⁵ This was thought to be the reason for the low degree of polymerization at the time of this experiment. To address this concern, DMF was used as a cosolvent with water, instead of a NaHCO_3 solution to polymerize MAMPSA.

A large quantity of PMAMPSA was needed for polymerizing PANI:PMAMPSA. The reaction was scaled up to use 11.7 g of MAMPSA with many of the same conditions used for the successful RAFT polymerization of AMPSA. To ensure that the polymerization proceeded to completion, 5x the amount of initiator was used. Additionally, the sodium salt form of MAMPSA was used to prevent hydrolysis of the RAFT agent. After 29 hours, the reaction had reached 73 % conversion, and was allowed to run for a total of four days to ensure all monomer had polymerized (Figure 5.21). At the end of the reaction, a small amount of monomer remained, possibly from the reaction terminating from some trace impurities in MAMPSA. To remove the remaining monomer, the reaction product was dissolved in water, then crashed out in acetone, washed first with acetone, diethyl ether, and finally hexane. The product was then dried *in vacuo*. No monomer was present in the final product, but trace DMF and acetone remained (Figure 5.22). The polymer was then converted from the salt form to protonated acid form using three molar equivalents of cation exchange resin. The product was then dried *in vacuo* to become a white, colorless solid. This product was then used to synthesize PANI:PMAMPSA.

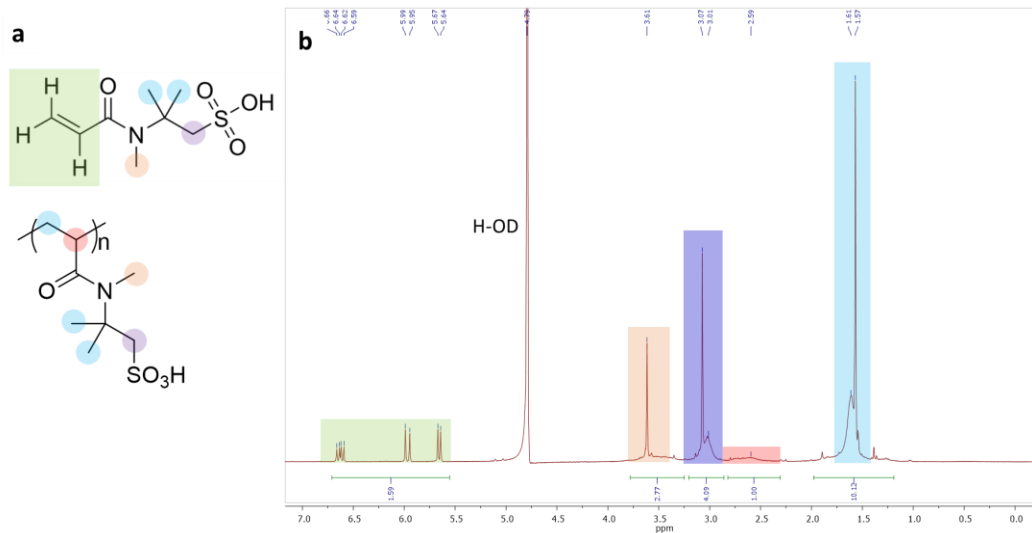


Figure 5.18. ^1H NMR spectrum of MAMPSA polymerization (b). Chemical structures of monomer and polymer (a) with peaks corresponding to their protons highlighted in blue, green, purple, and orange.

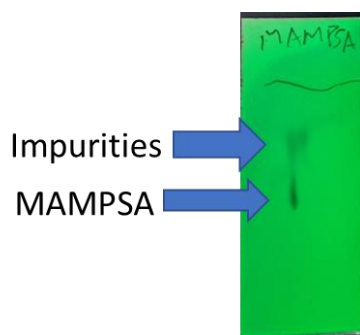


Figure 5.19. TLC plate indicating the presence of impurities in MAMPSA starting material.

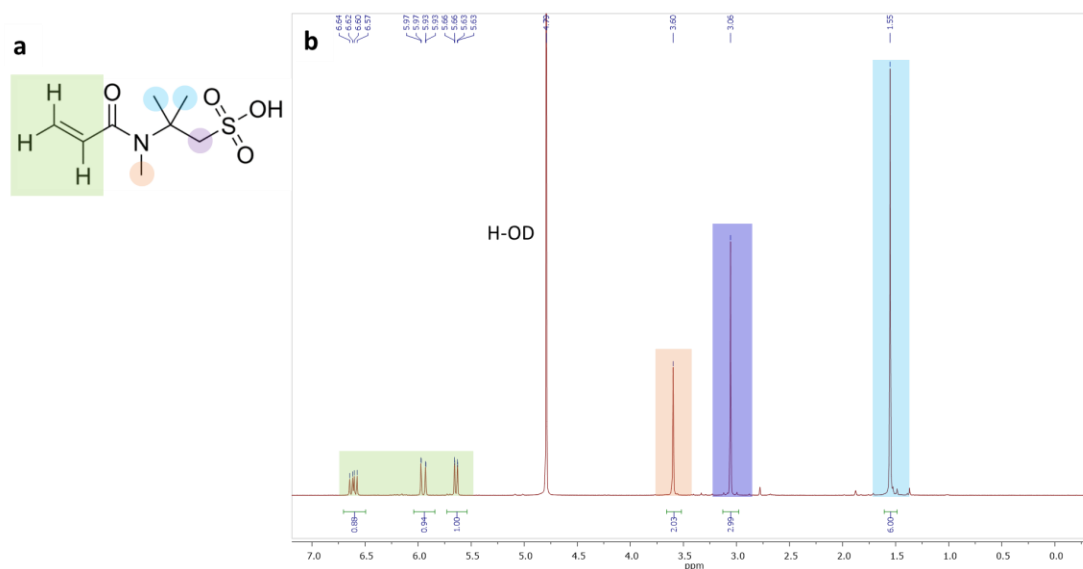


Figure 5.20. ^1H NMR spectrum of MAMPSA monomer used in RAFT polymerization (b). MAMPSA chemical structure (a) with peaks corresponding to their protons highlighted in blue, green, purple, and orange.

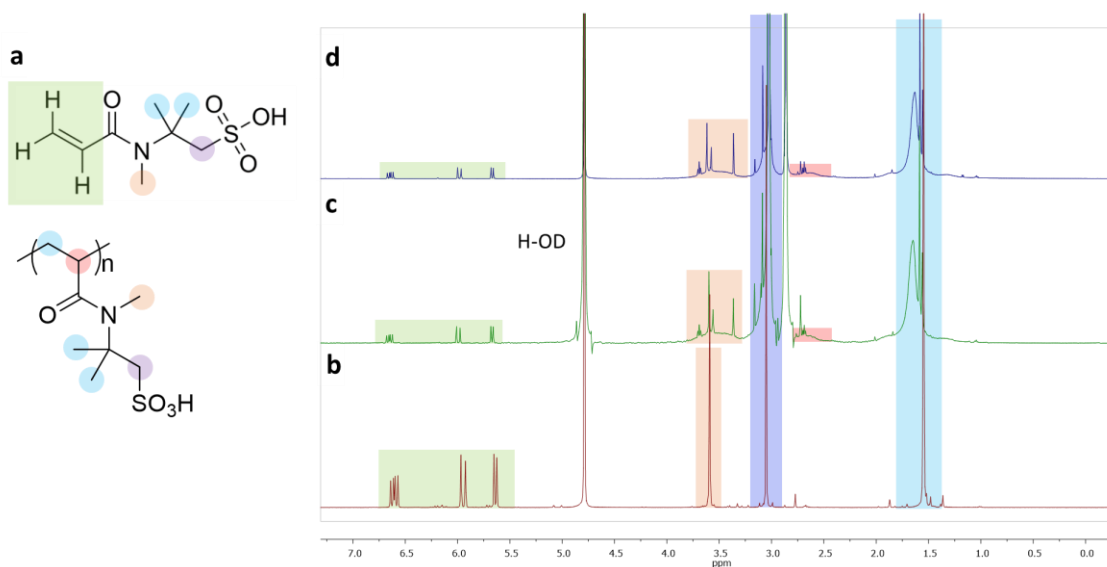


Figure 5.21. ^1H NMR spectrum of MAMPSA starting material (b) and products of MAMPSA polymerization with the RAFT method after 29 hours (c) and after four days (d). Chemical structures of monomer and polymer (a) with peaks corresponding to their protons highlighted in blue, green, purple, and orange.

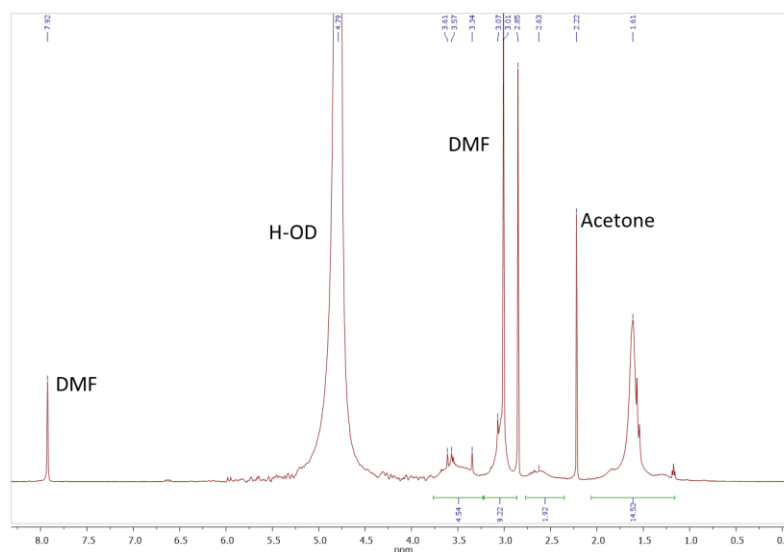


Figure 5.22. ^1H NMR spectrum of solvent-washed PMAMPSA product.

5.5 Synthesis of PANI:PMAMPSA

PANI:PMAMPSA synthesis was based on the procedure used to make PANI:PAMPSA in our previous work,¹ but scaled down before making larger quantities.

5.5.1 Procedure

1.13 g of PMAMPSA was dissolved in 7.61 mL deionized water in a 20 mL glass vial. 127 mg APS was then stir for two minutes with a Teflon stir paddle connected to a mechanical stirrer. 470 μL aniline was rapidly added and stirred thoroughly at 130 RPM. Material that accumulates on the stir paddle was scraped off and placed back into the mixture, and allowed to stir overnight. Figure 5.23 shows an image of the stirring PANI:PMAMPSA solution. The next day, the product was washed out with approximately 60 mL acetone and added to a glass beaker, covered with parafilm, and allow it to stir with the Teflon stir paddle at 130 RPM overnight. This was repeated twice, but with 40 mL acetone each time. When done, product was dried in a vented oven at 80 $^{\circ}\text{C}$ for 24 hours and stored in an airtight container.

5.5.2 Observation and Discussion

Some of the aniline took a while to dissolve, and some formed a dark residue on the top layer of the solution that became stuck on the paddle. This was scraped into the solution and stirred rapidly to dissolve it. After PANI:PMAMPSA was dried, the PANI:PMAMPSA ratio was analyzed with ^1H NMR (Figure 5.24). Results indicate that the uniform mixing resulted in few impurities remained.

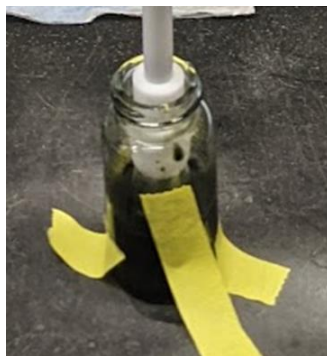


Figure 5.23. Image of polymerizing PANI to produce PANI:PMAMPSA in a vial and mixed using a Teflon stir paddle.

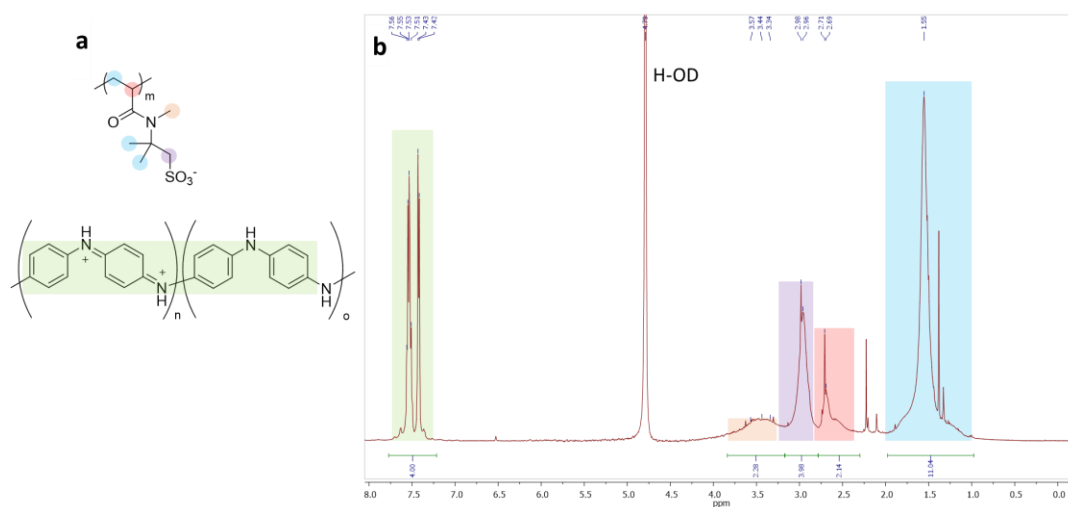


Figure 5.24. ^1H NMR spectrum of PANI:PMAMPSA product (b). Chemical structures of PANI and PMAMPSA (a) with peaks corresponding to their protons highlighted in blue, green, purple, red, and orange.

5.6 Conclusion and Outlook

In this work, we provided details of the synthesis of AMPSA derivatives with different levels of hydrogen bonding, which includes no hydrogen bonding (MAMPSA), and strong hydrogen bonding (urea-containing AMPSA derivative). These monomers, along with the strong hydrogen bonding squaramide monomer, were prepared for polymerization with ion exchange resin to convert them into their acid form. Importantly, the procedure for polymerizing ultra-high molecular weight AMPSA using a RAFT agent was optimized, and will later be used for polymerizing AMPSA derivatives by future members of our lab. Polymerization of PANI in an aqueous PMAMPSA solution was carried out on small scale, and will be scaled up for future experiments.

This work is incomplete, and requires the polymerization of each AMPSA-derivative monomer on a large scale, followed by the polymerization of PANI in the presence of each polymer solution. Their strain-rate adaptive behavior will then be tested and compared to that of the PANI:PAMPSA system in our previous work.¹ The work from this chapter brings us closer to allowing for a more detailed study on the role of hydrogen bonding of AMPSA in PANI:PAMPSA strain-rate adaptive conductive material, with the anticipated ability to use various hydrogen bonding to tune the strain-rate adaptive behavior for building more damage tolerant electronic material.

5.7 References

- (1) Hernandez, V.; Jordan, R. S.; Hill, I. M.; Xu, B.; Zhai, C.; Wu, D.; Lee, H.; Misiaszek, J.; Shirzad, K.; Martinez, M. F.; Kusoglu, A.; Yeo, J.; Wang, Y. Deformation Rate-Adaptive Conducting Polymers and Composites. *Small* **2023**, *19* (35), 1–12. <https://doi.org/10.1002/sml.202207100>.
- (2) J. Murphy, R.; M. Weigandt, K.; Uhrig, D.; Alsayed, A.; Badre, C.; Hough, L.; Muthukumar, M. Scattering Studies on Poly(3,4-Ethylenedioxythiophene)–Polystyrenesulfonate in the Presence of Ionic Liquids. *Macromolecules* **2015**, *48* (24), 8989–8997. <https://doi.org/10.1021/acs.macromol.5b02320>.
- (3) Takano, T.; Masunaga, H.; Fujiwara, A.; Okuzaki, H.; Sasaki, T. PEDOT Nanocrystal in Highly Conductive PEDOT:PSS Polymer Films. *Macromolecules* **2012**, *45* (9), 3859–3865. <https://doi.org/10.1021/ma300120g>.
- (4) Sezen-Edmonds, M.; Loo, Y.-L. Beyond Doping and Charge Balancing: How Polymer Acid Templates Impact the Properties of Conducting Polymer Complexes. *J. Phys. Chem. Lett.* **2017**, *8* (18), 4530–4539. <https://doi.org/10.1021/acs.jpcclett.7b01785>.
- (5) Yilgör, E.; Yilgör, İ.; Yurtsever, E. Hydrogen Bonding and Polyurethane Morphology. I. Quantum Mechanical Calculations of Hydrogen Bond Energies and Vibrational Spectroscopy of Model Compounds. *Polymer (Guildf)*. **2002**, *43* (24), 6551–6559. [https://doi.org/https://doi.org/10.1016/S0032-3861\(02\)00567-0](https://doi.org/https://doi.org/10.1016/S0032-3861(02)00567-0).
- (6) de Azevedo Santos, L.; Cesario, D.; Vermeeren, P.; van der Lubbe, S. C. C.; Nunzi, F.; Fonseca Guerra, C. σ -Electrons Responsible for Cooperativity and Ring Equalization in Hydrogen-Bonded Supramolecular Polymers. *Chempluschem* **2022**, *87* (2), e202100436. <https://doi.org/https://doi.org/10.1002/cplu.202100436>.
- (7) Dixon, D. A.; Dobbs, K. D.; Valentini, J. J. Amide-Water and Amide-Amide Hydrogen Bond Strengths. *J. Phys. Chem.* **1994**, *98* (51), 13435–13439. <https://doi.org/10.1021/j100102a001>.
- (8) Alsohaimi, I. H.; Khan, M. R.; Ali, H. M.; Azam, M.; Alammari, A. M. Solvent Extraction and Gas Chromatography–Mass Spectrometric Determination of Probable Carcinogen 1,4-Dioxane in Cosmetic Products. *Sci. Rep.* **2020**, *10* (1), 5214. <https://doi.org/10.1038/s41598-020-62149-x>.
- (9) Jackson, H. L.; McCormack, W. B.; Rondestvedt, C. S.; Smeltz, K. C.; Viele, I. E. Control of Peroxidizable Compounds. *J. Chem. Educ.* **1970**, *47* (3), A175. <https://doi.org/10.1021/ed047pA175>.

- (10) Kelly, R. J. Review of Safety Guidelines for Peroxidizable Organic Chemicals. *Chem. Health Saf.* **1996**, *3* (5), 28–36. <https://doi.org/10.1021/acs.chas.8b03515>.
- (11) Clark, D. E. Peroxides and Peroxide-Forming Compounds. *Chem. Health Saf.* **2001**, *8* (5), 12–22. [https://doi.org/10.1016/S1074-9098\(01\)00247-7](https://doi.org/10.1016/S1074-9098(01)00247-7).
- (12) Perrier, S. 50th Anniversary Perspective: RAFT Polymerization—A User Guide. *Macromolecules* **2017**, *50* (19), 7433–7447. <https://doi.org/10.1021/acs.macromol.7b00767>.
- (13) Millard, P.-E.; Barner, L.; Reinhardt, J.; Buchmeiser, M. R.; Barner-Kowollik, C.; Müller, A. H. E. Synthesis of Water-Soluble Homo- and Block-Copolymers by RAFT Polymerization under γ -Irradiation in Aqueous Media. *Polymer (Guildf)*. **2010**, *51* (19), 4319–4328. <https://doi.org/https://doi.org/10.1016/j.polymer.2010.07.017>.
- (14) Read, E.; Guinaudeau, A.; James Wilson, D.; Cadix, A.; Violleau, F.; Destarac, M. Low Temperature RAFT/MADIX Gel Polymerisation: Access to Controlled Ultra-High Molar Mass Polyacrylamides. *Polym. Chem.* **2014**, *5* (7), 2202–2207. <https://doi.org/10.1039/C3PY01750H>.
- (15) L. McCormick, C.; B. Lowe, A. Aqueous RAFT Polymerization: Recent Developments in Synthesis of Functional Water-Soluble (Co)Polymers with Controlled Structures. *Acc. Chem. Res.* **2004**, *37* (5), 312–325. <https://doi.org/10.1021/ar0302484>.

Chapter 6

Outlook

Chapter 1 of this dissertation discusses important fundamental properties of CPs, including conductivity and solubility, and how processing conditions can dramatically influence them. The following discussion provided valuable insight to important challenges in the field of AM of CPs, including the barriers to achieving truly 3D shapes with high conductivity. The following Chapters 2 and 3 provided new approaches we have taken that overcome these barriers, and provide detailed studies of how these processes influence their structure-conductivity relationships, which are essential to guiding new research of these new techniques for 3D printing with other CPs. These works also resolve the tradeoff between printability and material choice that are commonly encountered when 3D printing with CPs, and can be generalized to other 3D printing methods and materials. The final Chapters 4 and 5 focus on achieving structural design of conducting polymers at the intermolecular level (as opposed to the macro level with 3D printing) by careful control of their self-assembly environment. The detailed work of these studies should assist in the facile assembly of ordered CP structures for high conductivity, as well as provide guidance for synthesizing various ionic polymers that facilitate the strain-rate adaptive behavior of PANI:PAMPSA.

The work covered in this dissertation made several key contributions to their respective fields. In Chapter 2, we discovered and characterized the anisotropic conductivity that arises during the DIW printing of a doped PEDOT:PSS ink, developed a method for its removal, and were the first to produce DIW printed PEDOT:PSS that meets and exceeds the 1000 S/cm benchmark for high conductivity. These advances have the potential to expand the range of geometric complexity, provide guidance for predicting conductivity anisotropy when printing multiple layers, and expand the adoption of DIW printing PEDOT:PSS for high performance organic electronics. In Chapter 3, we addressed the compromise between conductivity and 3D shape complexity with our unique approach to casting a PEDOT precursor into removable intricate 3D molds, followed by solid-state polymerization into pure PEDOT structures. This represented an enormous increase of the content of CP and conductivity improvement by nearly two orders of magnitude compared to other VP-produced complex 3D shapes with CPs. We also demonstrated that the molten DBEDOT can act as a carrier for highly conductive silver flakes, boosting conductivity to over 8000 S/cm.

In Ch. 4, we found that the self-assembly of CPs into single crystals can be controlled using oligomers of the parent polymers, dramatically enhancing conductivity while remaining compositionally pure. The self-assembly of solution-processed CPs has previously been shown to occur via seeding from foreign molecules through π - π stacking, like carbon nanotubes, we identified a facile

method for controlling the morphology without addition of foreign molecules. In Chapter 5, we demonstrated the synthesis of monomers and polymers required for studying the strain-toughening mechanism that emerges partially from hydrogen bonding that occurs in self-assembled PANI:PAMPSA. This includes large scale synthesis of our methylated-AMPSA monomer, and polymerization conditions for high molecular weight PAMPSA solutions. These studies were documented in detail, and laid the groundwork for further studies of hydrogen bonding effects on strain-rate adaptive PANI:PAMPSA electronic materials.

Despite these many advancements in the fields of CPs and AM of CPs, several challenges remain to be addressed. The process of DIW printing PEDOT:PSS with a removable support gel is effective for achieving high conductivity and 3D design freedom, but results in vertically distorted shapes and overall uneven dimensions. Future work to resolve this issue can expand its adoption in the manufacturing of highly conductive 3D organic electronics. Additionally, improvements in our casting method for our PEDOT precursor could allow for the casting of larger, more complex 3D electronics. We also do not fully understand why the various stacked plate PEDOT structures form after solid-state polymerization, or how to control their formation. Further investigations could reveal new applications, including the facile manufacturing of high surface area or fracture resistant 3D electronics. The synthesis of AMPSA-derivatives with various levels of hydrogen bonding remains a challenge left for the field of wearable electronics, as this was not yet achieved in this work.

This dissertation focused on studying the fundamental processing-structure-property relationships of conductive polymers, and was less focused on their application. This leaves great opportunities for the development of our findings and techniques for high performance electronics applications in the future, including their use of as facile introduction of insulating barriers between printed electrodes with DIW printed PEDOT:PSS. With the help of our findings, we will likely also see a greater range of geometries available to producing with CPs and the development of the self-assembly process for other CPs. Our casting method for CPs opens the door for casting of other pure substances that are not currently compatible with common AM techniques. In our research, we successfully merged AM techniques with other manufacturing methods, and we expect to see this exploration continue in the field to expand the range of processable materials and geometric freedom.